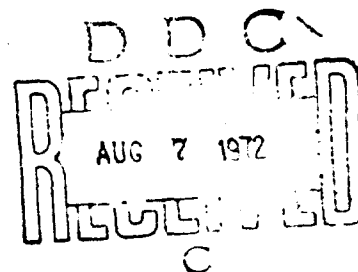UNIVERSITY OF MISSOURI

Rolla, Missouri

AN INVESTIGATION OF THERMAL-

MECHANICAL FRAGMENTATION OF ROCK

D D C

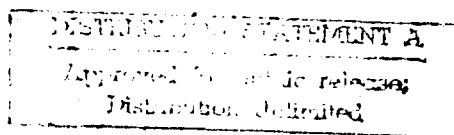AUG 7 1972

C

by

George B. Clark
Terry F. Lehnhoff
Vernon D. Allen
Mahendra R. Patel
Jaw K. Wang

NATIONAL TECHNICAL
INFORMATION SERVICE

Best Available Copy

June 1972

289

AN INVESTIGATION OF THERMAL-MECHANICAL
FRAGMENTATION OF ROCK

George B. Clark
Principal Investigator
(314)341-4365

Terry F. Lehnhoff
Project Engineer
(314)341-4365

UNIVERSITY OF MISSOURI
Rolla, Missouri
65401

ANNUAL TECHNICAL REPORT

June 1972

ACKNOWLEDGMENT

DOCUMENT CONTROL DATA - R & D

(Security classification of title, body of abstract and indexing annotation must be entered when the overall report is classified)

1. ORIGINATING ACTIVITY (Corporate author)	2a. REPORT SECURITY CLASSIFICATION
University of Missouri Rolla, Missouri 65401	Unclassified
	2b. GROUP

3. REPORT TITLE

An Investigation of Thermal-Mechanical Fragmentation of Rock

4. DESCRIPTIVE NOTES (Type of report and inclusive dates)

Annual Technical Report   2-19-71 to 4-19-72

5. AUTHOR(S) (First name, middle initial, last name)

George B. Clark, Terry F. Lehnhoff, Vernon D. Allen, Mahendra R. Patel, Jaw K. Wang

6. REPORT DATE	7a. TOTAL NO. OF PAGES	7b. NO. OF REFS
June 1972	267	76

8a. CONTRACT OR GRANT NO	9a. ORIGINATOR'S REPORT NUMBER(S)
H0210028	
b. PROJECT NO 1579	
c.	9b. OTHER REPORT NO(S) (Any other numbers that may be assigned this report)
d.	

10. DISTRIBUTION STATEMENT

Distribution of this document is unlimited

11. SUPPLEMENTARY NOTES	12. SPONSORING MILITARY ACTIVITY
	Advanced Research Projects Agency Washington, D.C. 20301

13. ABSTRACT

Thermal-mechanical methods of fragmenting rock were investigated to determine their feasibility and to evaluate parameters for possible application of such processes. Theories of temperature distribution and thermoelastic stresses were applied where possible. Most equations involving temperature dependent properties, moving heat sources, and more than one dimension are not susceptible to solution or to mathematical evaluation. The current theory of indentors was extended by means of the theory of plasticity to include factors such as bit shape and friction between the bit and rock. Application of a modified equation for the Rittinger crushing theory based upon surface energy particle size relationships was found to be useful in evaluating the surface energy for thermal-mechanical fragmentation. The Rittinger constant is one of the critical parameters which determines the resistance of rock to crushing. Fragmentation tests included (1) surface chipping-single pass, (2) surface chipping-multiple pass, (3) shallow kerfing, and (4) deep kerfing. Deep kerfing requires only a very small amount of heat for rock removal, although long kerf cutting requires the same specific mechanical energy as pneumatic drilling. The most promising result of the investigation is disclosed by the deep kerfing tests, which show that deposition of heat energy within the rock causes controlled fragmentation with the consumption of very small amounts of specific energy.

14. KEY WORDS	LINK A		LINK B		LINK C	
	ROLE	WT	ROLE	WT	ROLE	WT
thermal-mechanical fragmentation of rock						
specific energy						
bit penetration						
thermal stress						
temperature distribution						
flame jet						
pneumatic hammer						
rock fragmentation						
rapid excavation						

TABLE OF CONTENTS

TABLE OF CONTENTS

TABLE OF CONTENTS

LIST OF TABLES

LIST OF FIGURES

LIST OF FIGURES

LIST OF FIGURES

LIST OF FIGURES

LIST OF FIGURES

LIST OF FIGURES

LIST OF FIGURES

CHAPTER I

INTRODUCTION

Background for Investigation

Methods of excavating soft and medium-hard rocks have advanced in the last decade both in performance and cost advantages much more than methods of excavating hard rock. Difficulty in penetrating hard rocks with mechanical cutters has been the primary factor delaying the advancement of more nearly continuous methods of hard rock excavation. The problems of excavating hard rock by boring machines (bearing and cutter wear due to high thrust) for all types of openings are well-known, and currently drill and blast methods are usually required. New methods of disintegration are desired which may approach being continuous, and possess other favorable characteristics which will make them technically feasible and economically applicable.

Thus, rapid excavation of hard rock by mechanical cutters alone is not presently feasible, and currently used drill and blast methods of excavation are cyclic in nature and lack the advantages of continuous operation and smooth boring ability. When heat sources are used to excavate hard rock by melting, very large quantities of energy are required, and for removal of rock by spallation the process is usually limited to types of spallable rocks composed of a minimum of ten percent quartz. The combination of thermal weakening/spalling and mechanical disintegration (thermal-mechanical fragmentation) appears to offer a promising potential for hard rock excavation because of the non-cyclic nature, methods of application, potential economic feasibility, and possible applicability to hard rocks not containing quartz.

This research project to study the excavation of hard rock using combined mechanical and thermal methods of rock removal is concerned with theoretical studies of the process of heat weakening and spallation, including pertinent aspects of thermoelastic stresses, heat energy coupling efficiency, rock surface temperature, and temperature distribution with depth. Theoretical studies of disintegration include surface chipping for particular indentors, kerf ridge removal, energy requirements, and estimation of efficiency for heat assisted mechanical chipping. Types of rocks with dissimilar composition and spalling characteristics were selected for experimental examination to determine the applicability of the theoretical studies. Several important technical parameters of a technique utilizing pneumatic chippers and rock weakening by heat were investigated experimentally, and pertinent theories of thermoelasticity, heat transfer, and impact by two types of bits were studied in relation to fragmentation.

The experimental difficulties anticipated in the research were test equipment design, and devising techniques for collection of large fragments as well as small particles broken from the large blocks of rock. Evaluation of specific energy, surface energy, and efficiency of energy transfer were among the major technical problems to be solved.

The data and theory developed has added vital knowledge of the response of rock to combined high temperature and impact. The experiments were designed to lead to the development of the prototype of an excavation machine.

The disintegration of soft rock by tunnel boring machines exemplified many of the characteristics of excavation methods which are desired for shafts and tunnels in more effective excavation of hard abrasive rock.

2

In general, some of the more novel types of rock breakage that are being currently studied are aimed at the development of rapid methods of tunnel boring several years in the future.

Rock Properties

Considerable laboratory research has been performed on the properties of rock which affect their resistance to disintegration. Thermal and chemical means of weakening rock have been devised on small laboratory specimens, but none of these appear to have been applied to large blocks or to rock in situ. The science and technology of mechanical and thermal fragmentation, however, has advanced far enough that it has proven profitable to apply recent findings to disintegration of rock on a larger scale. Review and analysis of existing theory and data (Refs. 1-3) indicate that mechanical properties of rock such as strength, moduli, hardness, etc. measured by conventional methods, are often only indirectly related to rock resistance to disintegration processes. Thermal properties, however, can be utilized in extending the applications of the theory of thermal stresses, heat transfer, and related phenomena.

While extensive studies have been made of the fracture of metals and rock under static loads, only a relatively small amount of research has dealt with rock fracture under dynamic loads. Effective dynamic tensile strengths have been found to be 5 to 13 times as great as static (Ref. 4). However, most fracture studies were performed by means of the Hopkinson bar which breaks the rock by means of a pulse reflected from a free surface.

The ambient temperature static data available for the rocks tested in this project are listed in Table (A-1) of Appendix A.

Excavation System Characteristics

The critical characteristics of an effective method of rock disintegration-excavation system are:

1. Capable of operation in all types of rock and rock conditions

2. Minimum shutdown time

3. Continuous operation to approach simultaneous breaking, loading, and haulage

4. Economical operation costs

5. Favorable or tolerable environmental factors

6. Reasonable capital costs and depreciation

7. Reasonable overhead costs

The first step in the evaluation of a prospective method of excavation is the verification of its technical feasibility. If the investigation of the fragmentation basic process or processes establishes that critical parameters are favorable, then the feasibility of incorporating them into an operating system and the economics of the system must be established. Important specific factors which influence the overall evaluation are as follows:

Rock Disintegration and Excavation Parameters

A. Characteristics of technique

    1. State of research and development

        a. Theory

        b. Research methods

        c. Research data

        d. Development

        e. Application

2. Energy requirements

    a. Type, electrical, mechanical, chemical, etc.

    b. Source, fuel, explosives, etc.

    c. Degree of fragmentation

    d. Efficiency of energy transfer

    e. Efficiency of energy usage - specific energy of disintegration

    f. Overall efficiency of process

    g. Possible use of waste energy

3. Fracturing process

    a. Geometry of energy application, external, internal, etc.

    b. Temperature levels and effect

    c. Character of energy application - impact, thermal expansion, etc.

    d. Relationships to other techniques and possible complementary uses

    e. Degree of disintegration (2c above)

B. Application of Technique

1. Ability to control separation of rock masses

2. Ability to preserve strength of peripheral rock in opening

3. Ability to make smooth opening

4. Power requirements and efficiency

    a. At the rock interface

    b. Overall

5. Environmental factors, noise, fumes, etc.

6. Adaptability to changes in properties and structure of rock

7. Equipment requirements for application

    a. At face - state of development

    b. Back up - state of development

    c. Limiting requirements

8. Applicability

    a. To horizontal openings

    b. To vertical or inclined openings

9. Character of method using technique

    a. Cyclic

    b. Semi-cyclic

    c. Continuous

    d. Down time of continuous method

10. Thrust requirements

11. Metallurgical requirements of machines

12. Research and development requirements

    a. Type of additional research required

    b. Estimate of time for research and development

    c. Estimate of relative costs

13. Possible use of complementary methods

14. Relationships of disintegration to mucking, haulage and hoisting

15. Estimated costs - unit and overall

    a. Research and development

    b. Capital investment in operating machine

    c. Operating costs, energy, labor, etc.

    d. Support costs

    e. Overhead

    f. Other

16. Constraints

Excavation Techniques

The most critical factor in the functioning of a disintegration technique is almost always the effective transfer of breakage energy into the rock. Of almost equal importance is the efficiency and cost of producing the energy.

Processes of rock disintegration by drilling are similar to those which are used or proposed for use in full face disintegration of tunnels, shafts, etc. Characteristics of novel methods have been summarized (Ref. 4) according to status, rock removal mechanism, specific energy, maximum power to rock and maximum potential drilling rate, as well as those for conventional drills.

For full face disintegration versus drill hole cutting there are fewer restrictions on the power which can be delivered at the rock. Field tests have been made of several novel drills but the only ones in operation are conventional rotary and jet piercing, although the Russians claim to have used explosive drilling successfully to limited depths in some types of rock. In addition, shaped explosive charges may be employed to produce high velocity metallic jets which are effective in penetration. Some specific energy values for tunnel boring machines are available and much of the fragmentation energy is utilized in producing very fine particles.

The values of specific energy for drilling by Maurer (Ref. 4) give only the energy to fracture the rock, and not the total energy requirements or the efficiency of the system. Approximations for total energy requirements are available for some of the preferred methods (Table 1).

Table 1

Estimates of Total Energy Consumption*

joules/cc

Chemical explosive	10-30	total available energy
Pneumatic moil	30-110	total required energy
Flame jet	15,000+	spalling
Electron beam	12,000+	melting
Laser	12,000+	heat weakening and melting
Radiant heat	6,000	heat weakening and spallation

* From estimates given at Rapid Excavation Conference, Deerfield, Mass., July 20-25, 1969.

7

A study of the feasibility of flame jet tunneling by the United Aircraft Research Laboratories (UARL) (Ref. 5) concluded that it may be feasible in rocks with good spallability. One geometry favorable for suggested breakage was by means of annular kerfing and fracture of large blocks of the kerf with a breaker arm. Thus, the overall specific energy for combined thermal spalling and breaking was believed to be economical even though the specific energy of flame jet cutting may vary from 1500 to 6000 joules/cc. The predicted rate of advance for a 30 foot tunnel, however, was comparable only to rates achievable by conventional drilling and blasting.

For complete small particle fragmentation by flame jets major problems exist in environmental control in that noxious fumes and high temperatures are continuously created by the flames which cause the spallation. The attendant engineering problems and cost of creating acceptable environmental conditions increase rapidly with the increase in size of tunnel so that the rate of advance makes tunnels larger than 30 foot diameter impractical (Fig. 7, p. 33, Ref. 5). Mechanical breakage of rock between kerfs was not experimentally evaluated.

The investigators at UARL also evaluated the spallability of some rock types in the Northeast Corridor, i.e., between Washington, New York, and Boston. About one-third of them had high spallability indices. Thus, this method apparently has somewhat limited applicability for tunneling in this geographical area. The presence of mud seams or water in the face of a tunnel could stop spallation altogether.

Infrared heat units have been recently adapted for use at a copper mine for heat weakening and spallation of a shale ore bed. Their efficiency of heat generation and transfer into rock are both reported to be good. Temperatures are high and the energy has excellent penetrability,

i.e., usual heat diffusion processes are not involved to the same degree at the rock-air interface. The high intensity radiant heat units employed for this type of heating are stock items, but depth of penetration of infrared heat into rock has not been evaluated.

To the present, laser beams have been employed only in the heat weakening of small beams and cutting of slabs of rock in the laboratory. At their current energy levels their overall efficiency of transfer of energy to rock ranges from 3 to 6 percent for heating, and as high as 30 percent for melting. Their dispersed thermal effects are much the same as radiant heating, although more concentrated.

Thermal-mechanical Fragmentation

Thermal spalling may be caused either by (1) differential thermal expansion of mineral constituents, (2) thermal decrepitation, (3) expansion of entrapped water, or (4) thermal destruction of the binding material between grains.

The properties of rock significant in thermal weakening or disintegration (Ref. 6) are thermal expansion, temperature phase changes, diffusivity or conductivity, heat capacity, heat of fusion, heat of vaporization, decrepitation, and change in chemical form (Ref. 2). Some rocks with above ten percent quartz spall because of thermal expansion and phase changes (Ref. 6). Dolomites may spall because of a two-stage decomposition. Shales containing cognate water have been found to spall with considerable energy (Ref. 7), and some sandstones experience grain-by-grain disintegration because of weakening of the binding material by heat (Ref. 2).

The response of rocks to heat varies with the intensity of heat (temperature), the length of time of application, the nature of the energy which heats the rock, and the composition and structure of the rock. The same factors which cause spallation, which may be due to thermal expansion, decrepitation, expansion of entrapped water or destruction of

9

mineral grain binders, may also cause weakening of the rock structure. Such weakening changes the resistance of the rock to disintegration by various mechanical processes such as chipping, impact cutting or abrasion.

Fragmentation of solid rock caused by thermal expansion is produced by a set of stresses imposed on the rock material in a given set of conditions. Modification of the response of the rock may result if the imposed stress state and/or the properties of the rock material are altered. Thermal-mechanical fragmentation alters the rock material as well as increasing the local stress state. The material properties are changed during heating because of microcracks which form, and because the basic mechanical properties are different at elevated temperatures. The stress state is changed by the superposition of thermal and mechanical stresses and by the fact that the original continuous medium becomes discontinuous after thermal treatment.

Mechanical stresses are produced when indentors are forced or impacted against a rock surface. Wedge- and spherical-shaped tungsten carbide indentors are commonly used for hard rock and the force is usually supplied by pneumatic hammers or hydraulic loading of rolling cutters. A pneumatic hammer was used in this research. Fracturing occurs when induced stresses exceed the tensile or shear strength of the rock. Beneath the area of indentor contact a zone of finely crushed rock is created from which significant fractures are initiated. These fractures propagate along curved paths to the surface, breaking off chips of rock. The fine crushing results from intense stresses created by the initial approximate line or point contact of the indentor. It should be noted that the indentor impacts on softened or fractured material if thermal treatment precedes the mechanical device. However, fruitful theoretical studies of randomly discontinuous material are not possible with the present state-of-the-art.

The assumption that the material is continuous permits a reasonable first approximation that allows important process parameters to be investigated.

Nonuniform heating of rock produces thermal stresses by the interaction of forces from different local sections of the rock that expand different amounts, either due to rock geometry or the following factors. Because of the low thermal conductivity of rock (Table I, Appendix A) the surface may be at the spalling temperature while only 1/8 inch or less below the rock may be at its ambient temperature. This sharp thermal gradient is a primary factor in creating the thermal stresses that cause fracture. The nonhomogeneous or orthotropic composition of rock assists the formation of localized thermal stresses because individual grains and crystals of the rock have different coefficients of thermal expansion, and orthotropic rocks expand different amounts along two perpendicular axes. Other important processes in creating thermal stresses are the phase changes that occur in some minerals with increase in temperatures. Their importance is characterized by quartz, which undergoes 0.82 percent volumetric expansion during the alpha-to-beta phase transition at 573 degrees C. Minerals surrounding the quartz crystals constrain the expansion and thus produce high thermal stresses. High thermal stresses are also created in relatively uniform rock by the geometry of the heat source and its application on flat surfaces, in corners or holes in the rock.

Rocks of many types permanently lose strength after being heated, especially if the rock is heated to temperatures above 600 degrees C. Reasons for this permanent reduction in strength are chemical changes, spalling and/or anisotropic thermal expansion, and the formation of microcracks along grain boundaries. Microcracks form as the rock crystals and grains expand and contract due to heating and cooling. In this weakened condition a rock may be more susceptible to removal by some mechanical processes.

11

If mechanical chipping is applied to the rock while thermal stresses are still present, crack initiation and propagation may be enhanced due to the superposition of thermal and mechanical stresses. The direct combination of these two processes has been referred to as thermal-mechanical fragmentation.

Plan and Objectives of Research

The research program was divided into three general areas: (1) theoretical studies of heat energy coupling and the mechanics of heat weakening of rock by surface heating; (2) theoretical studies of mechanical disintegration (chipping) and the effects of heat thereon; and (3) laboratory investigations of the important parameters of heat assisted near surface chipping. Significant deep kerfing tests were performed for three rocks.

The heat energy coupling studies were concerned primarily with the efficiency of heat transfer from high temperature moving flame sources (such as flame jets and acetylene torches) into the surface of the rock. The classical equations for static, quasi-static and moving sources have been employed to describe the transfer phenomena into homogeneous solids and the equation for the quasi-static case was analyzed employing the parameters of the flame jet-rock system. For simple conditions, if the temperature distribution is known the thermoelastic stress field in the rock may then be calculated and possible modes of failure predicted, high stress concentrations being created by large thermal gradients.

The existing theories of penetration of indentors into rock required extension to apply theories of plasticity to the reaction of rock to pressure from wedge indentors of various angles and friction at the rock interface, for flat-edged indentors and for hemispherical indentors. Preheating of the rock and microfracturing decreased the effectiveness of the indentors in removing chips from some types of rock but also decreased the friction and wear in the indentors in some cases.

12

Experimental work was conducted to evaluate the basic parameters involved in the above theories and the extent to which the theories can be applied to six types of rock (Appendix A). This included (1) the evaluation of energy requirements for fragmentation with and without thermal weakening; (2) investigation of important parameters of fragmentation including width of kerf, optimum indexing, and size and shape of chippers; (3) temperature measurements of rock during thermal weakening; and (4) the development of tests to measure resistance to disintegration, and a comparison of results between mechanical and thermal-mechanical methods of disintegration.

Tests were conducted with a commercially available pneumatic chipper (jackhammer) equipped with cross-wedge and button bits. Heat tests were conducted largely with a standard flame jet, and a few tests were run with acetylene welding torches. A drop crushing test similar to that employed by Gross and Zimmerly (Ref. 8) offers promise as a means of evaluating rock resistance to impact and thermal breakage as well as for calculating values of breakage (surface energy) by means of Rittinger's law of crushing.

Variation in some parameters was somewhat restricted by the characteristics of the heat source (flame jet) and pneumatic chipper (jackhammer) chosen. That is, the flame jet operates essentially at one level of heat output which is required to maintain flame stability, and heat flux may be varied by changing the standoff distance. Likewise, the energy output of the jackhammer can be varied only over a small range, because of its optimum operating characteristics, and energy transmitted to the rock is difficult to measure accurately.

CHAPTER II

HEAT ENERGY COUPLING

Heat Coupling - Moving Flame Source

For one to evaluate the process of thermal fragmentation of rock materials resulting from the application of a heat source the temperature distribution inside the rock material must be determined. The heat energy coupled into a rock mass from an energy source must be known to determine whether the source can be economically used for thermal weakening, spalling, or splitting of rock materials. A combined experimental and numerical method was used to estimate the thermal energy crossing a rock surface from a flame.

Measurements of the surface and subsurface temperatures were made to define the heat penetration from a heat source into a rock material. From the temperature measurements the heat energy coupling efficiency was estimated.

General Theory

Heat Penetration. The temperature distribution within the rock material can be determined by either solution of heat transfer equations directly or experimental measurement of the temperatures. Rocks are complex materials with inherent inhomogeneity and anisotropy as well as temperature-dependent properties, and because of their character the heat conduction equation becomes nonlinear. The heat transfer equation for a moving heat source over a rock surface is not only nonlinear but transient and three-dimensional. A solution for a problem of this type is not available. An experimental approach was taken to measure the surface temperature and selected sub-surface temperatures of the rock. The experimental temperature measurement then defines the depth of penetration of the heat.

14

Several rock types were tested to determine if measurable differences in thermal response can be observed (as a function of mineral content). The surface temperatures were correlated with measurements made at various depths in order to better define the heat penetration characteristics. Similar tests were run by Browning, et al., (Ref. 9) using embedded thermocouples. Results of measurements made for a flame jet heat source will later be compared with similar measurements for other heat sources during the second phase of this research project.

Heat Energy Coupling

The calculation of the heat energy coupling efficiency requires the calculation of the heat energy entering the rock surface. The heat transferred to a plane surface normal to a gas jet was studied by J.E. Anderson and E.F. Stresino (Ref. 10) for various torches*. Their experimental work was performed using a copper plate which was cooled by water flowing past one side of the copper plate. The heat transferred to the plate was calculated from the rise in the temperature of the water. Copper was used because it is easily machined and has a high conductivity. The same procedure would not be possible with rock because of its low conductivity and brittleness. Other investigators have studied the heat transferred between a gas jet and a plane surface and attempted to obtain a correlation of gas properties with heat transferred. In all of these cases the plane surface was metallic, however, and the material properties remained relatively constant over the range of temperatures studied.

The methods described above are not applicable for rock materials because of their low conductivity and the difficulty in machining. It was therefore necessary to develop a new method of calculating the heat transfer

---

*Note: A recent technical note titled "Impingement Heat-Transfer Rates from Torch Flames" by E.H. Shulte, Jl. of Heat Transfer, pp. 231-233, May 1972 also investigates the heat transfer from a flame torch to a plane surface.

15

from a flame. Since a new method was required the temperature distribution obtained from the heat penetration study was used to estimate the heat entering the rock material. The problem of calculating the heat entering a body from the temperature history inside the body is known as the inverse problem of heat conduction.

Stolz (Ref. 11) and others (Refs. 12, 13, 14, 15) have solved one-dimensional inverse problems. Beck (Ref. 16) used a method of nonlinear estimation to solve a one-dimensional nonlinear inverse heat condition problem. The nonlinearity was due to temperature-dependent material properties. As in the direct method the complex material properties of rock and introducing more than one dimension makes the solution of the inverse problem very difficult. The inverse method is mathematically ill-posed (Refs. 15, 17) and as such can develop oscillations in the solutions.

The temperature histories obtained experimentally are three-dimensional in the space coordinates, thus giving rise to a three-dimensional inverse problem. Solving the three-dimensional nonlinear inverse problem is more difficult than solving the direct problem of heat conduction.

During the second phase of this investigation further consideration will be given to developing a method for converting the three-dimensional temperatures into surface data. A possible technique for eliminating the difficulties of inverting a three-dimensional nonlinear problem would be to devise a one-dimensional experimental test.

For calculation of specific energy of breakage for the fragmentation process an estimate of the heat energy coupling was required. An approximation of the energy entering the body was made from the specific heat and the measured temperatures. Calculation of the heat output of the torch was made based on the heat of combustion and the flow rate of the fuel.

16

The heat transferred from the flame jet into the rock passes through three regions:

1. Region I.   From the torch to the gas film - Forced Convection.

2. Region II.   Through the gas film to the surface - Conduction.

3. Region III. Through the rock material - Conduction. Figure (1) illustrates the three regions. Anderson and Stresino (Ref. 10) state that radiation from their torches to a metallic surface was small when compared to the heat transferred by convection. The same assumption was made in this report for the flame jet impinging on a rock surface. Three factors (Ref. 10) which complicate the analysis of a flame jet impinging on a surface are:

> "Reliable values of the effective thermal conductivity in the presence of dissociation-recombination reactions in a chemically complicated gaseous mixture are usually not available; the heat-transfer intensity distribution obtained when a gas jet impinges on a flat plate is imperfectly understood; and in practical cases such as those involving flames steep temperature gradients often exist in the gas stream."

Metzger (Ref. 18) studied the heating of a surface by a high velocity air jet. For a first approximation the results for an air jet can be used to analyze a flame jet.

One of the primary factors describing the efficiency of heat transfer from a hot gas to a solid is the value of the heat transfer coefficient. An equation by Metzger (Ref. 18) described by Carstens (Ref. 19) utilizes the relationship between Stanton, Reynolds, and Prandtl numbers and the model geometry for a circular nozzle:

$$(N_{St})(N_{Re})^{0.434}(N_{Pr})^{0.63} = 0.74 \left(\frac{R_o}{D}\right)^{-0.434} \tag{1}$$

The symbols employed are defined below. The above equation may be re-written in terms of basic quantities involved in the dimensionless factors as:

$$\left(\frac{h}{C_p g}\right)\left(\frac{DV\rho_g}{\mu}\right)^{0.434} \left(\frac{C_p \mu}{k}\right)^{0.63} = 0.74 \left(\frac{R_o}{D}\right)^{-0.434} \tag{2}$$

This may be rearranged and with R and V changed to units of in. and ft/sec, respectively, and the transfer coefficient expressed as:

$$h = 0.06225 \ C_p g \ \left(\frac{\mu}{V\rho_g R_o}\right)^{0.434} \left(\frac{k}{C_p \mu}\right)^{0.63} \tag{3}$$

Carstens, et al., (Ref. 19) utilized a plane front equation to define the temperature distribution within the rock, and the quantity of heat flowing into the rock. The latter was integrated over an area, approximated for short periods of time and summed for the total time to approximate a transient condition.

Temperature equation:

$$T_y = (T_f - T_R)\left[erfc\left(\frac{y}{2\sqrt{\kappa t}}\right) -exp\left(\frac{yh}{k_R} + \frac{\kappa t h^2}{K^2_R}\right)erfc\left(\frac{y}{2\sqrt{\kappa t}} + \frac{h\sqrt{\kappa t}}{K_R}\right)\right] + T_R \tag{4}$$

The rate of heat transfer is given by:

$$q = 2\pi R_o^2 h \ (T_f - T_s), \tag{5}$$

The total heat flow is calculated from:

$$Q = \int_0^t q \, dt \qquad (6)$$

Nomenclature for the above equations is as follows:

C_p Specific heat at constant pressure of exhaust gas - Btu/lb-F

D Exit diameter of jet nozzle - ft

g Mass velocity of exhaust at nozzle exit - lb/hr-ft^2

h Heat transfer coefficient in wall film - Btu/hr-ft^2-F

k Thermal conductivity of exhaust gas - Btu/hr-ft-F

k_R Thermal conductivity of rock - Btu/hr-ft-F

N_{Pr} Prandtl number - dimensionless

N_{Re} Reynolds number - dimensionless

N_{St} Stanton number - dimensionless

q Rate of heat transfer into rock surface - Btu/hr

Q Total heat transferred into rock in time, t - Btu

R_o Radius of rock wall target - in.

t Time - sec

T_f Exhaust gas temperature at wall - °F

T_R Equilibrium rock temperature prior to heat addition - °F

T_y Temperature in rock at distance y from surface - °F

T_s Temperature at rock surface - °F

V Exhaust gas velocity at nozzle exit - ft/sec

y Linear distance into rock from surface - ft

κ Thermal diffusivity of rock - ft^2/hr

ρ_g Exhaust gas density - lb/ft^3

μ Exhaust gas viscosity - lb/hr-ft
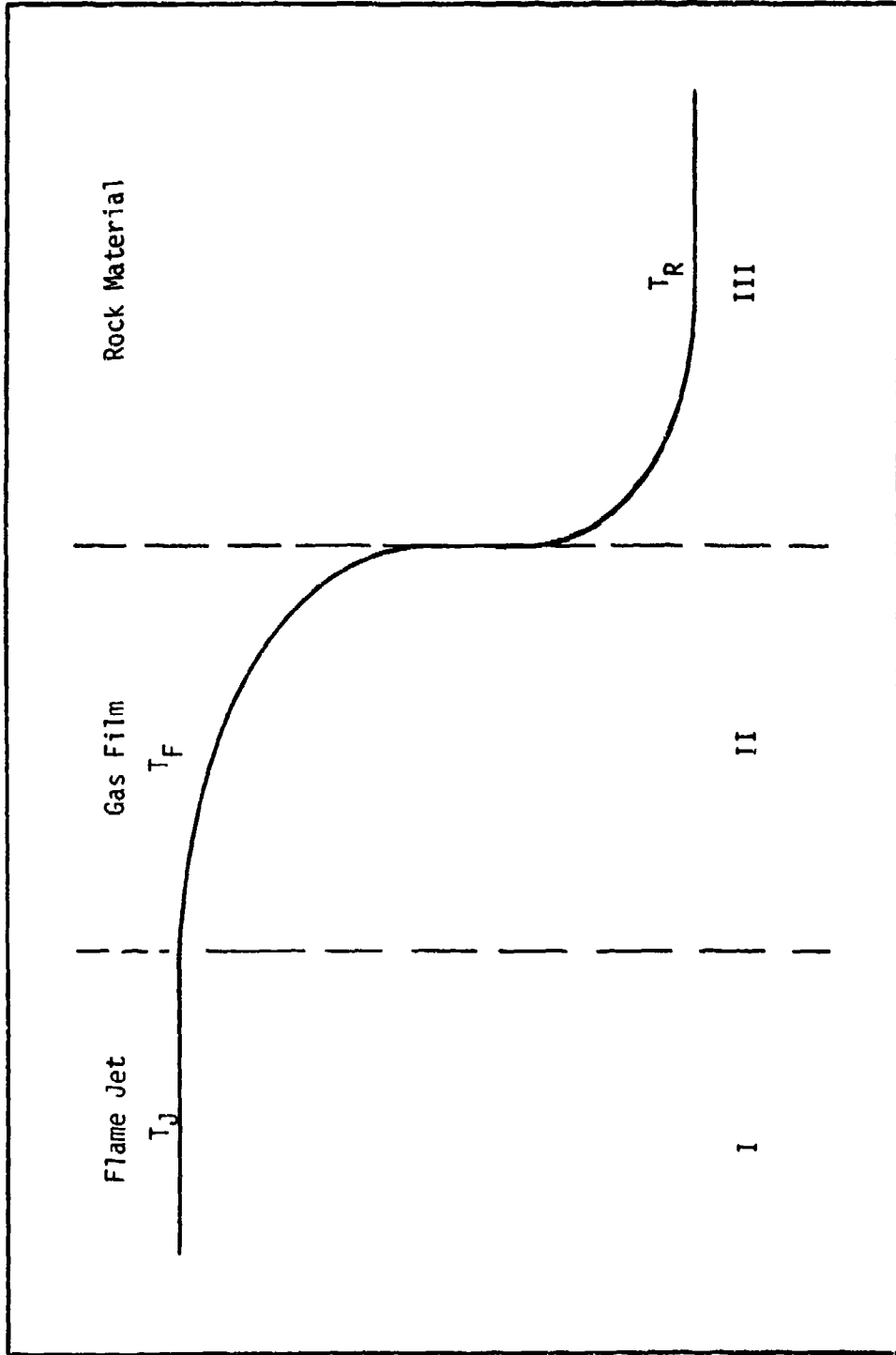
Fig. 1. Heat Transfer Regions

From the above equations it can be stated that the instantaneous rate of heat transfer into the rock depends upon the heat transfer coefficient, and the temperature difference between the rock surface and the gas temperature at the wall. When a flame jet is initially applied to the surface of a rock at ambient temperature, the temperature of the gas film at the surface is much lower than the exhaust gas temperature. Also, as the rock surface is heated, the temperature difference between the rock and the gas film decreases with time, even though the gas film temperature may also rise.

The rise in temperature of the surface of the rock depends in turn upon the rate at which heat is conducted into the rock from the surface, i.e., upon k_R and κ, both of which may also vary with temperature. The relationship between these thermal factors is $\kappa = \dfrac{k_R}{\rho C_R}$ where C_R is the heat capacity of the rock.

Inasmuch as the spallability and tendency to generate microfractures is largely dependent upon the temperature gradient, a low value of conductivity would appear to be one of the major contributing factors to rock spallability and microfracture.

Rosenthal (Ref. 20) was able to obtain a good correlation between a moving point source and experimental data for mild steel and an arc welder. Surface temperature curves with high gradients and a high peak temperature were obtained (Fig. 2). An arc welder will produce a heat source not unlike a point source while a flame jet is a source distributed over a finite area. The size of the area is dependent on the standoff distance of the torch from the surface. Rosenthal made a quasi-stationary assumption and derived an equation for the temperature distribution from a moving point source into a half space as

$$T - T_0 = \frac{q}{2\pi k}\, e^{-\lambda v \varepsilon}\, \frac{1}{r^*}\, e^{-\lambda v r^*} \tag{7}$$

21
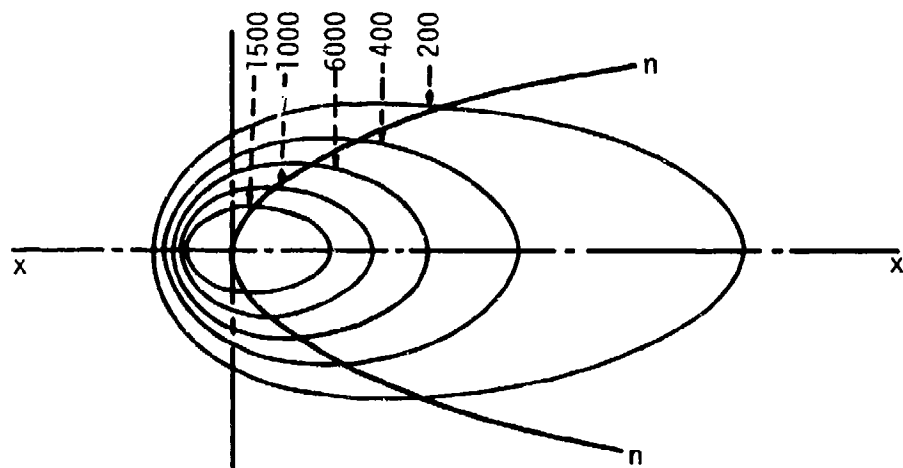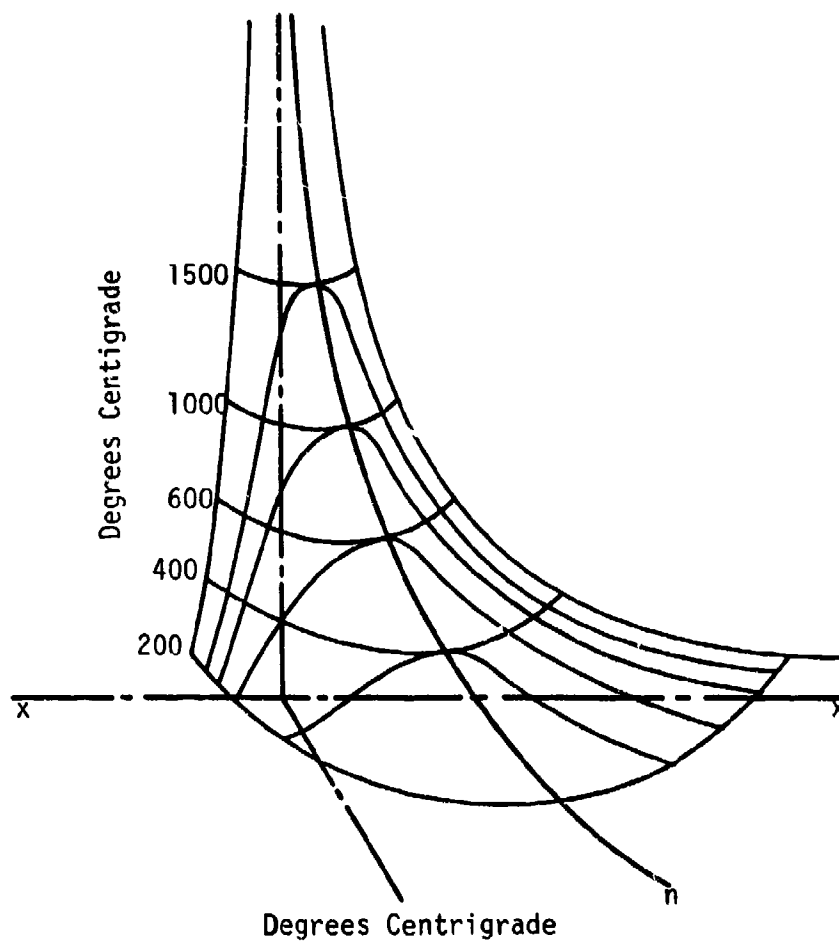
Fig. 2.   Temperature Distribution in Thick Butt Welded Plate -
            Mild Steel

22

where

  c = specific heat

  k = thermal conductivity

  q = rate of heat transfer into rock surface

  $r^* = \sqrt{\epsilon^2 + y^2 + z^2}$

  T_o = initial or reference temperature of surface

  v = velocity of the heat source

  x = direction of movement of the heat source

  ϵ = x-vt

  λ = cρ/2k

  ρ = density

The physical properties of Dresser Basalt and the speed of the flame
jet was used in equation (7) to calculate temperature distributions. A
source strength of 60 cal/sec was chosen to produce subsurface temperatures
similar to the experimental curves obtained for the flame jet. The peak
value of the subsurface temperature decreases rapidly with a depth of 1 mm
in Dresser Basalt (Fig. 3). From the isothermal diagrams made from the
temperature distribution (Figs. 4 and 5) it can be seen that for a point
source moving on Dresser Basalt the high thermal gradients all occur near
the source and the temperature falls off rapidly within the first milli-
meter of the surface. While the point source does not represent the flame
jet accurately, calculations indicate that the depth of penetration into
rock material is very shallow and the thermal gradients are highest with-
in one millimeter of the surface. This is borne out experimentally when
the flame torch is passed over a spallable material and a large number of
particles of 1 mm and smaller are produced.
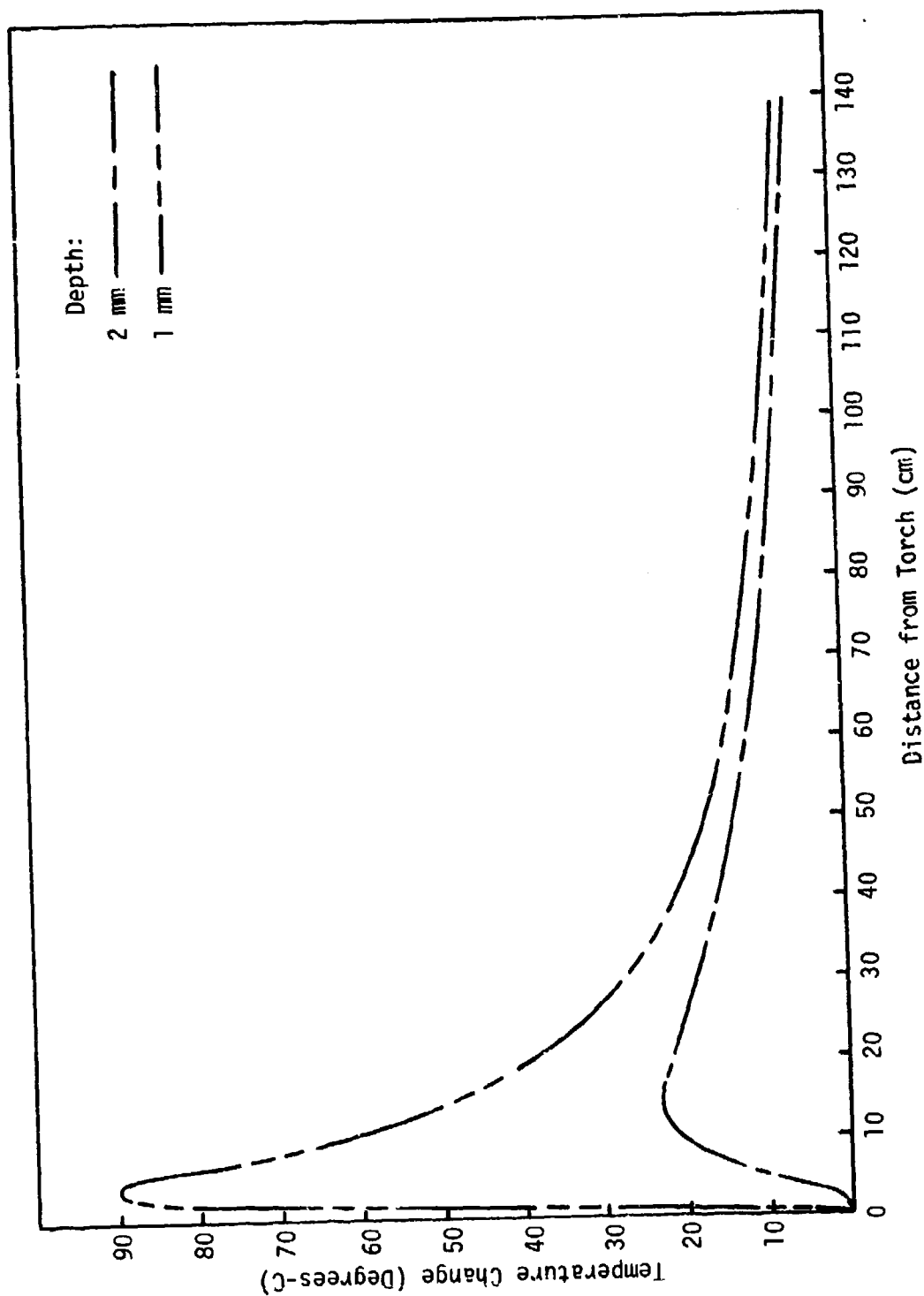
Fig. 3.   Subsurface Temperatures Point Source - Dresser Basalt
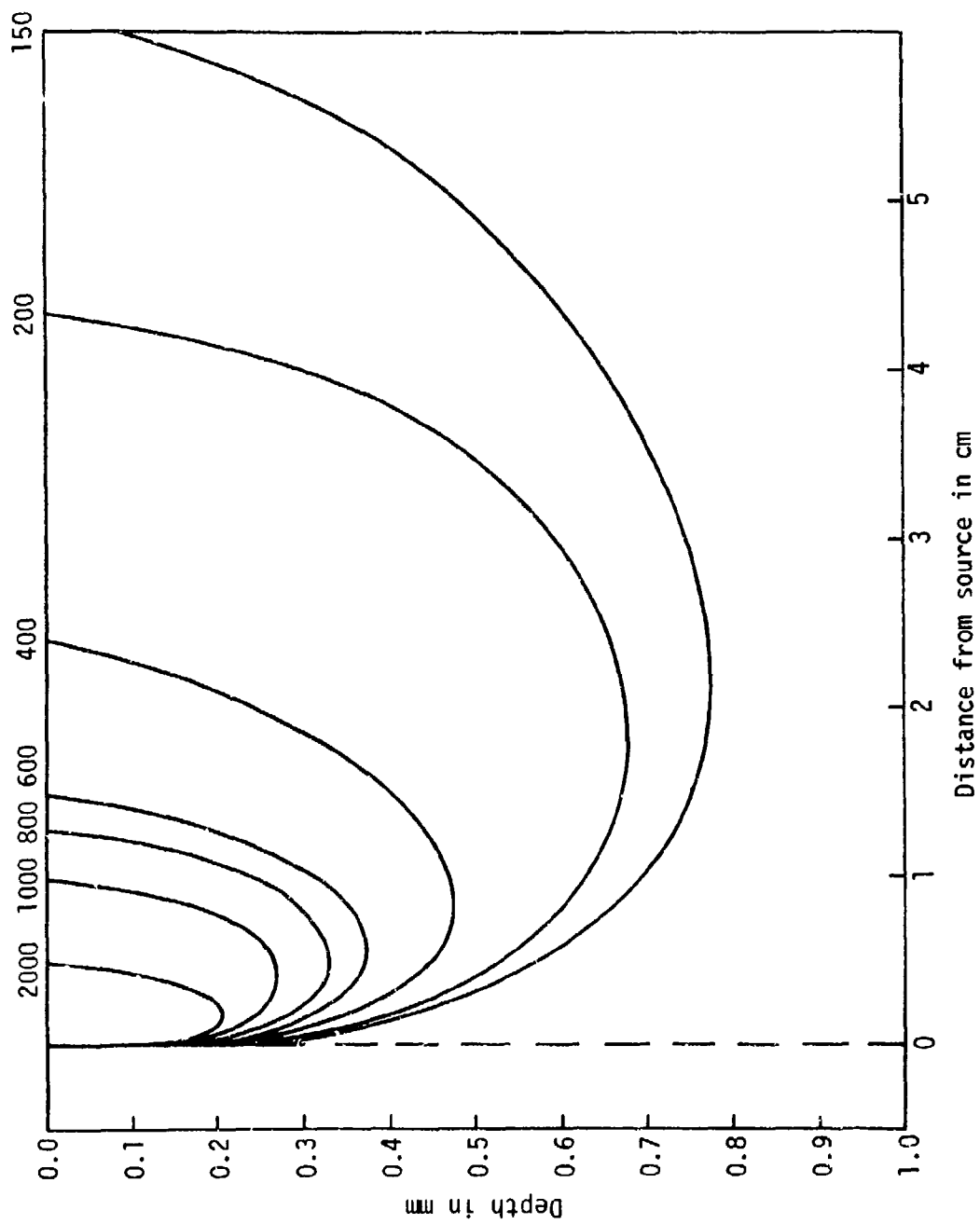
Fig. 4. Isothermal Lines for Point Source - Dresser Basalt
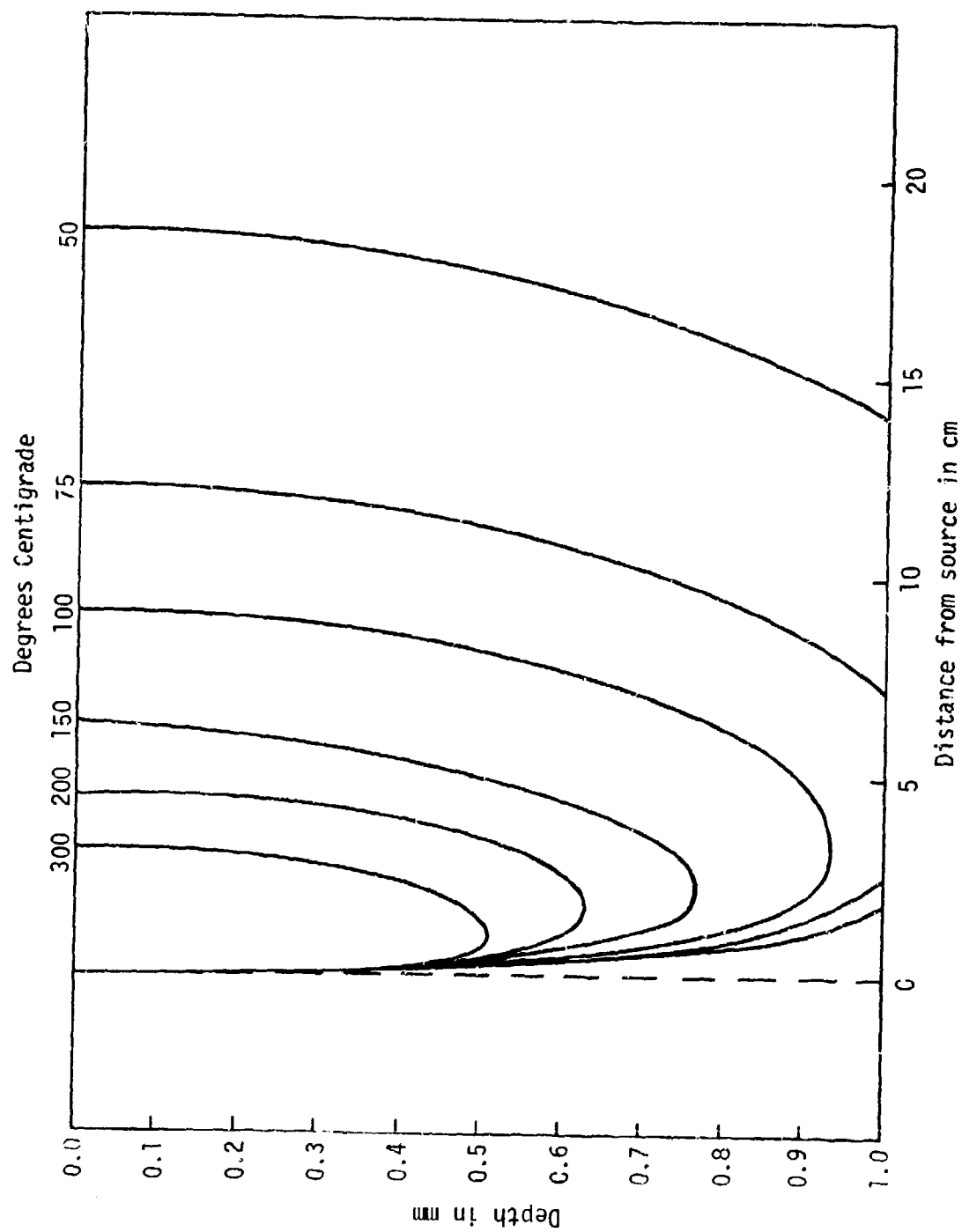
Fig. 5.   Isothermal Lines for Point Source - Dresser Basalt

While the 1 mm subsurface curve is much sharper than the experimental 1 mm curves the 2 mm analytical and experimental curves have much the same shape. The similarity of the deeper curves indicates that once the wave front has reached a sufficient depth it has dispersed enough that it makes little difference whether it was produced by a point or finite area source.

Temperature Measurements - Previous Research

Thirumalai (Ref. 21) employed a miniature oxy-hydrogen torch as a stationary heat source to study the temperature distribution. The torch delivered a heat flux of 170×10^4 watt/m^2 (150 Btu/ft^{2}sec). Thermocouples were embedded from the back side of the slabs of rock at varying depths from the test surface to determine thermal gradients (Table 2). Sioux quartzite spalled readily and showed the highest thermal gradient, while charcoal granite spalled only slightly with partial melting, and basalt melted at the experimental temperature. The latter also demonstrated an increase of thickness of the heat layer.

Experimental Procedure

A surface temperature resistive gage was bonded with ceramic cement to the surface of a 1' x 1' x 1" rock specimen. Chromel-alumel thermocouples (.005" diam) encased in Omegatite were placed in holes (2 mm diam) drilled in the rock slab from the back side (Fig. 6). One hole was drilled through the surface and a chromel-alumel thermocouple placed in the hole to expose the thermocouple to the surface. The torch was passed over the rock specimen at a constant speed and the temperature relative to the torch position recorded.

Preliminary surface temperature measurements were made at a specified point on the rock surface for three traverse speeds, three offset distances from the plane of the sensors, and the torch distance of 14 in. from the

Table 2. Experimental Maximum Temperature and Average Thermal Gradient of Heat Layer During Spalling (12)[1]

Depth of Central Sensor mm	Recorded Thickness of Heat Layer mm	Maximum Temperature during Spalling °C	Average Thermal Gradient °C/mm
		Sioux Quartzite	
1.59	0.85	222	262[2]
1.59	1.06	250	236[2]
6.35	1.02	194	191[2]
6.35	.85	194	229[2]
6.35	1.27	255	200[2]
9.53	.73	167	230[2]
12.70	1.02	194	191[2]
12.70	1.27	222	175[2]
		Charcoal Granite	
3.18	≤3.18	350	≤111[3]
3.18	≤3.18	320	≤102[3]
3.18	≤3.18	330	≤105[3]
		Dresser Basalt	
3.18	>3.18	---	<60[4]
3.18	>3.18	---	<65[4]

[1] Constant incident heat flux of 170×10^4 watt/m^2 (150 Btu/ft^2/sec) for all the tests.
[2] Progressive spalling.
[3] Partial melting - mechanical removal of the melt was necessary.
[4] No spalling - continuous melting - gradients calculated from the recorded rate of temperature rise.

Platinum Resistive Gage

4 mm

2 mm

1 mm

5.08cm

5.08cm

5.08cm

5.08cm

Alumel-Chromel
Thermocouple

Omegatite
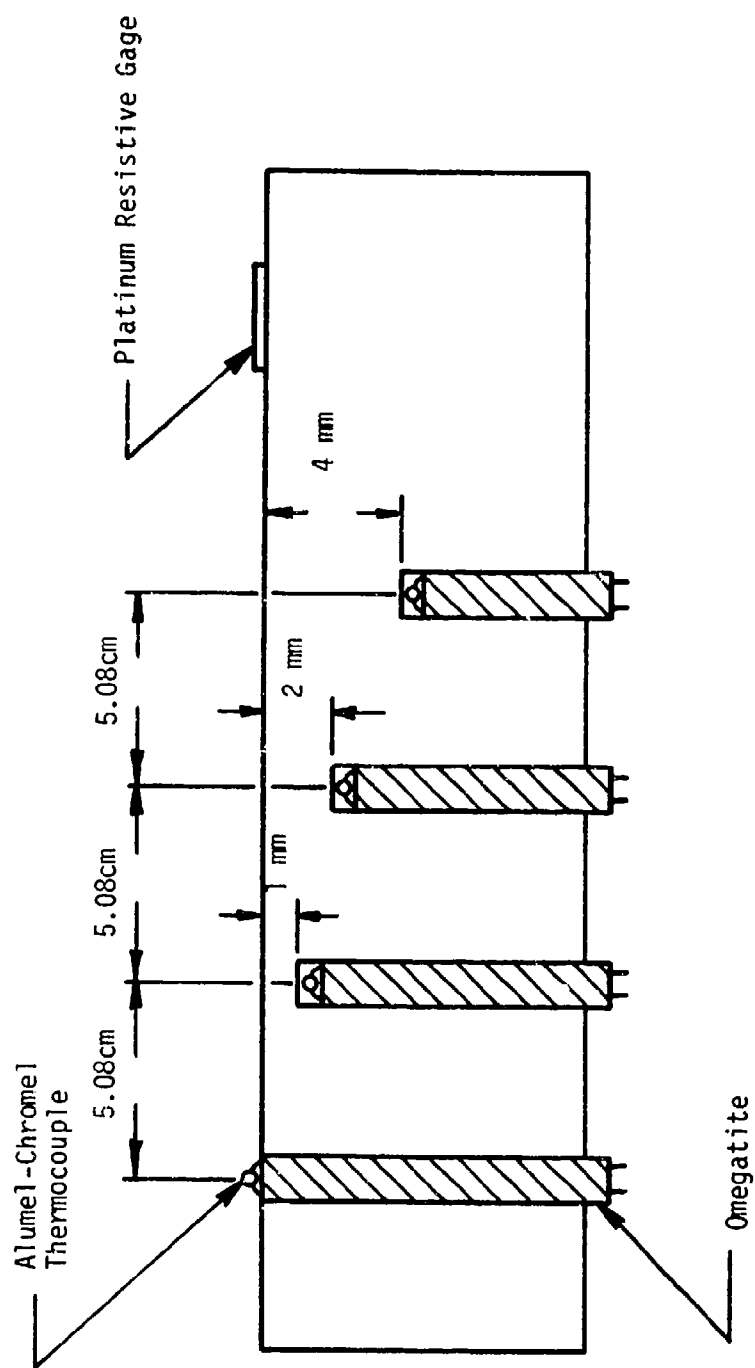
* Note: Basalt has additional sensors at 3mm, 5mm, 6mm

Fig. 6.   Locations of Temperature Sensors for Temperature Measurements

29

rock (Figs. 7, 8, and 9) using Missouri Red Granite. Temperature magnitude and duration increased with smaller offset and decrease in table speed. The block diagram (Fig. 10) illustrates the instrumentation by which surface temperatures were obtained.

Subsurface temperature measurements were made on the following rocks at the depths indicated for one traverse speed and three offset conditions:

A. Dresser Basalt   1 mm, 2 mm, 3 mm, 4 mm, 5 mm, 6 mm

B. Missouri Red Granite   1 mm, 2 mm, 4 mm

C. Charcoal Grey Granite   1 mm, 2 mm, 4 mm

D. Buena Black Granite   1 mm, 2 mm, 4 mm

Typical curves for Dresser Basalt (Figs. 11 and 12) show that the significant temperature rise occurs only near the surface. Other recorded temperature curves appear in Appendix B. The block diagram of Figure 13 illustrates the test setup used to obtain the subsurface temperature curves. The electronic equipment (Fig. 14) consisted of two Tektronix X549 dual trace storage oscilloscopes, four ice reference junctions, and a specimen of rock with four thermocouples.

Heat Source. The heat source used in the tests described in this chapter was an oxygen kerosene FSJ-6 stone-shaping flame jet torch. Stoichiometric calculations (manufacturer's) give the maximum combustion energy as 450,000 Btu/hr for complete combustion. The flame jet had an orange-yellow flame signifying incomplete combustion.

Although the flow on the kerosene and oxygen was closely controlled the temperature data indicated that there were differences in the torch temperature for different tests (Figs. 15 and 16). The gas film temperatures obtained when the torch was operated at standoff distances of 8, 10, and 14 inches (Figs. 15 and 16) show considerable scatter. The leveling

30
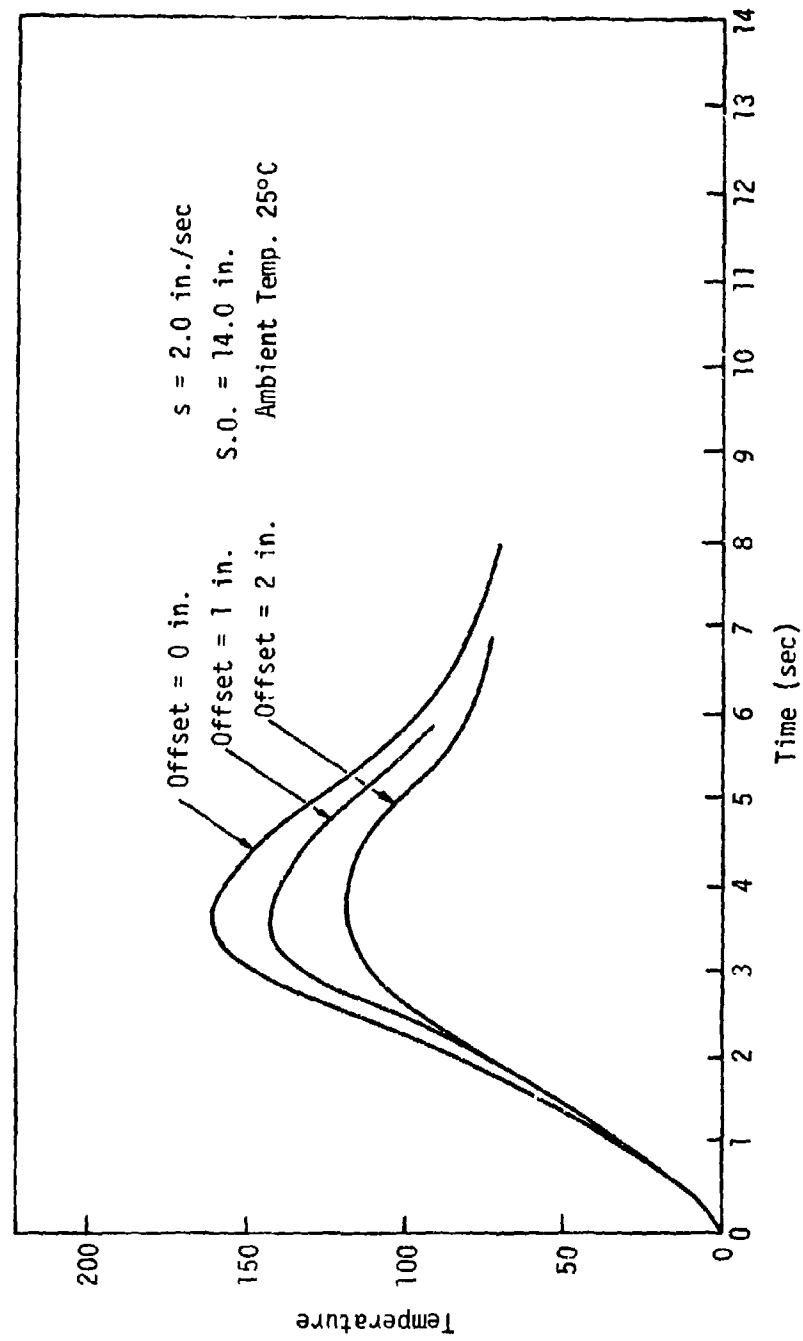
Fig. 7.   Surface Temperature at a Fixed Point due to a Moving Heat Source - (Mo. Red Granite)

31
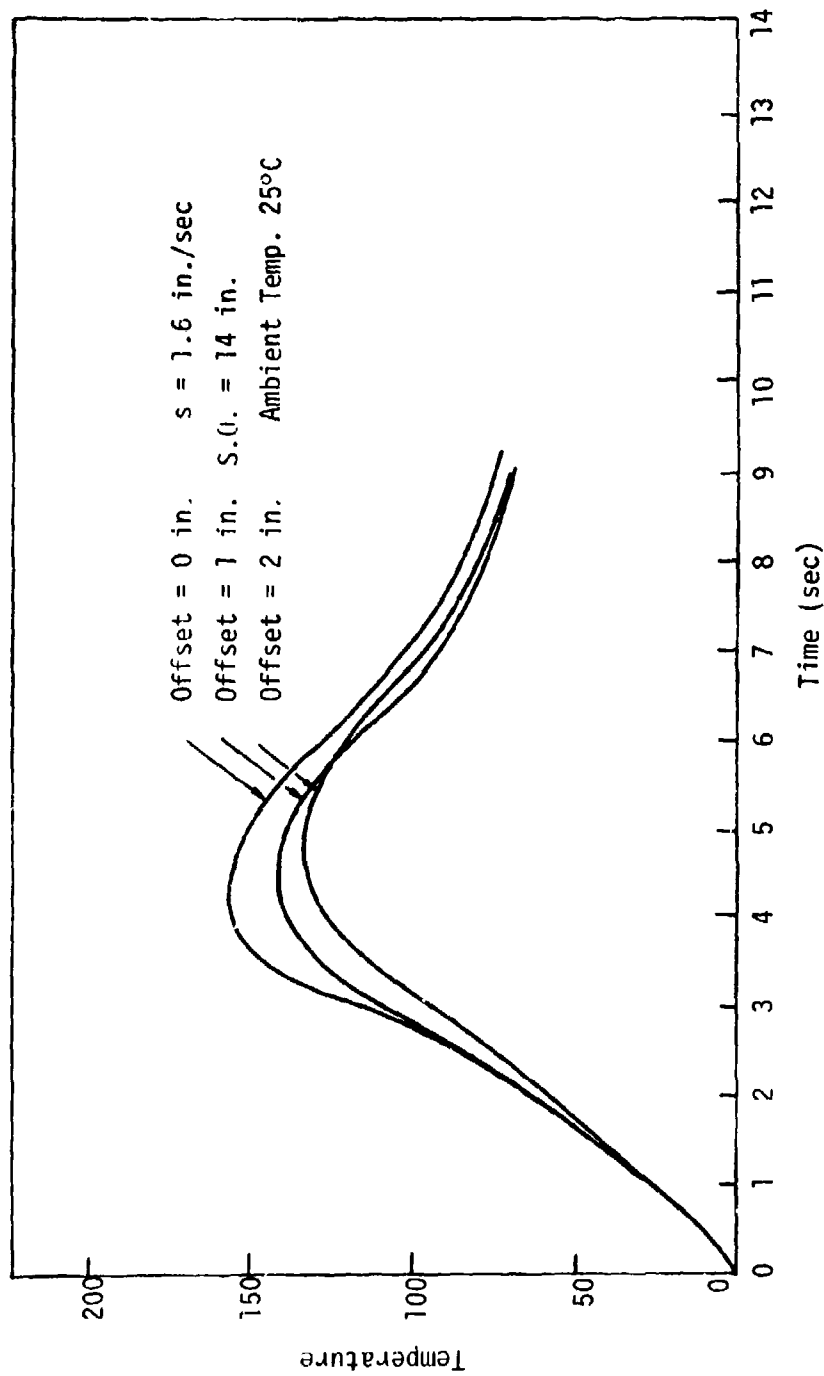
Fig. 8.   Surface Temperature at a Fixed Point due to a Moving Heat Source (Mo. Red Granite)

32
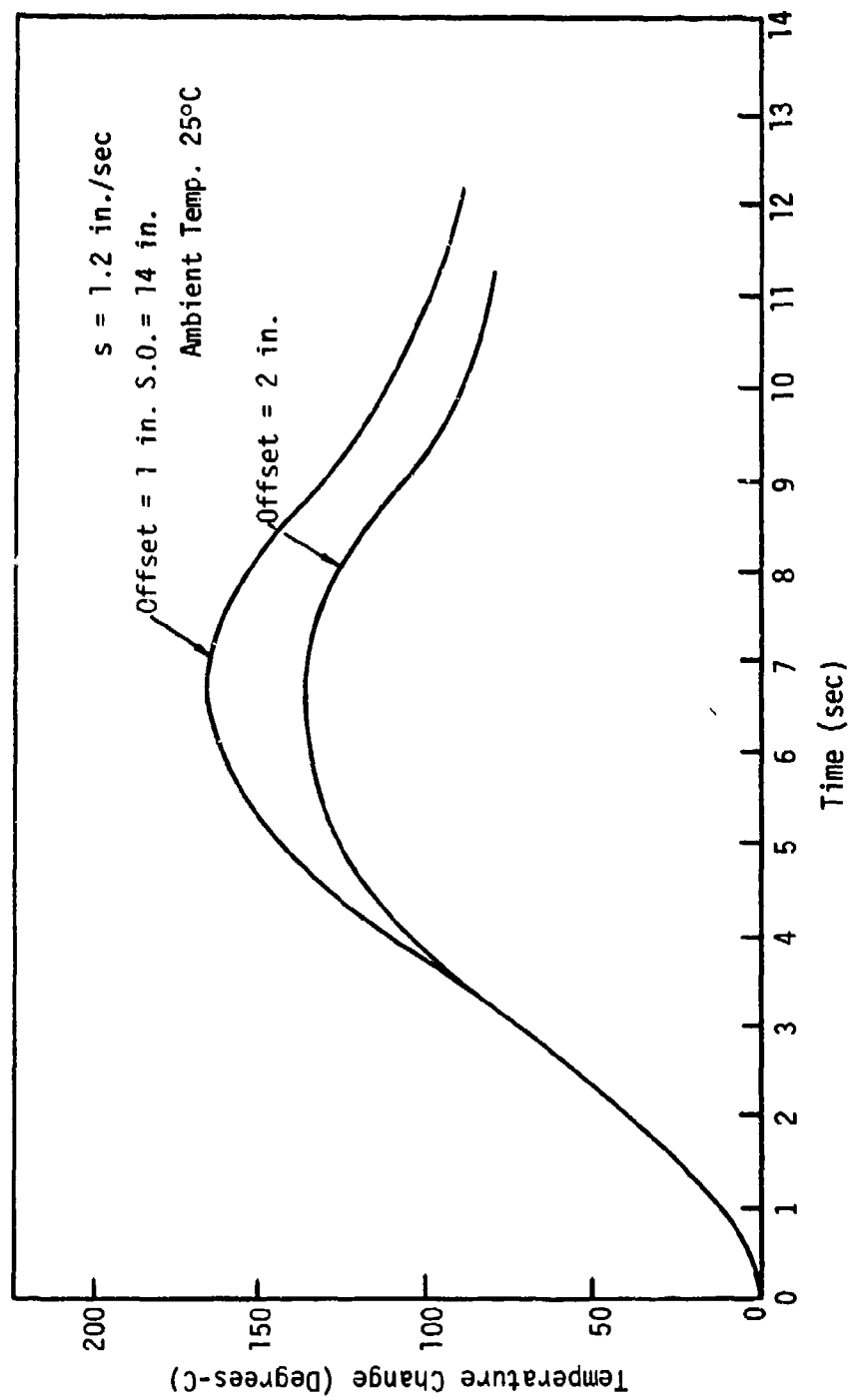
Fig. 9. Surface Temperature at a Fixed Point due to a Moving Heat Source (Mo. Red Granite)

33
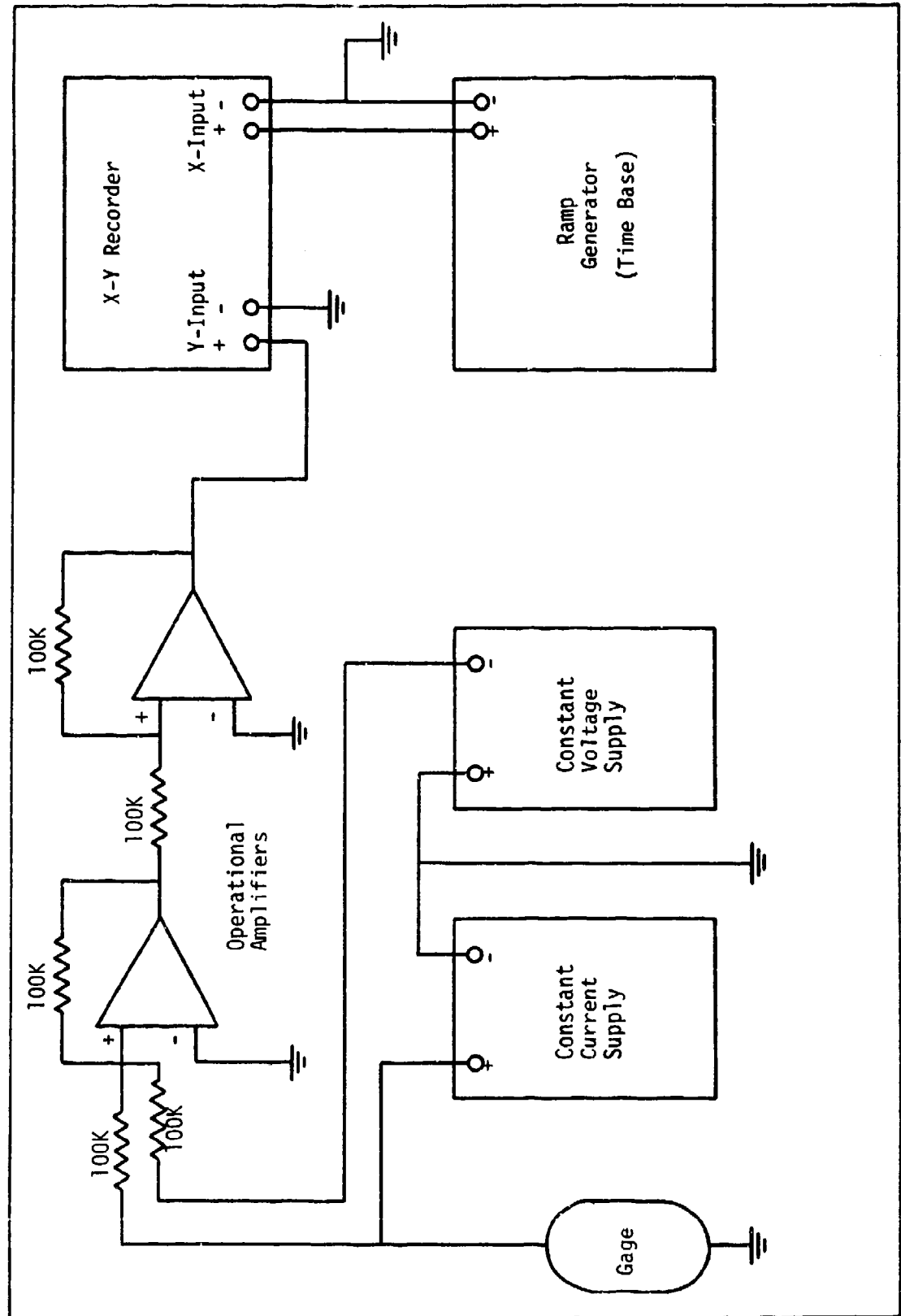
Fig. 10.   Temperature Measurement Instrumentation

Fig. 11. Subsurface Temperature Measurements - Dresser Basalt

Depths:
.6cm
.5cm
.4cm
.3cm
.2cm
.1cm

Heat Source - Flame Jet
Ambient Temperature - 11°C
Speed - 4.5 in/sec; 11.4 cm/sec
Distance - 10 in; 25.4 cm
Offset - 0 in; 0 cm

Distance of Torch from Thermocouple (cm)

Distance of Torch from Thermocouple (in.)

Temperature Change (Degrees - C)

35
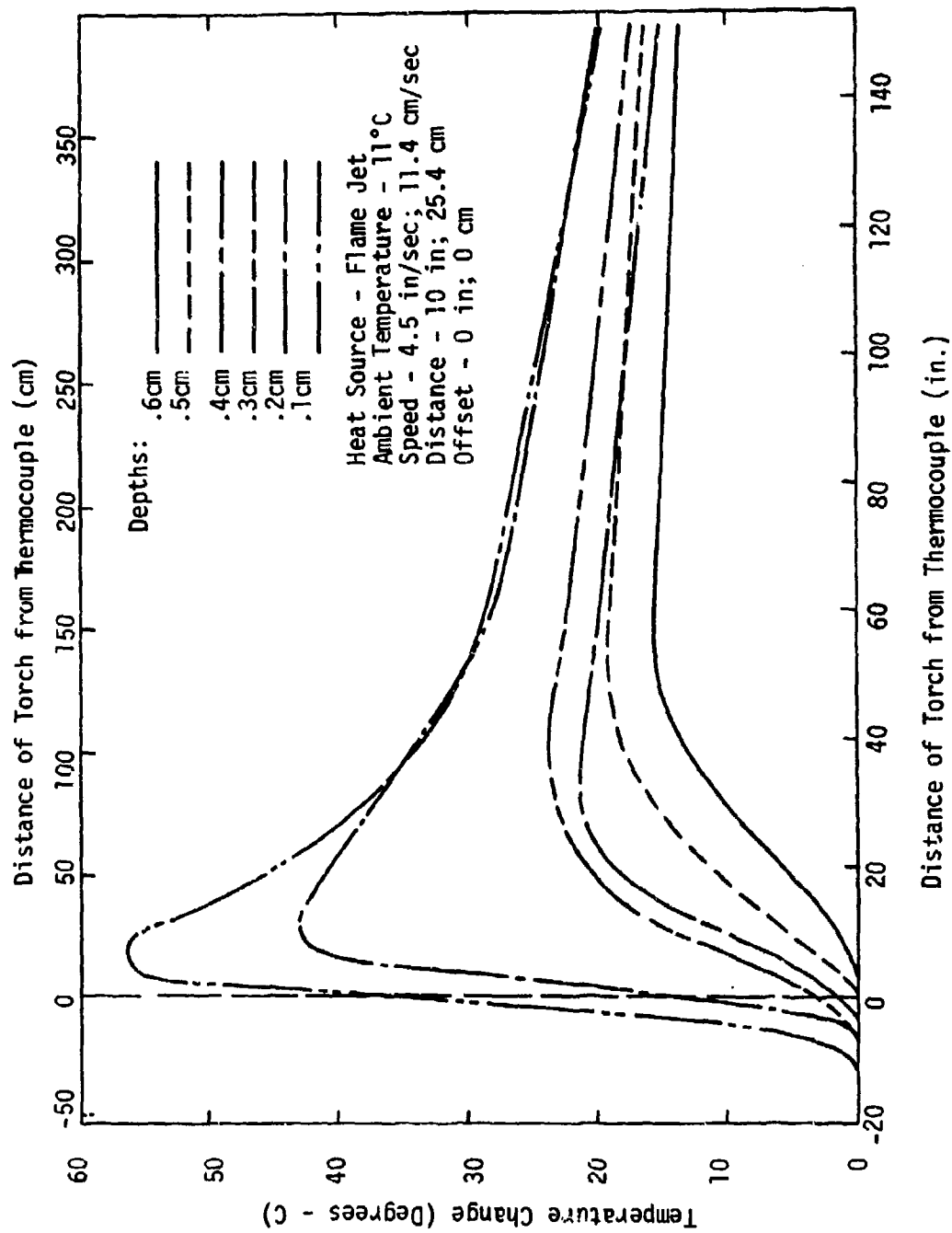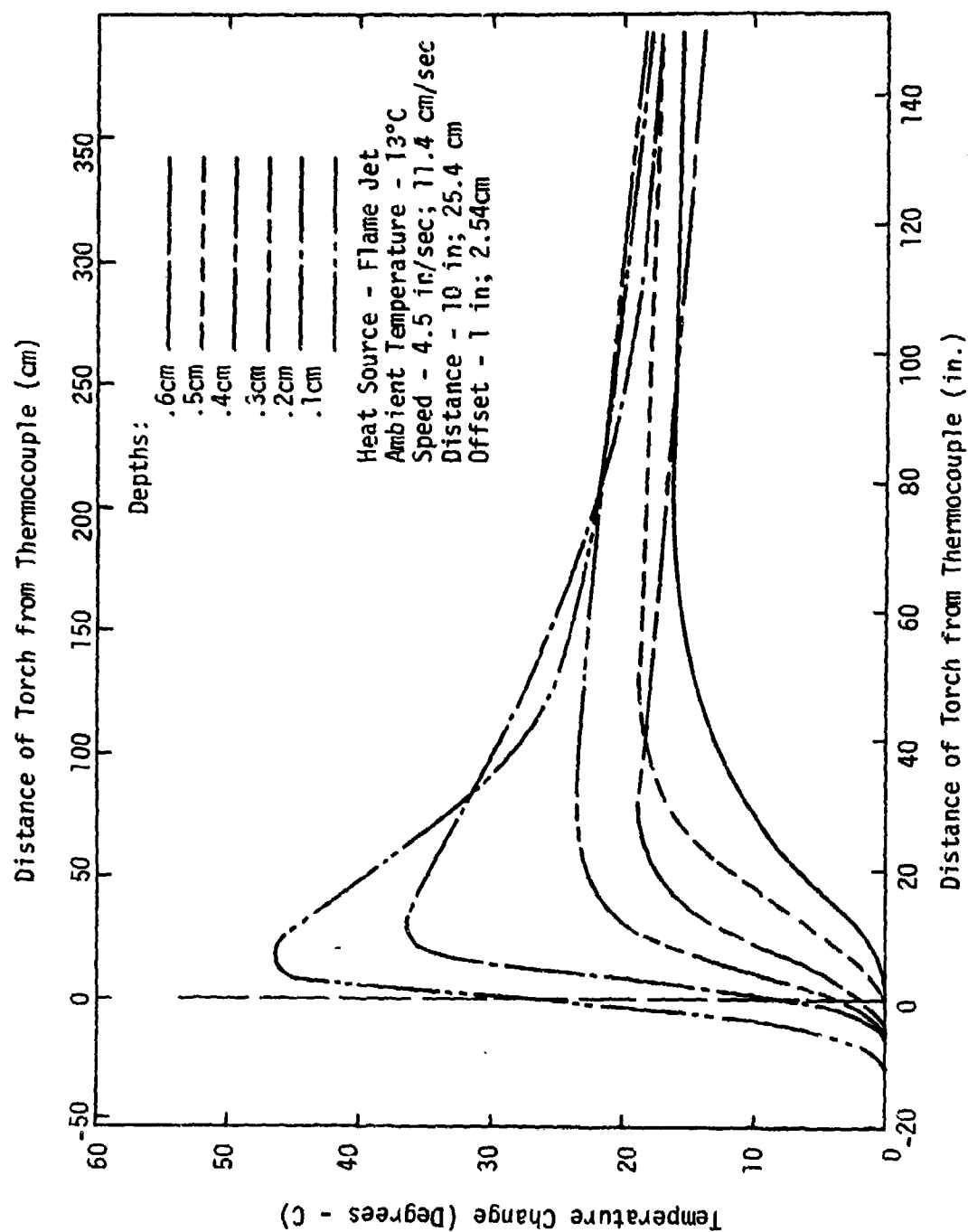
Fig. 12. Subsurface Temperature Measurements - Dresser Basalt
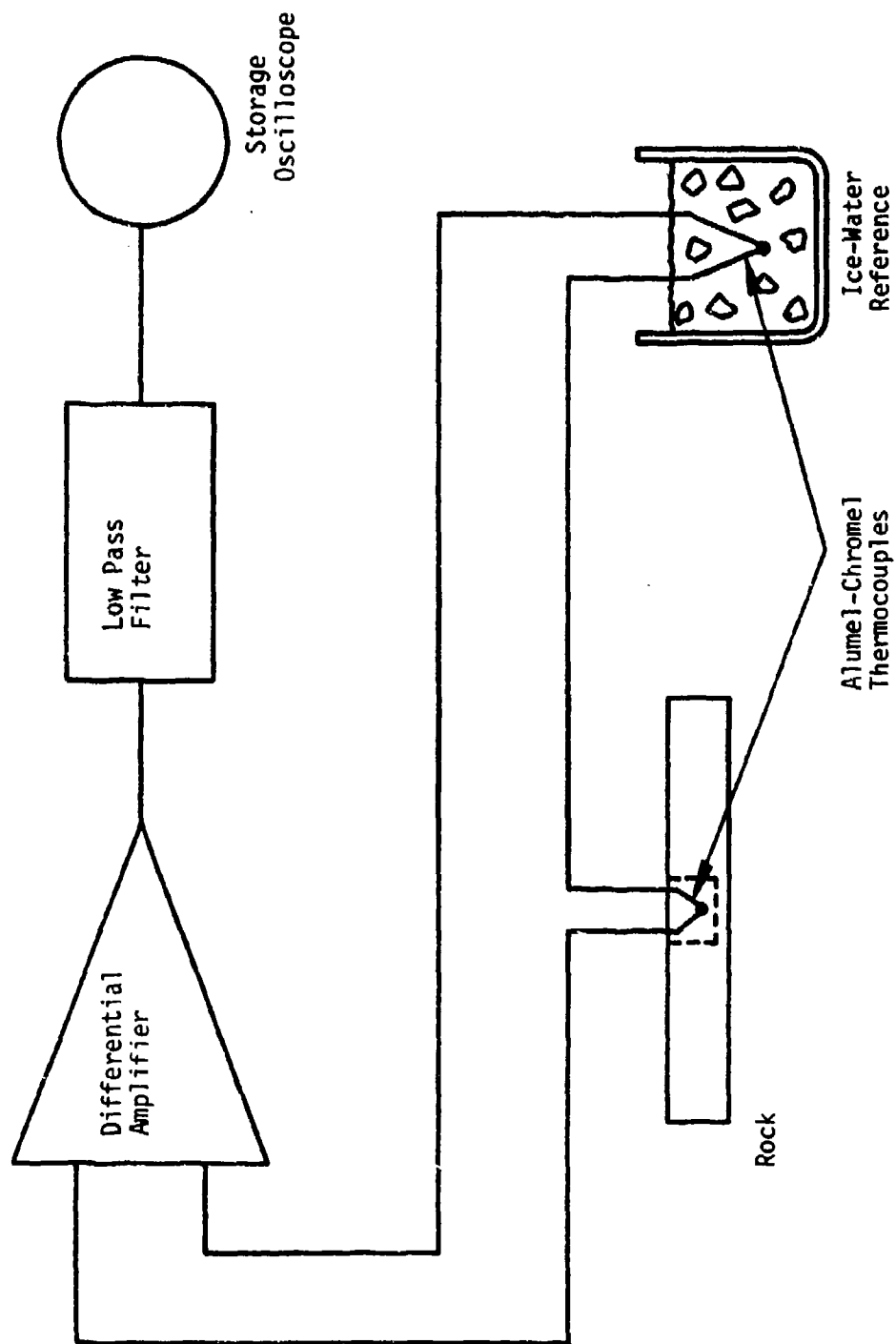
Fig. 13. Subsurface Temperature Measurement Instrumentation
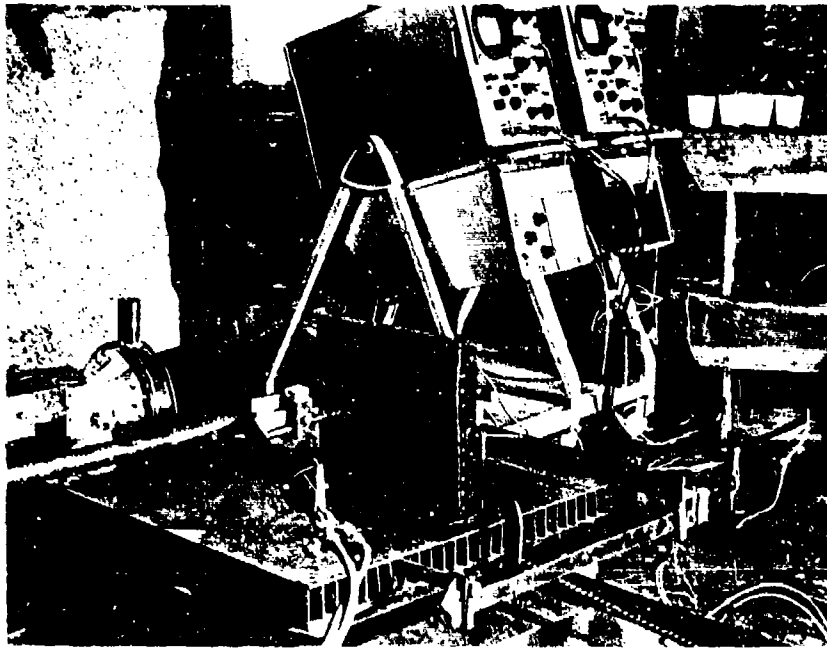
Fig. 14.   Subsurface Temperature Measurement Test Setup
shown with Acetylene Torch.
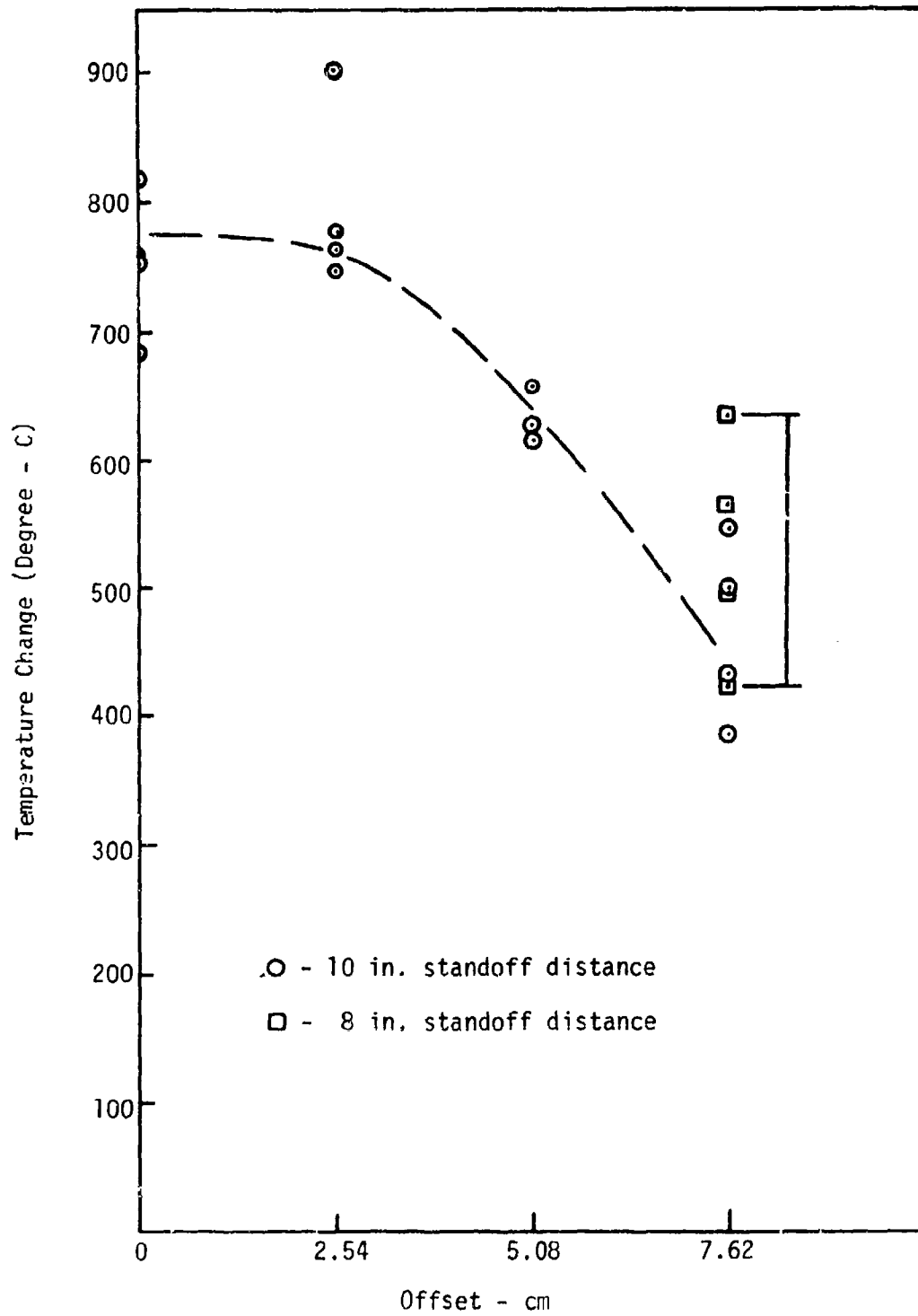
Fig. 15. Gas Film Temperatures

39
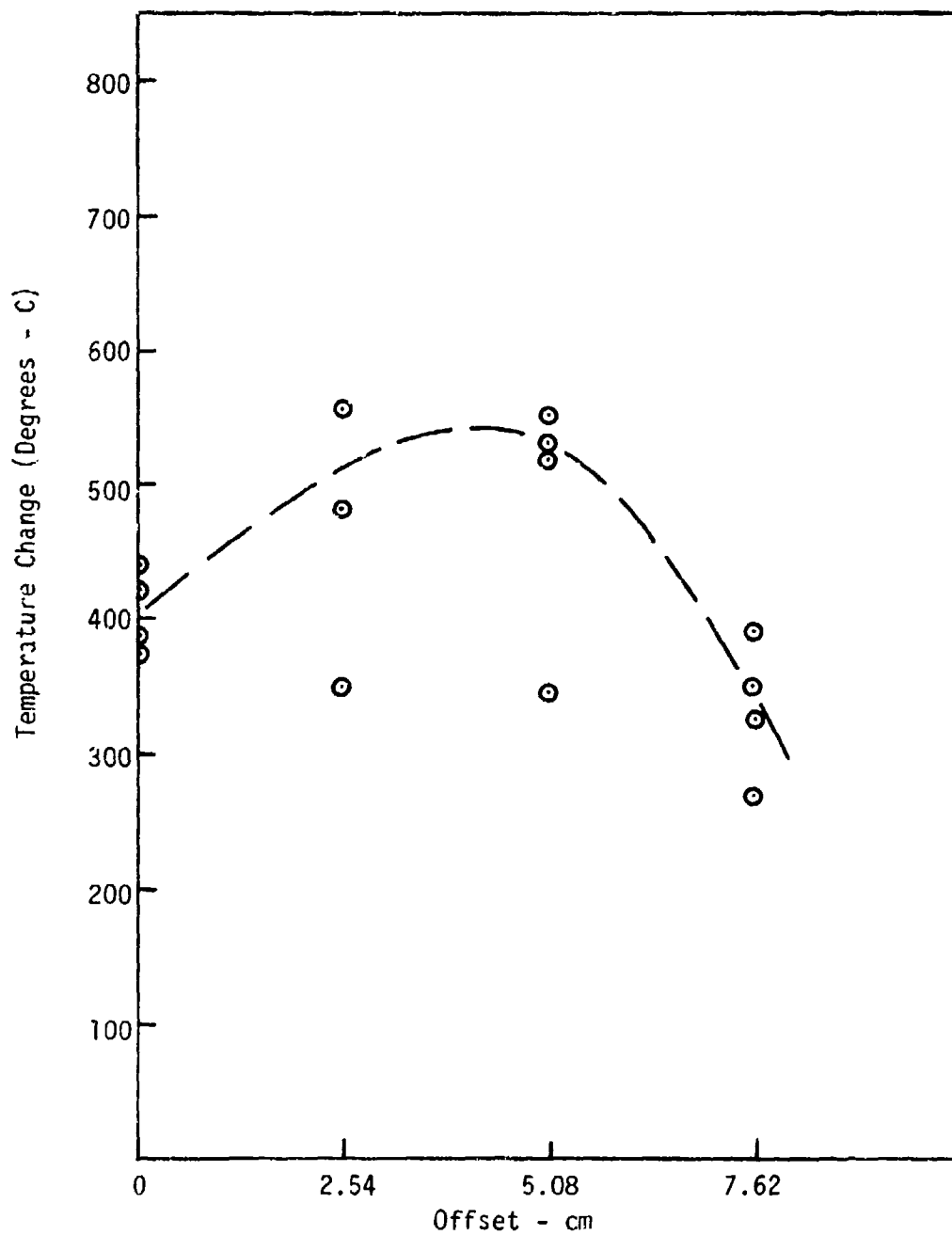
Fig. 16.   Gas Film Temperatures - 14 inch standoff

40

off of the curves near zero offset was expected (Ref. 10). The highest temperatures did not always occur at zero offset, probably resulting from one or more of the following factors:

1. Carbon builds up in the combustion chamber and gas accelerating nozzle due to incomplete combustion of the fuel.

2. The torch could not be adjusted to exactly the same operating conditions each time it was lighted.

3. Slight misalignment of the torch at standoff distances of 10 and 14 inches would be magnified on the surface of the rock.

4. The large standoff distances (10-14 inches) could allow a surface gas layer to build up around the stagnation point.

The problems of alignment and large surface gas layers should be minimized when the torch is moved closer to the rock in future tests. The carbon buildup in the torch has been slowed by preventing unburned carbon from remaining in the torch during shutdown. Experience in operating the torch plus repetition of some of the tests reduce the error due to improper adjustment of the torch.

The approximate upper and lower bounds of the surface temperature and approximate gradients within 1 mm of the surface for Missouri Red Granite were projected from measurements (Fig. 17).

Numerical Procedures

The maximum temperatures for the time histories were calculated for varying offset and depth (Fig. 18). For calculations the slab was divided (Fig. 19) to represent strips. An average temperature of a strip was calculated and the heat required to raise the temperature of the strips to the average temperatures was determined.
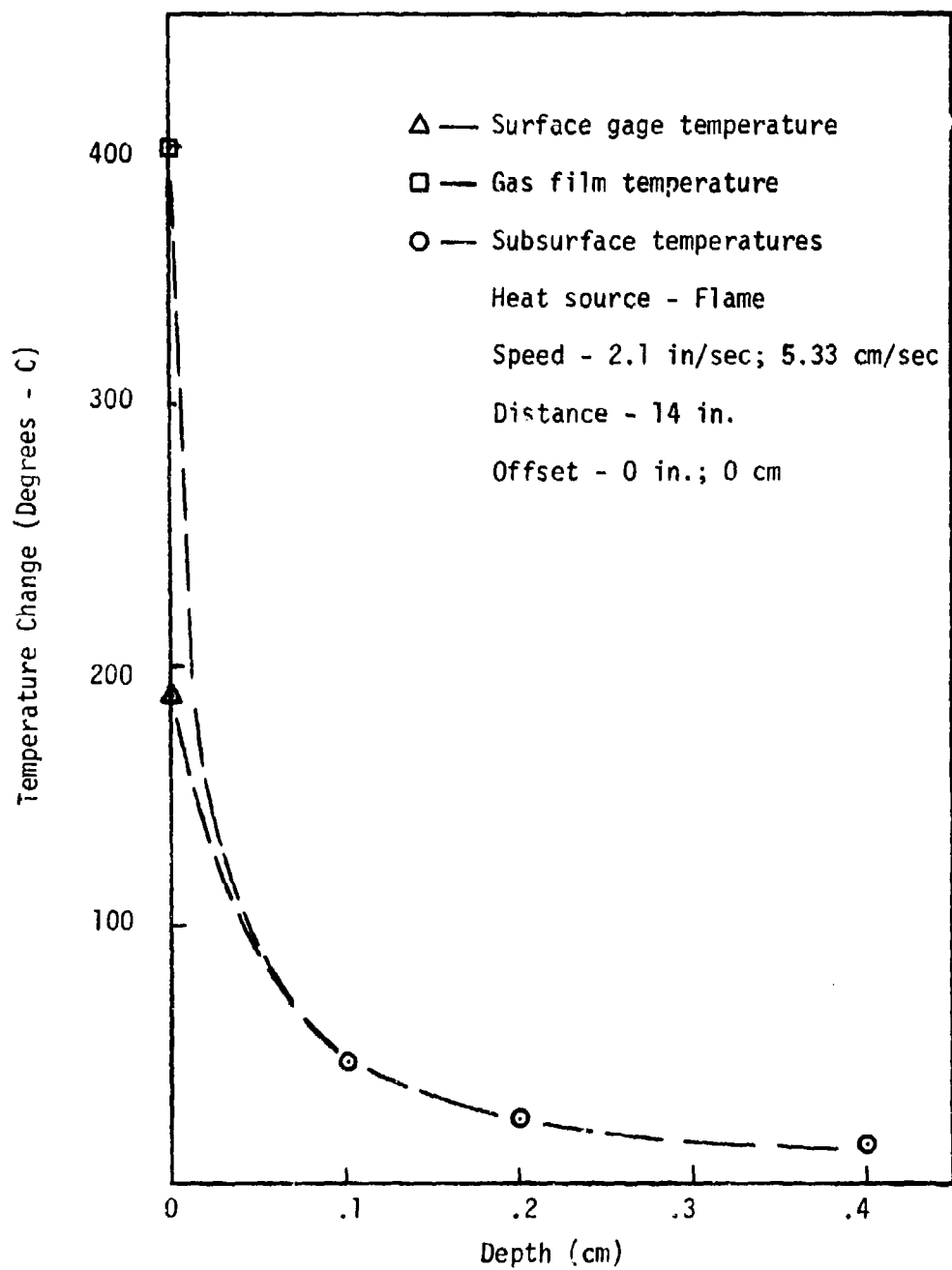
Fig. 17.   Approximate Temperature Distribution - Missouri Red Granite

Width (cm)

Depth (cm)

Depth \ Width	0.0	2.54	5.08	7.62
Gas film*	816*	746*	623*	428*
.1	56.5	46.5	49.	33.
.2	43.	36.5	37.	28.
.3	24.	23.5	23.	21.
.4	21.5	19.	19.	15.
.5	19.	19.	17.	12.5
.6	16.	16.	13.	7.5
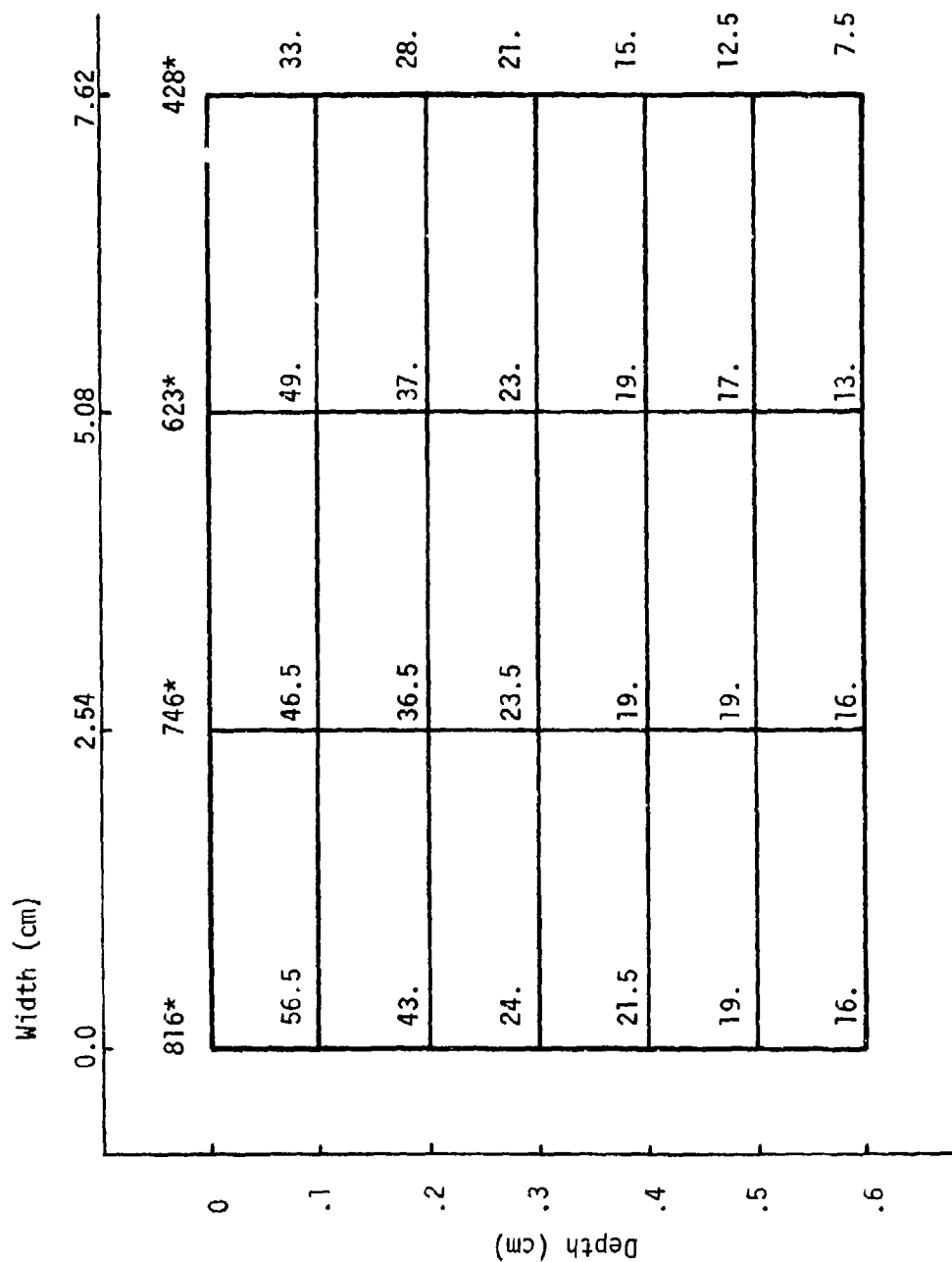
*Note: Gas Film Temperatures

Fig. 18. Subsurface and Gas Film Temperatures (Degrees - C)

43
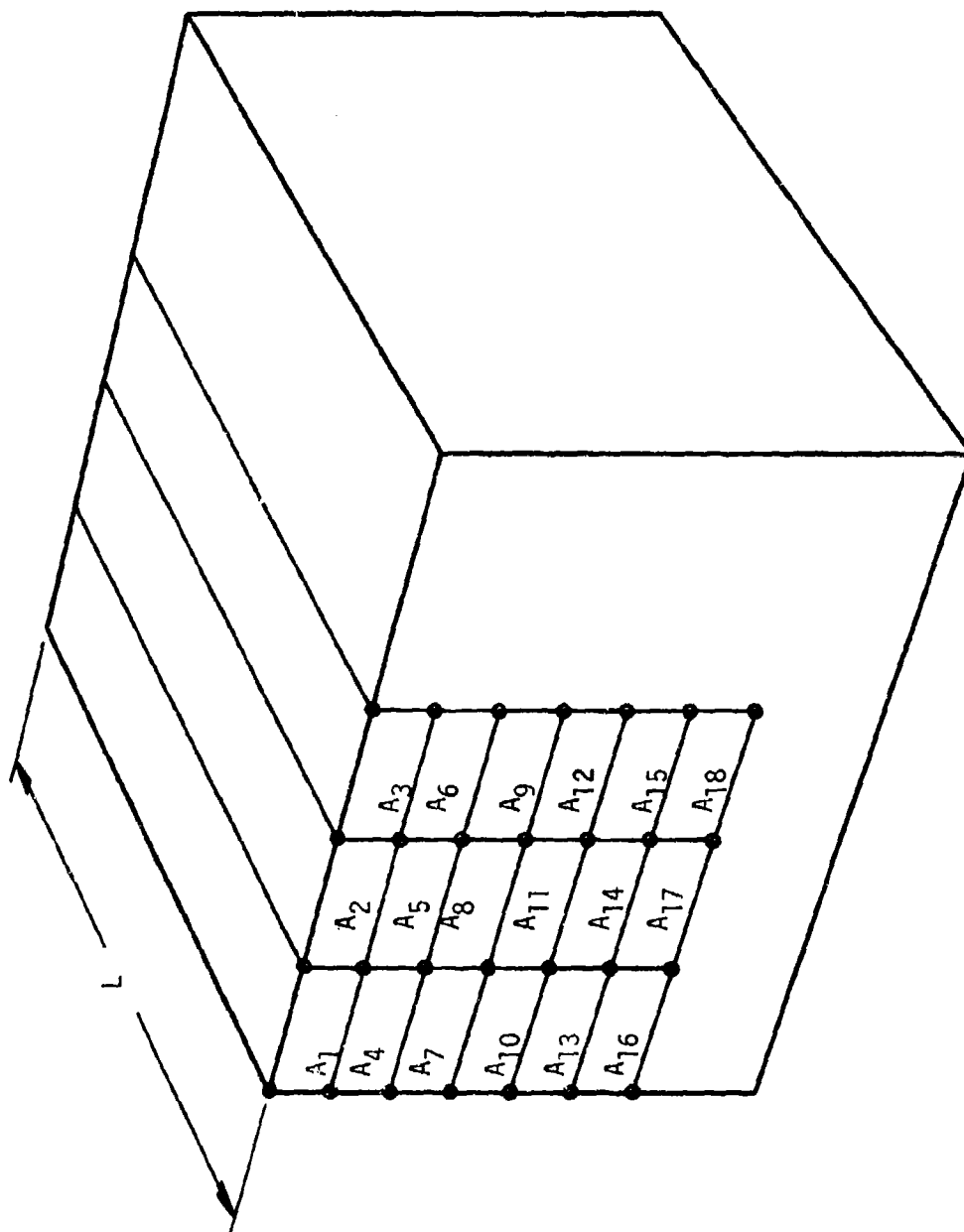
Fig. 19. Element Grid for Heat Energy Calculations

The total heat was then the sum of the heat that entered the strips.

$$Q_{total} = \sum_{i=1}^{n} q_i = \sum_{i=1}^{n} \rho L C_i A_i (T_i - T_o) \qquad (8)$$

where

C_i = specific heat at temperature T_i

A_i = cross-sectional area of the strip

T_i = maximum temperature of the strip

T_o = initial temperature of the slab

L = length of the slab

ρ = density of the slab

n = number of strips

The coupling effect can then be expressed as a percent of the total available heat energy from the torch.

$$\left(1 - \frac{Q_{torch} - Q_{total}}{Q_{torch}}\right) \times 100 = HEC \text{ (heat energy coupling)} \qquad (9)$$

The curves for Dresser Basalt were chosen to illustrate the calculation of heat energy coupling, for a table speed of 4.5 in./sec and a distance from the torch to the rock of 14 in. The choice of Dresser Basalt was made because temperatures had been recorded at six subsurface depths and some pertinent material properties could be found in References 22 and 23. The surface temperature measurements for basalt were not completed but were estimated. Three cases were chosen:

Case I.   Temperature at surface assumed to be between the gas film temperatures and the 1 mm subsurface temperature.

$$T = 250^{\circ}C$$

Case II.   Temperature of surface assumed to be at the gas film temperature.

Case III. Temperature of surface assumed to be the same as 1 mm subsurface temperature.

The density was assumed to be constant for all cases and equal to 2.70 g/cc. The heat input was considered to be centered along a line six inches long and moving with the speed of 4.5 in./sec for a distance of 1 cm. The rock heat capacity was taken as 960 joules/kg-$^{\circ}$K for temperatures below 100°C and as 980 joules/kg-$^{\circ}$K for temperatures less than 160°C. It was further assumed that all the materials within the 6 in. by 1 cm area directly under the source reached their peak temperatures simultaneously.

$$Q_{torch} = 11,523 \text{ joules}$$

For Case I.

$$Q_{total} = 1068 \text{ joules}$$
$$HEC = 9.3\%$$

For Case II.

$$Q_{total} = 2056 \text{ joules}$$
$$HEC = 17.9\%$$

For Case III.

$$Q_{total} = 650 \text{ joules}$$
$$HEC = 5.7\%$$

The low value of 5.7% coupling efficiency appears to be the most acceptable, although estimates by various investigators give values as high as 7 percent for an optimum standoff of about 6 inches. For an inverse square relationship the coupling efficiency for 14 in. standoff would be about 2 percent. Hence, the above approximate calculations are reasonably accurate in view of the acute difficulties involved in making near surface temperature measurements in rock.

47

CHAPTER III

THERMAL STRESSES

Introduction

The effects of thermal stresses induced by heat sources applied to
the surface of rocks and other brittle materials are determined by the
heat flux, diffusivity, conductivity, thermal coefficient of expansion,
fractures and flaws, rate of travel of moving sources, strength of rock,
and related factors. One of the important phenomena which has not been
considered in the literature is the effect of stress relief upon stress
distribution, failure mechanisms, heat transfer, and temperature distri-
bution after fractures are induced in the rock surface, or after spalla-
tion occurs.

One of the planned objectives of the theoretical analysis was to find
methods of numerical evaluation for solutions of equations for thermal
stress distributions in semi-infinite solids due to moving heat sources.
However, existing solutions are for point sources that involve mathe-
matical discontinuities which cannot be programmed in the computer to
obtain accurate calculated values. Also, the calculation of three-
dimensional stress distributions from known or measured temperature distri-
butions was found to require so much detailed programming as to be pro-
hibitive.

The results achieved in the analysis which was completed will serve
as a base for the future development of possible simplified methods of
calculation of thermal stresses. Existing solutions for temperature
distribution for a moving heat source are useful in determining the posi-
tion of critical thermal gradients. Although the state-of-the-art of
quantitative analysis of thermal shock is limited, concepts involved are

likewise useful in explaining observed phenomena in rocks. Steady state models employing the concept of bending stresses in a plate to simulate a heated surface, and a hemispherical heat source model are employed to define some of the effects of both surface and subsurface thermal gradients. In general, rock temperatures which cause spallation are relatively low, and the behavior of the rock is considered to be elastic.

Moving Heat Sources

The following describes the theoretical study of thermal stresses in rocks due to a moving heat source. The physical problem consists of obtaining the stress distribution in a rock semi-space due to a heat source of known strength, w, moving with a constant velocity, v, along the x_1-axis on the bounding plane $x_3 = 0$, as shown in the figure below.
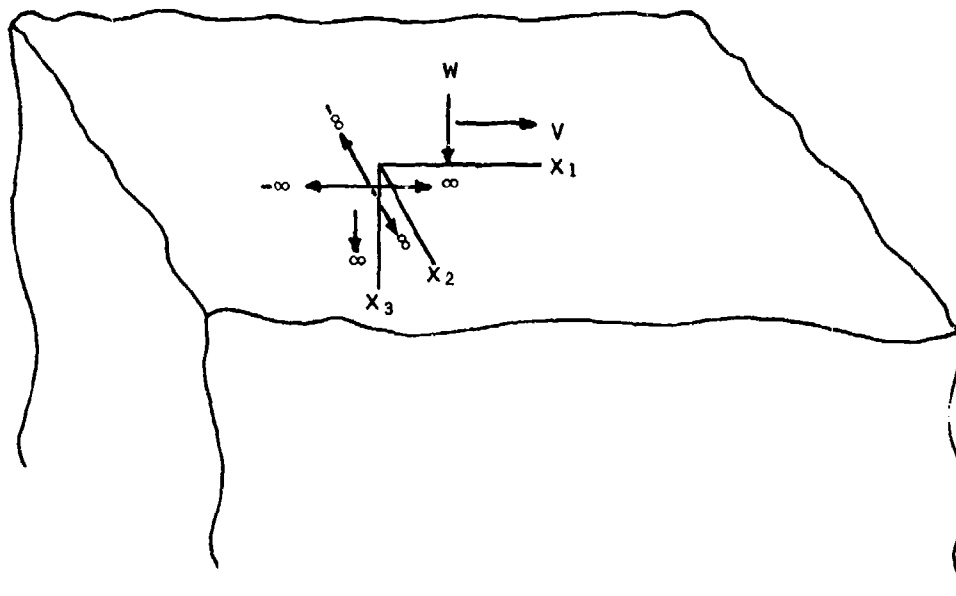
Fig. 20.   Point Source Moving on the Bounding Plane of a Semi-infinite Rock

In this analysis, the heat source is assumed to be moving steadily and continuously on the rock surface, and the resulting temperatures and displacements are small. The dynamic effects of thermal inertia can then be neglected and the analysis set within the framework of the linear theory of uncoupled thermoelasticity. For this case the stress problem becomes explicit, that is, the equations for the stresses are obtained from the known temperature distribution derived by solving a well-defined heat conduction problem.

Temperature Distribution. Rocks are complex materials with inherent inhomogeneity and anisotropy as well as temperature-dependent properties. The problem of thermal stress analysis in rocks, even under the above mentioned assumptions, is an extremely difficult one. An exact solution of the temperature problem in itself is a formidable task because it involves:

1. A three-dimensional formulation

2. Nonhomogeneous and anisotropic material

3. Temperature-dependent properties, and

4. Transient analysis as a result of the motion of the heat source

It should be noted that the inclusion of each of these factors involves a different formulation of the problem. Moreover, the problem is not linear in that the solution to an equation involving two or more of the above factors cannot be obtained by combining the solutions to the problems involving each of these factors separately. That is, there does not exist a general method for the solution of nonlinear partial differential equations.

Numerous analytical methods have been developed for solving the nonlinear equations of unsteady state heat conduction, each with its own

50

limitations and rather narrow field of application (Refs. 24-28). Many of these methods are attractive only theoretically as their practical applications lead to cumbersome mathematical operations that cannot always be performed without very special techniques or simplifying assumptions (Refs. 20, 29-33). In order for one to be able to develop a workable solution to thermal stress problems in rocks, simplifying assumptions are introduced based on such practical considerations as the behavior of rock properties and the main objective of the research.

On a macroscopic scale, the rock body may be treated as homogeneous material because of its large mass and random crystal orientation. Also, due to the manner of their formation, in general, rocks exhibit different properties in directions parallel and perpendicular to structure such as bedding, but for a first approximation may be treated as isotropic solids (Ref. 34). The main objective of this phase of research was to study the influence of the temperature dependence of the thermal and elastic properties of rocks on the stresses produced by a moving heat source. This, combined with the fact that in the literature the temperature-dependent rock properties are almost invariably obtained by assuming the material to be homogeneous and isotropic justifies the using of simplified analysis (Refs. 23 and 35).

Under these assumptions, the mathematical equations for the heat conduction problem are as follows. The governing equation is:

$$\rho C(T) \frac{\partial T}{\partial t} = \frac{\partial T}{\partial x_1} \quad k(T) \frac{\partial T}{\partial x} + \frac{\partial}{\partial x_2} \quad k(T) \frac{\partial T}{\partial x_2}$$

$$+ \frac{\partial}{\partial x_3} \quad k(T) \frac{\partial T}{\partial x_3} + w \, \delta(x_1 - vt, 0, 0; t)$$

(10)

51

Boundary Conditions:

1. $\frac{\partial T}{\partial x_3}$ $(x_1, x_2, 0; t) = 0$, if it is assumed that the   (11)

   bounding plane $x_3 = 0$ is thermally insulated.

   Also, note that $T(vt, 0, 0; t) \rightarrow \infty$.

2. $T(R; t) = T_0$, $R \rightarrow \infty$.   (12)

Initial Condition:

   $T(R; 0) = T_0$.   (13)

In these equations, the following notations are used:

x_1, x_2, x_3 = space variables, cm

$R = (x_1^2 + x_2^2 + x_3^2)^{\frac{1}{2}}$ = space norm in the x_i space

t = time variable, sec

$T = T(x_1, x_2, x_3; t)$ = temperature, °C

T_0 = initial or reference temperature

$\rho C(T)$ = volume heat capacity , $\frac{cal}{cm^3 - °C}$

$k(T)$ = thermal conductivity, $\frac{cal}{sec - cm - °C}$

w = rate of heat source, $\frac{cal}{sec}$

$\delta(x_1 - vt, 0, 0; t)$ = Dirac Delta function defined as:

       $= 0$, $x_1 \neq vt$

       $= 1$, $x_1 = vt$, $x_2 = x_3 = 0$ at time $= t$ sec

Quasi-Stationary Approximation

The mathematical analysis of the system of equations (10-13) is greatly simplified if it is assumed that the state of temperature is quasi-stationary. Bornefeld (Ref. 36) experimentally established that the temperature distribution in a solid heated by a moving heat source, except during the initial transient period, remains stationary when referred to a coordinate system moving with the source. Based on this assumption, Rosenthal (Ref. 20) ʳived his classic theory of moving heat sources for homogeneous, isotropic materials having constant thermal properties.

The governing heat conduction equation for this case is

$$\nabla^2 T = \frac{1}{\kappa} \frac{\partial T}{\partial t} \tag{14}$$

where

$$\nabla^2 = \frac{\partial^2}{\partial x_1^2} + \frac{\partial^2}{\partial x_2^2} + \frac{\partial^2}{\partial x_3^2}, \text{ the Laplacian, and} \tag{15}$$

$$\kappa = \frac{k}{\rho C}, \text{ the diffusivity.}$$

If a new coordinate system, ξ_i, moving with the source is introduced, then

$$\xi_1 = x_1 - vt, \quad \xi_2 = x_2, \quad \xi_3 = x_3 .$$

Hence, the governing equation in the moving system ξ_i becomes

$$\frac{\partial^2 T}{\partial \xi_1^2} + \frac{\partial^2 T}{\partial \xi_2^2} + \frac{\partial^2 T}{\partial \xi_3^2} = \frac{1}{\kappa} \frac{\partial T}{\partial t} - \frac{v}{\kappa} \frac{\partial T}{\partial \xi_1} . \tag{16}$$

For the quasi-stationary temperature distribution

$$\frac{\partial T}{\partial t} = 0$$

and the governing equation reduces to

$$\frac{\partial^2 T}{\partial \xi_1^2} + \frac{\partial^2 T}{\partial \xi_2^2} + \frac{\partial^2 T}{\partial \xi_3^2} = -\frac{v}{\kappa}\frac{\partial T}{\partial \xi_1} \ . \tag{17}$$

This equation is further simplified by putting

$$T = T_0 + \exp\left(\frac{v\xi_1}{2\kappa}\right) \psi(\xi_1, \xi_2, \xi_3) \tag{18}$$

After substitution, the following equation is obtained:

$$\frac{\partial^2 \psi}{\partial \xi_1^2} + \frac{\partial^2 \psi}{\partial \xi_2^2} + \frac{\partial^2 \psi}{\partial \xi_3^2} = \left(\frac{v}{2\kappa}\right)^2 \psi \tag{19}$$

or in the usual symbolic form

$$\nabla^2 \psi = \left(\frac{v}{2\kappa}\right)^2 \psi \tag{20}$$

The function $\psi = \psi(\xi_i)$ is to be determined from the above equation and the boundary conditions.

Numerical Techniques

The above discussion suggests that one approach for the solution of the temperature problem in rocks is to oversimplify the problem and then use one of the applicable analytical methods. An alternative approach is to obtain the solution numerically. This approach has the advantage that it does not require oversimplification. The obvious disadvantage is that solution can be obtained for a finite region and finite time only because the numerical treatment of the problem imposes restrictions on computing time and storage.

The most common methods of obtaining a numerical solution are:

1. The finite-element techniques, and

2. The finite-difference techniques

The steep temperature gradients in rocks (Ref. 37) require very small-sized elements (small grid size in the case of difference methods). The use of the finite-element techniques was deemed impracticable initially, due to the large storage and time requirements and nonavailability of a three-dimensional dynamic code. Effort has therefore been concentrated on finite-difference techniques.

Three well-known finite-difference approximations are (Refs. 38 and 39):

1. Forward difference (explicit scheme),

2. Backward difference (implicit scheme), and

3. Crank-Nicolson (Ref. 40) and other combination schemes (combination of the first two schemes).

The explicit schemes suffer because of stability criteria, hence, prohibitively small time increments must be used. The implicit methods lead to a set of simultaneous equations which must be solved at each time step. Thus, these techniques, while otherwise efficient, soon become impractical as the number of nodes increases. The combination schemes have a higher order accuracy compared to the other two types of approximations, but they too suffer from the last mentioned limitation and cannot be effectively employed for most problems involving large numbers of nodes.

After an extensive survey of difference methods was made, the alternating direction implicit (ADI) technique of Douglas (Ref. 41) (discovered independently by Brian [Ref. 42]) was chosen for the solution of the temperature problem. This technique was first introduced by Peaceman and Rachford (Ref. 43) and Douglas and Rachford (Ref. 44). Being unconditionally stable, as the backward-difference and the combination schemes, the ADI techniques require the solution of many small independent systems of simultaneous equations instead of one large system. Furthermore, each system is tridiagonal and a very efficient method for solving the tridiagonal system (Thomas algorithm) without iteration is well known (Ref. 43).

<u>Jump Condition</u>. Since the heat source is acting on a finite area of the bounding plane $x_3 = 0$, the boundary condition on this plane involves a discontinuity. In equation (10) the assumption that the source is acting at a single point was introduced primarily to simplify the preliminary numerical analysis. For this case, the boundary discontinuity gives rise to a step function as shown below by the jump condition (Eq.22).

For programming convenience, the governing equation (10) is replaced by the equivalent system of the homogeneous equation:

$$\frac{\partial}{\partial x_1} \left\{ k(T) \frac{\partial T}{\partial x_1} \right\} + \frac{\partial}{\partial x_2} \left\{ k(T) \frac{\partial T}{\partial x_2} \right\} + \frac{\partial}{\partial x_3} \left\{ k(T) \frac{\partial T}{\partial x_3} \right\}$$

$$= \rho C(T) \frac{\partial T}{\partial t}$$

(21)

and the jump condition

$$-k \frac{\partial T}{\partial x_3} (x_1^- - vt, 0, 0; t) + k \frac{\partial T}{\partial x_3} (x_1^+ - vt, 0, 0; t) = w \qquad (22)$$

with the continuity requirement

$$T(x_1^- - vt, 0, 0; t) = T(x_1^+ - vt, 0, 0; t) \qquad (23)$$

The (-) and (+) superscripts denote, respectively, the x_1-coordinates of the points just to the left and just to the right of the point $x = vt$.

The presence of the jump condition greatly complicates the analysis in some cases. Special finite-difference analogs must be obtained to approximate this type of jump condition.

For the investigation of the accuracy and consistency of the difference analogs that were derived, it was necessary to solve a simple problem involving a similar jump condition. A two-dimensional problem of heat flow in a thin plate of constant thickness g, heated by a source

moving along one of its edges was selected (Fig. 21). The analytical solution for this problem, based on the assumption of constant properties and a quasi-stationary state is given by Rosenthal (Ref. 20).
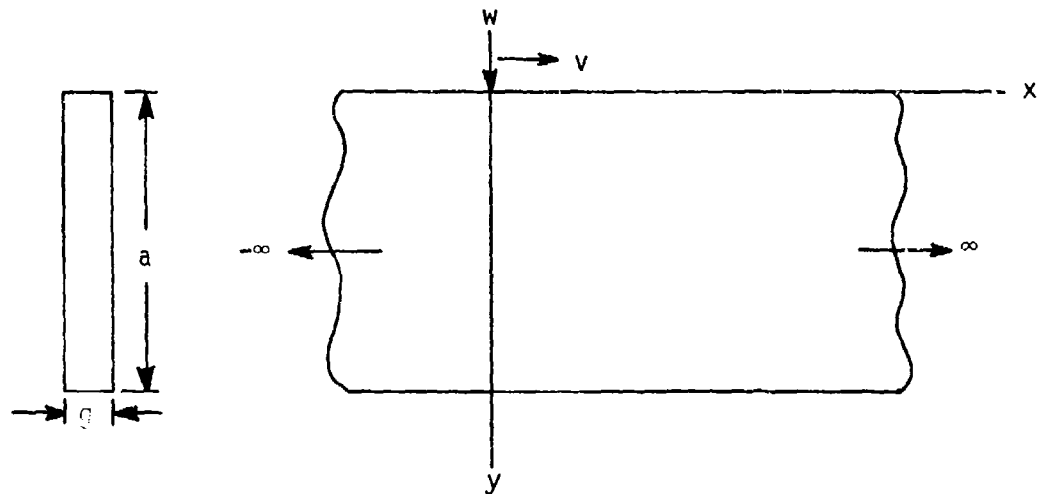
Fig. 21. Point Source Moving along an Edge of a Thin Plate

The system of governing equations for this problem involves the governing homogeneous equation

$$k\left(\frac{\partial^2 T}{\partial x^2} + \frac{\partial^2 T}{\partial y^2}\right) = \rho C \frac{\partial T}{\partial t} \tag{24}$$

the jump condition

$$-k\frac{\partial T}{\partial y}(x^- - vt, 0; t) + k\frac{\partial T}{\partial y}(x^+ - vt, 0; t) = w \tag{25}$$

and the continuity requirement

$$T(x^- - vt, 0; t) = T(x^+ - vt, 0; t) \tag{26}$$

Finite-Difference Approximation. In the figure below let the source be at node 5 at time t. Let the grid ratio $\frac{\Delta x}{\Delta t} = v$ so that in one time step the source advances by one space step in the x-direction.
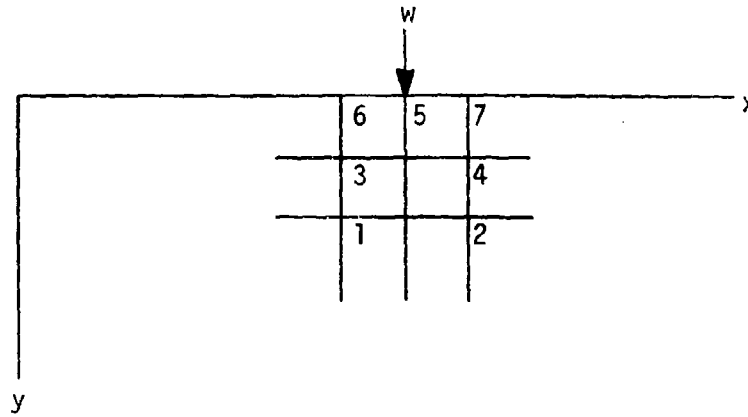
Fig. 22. Finite-Difference Grid for the Jump Condition Approximation

Let $\Delta x = \Delta y = h$.

The use of the three point forward difference formulas yields

$$\frac{\partial T}{\partial y}\bigg|_7 = \frac{1}{2h} (-3 T_7 + 4 T_4 - T_2)$$

and

$$\frac{\partial T}{\partial y}\bigg|_6 = \frac{1}{2h} (-3 T_6 + 4 T_3 - T_1).$$

Since the source has moved from node 6 to node 5, the continuity condition at node 5 is approximated by

$$T_6 = T_5$$

and substitution of the last three equations in the jump condition (25) yields:

$$T_5 = \frac{2wh}{3k} + T_7 + \frac{4}{3}(T_3 - T_4) + \frac{1}{3}(T_2 - T_1) \qquad (27)$$

In the case of a stationary jump, the effect of the discontinuity gradually dies out with each iteration and the number of minimum iterations required to smooth out the discontinuity is proportional to the grid size (Ref. 38). The problem of a moving heat source involves a "moving discontinuity". To smooth out this type of discontinuity, a very large number of iterations are required at each time increment. The approximation (27) was found to be impractical for the problem under consideration, as the results obtained by using a practically allowable smallest value of h and a large number of iterations were unacceptable.

Other approximations were obtained by replacing the jump condition by a flux boundary condition. One approximation of this type was

$$-k \frac{\partial T}{\partial y}\Big|_5 = w ,$$

and the other, based on an average value was

$$1/2 \left\{ -k \frac{\partial T}{\partial y}\Big|_5 -k \frac{\partial T}{\partial y}\Big|_6 \right\} = w .$$

Again, in both of these cases, the same computational conditions as for equation (27) were found to be true.

Stress Distribution. As mentioned in the previous section, the stress problem in the case of uncoupled theory of linear thermoelasticity is an explicit one. The method proposed for the analysis of the thermoelastic problem under consideration was to obtain the temperatures by

59

solving the heat conduction problem and then use these values to solve
the stress problem numerically by using one of the available finite ele-
ment codes. This method of analysis was chosen after a detailed survey
of existing techniques for the solution of nonlinear problems of transient
thermal stresses (Refs. 45-50). It is important to note that the term
"nonlinear" here refers to the elastic solution of problems having vari-
able material properties and not to the conventional usage for plastic
analysis.

The problem of a semi-infinite elastic solid with a plane boundary,
commonly known as the problem of Bossinesq and Cerruti, has been the ob-
ject of study by numerous researchers. On the other hand, few problems
are solved with nonlinear material properties. Some of these are given
in References 51-54. Analyses given in these references are limited to
one-or two-dimensional problems only.

Nowacki's Solution. For the purpose of preliminary analysis, solu-
tion to a semi-infinite rock semi-space problem was attempted assuming
the material to be homogeneous, and isotropic with temperature independent
properties. A closed form solution for this problem is given by Nowacki
(Ref. 49) and is described in Appendix C.

From the solution, given by equation (C-2) it is seen that the tempera-
ture at the origin, $R = 0$ tends to infinity. Similarly, the stresses σ_{ij}
in the infinite space become infinite at $R = 0$. The expression (C-4) for
the stresses $\bar{\bar{\sigma}}_{ij}$ involves an improper double integral which is too com-
plicated to be performed analytically. An attempt to evaluate this inte-
gral numerically using Simpson's rule together with Newton's 3/8 formula
(Ref. 55) was unsuccessful as the function $p(\eta_1, \eta_2, 0) = -\bar{\sigma}_{33}(\eta_1, \eta_2, 0)$
becomes singular at the origin, $R = 0$.

60

As an alternative, the following approach was taken. From equation (C-2) temperatures were obtained for different values of $R = R(\xi_1, \xi_2, \xi_3)$, omitting the pole $R = 0$ where $T \to \infty$. An attempt was made to use these temperature values explicitly in the three-dimensional finite element code ELAS (Ref. 56). The steep temperature gradients in the vicinity of the source required extremely small-sized elements, 0.01 cm-side cubes, for the problem attempted. A sufficiently large volume must be considered in order to accurately approximate the boundary conditions of zero-stress at points far removed from the heat source. Thus, a grid consisting of extremely small-sized elements surrounding the source and progressively increasing-sized elements away from the source is required. Setting up of such a grid in three dimensions poses serious problems. The total number of nodes and elements becomes prohibitively large even when only a small block is to be analyzed. This approach thus involved serious computer storage and time considerations and was deemed impracticable in view of the available computer facilities.

Approximate Models

Other thermal stress models offer a basis for indicating some of the important phenomena involved in spallation such as temperature gradient for a moving source, the plate bending model and a hemispherical source model, the latter two being steady state in character. Some of the concepts of thermal shock appear to have application.

Temperature Distribution - Moving Source. Rosenthal (Ref. 20) has, in addition to equations for two-dimensional heat flow for a quasi-stationary state, developed a three-dimensional equation which is useful in an analysis of temperature effects of moving heat sources on rock surfaces.

The expression for three-dimensional heat flow may be obtained from equation (10) to yield in polar coordinates

$$\frac{d^2\psi}{dR^2} + \frac{2}{R}\frac{d\psi}{dR} - \left(\frac{v}{2\kappa}\right)^2 \psi = 0 \, , \tag{28}$$

where

$$R = (\xi^2 + y^2 + z^2)^{\frac{1}{2}}$$

$$\xi = x - vt \, .$$

Also,

$$\frac{d^2\psi}{dR^2} + \frac{2}{R}\frac{d\psi}{dR} = \frac{1}{R}\frac{d^2R\psi}{dR^2} \tag{29}$$

hence,

$$\frac{d^2R\psi}{dR^2} - \left(\frac{v}{2\kappa}\right)^2 R\psi = 0 \tag{30}$$

The boundary conditions are

$$\left.\begin{array}{l} \dfrac{\partial T}{\partial \xi} \to 0 \text{ for } \xi \to \pm \infty \\[2mm] \dfrac{\partial T}{\partial y} \to 0 \text{ for } y \to \pm \infty \\[2mm] \dfrac{\partial T}{\partial z} \to 0 \text{ for } z \to \infty \end{array}\right\} \tag{31}$$

The temperature distribution for an infinitely thick plate is then given by

$$T - T_0 = \frac{w}{4\pi k R} \exp\left\{-\frac{v}{2\kappa}(\xi+R)\right\} \tag{32}$$

For a point source the temperature becomes infinite at R = 0.

Rosenthal (Ref. 20) employed equation (28) to describe the tempera-
ture distribution in thick plates subjected to the heat generated in
mild steel by the arc of a welding electrode (Fig. 2).

The characteristics of the temperature distribution are given (Ref. 20)
as follows:

1. The temperature rise is much steeper than the fall, creating a
    very high thermal gradient in the surface of the material in
    front of the source.

2. Because heat does not propagate instantly the temperature maxi-
    mum envelope lags behind the heat point, the lag being a func-
    tion of source speed and diffusivity.

3. The curve n-n (Fig. 2) separates the areas of rising and fall-
    ing temperatures.

Thermal Stress-Plate Bending Model. Thirumalai (Ref. 37) treats a
thin heated layer of rock on the surface of unheated rock as a thermal
inclusion in the form of a plate. The boundary stresses of the plate
are:

$$\sigma_{xx} = \sigma_{yy} = -E\alpha\Delta T/(1-\nu) \tag{33}$$

$$\sigma_{zz} = 0$$

where

E = Young's modulus

α = coefficient of thermal expansion

ΔT = temperature difference per unit depth

ν = Poisson's ratio

63

The temperature difference and restraint of the plate cause a bending stress, M_1, per unit length:

$$M_1 = \int_h \sigma_{xx} \, zdz = - \frac{E}{1-\nu} \int_h \alpha \Delta T z dz \tag{34}$$

It may be shown (Ref. 37) for the assumptions made that for a given rock, failure by thermal spalling depends upon the associated shear strain.

Thermal Stress-Hemispherical Source. Both the thermal shock and thermal plate bending models attribute failure in spallation to the stress accompanying shear strain. However, each assumes uniform heating over a surface and a constant temperature gradient to a specified depth. While a moving source and three-dimensional models are desirable, closed solutions have been obtained only for point sources and these have not proven amenable to computer analysis because of mathematical discontinuities.

A steady state hemispherical source model solved by Sternberg and McDowell (Ref. 57) sheds some further light upon the effects of source boundaries, stress gradients on the surface and at depth.

Thus, for a hemispherical temperature distribution over a circular region of exposure $0 \leq r \leq a$, $z = 0$, the heat flux is

$$f(Q) = c \left[1 - \left(\frac{r}{a} \right)^2 \right]^{\frac{1}{2}} \tag{35}$$

The solution to the steady-state thermoelastic problem described is found as follows. Let λ_1 be the positive root of the equation

$$\frac{r^2}{a^2 + \lambda} + \frac{z^2}{\lambda} = 1 \; , \tag{36}$$

and define η by

$$0 < \eta = \tan^{-1} \frac{a}{(\lambda_1)^{\frac{1}{2}}} \leq \pi/2 \tag{37}$$

The solution to the problem is given by

$$T = \frac{cz}{a} \left(\frac{a}{(\lambda_1)^{\frac{1}{2}}} - \eta \right)$$

$$u_r = \frac{\pi a^2 \beta c}{6 r G} \left\{ 2 + \frac{3r^2 z}{a^3} \left[\frac{a}{(\lambda_1)^{\frac{1}{2}}} - \eta \right] - \frac{z}{(\lambda_1)^{\frac{1}{2}}} \left(3 - \frac{z^2}{\lambda_1} \right) \right\}$$

$$u_z = \frac{\pi a \beta c}{4 G} \left[\left(\frac{r^2}{a^2} - \frac{2z^2}{a^2} - 2 \right) \eta + \frac{2z^2}{a(\lambda_1)^{\frac{1}{2}}} - \frac{r(\lambda_1)^{\frac{1}{2}}}{a(a^2 + \lambda_1)} \right]$$

$$\sigma_{rr} = \frac{\pi a^2 \beta c}{3 r} \left\{ - 2 + \frac{3r^2 z}{a^3} \left[\eta - \frac{a}{(\lambda_1)^{\frac{1}{2}}} \right] + \frac{z}{(\lambda_1)^{\frac{1}{2}}} \left(3 - \frac{z^2}{\lambda_1} \right) \right\} \tag{38}$$

$$\sigma_{\Theta\Theta} = \frac{\pi a^2 \beta c}{3 r^2} \left\{ 2 + \frac{3r^2 z}{a^3} \left[\eta - \frac{a}{(\lambda_1)^{\frac{1}{2}}} \right] + \frac{z}{(\lambda_1)^{\frac{1}{2}}} \left(\frac{z^2}{\lambda_1} - 3 \right) \right\}$$

Here, $\beta = \frac{\alpha}{\pi} G(1+\nu)$ and G is the shear modulus of the material. In equation (38), u_r and u_z denote the displacements in the r and z directions and σ_{rr} and $\sigma_{\Theta\Theta}$ denote the radial and tangential stresses, respectively.*

---

* Note: A doctoral dissertation titled "Thermal Fracturing of Hard Crystal-line Rock" by P.J. Lauriello, Rutgers University, October 1971, and presented as a paper at the 14th Rock Mechanics Symposium, discusses the thermal stress distribution in a semi-infinite region due to radiation of a finite spot on the surface. The source is stationary; however, it appears that the solution could be modified to study the effect of moving sources. Lauriello has also modified his solution for localized dielectric heating at the semi-infinite region and for convective heating of a finite spot on the surface.

The thermal gradients (Fig. 23)* are greatest at the surface of the material near the edge of the heat source. The radial and tangential stresses are likewise of highest magnitude in the same locality. It is of interest to note that the tangential stresses become compressive at positions only a short distance under the heat source.

The radial and tangential stresses at the surface are principal stresses and the shear stress, equal to one-half their algebraic difference, is greatest at a point just under the edge of the heat source. Assuming that the stress pattern is somewhat similar for a moving heat source, both high tensile and high shear stresses exist behind the heat front, particularly if the rise in temperature is rapid. Thus, it would be reasonable to hypothesize that spallation is due to both tensile and shear failure, with most of the cracks originating at or near the surface.

Thermal Shock. Thermal shock describes the phenomena associated with sudden transient changes in temperature of a body, as differentiated from conditions of static or slowly changing thermal stress. No definition appears to be given in the literature of the rate of stress change which describes the state of thermal shock. However, an index of merit is used to indicate the relative resistance to thermal shock of a material. It is of particular interest in conjunction with sudden heating or cooling of brittle materials because of cracking, spallation and failure.

---

* These results were obtained using the following values for Dresser Basalt:

$a = 3$ cm

$c = 600°c$

$\alpha = 10^{-4} \frac{cm}{cm-°C}$

$\nu = 0.24$
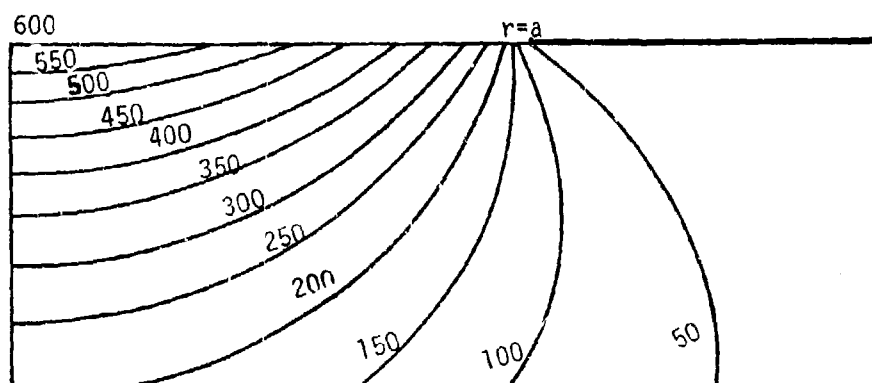
Isothermal Lines, °C
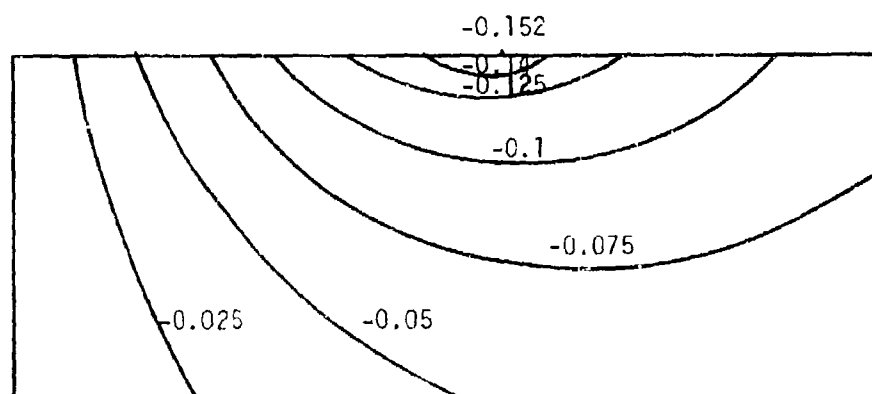
Normalized Radial Stress, $\dfrac{\sigma_{rr}}{G}$
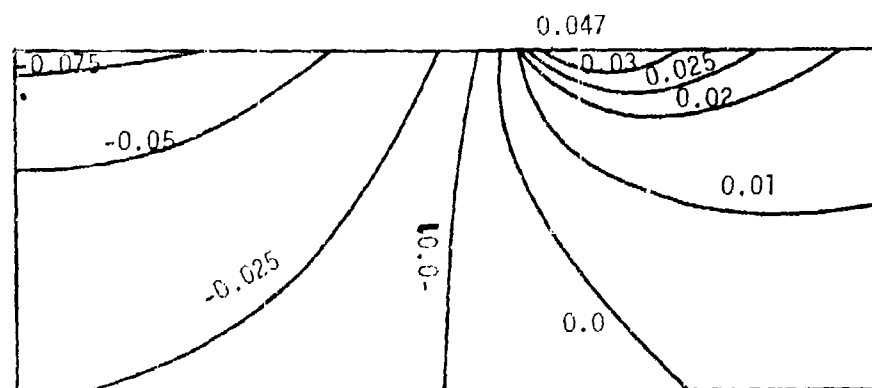
Normalized Tangential Stress, $\dfrac{\sigma_{\theta\theta}}{G}$

Fig. 23. Temperature Stress Distribution - Hemispherical Heat Source - Steady State

67

The rates of traverse employed in the experimental work in this project were as high as 4.5 in./sec with high flame temperatures and relatively high surface film temperatures. Also, if water is used to cool the rock after the passage of the flame jet, the rock surface experiences a transient thermal shock.

If one surface of a flat plate of uniform temperature is suddenly immersed in a medium of lower temperature, the following equation can be written for the stress in a plate with elastic temperature-independent properties (Ref. 58):

$$\sigma^* = \frac{T_{av} - T}{T_0} \tag{39}$$

where σ^* is the ratio of the stress developed to that which would be developed if the thermal expansion were unrestrained. Also,

$$\sigma^* = \frac{\sigma(1-\nu)}{E\alpha T_0} \tag{40}$$

where

σ = stress

ν = Poisson's ratio

E = Young's modulus

α = coefficient of thermal expansion

T_{av} = ave. temp. across plate thickness

T = temperature at a point

T_0 = ambient temperature of plate

For thin plates it has been found that the surface stress is strongly dependent upon the heat transfer coefficient h and the heat conductivity k, the stress being proportional to h/k. For a plate of a given thickness it can be shown that the maximum shock temperature which it can withstand is proportional to $k\sigma_b/E\alpha h$, where σ_b is the breaking stress. The tests

68

to determine the relative shock merits of materials consisted of subjecting discs 2 in. diam by 1/4 in. thick to repeated thermal shock cycles until they failed, i.e., they were heated in a furnace and quenched in water.

For thick plates the surface temperature can be changed long before the temperature of the inner part of the body. For heat immersion the surface layers cannot expand and under these conditions of constraint the surface stress developed is $E\alpha T_o/(1-\nu)$ which is relatively independent of the heat transfer coefficient or conductivity of the material, particularly if the latter is small. For poor heat conductors such as rock only the material near the surface is heated and the high compressive stresses are limited to only the surface layers. The better the conductivity the greater the depth of material that is under compressive stresses.

The above failure mechanisms are valid only for the rupture of plates, which is caused by the differential expansion of the inside and outside layers of the plate. The mechanism of spallation of the surface of a thick solid involves a different combination of parameters. That is, in rock spallation a maximum size of chip or fragment is desired. It should be noted that in a heating process the whole surface of a solid is in compression, and spallation occurs by means of shear. On the other hand, when the surface of a body is cooled, it fails either in tension or shear. For rocks the latter process appears to be advantageous because the tensile strength of rock is very low.

In a study of the spallation of ceramic materials used as liners for rocket nozzles and surfaces in similar environments, Newman (Ref. 59) points out that when severe gradients are present thermal stresses arise because the material is not free to expand. For brittle materials failure

in tension by cooling is of primary concern. However, for many aerospace
uses (with which Newman was concerned) materials are not cycled or cooled,
but are heated only once. The failures due to heating only are the result
of shear stresses, the cracks following shear lines at 45 deg to the surface.

The assumptions for a simple model utilized by Newman were that:

1. The model was a flat plate with a very high convective heating
   rate.

2. Failure occurs at the surface as a result of shear stresses
   which are proportional to the temperature gradient.

3. Crack propagation is governed by Weibull failure statistics,
   propagating to a depth where the shear stress level is about
   5 percent of reported shear strengths.

4. Failure is said to take place where two (2 crack model) or three
   (3 crack model) intersect.

While the geometry considered is for a thin plate, the assumption of
very large values of tne heat transfer parameter, $\beta = h\, a/k^*$, and short
reduced heating times, $\tau = kt/\rho Ca^2$, results in a very small temperature
rise at the back of a plate of thickness 2a. Therefore, the arguments
are assumed to apply to a semi-infinite model.

The Fourier one-dimensional heat equation is then

$$\frac{\partial^2 \theta}{\partial \zeta^2} = \frac{\partial \theta}{\partial t} \tag{41}$$

---

* a is half the thickness of the plate, and
  h is the heat transfer coefficient

with boundary conditions

$$\left. \begin{array}{c} \theta(\zeta,0) = \theta_0 \\[2ex] \left(\dfrac{\partial \theta}{\partial \zeta}\right) \zeta = 0 = \beta\theta \end{array} \right\} \tag{42}$$

The solution for (42) is

$$\frac{\theta}{\theta_0} = \text{erf}\left[\frac{\zeta}{2\sqrt{t}}\right] - \exp\left[\beta\zeta + \beta^2 t\right] \text{erfc}\left[\frac{\zeta}{\sqrt{t}} + \beta\sqrt{t}\right]$$

where

$$\theta = \frac{T - T_0}{T_e - T_0}$$

$$\zeta = \frac{x}{a}$$

71

The shear strain may be approximated as follows (Ref. 60):
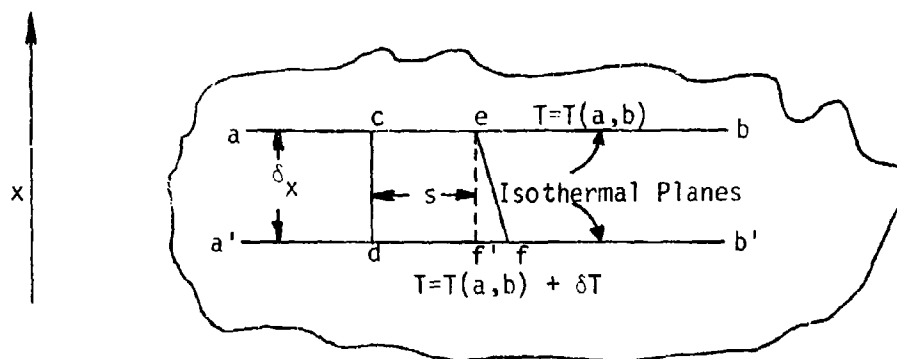
Fig. 24. Diagram Showing Shear Strain Developed by a Temperature Gradient (after Norton, Ref. 60)

The surfaces ab and a'b' (Fig. 24) are isothermal planes parallel to the surface at temperatures T and T + δT.

$$\varepsilon = S\alpha \frac{dT}{dx} \tag{43}$$

where S is a characteristic size of an element of brittle material.

It is recognized that the above equation serves largely as an illustrative method, and is used here to give only a first approximation for the stresses occurring at the heat front in the rock surface.

Using this model, Newman points out that a plot (Fig. 25) of ε vs. $\frac{\partial \sigma}{\partial t}$ for β = 100 as a function of t, shows that the gradient which will influence failure is given by the envelope to the individual stress curves. This model shows that for small t the heat penetration is shallow, but the stress gradient is high. If one assumes a minimum

72
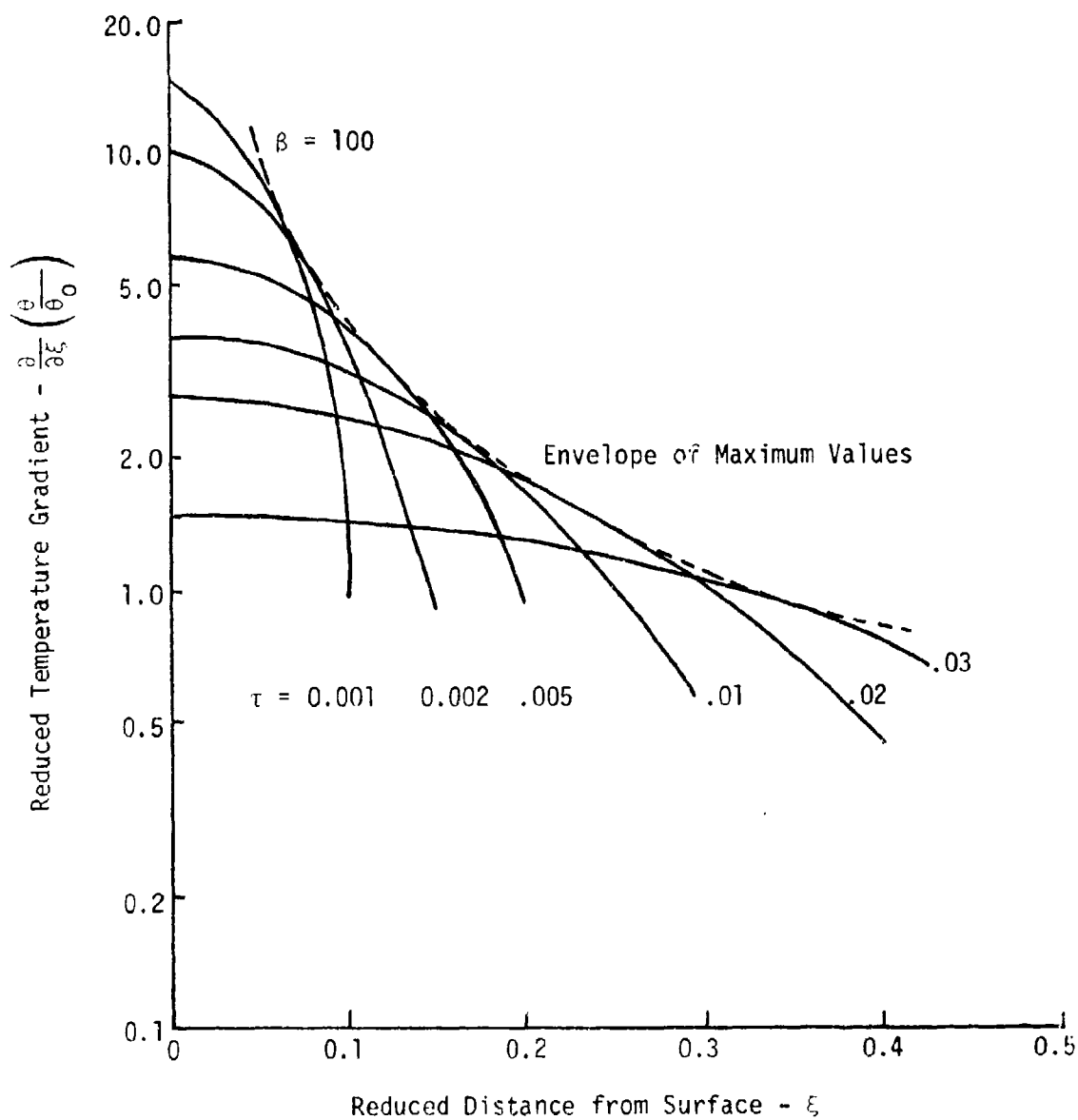
Fig. 25.   Reduced Temperature Gradient as a Function of Both
            Reduced Distance and Reduced Time (after Newman, Ref. 60)

stress gradient below which fracture will not occur, then few fractures originate at any appreciable distance below the surface. Likewise, the thermal strain energy required to maintain crack propagation diminishes rapidly with depth.

The value of strain along the envelope, which influences failure, is given by

$$\varepsilon \approx \left(\frac{S\alpha\theta_0}{a}\right)\left(\frac{\partial\theta/\theta_1}{\partial\xi}\right)_{max}$$

The probability of crack initiation is assumed to follow the statistical model developed by Weibull (61), also called the "risk of rupture criterion" for thermal shock:

$$R = \int_V f(\sigma_i) \, dV_i \tag{44}$$

where σ_i is the stress in a volume element dV_i and the integration is performed for the whole volume under stress.

This may also be expressed in terms of strain (Ref. 59) for the probability of a single crack in the body:

$$F(\varepsilon) = 1 - \exp\left[-A \int_0^{x_c} n(\varepsilon) \, dx\right] \tag{45}$$

where x_c is the maximum crack depth and $n(\varepsilon)$ is the Weibull material function. The probability that second and third cracks will form to release a fragment is the probability that they are near enough to intersect the other cracks. Employing the Weibull distribution $n(\varepsilon) = K^m$ Newman shows that the depth of crack to be expected is dependent upon the rate of heating, being lower for higher heating rates (Fig. 26) where

$$S_0 = \frac{\sigma}{E\theta\alpha} = 0.002$$

$$S = 10^{-4} \text{ cm}$$

$$a = 1 \text{ cm}$$

$$m = 5$$

$$A = 1 \text{ cm}^2 \quad \text{(area)}$$

74
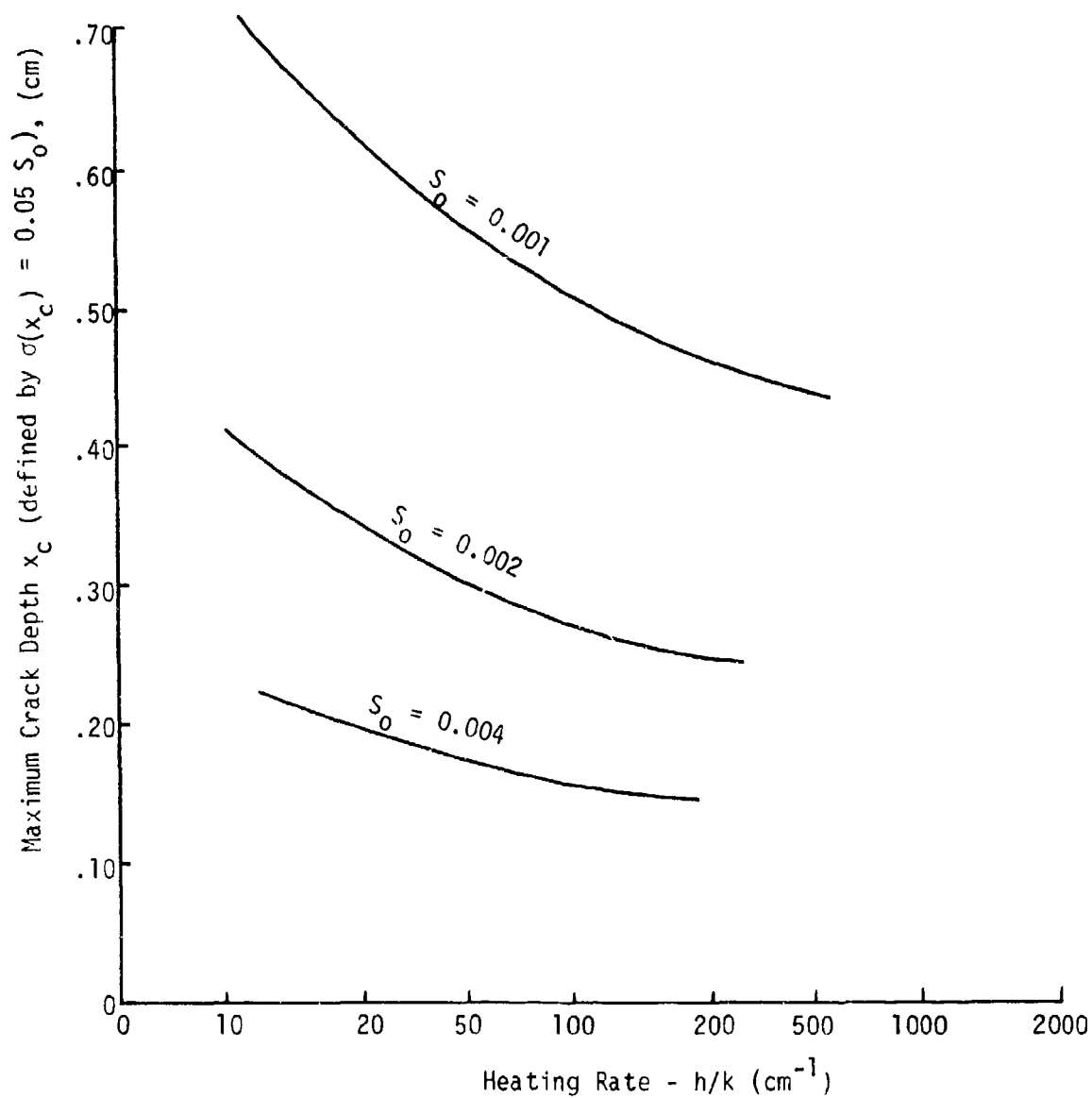
Fig. 26.   Maximum Crack Depth for Various Heating Rates

For useful application the Weibull function must be known, and it has been found that only one-dimensional models can be scaled and this scaling is restricted to small temperature gradients. None of the analyses given by Newman and others consider the effect of stress relieving. For example, some ceramics are more stress resistant where flaws have been deliverately introduced. However, small local flaws may contribute to spallation.

Crack Propagation

Sih and Liebowitz (Ref. 62) show for a condition of steady heat flow that when there is a crack in a solid whose thermal conductivity is different from the surrounding material, the local temperature gradient is intensified. The increase in temperature gradient is accompanied by increased thermal stresses which may cause propagation of imperfections. It has been shown further that for steady state temperature distributions the stresses at the tips of Griffith cracks are the same as those induced by mechanical forces as described by the $1/\sqrt{r}$ (r=crack tip radius) singularity. Hence, stress intensity factors and crack prediction caused by heat flow may be analyzed in conformance with the Griffith-Irwin theory of isothermal crack growth and propagation.

An energy balance equation can be set up for fracture problems where inertia is not negligible (Ref. 63). If it can be assumed that the energy dissipation around the crack tip is small, the energy required for such dissipation is given by:

$$\dot{u} - \dot{v} - \dot{T} = \dot{E}_c \tag{46}$$

where

$\dot{u}$ = time rate of external work

$\dot{v}$ = time rate of elastic energy

$\dot{T}$ = time rate of kinetic energy for a small region at the crack tip

$\dot{E}_c$ = rate of crack closure energy

For application to fracture propagation caused by thermal stress the external work is furnished by the heat transferred to the rock, part of which is converted to elastic energy. In crack formation there must be sufficient thermal and elastic energy present to initiate a crack and to cause it to propagate.

If $\dot{D}$ is the rate of dissipative energy, the Griffith criterion states that the crack will propagate in the direction where the $\dot{E_c}/\dot{D}$ ratio is a maximum. While the initial direction of a fracture from a notch is determined by several factors, the plane of maximum tensile or shear stress may be the plane of fracture, which may be applicable in deep kerfing.

<u>Strain Failure</u>. Thirumalai (Ref. 37) notes that the shear strain of rock at failure may be taken as the sum of the elastic ε_e, and inelastic, ε_i, strains:

$$\varepsilon_f = \varepsilon_e + \varepsilon_i \tag{47}$$

and the degree of proportionality of elastic strain is given by

$$\varepsilon_p = 100 \ \varepsilon_e / (\varepsilon_e + \varepsilon_i) \tag{48}$$

Measurements (Ref. 37) of shear strain parameters were performed on a punch type shear apparatus and the inelasticity was determined by stress recycling. The shear strength of quartzite and basalt (Table 3) were found to be the highest, and the shear strain to cause failure in the basalt was higher than that for the granites. This factor plus the low thermal gradients occurring in basalt partially explain its low spallability.

Table 3. Total Strain at Shear Failure and Degree of Elasticity for Three Test Rocks*

Sioux Quartzite

Specimen number	Shear Strength psi	Shear Strength N/mm²	ε_f	ε_e	ε_p percent
1	11,880	83.4	0.0287		
2	10,897	76.5	.0287		
3	10,897	76.5	.0325	0.0239	74
4	7,948	55.8	.0287		
5	11,866	83.3	.0315	.0239	76
6	9,914	69.6	.0287	.0210	74
7	12,863	90.3	.0315	.0249	79
Mean value....			.0300		76
Standard deviation..			.0017		2.36

Charcoal Granite

Specimen number	Shear Strength psi	Shear Strength N/mm²	ε_f	ε_e	ε_p percent
1	7,550	53.0	0.0315	0.0216	69
2	0,017	63.3	.0315	.0226	69
3	7,749	54.4	.0296	.0195	66
4	7,265	51.0	.0306	.0210	69
5	7,749	54.4	.0315	.0210	67
Mean value....			.0309		68
Standard deviation..			.0008		1.41

Dresser Basalt

Specimen number	Shear Strength psi	Shear Strength N/mm²	ε_f	ε_e	ε_p percent
1	9,117	64.0	0.0363		
2	12,849	90.2	.0363	0.0277	76
3	9,900	69.5	.0363	.0268	74
4	13,381	97.1	.0344	.0258	75
5	12,849	90.2	.0344	.0254	74
6	9,900	69.5	.0344	.0254	74
Mean value....			.0354		75
Standard deviation..			.0010		0.89

* The tests were run without stress cycling.

CHAPTER IV

MECHANICAL FRAGMENTATION

Introduction

Analytical studies of mechanical fragmentation of rocks for different indentors have been made by using the slip-line method. Four indentors, two yield criteria and three interface conditions between rock and indentor were studied. They are

A. Indentors

1. Indentor No. 1 - Wedge indentor

2. Indentor No. 2 - Indentor with blunt point

3. Indentor No. 3 - Cylindrical indentor

4. Indentor No. 4 - Indentor with round point

B. Yield Criteria

1. Maximum shear theory

2. Internal friction theory (Coulomb's yield criterion)

C. Interface Conditions

1. Smooth surface

2. Rough surface

3. Frictional surface

General Theory

The slip-line theory was developed to analyze plane strain deformation of a rigid perfectly plastic isotropic solid (Ref.64). The equilibrium equations for plane plastic flow are

$$\frac{\partial \sigma_{xx}}{\partial X} + \frac{\partial \tau_x}{\partial yy} = 0$$

$$\frac{\partial \tau_{xy}}{\partial X} + \frac{\partial \sigma_{yy}}{\partial y} = 0$$

(49)

79

For the maximum shear theory, let

$$\sigma_{xx} = P + K \cos 2\Theta$$

$$\sigma_{yy} = P - K \cos 2\Theta \qquad\qquad (50)$$

$$\tau_{xy} = K \sin 2\Theta$$

where $P = 1/2(\sigma_{xx}+\sigma_{yy})$ is the hydrostatic part of the stress tensor and Θ is the angle measured from the x-axis to the direction of the algebraically maximum principal stress shown in (Fig. 27).

Substitution of equation (50) in equation (49) gives partial differential equations of the hyperbolic type which can be solved by the method of characteristics (Ref. 64,65). The characteristic (slip-line) directions are

$$\frac{dy}{dx} = \tan(\Theta \pm \frac{\pi}{4}) \qquad\qquad (51)$$

which show that the two families of slip-lines, α and β, form an orthogonal network. Along the slip-lines

$$P \pm 2K\Theta = \text{constants} \qquad\qquad (52)$$

Similarly, for the internal friction theory a stress circle is tangent to the envelope and the governing stress equations are hyperbolic (Fig. 28). The direction of the slip-lines is given by the orientation of the planes specified by the points of contact of the stress circle with the yield envelope. Two families of slip-lines exist which are inclined at angles of $\pm (\frac{\pi}{4} - \frac{\phi}{2})$ to the direction of the algebraically maximum principal stress. Along the slip-lines

$$\frac{dy}{dx} = \tan(\Theta \pm \mu), \text{ where } \mu = \frac{\pi}{4} - \frac{\phi}{2} \qquad\qquad (53)$$

and

$$\frac{1}{2} \cot \phi \ln(\sigma) \pm \theta = \text{constants} \tag{54}$$

where

$$\sigma = \frac{1}{2}(\sigma_{xx} + \sigma_{yy}) + K \cot \phi$$

In equations (52) and (54), σ is a function of θ. It is necessary to know how θ varies along the slip-lines in order to obtain σ. The solutions which assume that θ is constant along one or both families of slip-lines are frequently applied to this problem (Ref. 66,67) and are used in the following analyses.

Slip-line Fields. Two possible slip-line fields, as proposed by Prandtl and Hill (64) are shown in Fig. 29. Hill takes into account the surface displacement next to the wedge. The position of the dis-placed surface is determined based on the assumption of constant volume. Hill's proposed slip-line field was applied in this study.

The proposed slip-line field (Fig. 29) applied to the smooth surface of wedge indentors, can be divided into three regions. In regions I and III, the two families of slip-lines are straight lines and intersect at the constant angle $(\frac{\pi}{2} - \frac{\phi}{2})$*, i.e., θ is constant and the stresses are constants throughout the region. They are the "constant regions". In region II, θ is constant along one family of slip-lines, the other family is composed of circles or exponential spirals, which is the "centered fan" or "radial shear region". Every proposed slip-line field used in this study will be the combination of these three basic regions.

---

*For maximum shear theory the angle is $\frac{\pi}{2}$, i.e., $\phi = 0$.

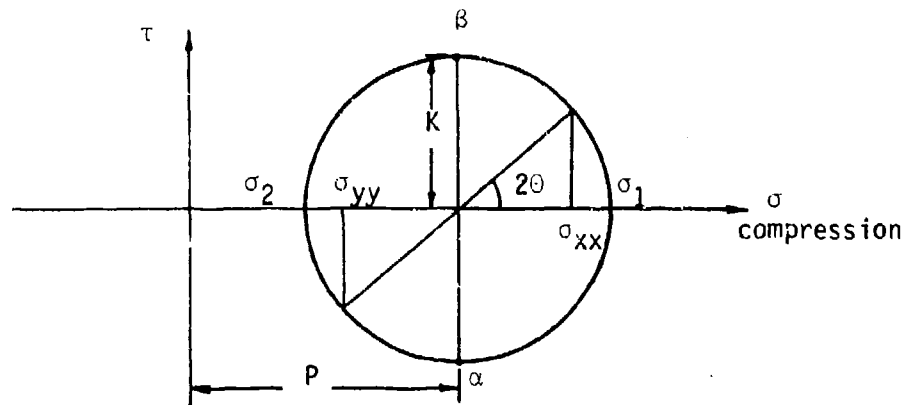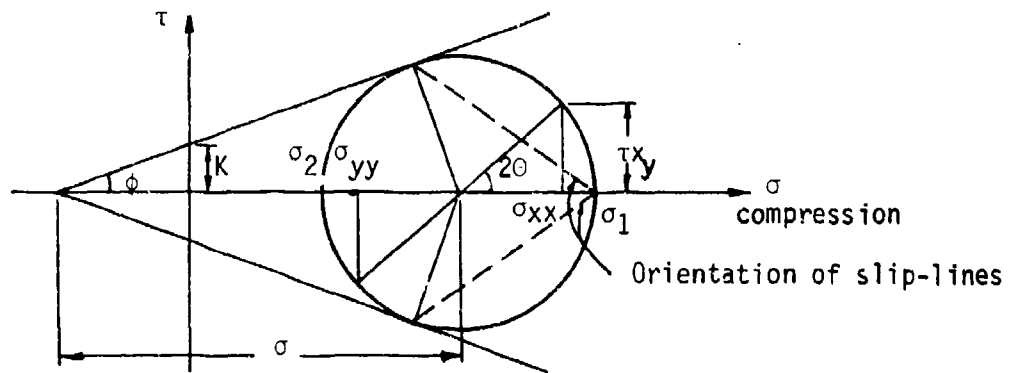Fig. 27. Mohr Diagram for Maximum Shear Theory

Fig. 28. Mohr Diagram for Internal Friction Theory

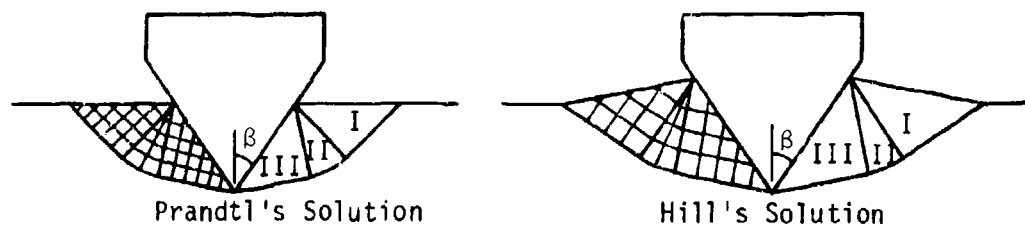Prandtl's Solution   Hill's Solution

Fig. 29. Two Possible Slip-line Fields Proposed by Prandtl and Hill

<u>Interface Conditions.</u> These are considered for three conditions.

(A) Smooth Surface:

The proposed slip-line fields for the smooth surface for indentors are shown in Figures 30(a & c) and 31(a & c), (at $\eta = 45°$). In this case, the algebraically maximum stress acts normal to the bit-rock interface and is assumed to be constant along the length of the edge. The stress at the interface can be expressed as:

$$\sigma_n = 2\ K(1 + \psi) \qquad = \text{normal stress}$$

$$\tau_n = 0 \qquad = \text{shear stress}$$

$$\text{(55a)}$$

for the maximum shear theory and as

$$\sigma_n = \frac{2\ K(1 + \sin\phi)^2}{\sin 2\phi}\ \exp(2\psi\tan\phi) - K \cot \phi$$

$$\tau_n = 0$$

$$\text{(55b)}$$

for the internal friction theory

where ψ is the direction change of one slip-line from the interface to the rock surface.

(B) Rough Surface:

The proposed slip-line fields for a rough surface are shown in Figures 30(b & d), 31(b & d), and 39. Since two families of slip-lines always intersect at the same angle $(\pi/4 - \phi/2)$ or $(\pi/4 + \phi/2)$, if β is greater than $(\pi/4 - \phi/2)$, then a "false nose" region will be created. The "false nose" region is a constant region and moves downward with the bit. If β is less than $\pi/4 - \phi/2$, then the interface coincides with a slip-line of the shear region. The stress at the interface (or the edge of the

false nose, if β is greater than π/4 - φ/2) can be expressed as:

$$\sigma_n = K (1 + 2\psi)$$

$$\tau_n = K$$

(56a)

for the maximum shear theory and

$$\sigma_n = K \cot \phi \ [(1 + \sin\phi) \ \exp(2\psi\tan\phi) - 1]$$

$$\tau_n = (1 + \sin\phi) \ \exp(2\psi\tan\phi)$$

(56b)

for the internal friction theory.

(C) Frictional Surface:

In this case, the slip-line field is between the smooth and rough conditions. Assume η is constant along the indentor surface. From the smooth to the rough condition, η will change from (π/4 + φ/2) to zero. In proposed fields for the different indentors (Fig. 30(a & b) and Fig. 31(a & b)) if the β angle is greater than (π/4 - φ/2), then the frictional surface has the same slip-line field as the rough surface.

The stresses at the interface at β < (π/4 - φ/2) will be:

$$\sigma_n = K (1 + 2\psi + \sin 2\eta)$$

$$\tau_n = K \cos 2\eta$$

(57a)

for the maximum shear theory and

$$\sigma_n = \frac{K (1 + \sin\phi)}{\cos\phi} \ [\frac{1}{\sin\phi} - \sin (\phi - 2\eta)] \ \exp(2\psi\tan\phi) \ - K \cot \phi$$

$$\tau_n = \frac{K (1 + \sin\phi)}{\cos\phi} \ \cos(\phi - 2\eta) \ \exp(2\psi\tan\phi)$$

(57b)

for the internal friction theory.

30(a)

Indentor No. 1

$0° \leq \eta° \leq 45°$

$\phi = 0°$

false nose

$\frac{\pi}{4}$

30(b)
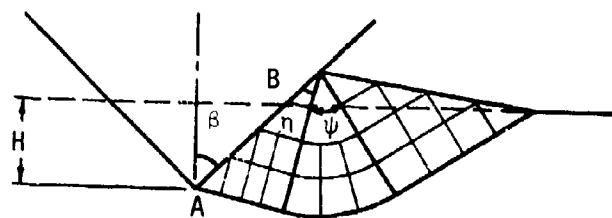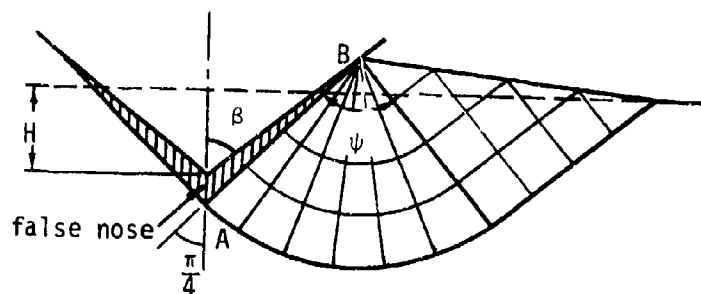
Indentor No. 1

$\beta > 45°$

$0° \leq \eta \leq 45°$

$\phi = 0°$

false nose

30(c)

Indentor No. 2

$0° \leq \eta \leq 45°$

$\phi = 0°$

false nose

30(d)
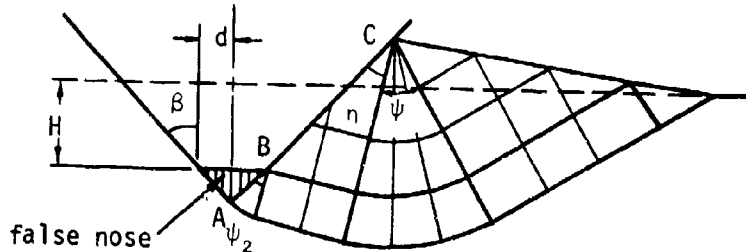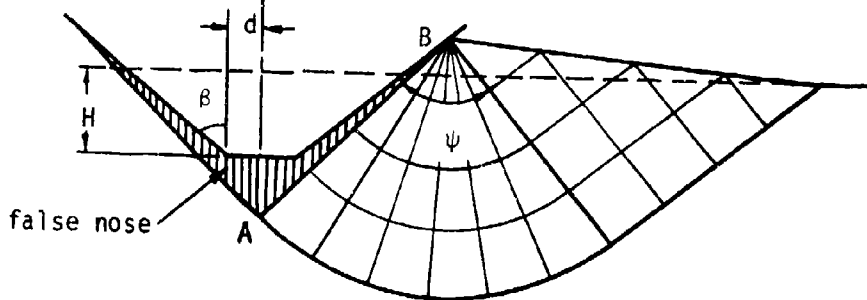
Indentor No. 2

$\beta > 45°$

$0° \leq \eta \leq 45°$

$\phi = 0°$

Fig. 30. Slip-line Field for Indentors No. 1 and No. 2 for $\phi = 0°$
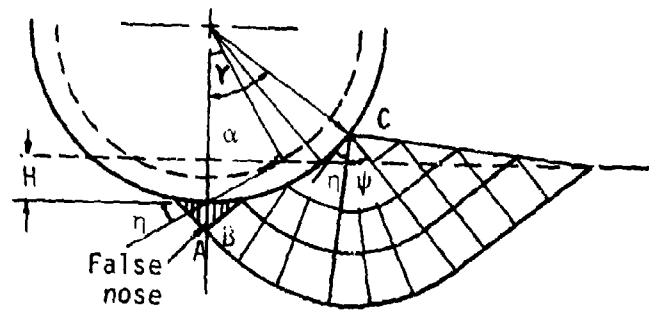
Indentor No. 3

$0° \leq \eta \leq 45°$

$\phi = 0$

31(a)
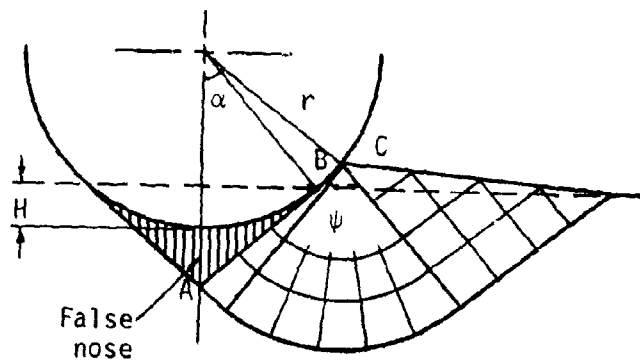
Indentor No. 3

$\eta = 0°$

$\phi = 0°$

31(b)
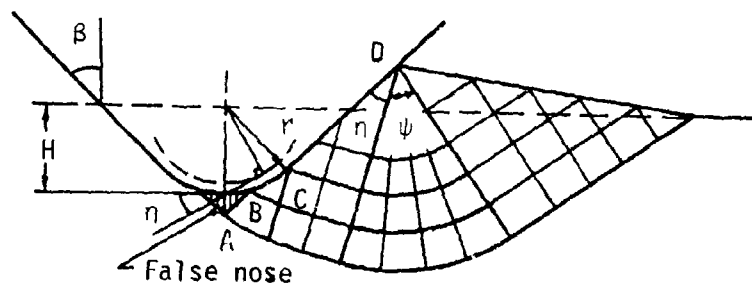
Indentor No. 4

$0° \leq \eta \leq 45°$

$\phi = 0°$

31(c)
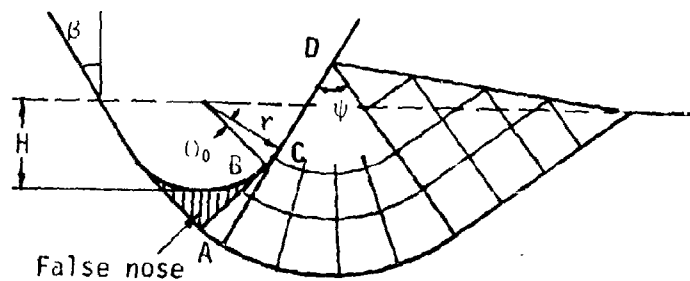
Indentor No. 4

$\beta \leq 45°$

$\eta = 0°$

$\phi = 0°$

31(d)

Fig. 31. Slip-line Fields for Indentors No. 3 and No. 4 for $\phi = 0°$

The force-penetration characteristic can be obtained by integrating the interface stresses along the tooth profile (the formulas for different indentors and surface conditions are listed in Appendix D-Ref. 68). The work accompanying the penetrating force has been integrated for unit depth using the equation

$$W = \int_0^1 FdH$$

Numerical Results

The numerical results for four indentors were obtained for the maximum shear theory (Fig. 32 to 38), and for the internal friction theory (Fig. 40 to Fig. 45).

The force-depth curves for indentor No. 2 (Fig. 32) are nearly linear, and the magnitude of the penetration force is proportional to the width d of the bit tooth. As d approaches zero, the curves become linear, which is the condition for indentor No. 1. The force necessary to penetrate the rock increases rapidly for both increase in friction and the width of the nose of the indentor. The penetration forces for different interface conditions (varying η)(Fig. 33) increase nonlinearly with respect to η. This nonlinear relationship is also true for different indentors and wedge angles(Fig. 35 and Fig. 41).

The force-angle and work-angle values for a unit depth penetration (Fig. 34) increase rapidly with an increase in $\phi > 45°$. Static energy was calculated by integrating the current force at depth H from zero to a unit depth. For the force-penetration characteristic for the cylindrical indentor (Fig. 35) as H increases the force approaches a constant value

87
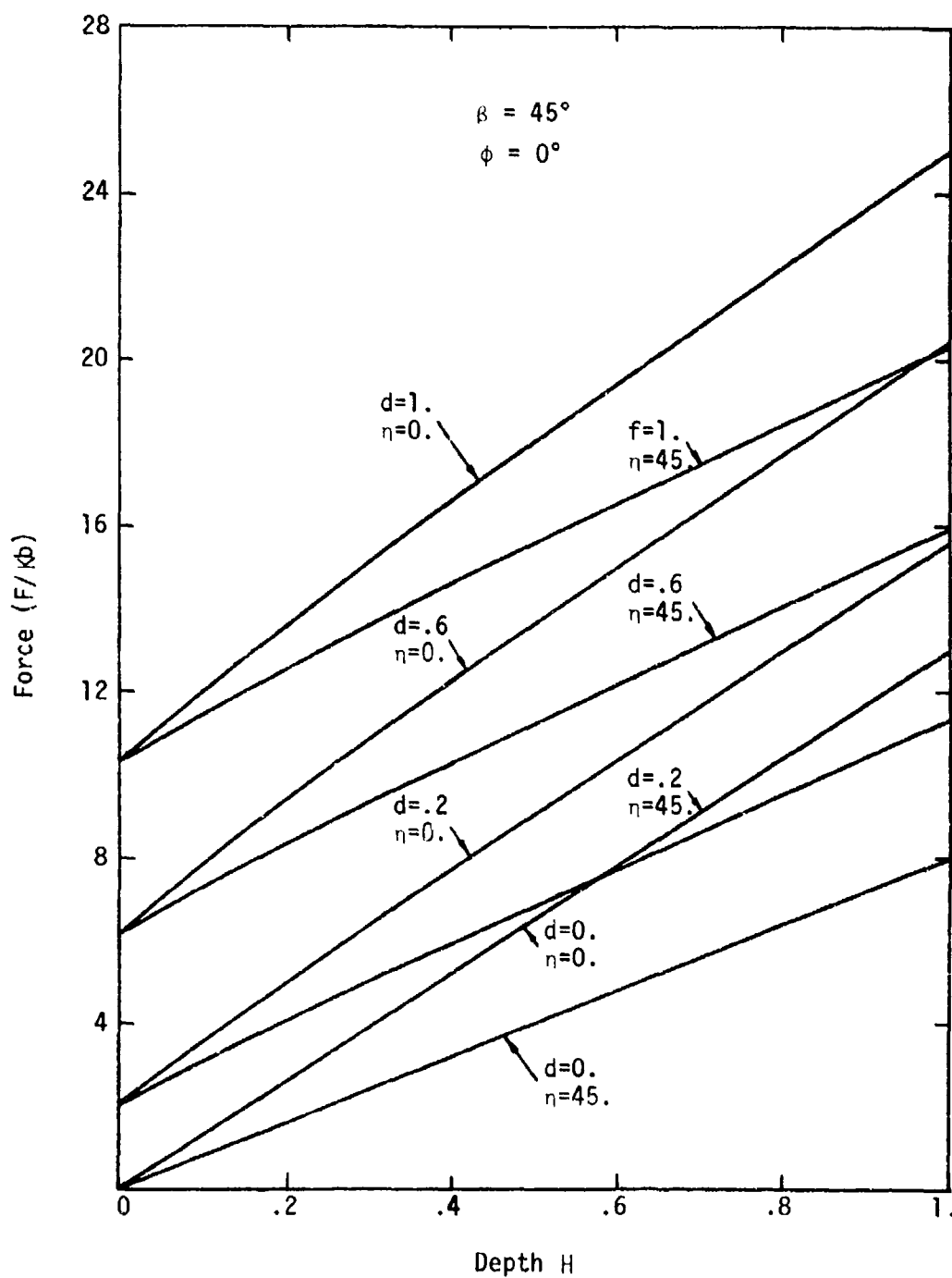
Fig. 32. Force-Depth Diagram for Indentors No. 1 and No. 2 For $\phi = 0°$
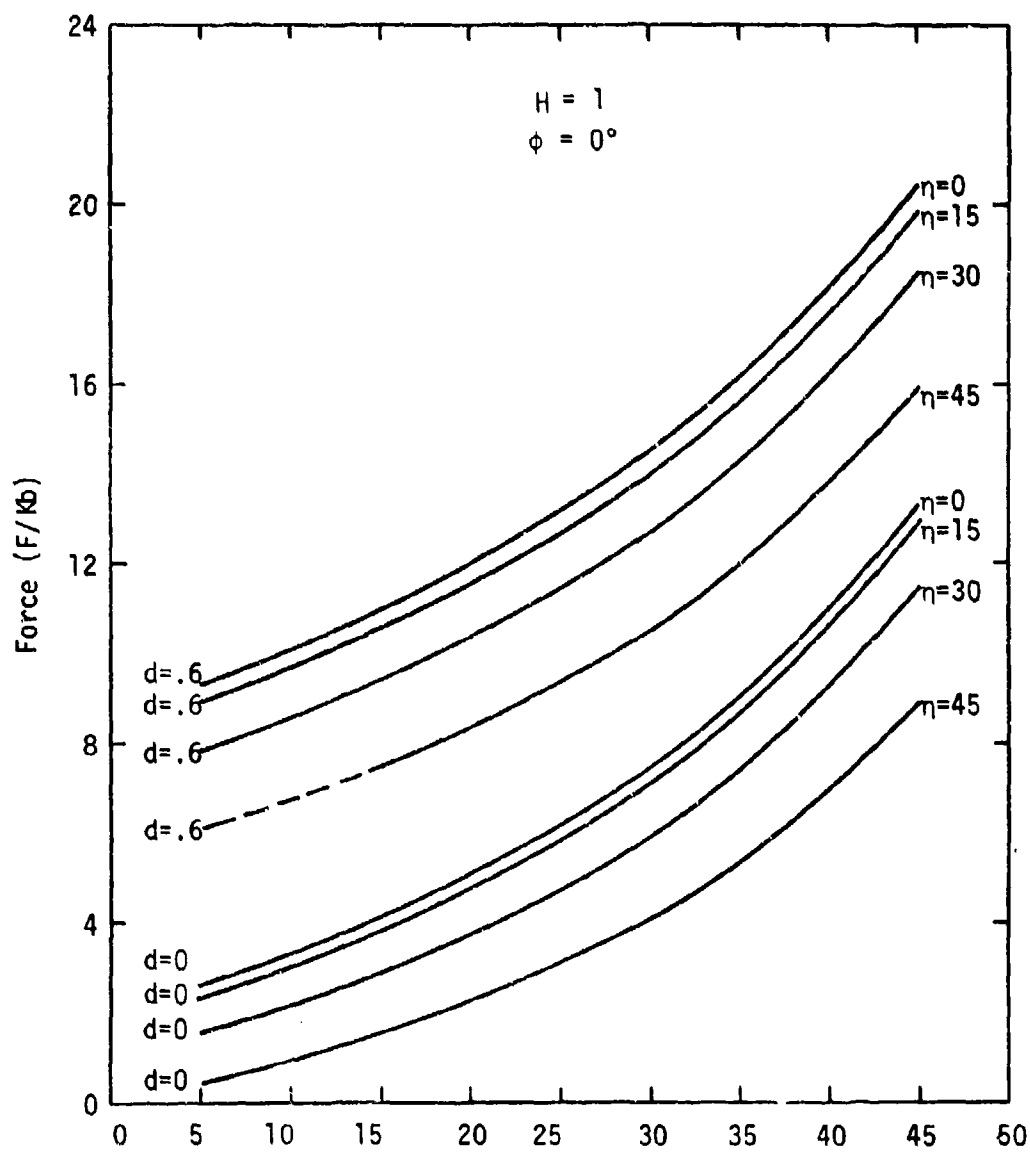
Fig. 33. Force-Angle Diagram for Indentors No. 1 and No. 2 for $\phi = 0°$
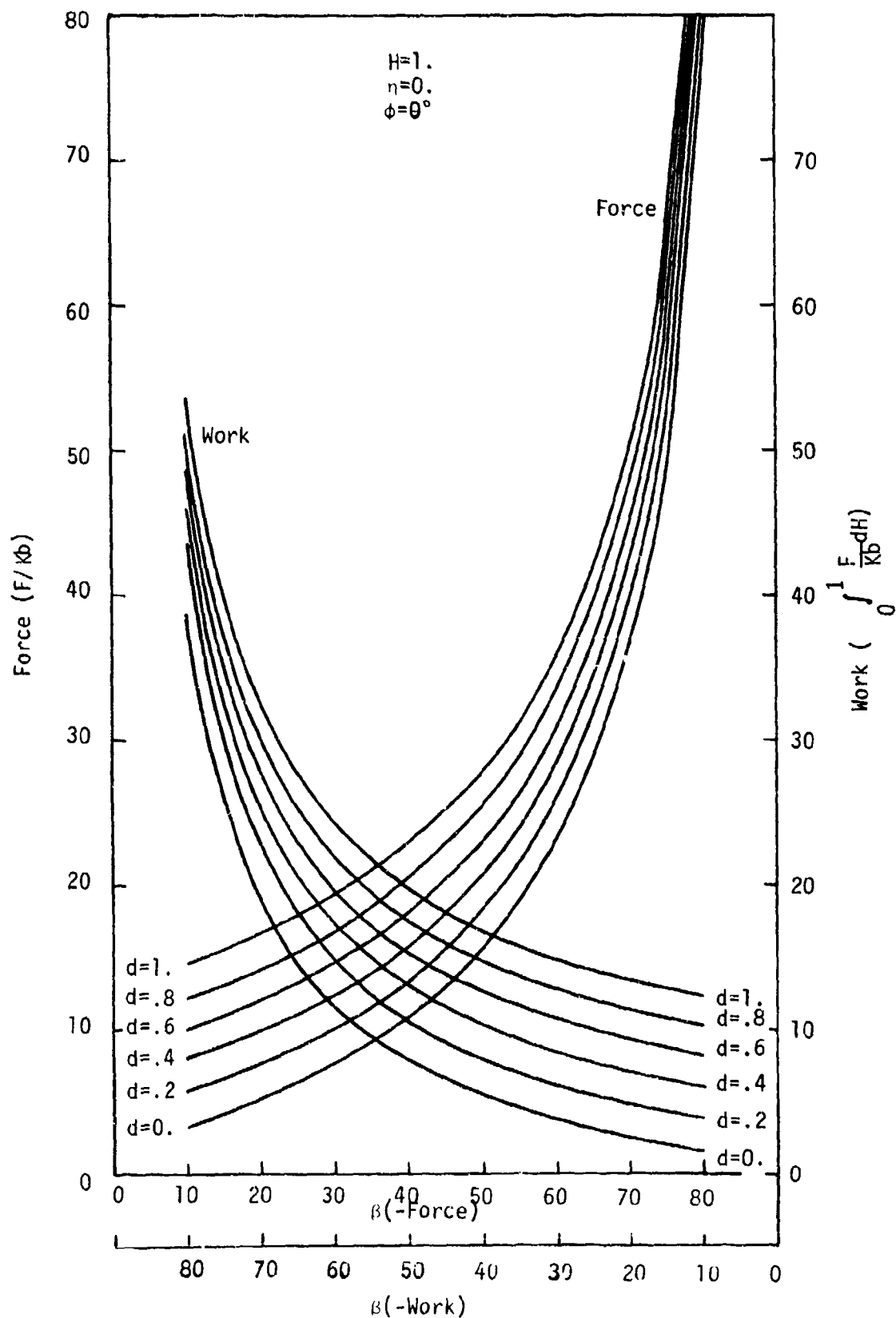
Fig. 34. Force-Angle Diagram for Indentors No. 1 and No. 2 for $\phi = 0°$

90
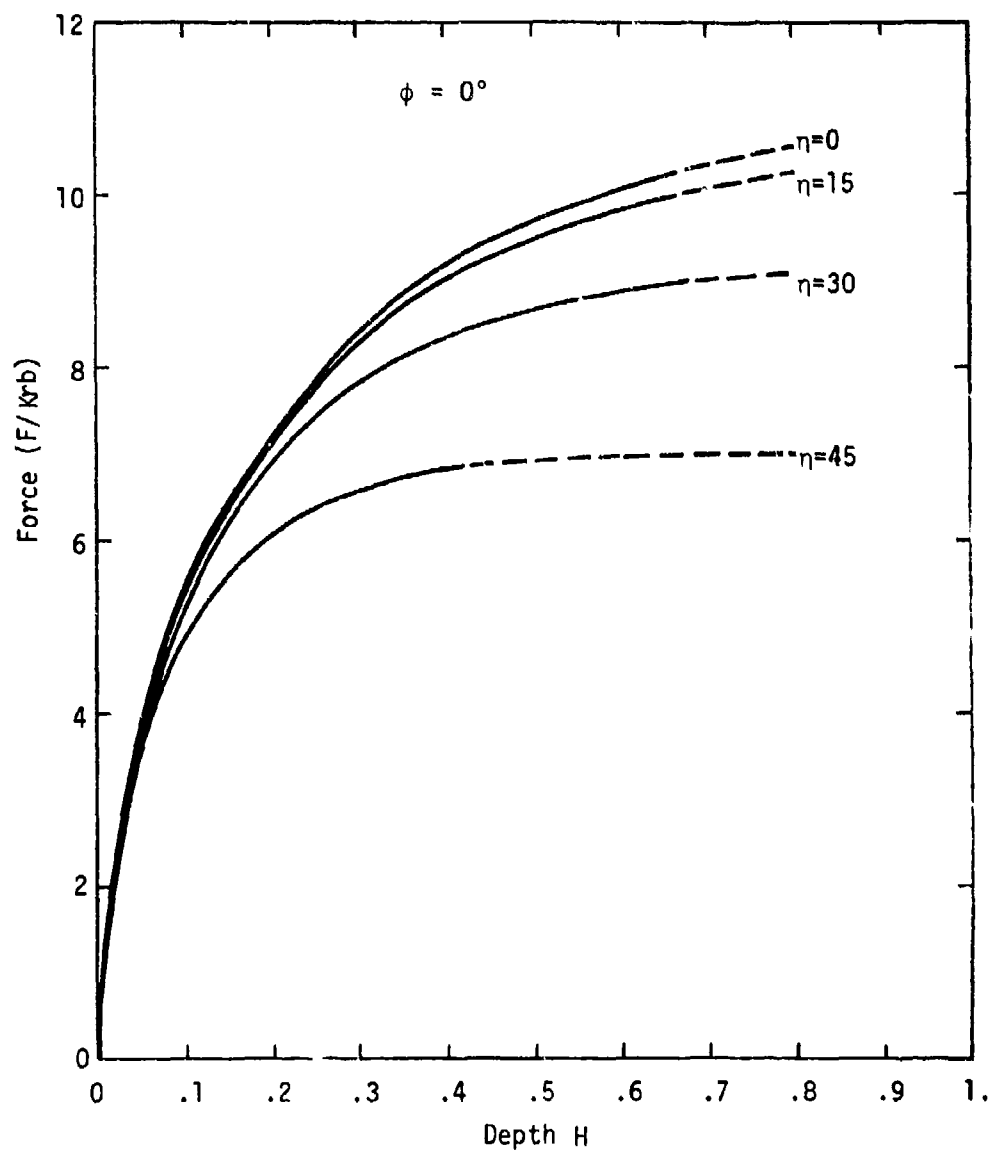
Fig. 35. Force-Depth Diagram for Indentor No. 3 for $\phi = 0°$

and the assumed slip-line field is doubtful above a certain depth of penetration. The dashed line sections show the uncertain region of the slip-line field.

The force-depth relationships for round nosed indentors (Fig. 36 & 38) No. 3 and No. 4 for different values of β and η increase rapidly with the initial penetration, but level off rapidly for small values of β. The force-angle and work-angle for a unit depth of penetration (Fig. 38) are less than for wedge shaped bits for large values of β. The variation of the penetration force from a wedge indentor (r=0) to a round-point dull indentor shows that an increasing amount of energy is consumed as a wedge indentor wears to a dull rounded point.

Figures 40 to 45 were plotted for the internal friction theory using the same coordinates as for the maximum shear theory, which shows that the penetration force increases exponentially with respect to ψ as well as to ϕ.

Since ψ is a function of η, the penetration force also increases with increasing interface friction (Figs. 41 and 43). The rapid increase of force with the internal friction (ϕ)(Fig. 46) is critical above values of 30° to 40° depending upon the value of β.

Energy Calculations

From the stress field study, for a given energy per blow of a pneumatic hammer the depth of penetration can be predicted from the energy-depth curve (Fig. 47). To illustrate effects of parameters the following values are selected:

92

$$\phi = 40°$$

$$b = 2''$$

$$\eta = 0°$$

$$\beta = 0°$$

$$r = 1/32 \text{ in. and } r = 0. \text{ in.}$$

The above values are applicable to the bits used in the experimental part of this work. If the compressive strength σ_0 is known for the relationship $K = \dfrac{\sigma_0 \cos\phi}{2(1 + \sin\phi)}$, the K values for the following rocks are obtained:

Rocks	K(psi)
Charcoal Grey Granite	7,759
Kitledge Pink Granite	5,662
Dresser Basalt	10,112
Black Granite (Buena Gabbro)	7,549
Missouri Red Granite	5,380
Sioux Quartzite	11,347
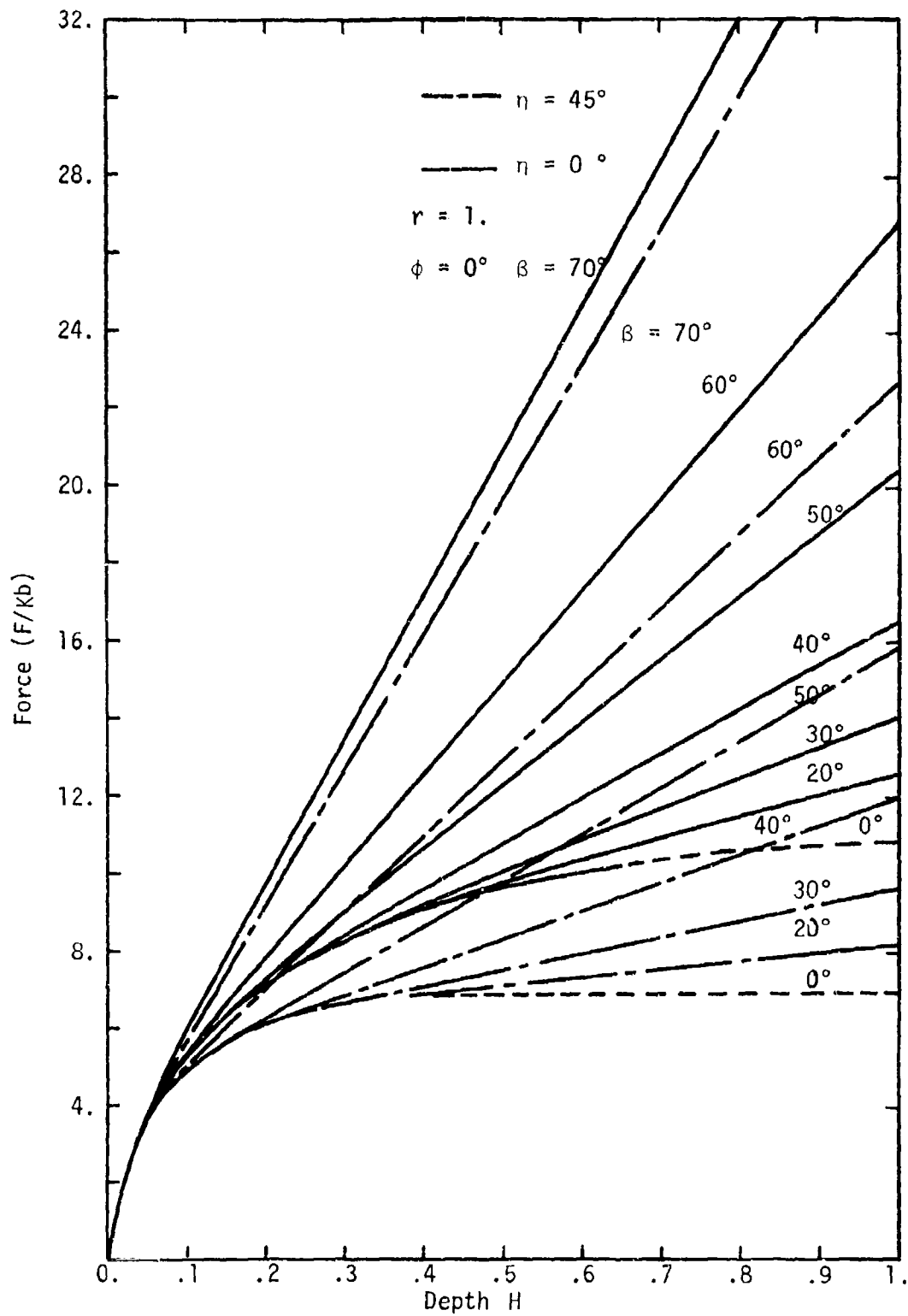
Fig. 36. Force-Depth Diagram for Indentors No. 3 and No. 4 for $\phi = 0°$ and $r = 1$.

94
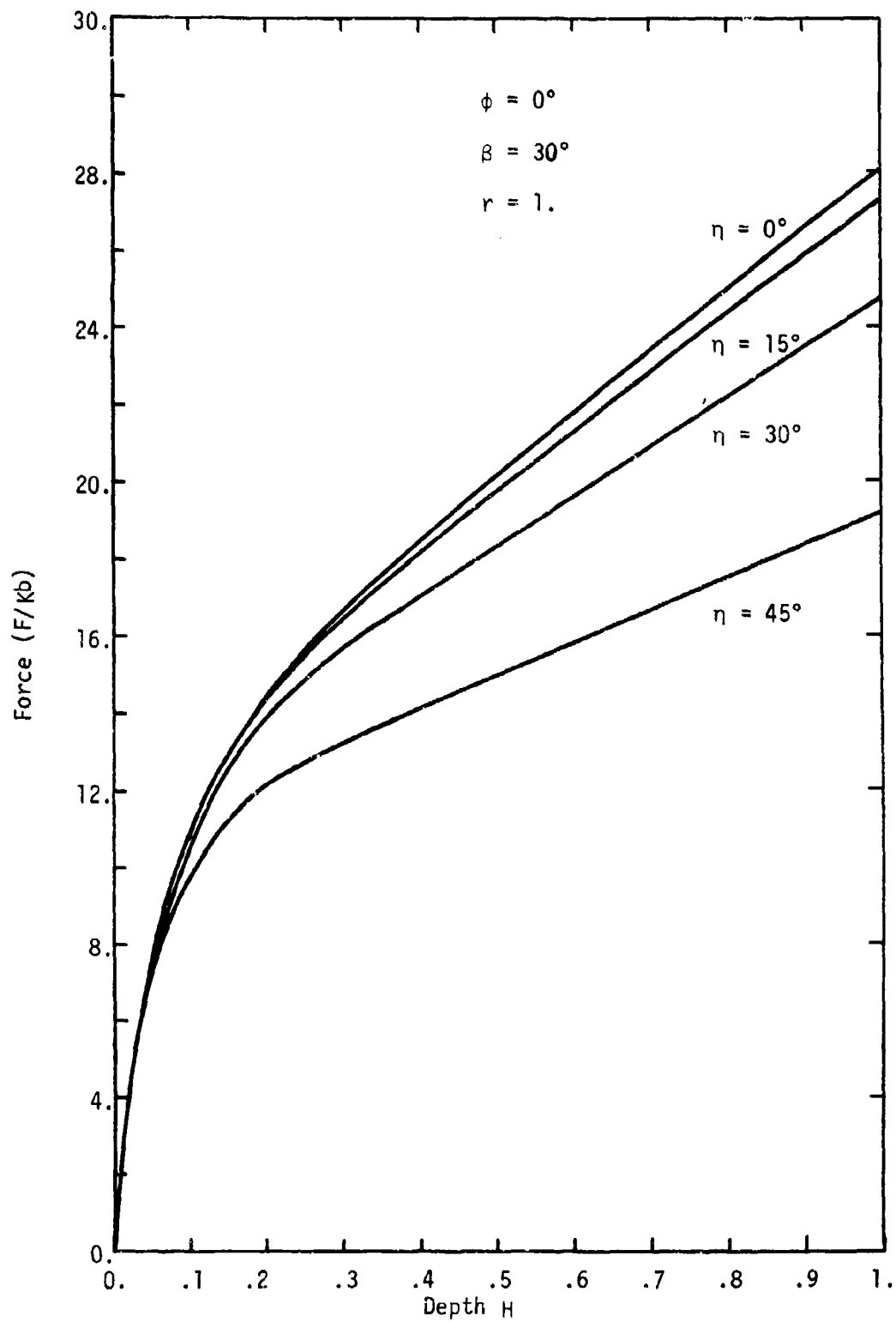
Fig. 37. Force-Depth Diagram for Indentor No. 4 for $\phi = 0°$, $\beta = 30°$, and $r = 1$.
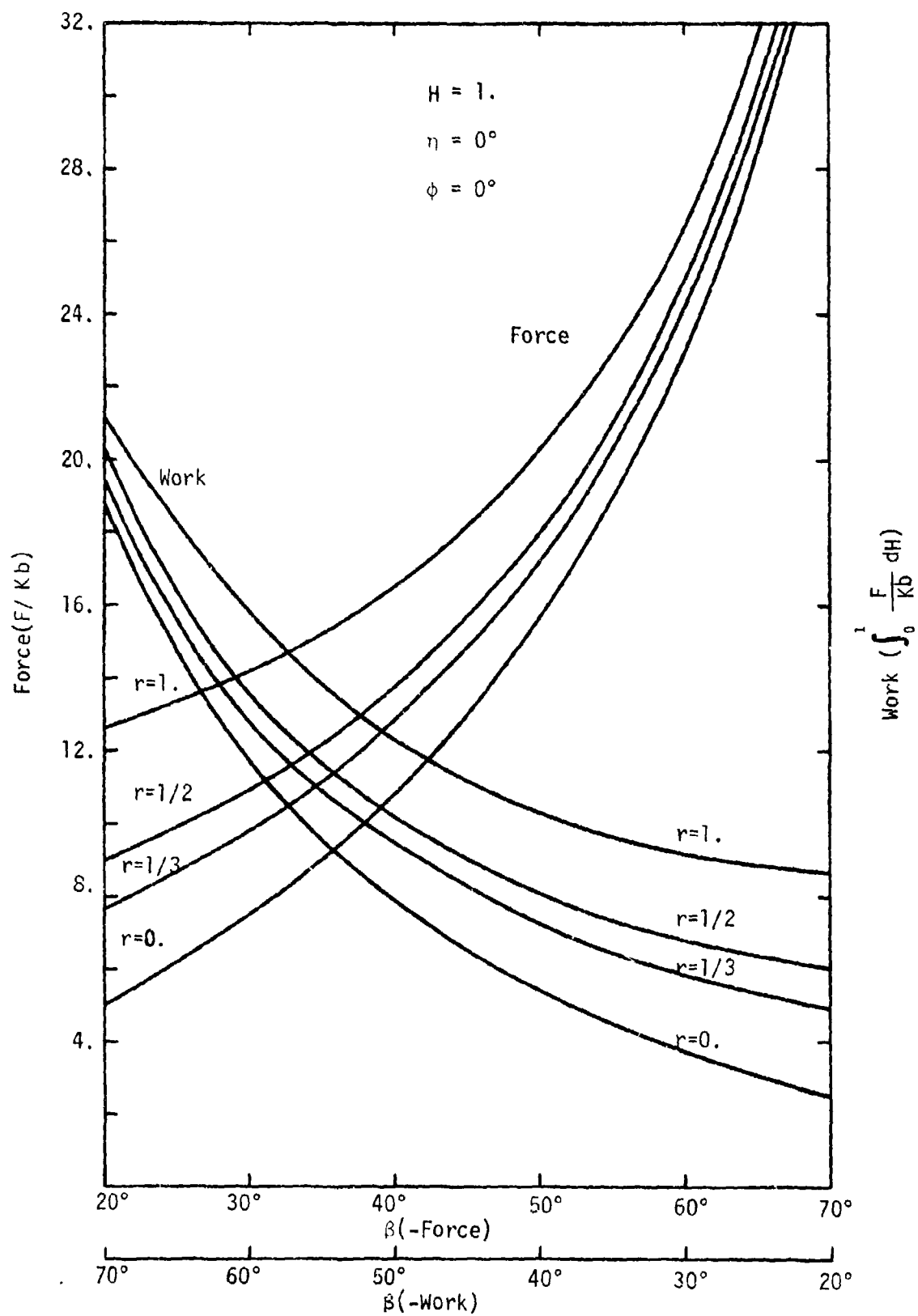
95

Fig. 38. Force-Angle Diagram for Indentor No. 4 for H = 1, η = 0°, and φ = 0°.

96

Indentor No. 1

$$\beta > \frac{\pi}{4} - \frac{\phi}{2}$$

IV-13(a)

Indentor No. 2

$$\beta > \frac{\pi}{4} - \frac{\phi}{2}$$

IV-13(b)

Indentor No. 3

$$\alpha > \frac{\pi}{4} + \frac{\phi}{2}$$

IV-13(c)

Indentor No. 4

$$\beta > \frac{\pi}{4} - \frac{\phi}{2}$$
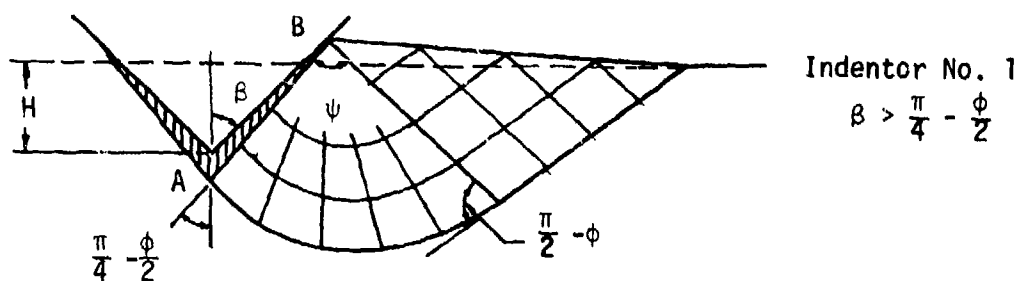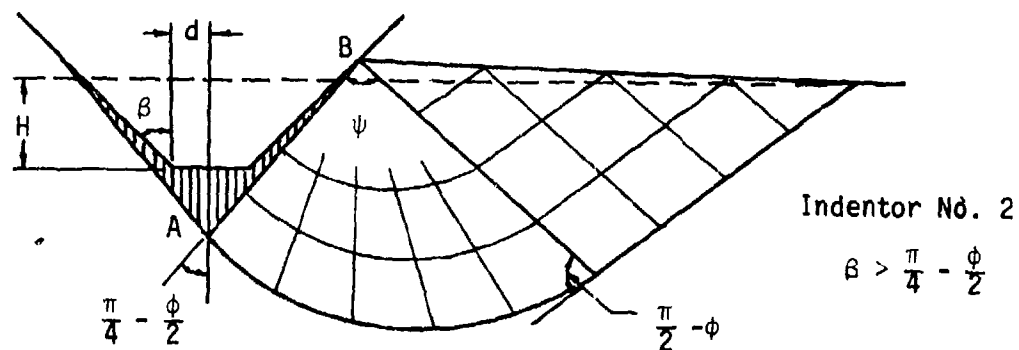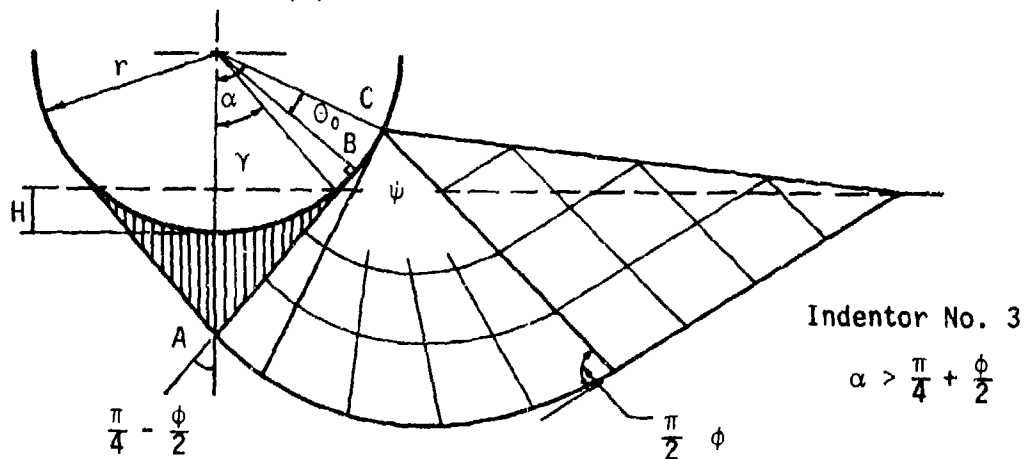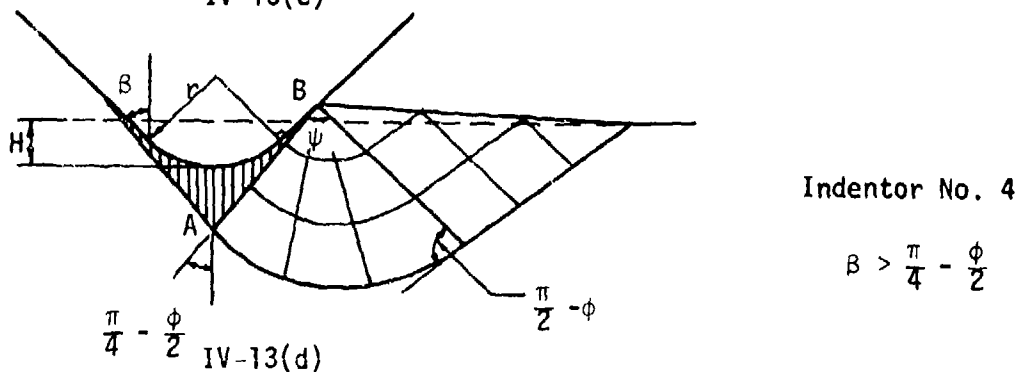
IV-13(d)

Fig. 39. Slip-Line Fields for Indentors No. 1 to No. 4 for $\phi \neq 0°$ And $\eta = 0°$
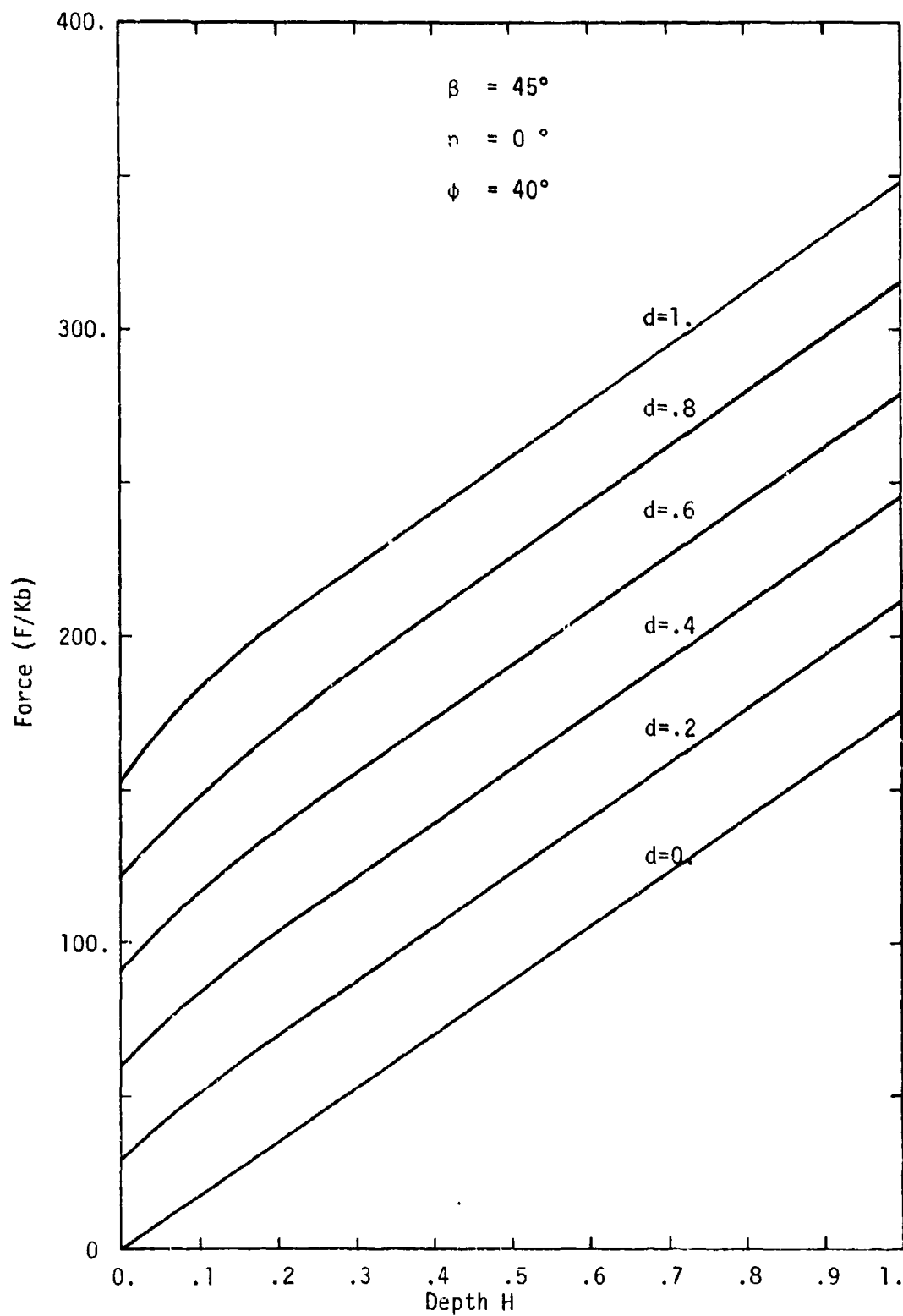
Fig. 40.   Force-Depth Diagram for Indentors No. 1 and No. 2 for ϕ = 40°, η = 0° and β = 45°

98
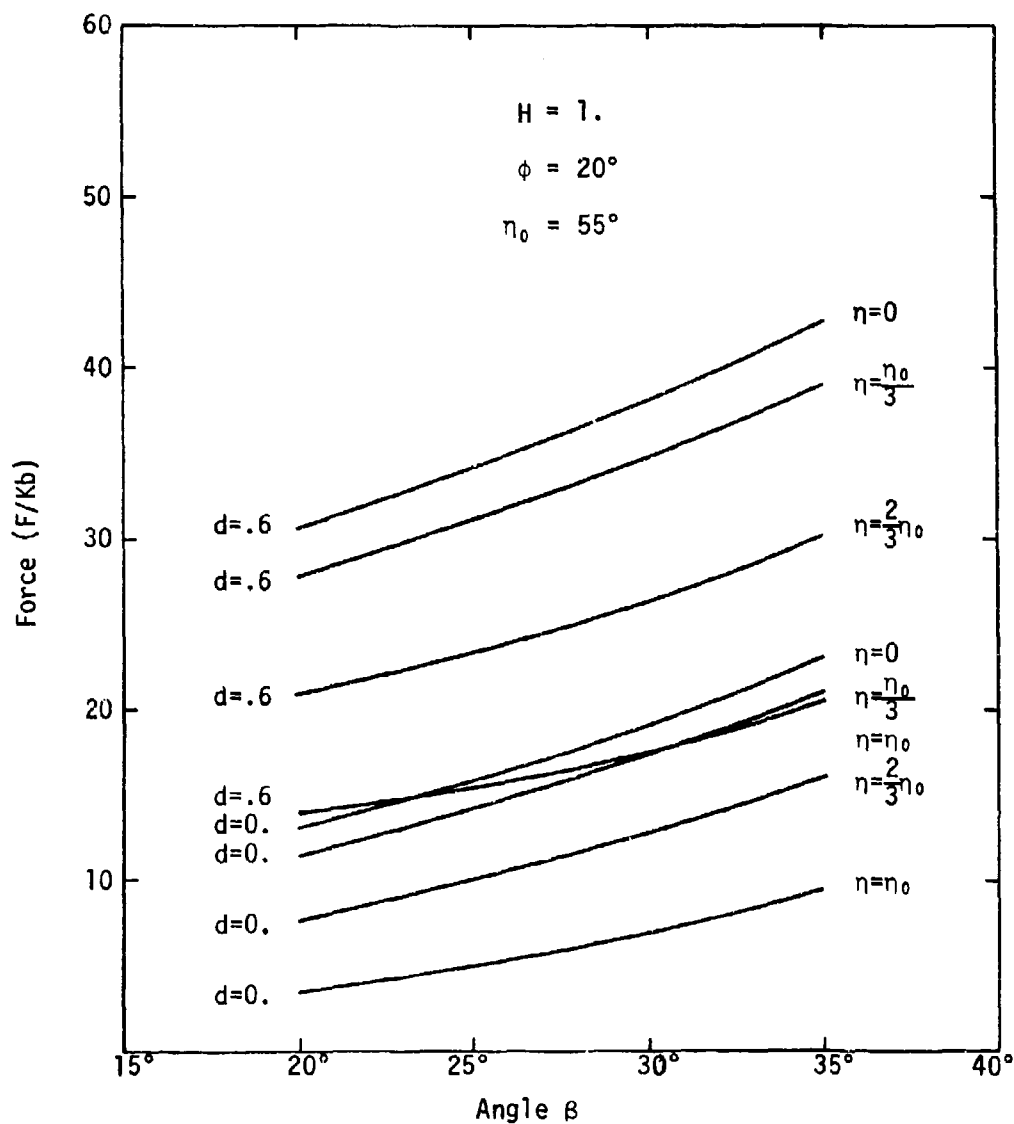
Fig. 41. Force-Angle Diagram for Indentors No. 1 and No. 2 for $\phi = 20°$ and $H = 1$.

99
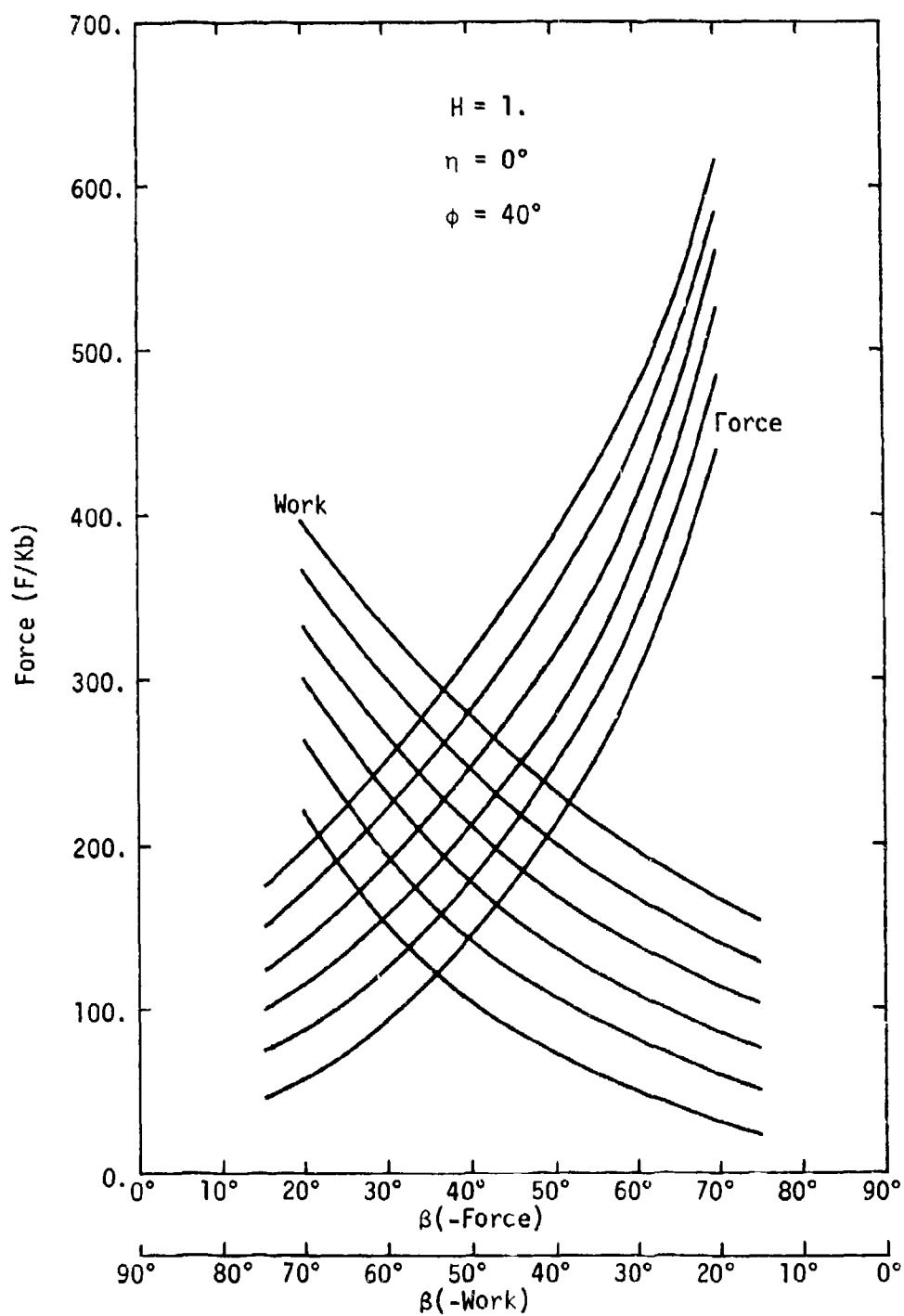
Fig. 42.   Force-Angle Diagram for Indentors No. 1 and No. 2 for H = 1.,
η = 0°, and φ = 40°

100
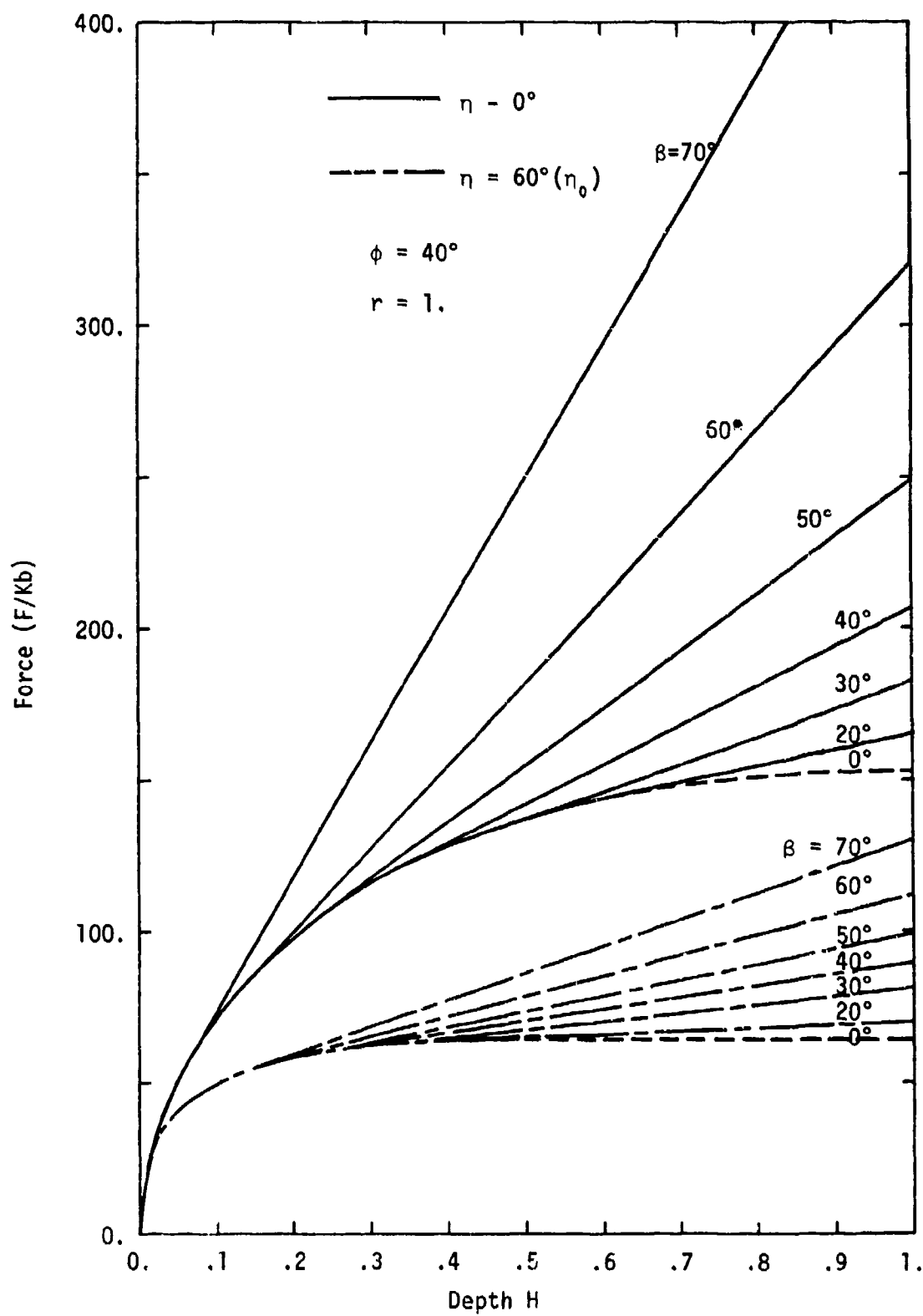
Fig. 43.   Force-Depth Diagram for Indentors No. 3 and No. 4 for r = 1. and φ = 40°

101
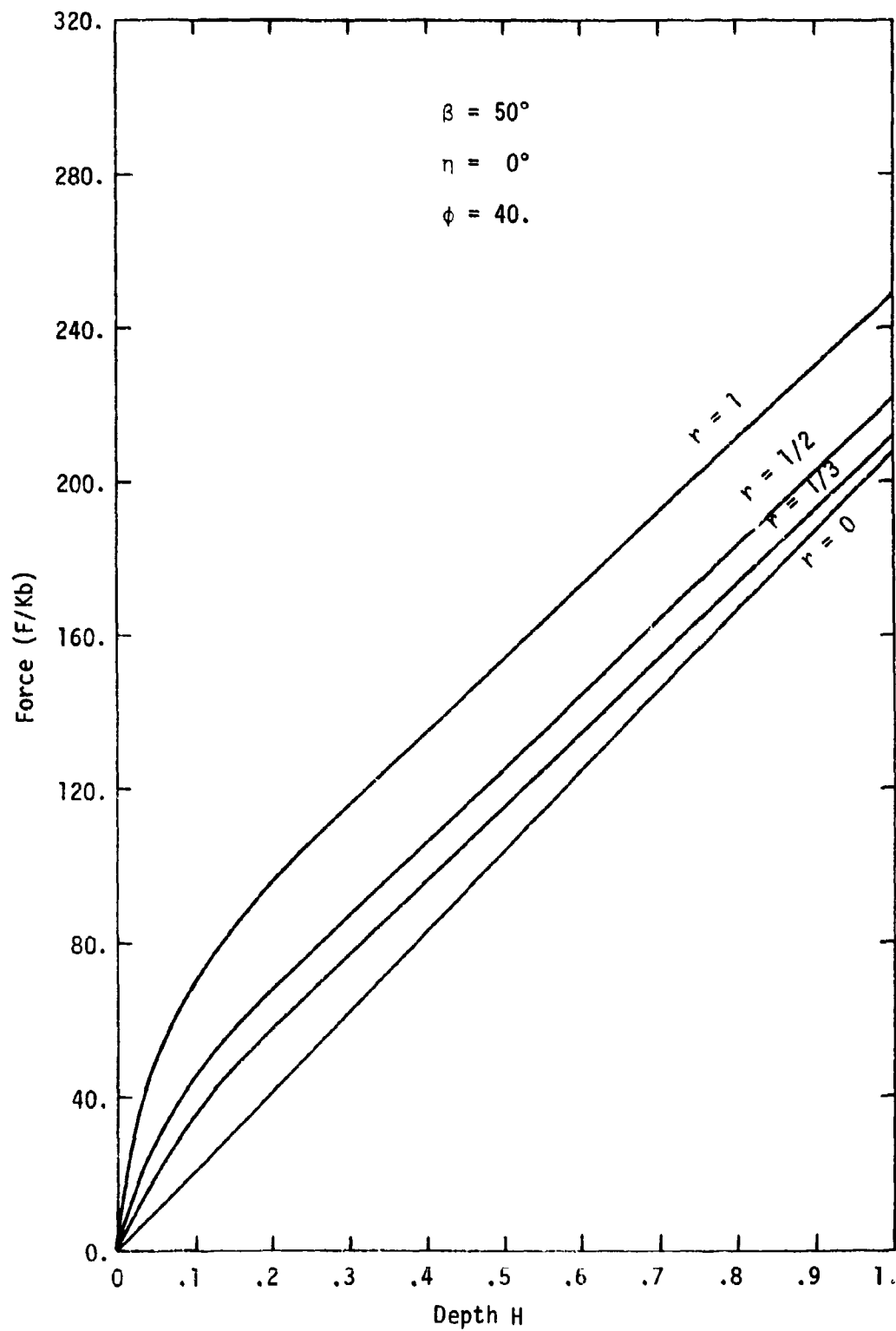
Fig. 44. Force-Depth Diagram for Indentor No. 4 for $\phi = 40°$, $\eta = 0°$, and $\beta = 50°$.
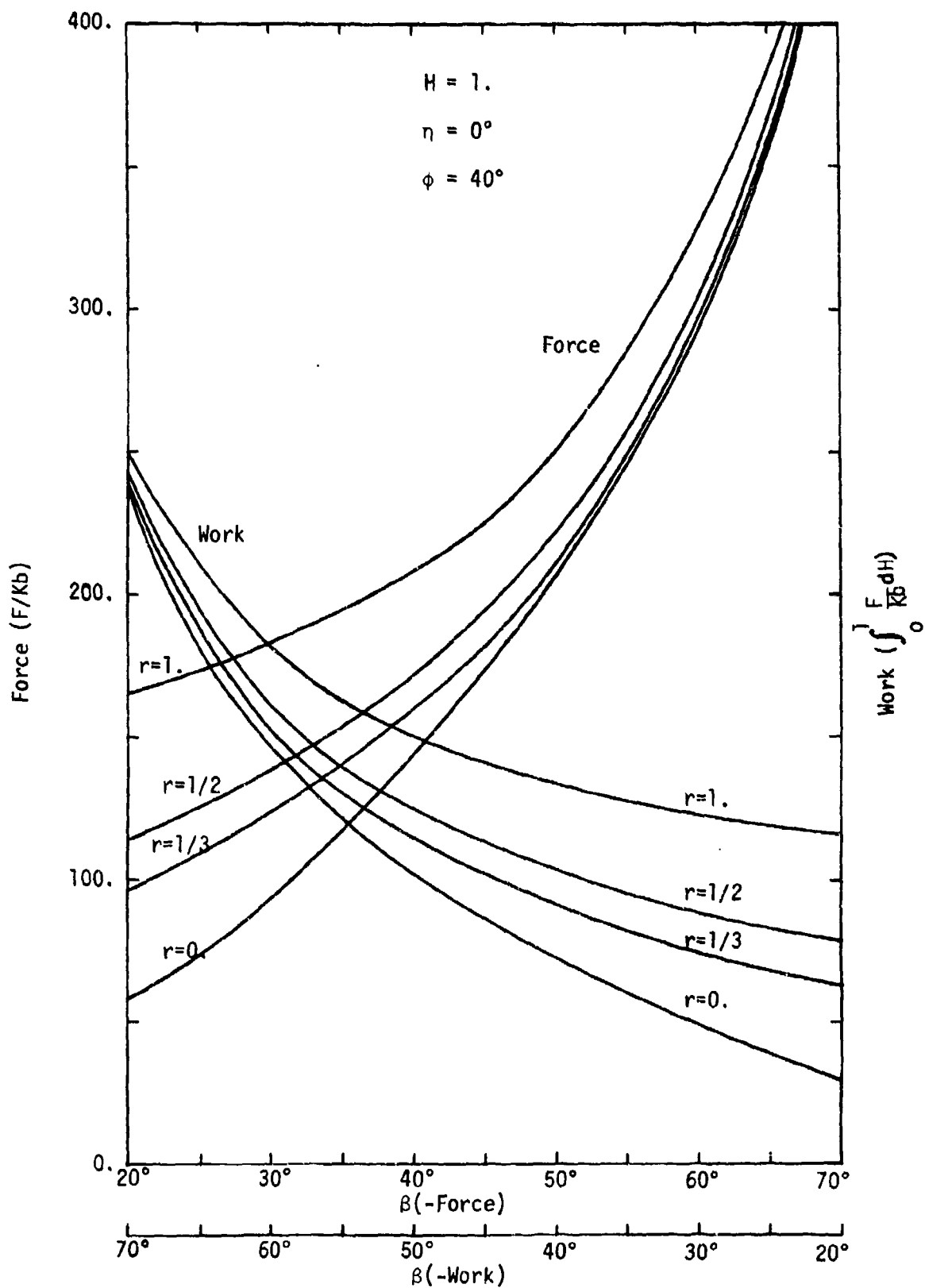
Fig. 45.   Force-Angle Diagram for Indentor No. 4 for H = 1, η = 0°, and φ = 40 °

103
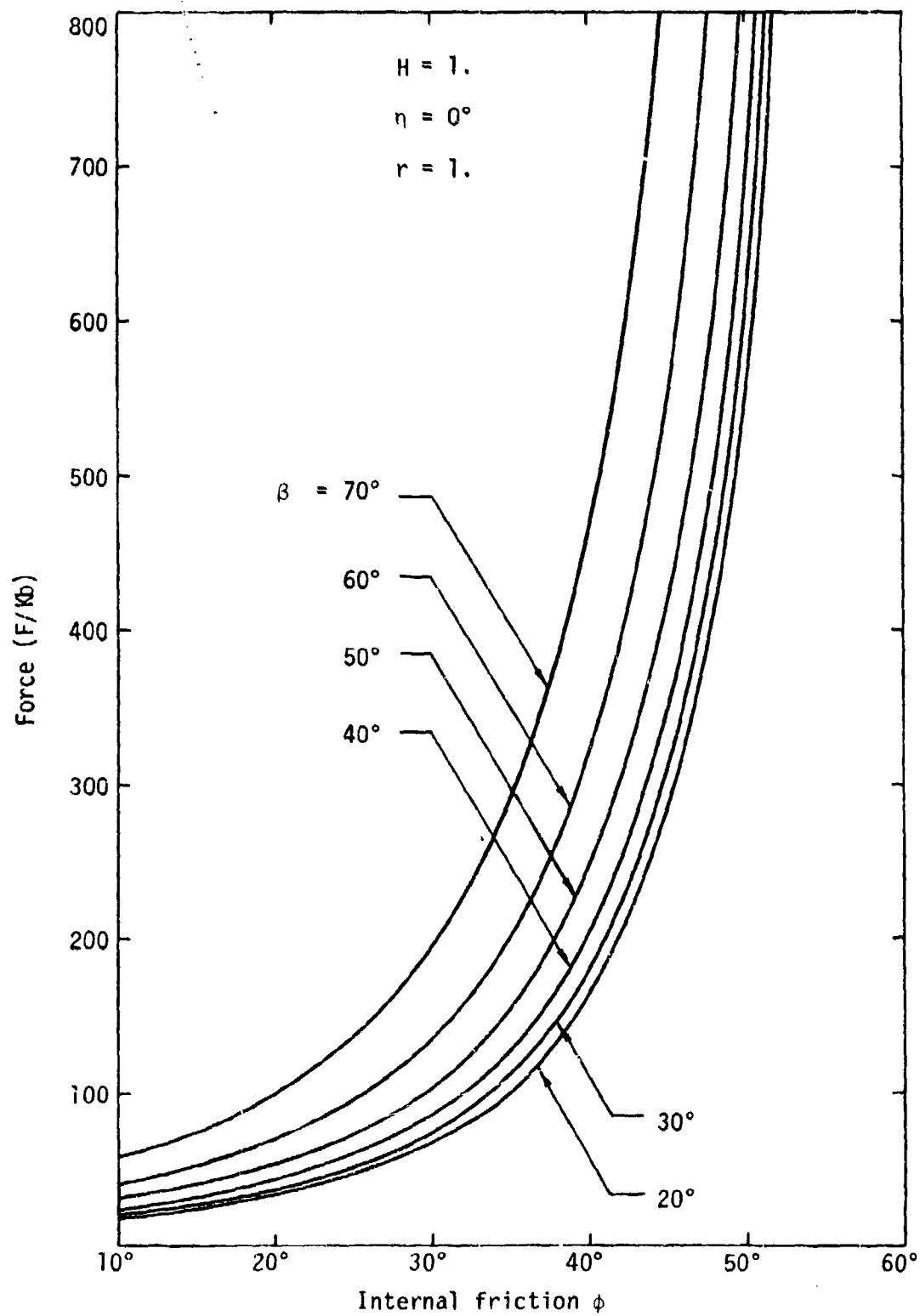
Fig. 46.   Force-Internal Friction Diagram for Indentor No. 4 for η = 0°
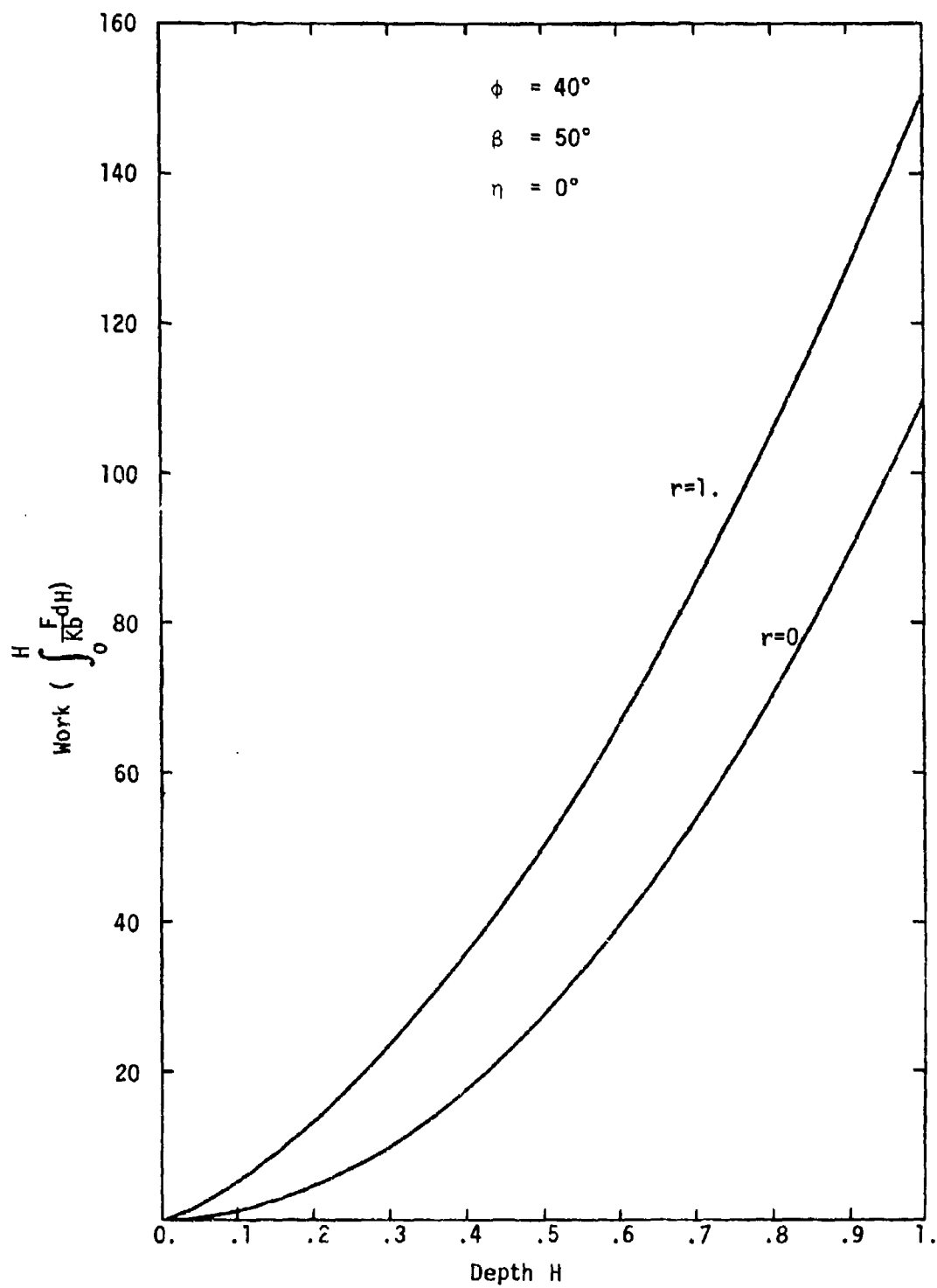
Fig. 47.   Work-Depth Diagram for Indentor No. 1 and No. 4 for ϕ = 40°, β = 50°, and η = 0°

The jackhammer output energies per blow (65% efficiency) are:

Throttle Setting	Energy (ft-lb/blow)
1	8.16
2	16.35
3	18.10
4	19.15

Now let us assume that the dimensionless length equals 1/32 inch. For a given K, b and W (energy/blow), $\frac{W}{Kb}$ can be calculated and from Fig. 47 the penetration depth is obtained. For example, for Grey Granite, Throttle #3

$$K = 7,759 \text{ psi}, \quad W = 18.10 \text{ ft-lb/blow}$$
$$b = 2 \text{ in.}, \quad r = 1/32 \text{ in. and 0 in.}$$

Then,

$$\frac{W}{Kb} = \frac{18.1 \times 12 \times 32}{\frac{7759}{32 \times 32} \times 2 \times 32} = 14.33$$

From Fig. 47, for $\frac{W}{Kb}$ = 14.33,

$$H = .21 \times 1/32 = .00656 \text{ in., for } r = 1/32 \text{ in.}$$
$$H = .36 \times 1/32 = .01124 \text{ in., for } r = 0 \text{ in.}$$

The other penetration depths for different rocks and conditions are listed in Table 4.

Table 4. Single blow penetration depth

ROCKS	Depth in. (r = 1/32 in.)				Depth in. (r = 0 in.)			
	Thro. No. 1	Thro. No. 2	Thro. No. 3	Thro. No. 4	Thro. No. 1	Thro. No. 2	Thro. No. 3	Thro. No. 4
Grey Granite	.0038	.0061	.0066	.0068	.0075	.0106	.0112	.0116
Kitledge Pink Granite	.0045	.0077	.0083	.0086	.0086	.0125	.0131	.0136
Basalt	.0030	.0051	.0054	.0056	.0064	.0094	.0098	.0101
Buena Black Granite	.0039	.0063	.0067	.0070	.0076	.0108	.0114	.0117
Missouri Red Granite	.0047	.0079	.0085	.0088	.0090	.0128	.0135	.0139
Sioux Quartzite	.0028	.0045	.0051	.0052	.0063	.0086	.0094	.0096

If depths of penetration are known then the required energy can be calculated. The region of triaxial compression (false nose) extends beyond the depth calculated in Table 4. The actual depth can be determined experimentally.

The above studies of a single bit penetration on a semi-infinite rock give preliminary information on surface chipping of rocks for different indentors. For evaluation of disintegration phenomena and the process of kerf ridge removal, further studies on rock properties, interface friction, dynamic fracture, indexing, and displacement field coupling will be necessary.

CHAPTER V

SPECIFIC ENERGY

Introduction

Although a large number of attempts have been made to ascertain the basic relationship between the particle size distribution of crushed and ground material and the energy required to accomplish the degradation, empirical equations have been established which apply for the most part only to the particular experiments performed.

Fundamentally, the amount of energy consumed in fracture and crushing is proportional to the new surface area formed, provided the original material is homogeneous and isotropic. Likewise, if this law is to be applied in the form of the well-known Rittinger equation, then the particles must all be assumed to be the same shape and free from cracks resulting from the crushing process.

Crushing Laws

Charles (Ref. 69) has shown that both the Kick and Rittinger laws of crushing are special cases of the expression

$$E = \int_{x_1}^{x_2} - C \, dx/x^n \tag{58}$$

where $n = 1$ and 2 for the above two laws, respectively, and x is the particle dimension.

He also pointed out that for a given cumulative distribution

$$y = f(x) \tag{59}$$

where y = weight percent less than a size x, the energy required to reduce a weight, dy, from size x_m to x is

$$dE_1 = \int_{x_m}^{x} - C \, dx_1/x_1^n (dy) \tag{60}$$

108

The total energy is given by

$$E = \int_0^E \int_0^{100} dE_1 dy \qquad (61)$$

or

$$E = \int_{x_0}^k \int_{x_m}^x (-C\, dx_1/x_1^\eta) f^1(x) dx \qquad (62)$$

where k is the size modulus, taken as the value of x (largest size) at the 100 percent intercept, and C is a constant. For the Schuhman equation

$$y = 100(x/k)^\alpha \qquad (63)$$

the energy relationship may be derived from the above for large x_m and small x_0 as

$$E = \frac{C\alpha}{(n-1)(\alpha-n+1)} k^{1-n} \qquad (64)$$

That is, for constant α, C and n, a plot of E versus k permits the evaluation of n for a particular process and for crushing equipment design.

On the basis of single fracture processes and the occurrence of flaws according to the Poisson distribution law for edge flaws, area flaws and volume flaws (Ref. 70) Gilvarry derived an expression for cumulative fractions for geometrically similar fragments as:

$$y = 1 - \exp\left\{-\left[\frac{x}{k} + \left(\frac{x}{j}\right)^2 + \left(\frac{x}{\ell}\right)^3\right]\right\} \qquad (65)$$

where k, j, ℓ are constants with units of length denoting the spacing of the three types of flaws, respectively, noted above. For small x the (x/k) term becomes dominant and corresponds to the hypothesis that "the dominant mechanism producing fragmentation is the activation of edge flaws" (Ref.70). The activation of surface and volume flaws, then, is important only when a small number of large fragments is produced.

109

It should be noted that in addition to the assumption that all particles are geometrically similar, the Poisson distribution function does not allow for flaw depletion.

In a recent analysis of thermal crushing of rock, Thirumalai and Cheung (Ref. 71) assumes that the volume flaws dominate the fragmentation of spherical specimens of rock subjected to sudden intense surface heating, giving

$$y = \left(\frac{x}{\ell}\right)^3 \tag{66}$$

for $x << \ell$. Thus, equation (66) reduces to

$$E = \left[\frac{3C}{(n-1)(4-n)}\right] \ell^{1-n} \tag{67}$$

A study of the empirical laws of crushing and grinding, and experimental results obtained for various types of crushing show that the amount of energy required is a function of the properties of the material being crushed, the method of crushing, the size of the particles produced, heterogeneity, distribution of flaws, and several other factors.

Specific Energy and Resistance to Fragmentation

Some basic factors in the investigation of thermal-mechanical rock fragmentatior   1) the energy required for fracture, (2) energy distribution in fr   ɔups (screen fractions) according to size, and (3) a simple test wh   n be employed to predict resistance to fragmentation.

A drop crushing test utilized by Gross and Zimmerly (Ref. 8) has been employed by several investigators to approximate the energy required to crush brittle materials. The apparatus consists essentially of a steel mortar (anvil) with a plunger or piston. Cylindrical specimens of rock are placed in the mortar under the piston and a weight is dropped on it (Fig. 48). The energy absorbed by the system is subtracted from the total

110

Drop
Weight

Anvil

Aluminum
Cylinders

Pedestal
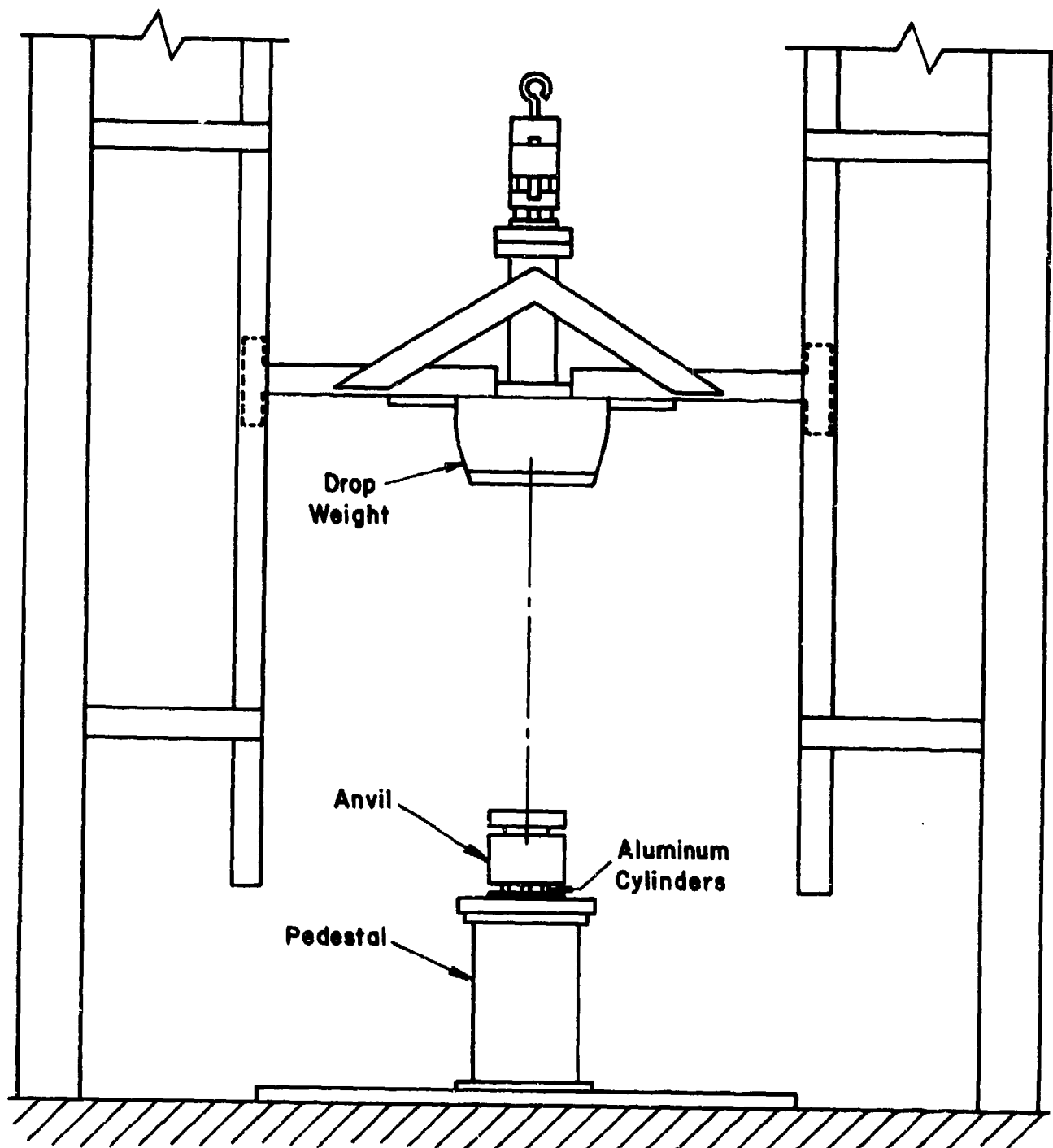
Fig. 48. DROP TEST MACHINE

drop weight energy and the remainder is assumed to be used in crushing. The crushed material is screened (Appendix E) and the Rittinger constant is evaluated by the equation

$$E_r = K_r \left[\sum_i \frac{\%_i}{S_i d_i} - \frac{100}{d_o} \right] \qquad (68)$$

where

E_r = crushing energy per unit volume

K_r = Rittinger constant

$\%_i$ = percent of given particle size

d_i = average particle diameter of i th screen fraction

d_o = diameter of unbroken specimen

S_i = shape factor for i th screen fraction (S_i = 1.0 for drop tests)

Equation (68) is derived from Rittinger's statement that the total energy required for crushing is proportional to new surface area formed. It assumes that all of the particles formed are of the same shape. To adjust for irregular, flat or elongated particles an average or effective particle shape factor (Appendix E) is introduced, its value being less than one. In practice its value is determined from observation of particle shapes in each screen size fraction (Appendix E).

The theories that relate energy to surface area assume (Ref. 72) that the particles are spherical or cubic in shape. Since some of the particles collected from the thermal-mechanical fragmentation tests were flat chips, it was necessary to apply a particle shape correction factor.

Assuming that all particles were cubes having side d gives a surface area of $6d^2$. If the cube is split in half, the surface becomes $6d^2 + 2d^2$. For each additional split $2d^2$ surface area is created. Thus, cutting the cube by a number of parallel planes results in an increased surface area

112

equal to twice the number of resulting parallelopipeds less one times the square of the diameter. Expressing the average thickness of the particles as a percentage of the observed diameter will give the new surface area as:

$$\text{surface} = 6d^2 + 2\left(\frac{100}{\delta} - 1\right)d^2$$

where

d = observed diameter

$\delta = \frac{100\ t}{d}$, thickness of particles in percent of observed diameter

Letting $c = \frac{100}{\delta} = \frac{d}{t}$ the equation becomes:

$$\text{surface} = d^2(4 + 2c)$$

For the divided cube, the specific surface (surface per unit weight) becomes:

$$S_w = \frac{S_n}{\text{weight}} = \frac{(4 + 2c)d^2}{d^3\rho} = \frac{(4 + 2c)}{d\rho}$$

where

S_w = specific surface

S_n = surface of divided cube

ρ = density

From statistics, the corrected diameter (harmonic mean diameter) is expressed by

$$d_{cor} = \frac{6}{\rho S_w}$$

where

d_{cor} = corrected diameter.

Substituting for S_w gives:

$$d_{cor} = \frac{6}{\rho S_w} = \frac{6}{\rho \frac{(4 + 2c)}{d\rho}} = \frac{6}{4 + 2c}\ d = \frac{3t}{2t + d}\ d \qquad (69)$$

For a given sample, average thicknesses of particles retained on different screens were obtained and were plotted against their corresponding average screen diameters on a log-log scale. The points were observed to lie approximately on a straight line. Since it was not possible to measure the thicknesses of small-sized particles, a logarithmic least-square straight line (Ref. 73) was passed through the points for which thicknesses were measurable.

The equation of the least-square straight line is given by

$$\log_{10} t = A \log_{10} d + B. \qquad (70)$$

The constants A and B are obtained from solution of the normal equations

$$\sum_n \log_{10} t = A \sum_n \log_{10} d + nB$$

$$\sum_n (\log_{10} t \cdot \log_{10} d) = A \sum_n (\log_{10} d)^2 + B \sum_n \log_{10} d$$

and are given by

$$A = \frac{\left(\sum_n \log_{10} d\right)\left(\sum_n \log_{10} t\right) - n \sum_n \left(\log_{10} d\right)\left(\log_{10} t\right)}{\left(\sum_n \log_{10} d\right)^2 - n \sum_n \left(\log_{10} d\right)^2}$$

$$B = \frac{\sum_n \log_{10} t - A \sum_n \log_{10} d}{n}.$$

In the above equations n is the total number of points.

The point of intersection of the least-square straight line with the average screen diameter equal to the average particle size line, t = d, is given by

$$d = t = d^A \cdot 10^B \qquad (71)$$

114

For screen sizes larger than that given by equation (71) the thicknesses are modified using the least-square straight line, equation (70). The modified thicknesses are used in equation (69) to correct the diameters. For screen sizes smaller than that given by equation (70), the particles are assumed to be cubic and no correction for the diameter is required.

Once the Rittinger constant K_r is determined for a given rock the value of the breakage energy of the fragments from chipping and thermal spallation may be approximated from screen analysis as well as the energy distribution among the particle size fractions.

Usually the factor $100/d_o$ is small in comparison to the other terms and may be neglected, in which case equation (68) becomes

$$E_r = K_r \sum \frac{\%_i}{S_i d_i} \qquad (72)$$

Assuming that K_r is known and a given specific energy is desired, an equivalent particle diameter of material may be calculated. For example, for $K_r = 3.0 \times 10^{-3}$, $E_r = 10$ joules/cc and $S = 1.0$, the equivalent particle diameter is $d_i = 3 \times 10^{-4}$ cm. This calculation is in a sense an estimation of the effective average particle surface area which should be sought in a given process if the specific energy of 10 joules/cc is desired.

The shape factors S_i were calculated for fragmented rocks as a function of particle size, as previously described, larger corrections being required for large particles, the factors being employed for the chipping tests only. Measurements of particles from the drop crushing tests indicated that they were approximately equidimensional and no correction factor was applied. The probability that incomplete fractures are induced in otherwise intact particles is hypothetically a function of particle size. The existence

115

of partial fractures represents surface energy, and could be entered
into the Rittinger equation by decreasing the value of the shape factor.
However, for particle size distributions having even small amounts of
fine material, the latter dominates the calculations and the shape fac-
tors have little effect on the value of K_r.

In view of the above it is logical to assume that the effective Rit-
tinger values are useful to approximate the actual energy of breakage for
particle size distributions that are reasonably similar. The limits of
parameters which define such similarity have not been investigated and
are to be the subject for further research.

The values in Table 5 and the figures in Appendix E show the Rittinger
constant actually varies with a number of test parameters. Its value de-
pends on drop height, drop weight, specimen geometry, the number of drops
and other factors. This variation can be minimized by standardization
of the test procedure.

Drop crushing tests (Table 5) were conducted with the specimens
placed on edge as in the Brazil tension test. Just as Protodyakonov used
an impact test on multiple fragments as a measure of hardness it is ex-
pected that with some modification of the drop crushing test it will be
possible to determine a controlling factor in the resistance of rocks
to thermal-mechanical fragmentation by a standardized crushing test.
The values of the Rittinger constant for thermally treated and untreated
specimens may provide a measure of the relative resistance to thermal-
mechanical fragmentation.

The column titled "Specific Surface Breakage Energy" in Table 9
shows how the Rittinger constant as determined from drop tests can be
used in a fragmentation test to determine the response of the rock to

116

Table 5. Rock Fragmentation (Crushing) Constants

Test No.	Specimen	Specimen Type[1]	No. Drops	Drop Height (ft)	Energy into Rock (joules)	K_r[2]	K_k[3]	K_b[4]
1	Missouri Red Granite	1	1	5	626.47	.00566	.33858	.08508
2	"	1	1	10	544.71	.00303	.27299	.05880
3	"	1	2	1	401.10	.00485	.24740	.07030
4	"	1	2	3	592.37	.00317	.26774	.05909
5	"	1	2	5	521.52	.00299	.23146	.05171
6	"	2	1	2	417.38	.00491	.29280	.07477
7	"	2	1	4	382.39	.00410	.25262	.06174
8	"	2	1	5	416.97	.00379	.27633	.06400
9	"	2	1	10	257.64	.00188	.15207	.03305
10	Charcoal Grey Granite	1	1	5	509.86	.00449	.28331	.07079
11	"	1	1	10	660.85	.00412	.33665	.07677
12	"	1	2	1	463.75	.00613	.29134	.08476
13	"	2	1	2	440.56	.00558	.35271	.09093
14	"	2	1	4	533.31	.00454	.36135	.08248
15	"	2	1	5	449.38	.00444	.31293	.07470
16	"	2	1	10	440.56	.00281	.23838	.05192
17	Kitledge Pink Granite	1	1	5	672.58	.00444	.35375	.07906
18	"	1	1	10	568.16	.00361	.27944	.06302
19	"	1	2	1	463.75	.00429	.26031	.06626
20	"	2	1	2	417.38	.00437	.27233	.06775
21	"	2	1	4	371.00	.00320	.22442	.05231
22	"	2	1	5	223.81	.00205	.12891	.03063
23	"	2	1	10	173.91	.00143	.09396	.02156
24	Black Granite (Buena Gabbro)	1	1	5	695.63	.00791	.43169	.11540
25	"	1	1	10	463.75	.00391	.25957	.06383
26	"	1	2	1	463.75	.00682	.34256	.09952
27	"	2	1	2	417.38	.00690	.39482	.10851
28	"	2	1	4	510.13	.00645	.38422	.09749
29	"	2	1	5	579.69	.00486	.41011	.09170
30	"	2	1	10	243.40	.00221	.16490	.03770
31	Sioux Quartzite	1	1	5	465.11	.00484	.29000	.07630
32	"	1	1	10	676.37	.00396	.36273	.07906
33	"	1	2	1	417.38	.00690	.30176	.09211
34	"	2	1	2	463.75	.00758	.42778	.11468
35	"	2	1	4	556.50	.00608	.41567	.10022
36	"	2	1	5	672.30	.00620	.44858	.10698
37	"	2	1	10	811.57	.00751	.49679	.11805

Table 5. Rock Fragmentation (Crushing) Constants - Continued

Test No.	Specimen	Spec-imen Type[1]	No. Drops	Drop Height (ft)	Energy into Rock (joules)	K_r^2	K_r^3	K_r^4
38	Dresser Basalt	1	1	5	846.14	.01811	.61479	.20823
39	"	1	1	10	927.50	.01186	.52120	.15473
40	"	1	2	1	463.75	.01891	.39242	.15849
41	"	2	1	2	417.38	.01564	.46303	.17136
42	"	2	1	4	579.69	.01446	.55401	.18307
43	"	2	1	5	626.06	.01594	.58814	.19185
44	"	2	1	10	347.81	.00858	.29238	.09251

[1] One specimen (1), 2.75" long by 1" diameter placed on edge
Two specimens (2), each 1" long by 1" diameter placed on edge

[2] Rittinger constant

[3]Kick constant

[4] Bond constant

variations in different test parameters. Particle size distributions from fragmentation tests may be used with the Rittinger constant to indicate the specific energy differences due to bit size and style, offset, kerfing, simultaneous versus independent operation of heat source and mechanical device, traverse speed, etc.

Total Crushing Energy

Many of the empirical crushing laws utilize the total process input energy to determine that required for particle size reduction. However, for thermal, mechanical, explosive, or other fragmentation processes there is an inherent amount of waste energy which is not utilized directly for fracturing.

For example, in the process of blasting with a completely confined explosive as much as 75 percent of the total available energy from the gaseous products of detonation may be absorbed by the rock. However, depending upon the geometry of the rock, i.e., number of free faces, as little as about 1/6 of the energy may be utilized in fragmentation, the remainder being dissipated into the surrounding rock as stress waves, and in kinetic energy of flying fragments, etc. For mechanical breakage by a pneumatic drill, only a portion of the energy of impact causes pulverization, fragmentation and fracture, the remainder being dissipated into the rock, in friction losses, etc.

For thermal fragmentation by sources applied to a plane surface much heat energy may be lost to the surroundings, and of the heat transmitted to the rock only a fraction of it is absorbed in fracture processes, the remainder showing up as residual heat in the rock.

The calculated values of the effective Rittinger constant determined by drop crushing tests are assumed to be representative of the fracture

(comminution) energy only, and hence, can be utilized as a basis for determining the approximate efficiency of other fragmentation processes resulting in similar particle size distributions for tne same material. They also furnish approximate energy values for defining an engineering index property for resistance to fragmentation.

For calculation of energy requirements and work indices for industrial crushing, the parameters are often defined for a certain percentage of crushed material less than a certain size, and others consider only particle size distributions down to a certain cutoff size, neglecting very fine material. Hence, comparisons of energy consumption recorded in the literature for the several fragmentation processes in use or under investigation, should take into account possible differences in the bases for calculations.

For many brittle materials the surface energy may be taken as a measure of useful energy expended, and the Rittinger law (Fig. 49) as a good first approximation for specific energy values. Factors discussed above would cause apparent deviations from the Rittinger law depending upon how the energy input is evaluated. For all empirical laws, however, it is obvious that energy consumption can be drastically reduced by lessening the amount of fine material produced in the fragmentation process.
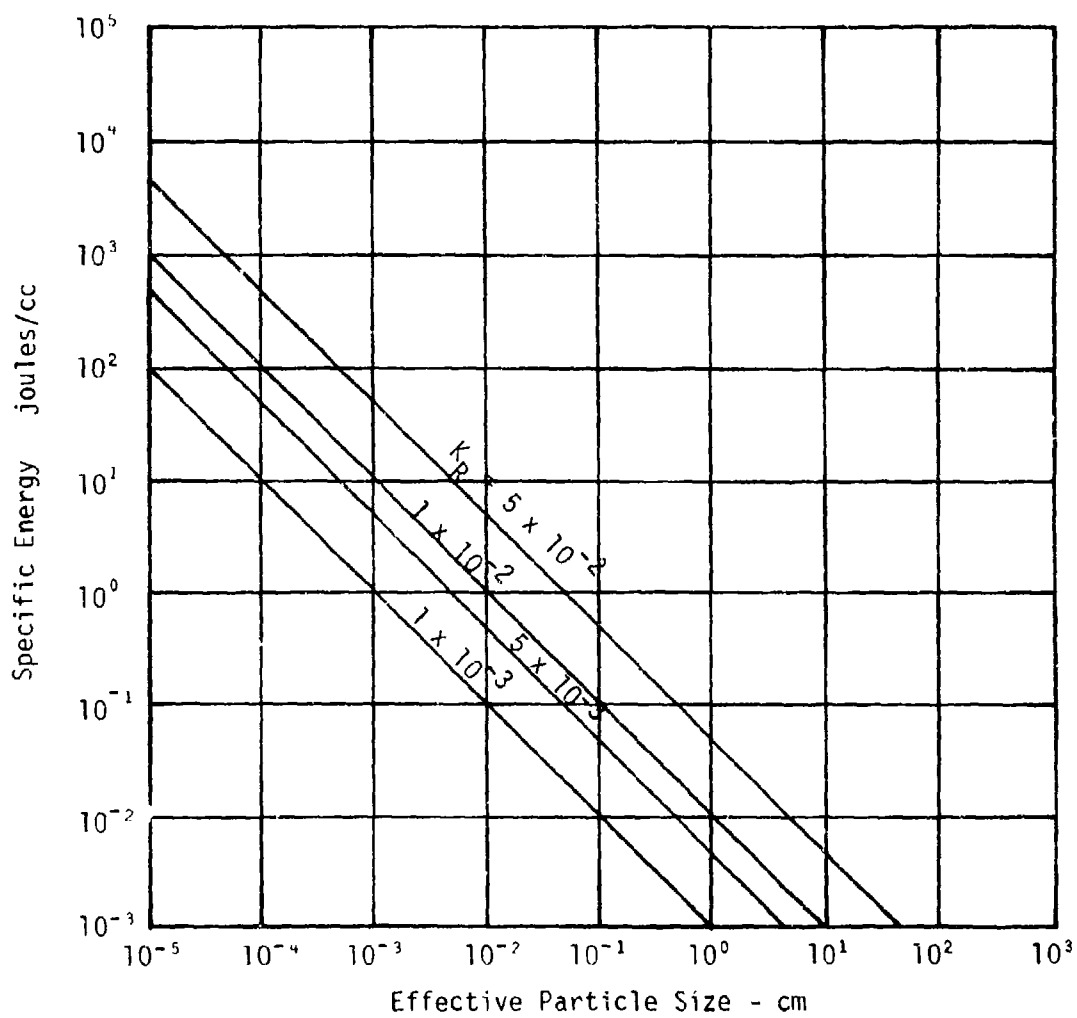
Fig. 49. Energy-particle size relationship - Rittinger law.

CHAPTER VI

THERMAL-MECHANICAL FRAGMENTATION TESTS

Introduction

In order to reduce scaling (similitude) problems to a minimum, to utilize full-scale equipment, and to provide large enough specimens to furnish a reasonable representation of large rock masses, all thermal fragmentation tests were carried out on blocks of rock about 30 inches on each side. It was desirable to vary parameters such as speed of traverse, magnitude of heat flux, intensity and frequency of bit impact, as well as characteristics of the bits employed. Inasmuch as an evaluation of specific energy of fragmentation is of vital interest, the experimental system was designed so that cuttings from drilling and fragments from spallation could be collected for screen analysis. Although some finer particles were lost, it is believed that the losses were not significant except on the preliminary series of tests on Missouri Red Granite, which were used to determine the operating characteristics of the equipment.

Thermomechanical Test Equipment*

Mounting Frame. The rock test specimens for thermomechanical fragmentation as indicated above were 30 in. (approximately) cubes weighing about one and one-half tons. The test apparatus was designed so that it would mechanically move the test blocks longitudinally across the points of action of the pneumatic hammer and flame jet. A steel framework was

*Note: Equipment designed, built and tested under THEMIS Contract No. DACA-45-69-C-0087.

Fig. 50. Schematic of Experimental Apparatus for Thermo-mechanical Fragmentation
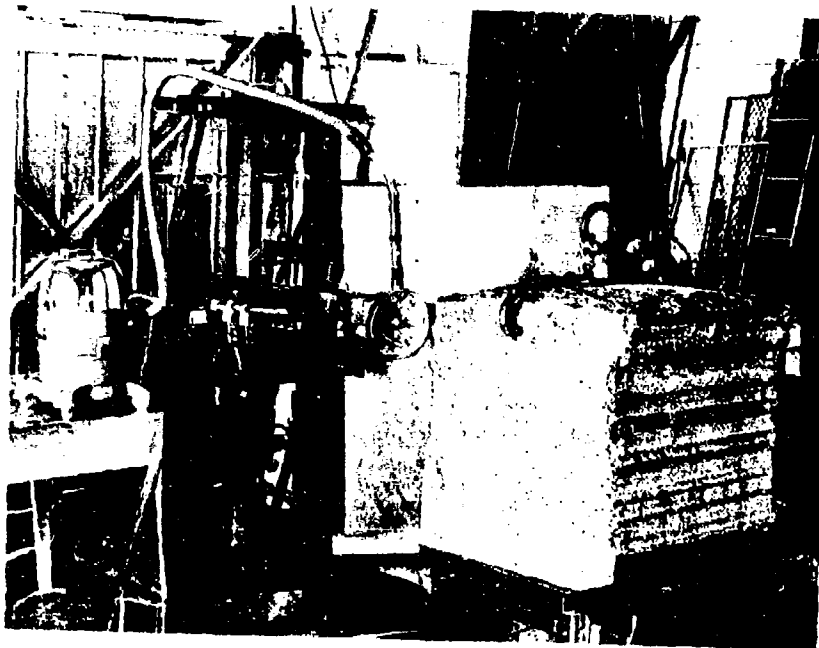
123

Fig. 51.   Thermal-Mechanical Fragmentation Apparatus

constructed for mounting the latter equipment and the system (Figs. 50 & 51) provided transverse as well as vertical movement of the hammer and jet relative to the rock. The cutting face of the rock was placed in a vertical position to prevent secondary breakage of particles by the jackhammer by allowing the particles to fall from the vertical face of the rock. Also, this permitted the thrust of the jackhammer against the rock to be controlled by means of an air cylinder.

Flame Jet. An FSJ-6 stone-shaping torch was the primary source of heat for thermal weakening/spalling. The torch was operated on oxygen and No. 1 fuel oil at pressures and flow rates suggested by the manufacturer (Table 6). Stoichiometric calculations give the maximum combustion energy as 1.78×10^5 j/sec for the recommended operating conditions. Complete combustion of hydrocarbons produces a blue flame, but the flame jet has an orange-yellow flame indicating the presence of unburned carbon particles. Losses from incomplete combustion and other waste heat such as the energy in the cooling water reduce the maximum available energy. The actual energy available to the rock is reduced because of the relatively small portion of the gas in contact with the rock and the short residence time, resulting in large residual heat and kinetic energy losses in the high velocity exhaust gases. Losses due to vaporization of the cooling water were avoided by modifying the torch so that the water was not directed against the rock surface. The standoff distance from the torch to the rock surface and the rate of traverse of the rock are two primary factors which affect the heat coupling efficiency and the consequent energy input into the rock. Estimates indicate that the maximum heat energy available to the rock varies from 6 to 8 percent of the total combustion energy (Ref. 19).

The temperature of the flame is approximately 2400 deg C and the velocity of the exhaust gas varies from 4,000 to 10,000 ft/sec (Ref. 19). The combustion chamber is one-inch inside diameter and the exhaust nozzle is 3/16 in. DeLaval type.

Table 6. Recommended Operating Conditions for FSJ-6 Flame Jet

Consumable	Operation		Operation	
	Flow Rate	Pressure ($lb/in.^2$)	Flow Rate	Pressure ($lb/in.^2$)
Oxygen	100 (ft^3/hr)	150	500 (ft^3/hr)	135
No. 1 Fuel Oil	15 (lb/hr)	120	22 (lb/hr)	120
Water	85 (gal/hr)	65	85 (gal/hr)	65

Pneumatic Hammer. The mechanical removal of rock was accomplished by a pneumatic hammer. The work output of a pneumatic hammer is given by Pfleider and Lacabanne (Ref. 74) as:

$$E_1 = \frac{CP^{3/2}A^{3/2}S^{1/2}}{W^{1/2}}$$

where

E_1 = pneumatic hammer work output (ft-lb/min)

C = constant

P = mean effective air pressure ($lb/in.^2$)

A = area of piston face ($in.^2$)

S = length of working stroke (in.)

W = weight of piston and rifle nut (lb)

126

The above equation is derived as follows:

Factor	Equation	Dimensions
Force on working face of piston	$F = PA$	(lb)
Work on power stroke	$e = \dfrac{PAS}{12}$	(ft-lb)
Acceleration of piston on power stroke	$a = \dfrac{PAg}{W}$	(ft/sec^2)
Time of power stroke	from $S = 1/2\, at^2$ $t = \left[\dfrac{WS}{6PAg}\right]^{\frac{1}{2}}$	(sec)
Time of piston round trip	$T = (1+K)\left[\dfrac{WS}{6PAg}\right]^{\frac{1}{2}}$	(sec/blow)
Blow per minute	$n = \dfrac{60}{1+K}\left[\dfrac{6PAg}{WS}\right]^{\frac{1}{2}}$	(blow/min)
Total work output per minute (work per blow x blows per min.)	$E_1 = \dfrac{(60)\,6^{\frac{1}{2}}\,g^{\frac{1}{2}}}{12(1+K)}\;\dfrac{P^{3/2}A^{3/2}\,S^{1/2}}{W^{\frac{1}{2}}}$	(ft-lb/min)

The constant "C" is determined from the value of K (fraction of time of piston power stroke required for return stroke), since:

$$C = \frac{(60)\,6^{\frac{1}{2}}\,g^{\frac{1}{2}}}{12(1+K)}$$

The mean effective pressure is a function of thrust and throttle setting. The cylinder jacket of the pneumatic hammer was drilled and tapped and a pressure transducer was installed to monitor the pressure. The average output of the transducer was taken as the mean effective pressure. The area of the piston for the pneumatic hammer used in this research was 5.363 in.^{2}. The inlet operating pressure was maintained at approximately 90 lb/in.^{2} in. in order to permit the use of the manufacturer's value of 2-9/16 in. for the working stroke. The weight of the piston and rifle nut is 4.31 lb.

Thrust Cylinder. Initially it was planned to position the jackhammer relative to the rock and to clamp it during a test. This proved unsatisfactory because the jackhammer could not move longitudinally with the contour of the rock face. A screw carriage was then employed on which to mount the jackhammer which allowed the operator to move the jackhammer during the test to prevent stalling, but it also permitted the thrust to vary. Finally an air thrust cylinder was installed which permitted transverse movement of the jackhammer while a constant thrust was maintained against the rock. Calibration of the air cylinder indicated that a pressure of 13.2 lb/in.^{2} was necessary to produce a desired thrust of 80 lb.

Rock Table. The movement of the rock relative to the flame jet and jackhammer was accomplished by placing the test block on a movable table mounted on wheels on an inverted angle iron track. The speed of the table was calibrated and operating speeds selected between 0.51 in./sec and 4.5 in./sec. At speeds less than 0.51 in./sec, the jackhammer began drilling a hole rather than traversing the face.

Table 7. Energy vs Table Speed for Table 8

| | Output Energy[3] (joules) | | | |
	Table Speed 0.50 in/sec	Table Speed 0.95 in/sec	Table Speed 1.40 in/sec	Efficiency Percent
Jackhammer[1]	75,800	40,350	27,580	65
Flame Jet[2]	10.51×10^6	5.59×10^6	3.82×10^6	2-7

---

[1] Based on 77,350 joules/min

[2] Based on 10.72×10^6 joules/min

[3] Thirty inches of travel

Table 8. Calibration Data for J50A Jackhammer*

Throttle Setting	Calibration Thrust (1b)	Mean Effective Pressure (1b/in.^{2})	Frequency (blows/sec)	Output Energy (joules/min)
1	26.0	11.5	16.9	19,320
	57.0	12.0	18.5	20,600
	92.0	11.5	18.9	19,320
2	26.0	22.0	26.0	51,130
	57.0	21.5	26.0	49,400
	92.0	22.0	25.0	51,130
3	26.0	27.0	29.0	69,420
	57.0	26.0	29.0	65,680
	92.0	26.0	29.0	65,680
4	26.0	31.0	30.0	85,520
	57.0	29.0	30.0	77,390
	92.0	27.0	29.0	69,520
5	26.0	30.0	31.0	81,410
	57.0	28.0	29.0	73,410
	92.0	27.0	29.0	69,520

* Line pressure 90 1b/in.^{2}

Stroke 2-9/16 in.

130

Preliminary Tests

Initial tests were conducted with the thermal fragmentation equipment to determine its stability, strength, operating characteristics, and to obtain initial test results to establish optimum values for such factors as jackhammer thrust, table speed, and standoff for the flame jet. Some welds were strengthened in addition to the modifications noted earlier; a vacuum system to collect fine particles was installed after this first series of tests.

The variables utilized in the calibration tests were table speed, fragmentation without and with heat, and flame jet standoff (Table 9). Eighteen tests were run, four of which were shallow kerfing experiments. Particulate material was collected, weighed and subjected to a screen analysis. The specific breakage energy was then calculated using a value of K_r determined from drop crushing tests. These values of specific energy are low because some of the very fine material was not recovered before the subsequent installation of the vacuum system.

Some of the usable ranges of operation of the segments of the apparatus are interdependent. For example, if the thrust of the jackhammer is too high it will drill a hole into the rock and will jam the table. The flame jet cannot be operated simultaneously with the jackhammer because the high velocity gases disperse the fine cuttings.

Table Speed. For the initial tests (Table 9) speeds ranging from 0.5 to 1.4 in/sec were employed. Higher speeds were later needed and a larger pulley was installed on the motor drive for subsequent experiments.

In the first group of tests it was found that a table speed of 0.95 in/sec gave the lowest specific energy for pneumatic chipping and this

131

Table 9. Thermomechanical Fragmentation - Preliminary Tests

Description of Test	Material Removed (grams)	(cc)	Total Surface Breakage Energy (joules)	Specific Surface Breakage Energy (joules/cc)	Total** Energy (joules)	Specific Energy (joules/cc) JH	Total
1a TS 0.50 B1 NK w/o heat	413.6	159	4554	28.63	49,270	309	309
b TS 0.95 B1 NK w/o heat	285.2	110	3220	29.37	26,227	239	239
c TS 1.40 B1 NK w/o heat	185.3	71	2286	32.08	17,927	252	252
2a TS 0.50 B1 NK NO 10 in.*	542.5	209	3522	16.89	364,570	235	1747
b TS 0.95 B1 NK NO 10 in.	425.1	164	2944	18.02	193,927	160	1186
c TS 1.40 B1 NK NO 10 in.	198.5	76	1686	22.07	132,527	236	1735
3a TS 0.95 B1 NK w/o heat	285.2	110	3220	29.37	26,227	239	239
b TS 0.95 B1 KA w/o heat	491.8	189	5001	26.44	26,227	138	138
c TS 0.95 B1 KB w/o heat	429.1	165	4213	25.53	26,227	158	158
4a TS 0.95 B1 NK NO 10 in.	425.1	164	2944	18.02	193,927	160	1186
b TS 0.95 B1 KA NO 10 in.	869.1	334	3008	8.99	193,927	79	580
c TS 0.95 B1 KB NO 10 in.	673.0	259	3401	13.15	193,927	101	749
5a TS 0.95 B1 NK w/o heat	285.2	110	3220	29.37	26,227	239	239
b TS 0.95 B2 NK w/o heat	237.1	91	2381	26.12	26,227	283	287
c TS 0.95 B3 NK w/o heat	239.4	92	2781	30.21	26,227	285	284
d TS 0.95 B4 NK w/o heat	365.4	140	3646	25.95	26,227	187	186
6a TS 0.95 B1 NK w/o heat	285.2	110	3220	29.37	26,227	239	239
b TS 0.95 B1 NK NO 14 in.	344.1	132	2403	18.16	193,927	199	1465
c TS 0.95 B1 NK NO 10 in.	425.1	164	2944	18.02	193,927	160	1186
d TS 0.95 B1 NK NO 6 in.	796.4	306	4846	15.83	193,927	86	633
7a TS 0.95 B1 NK NO 10 in.	425.1	164	2944	18.02	193,927	160	1186
b TS 0.95 B1 NK Off 1 10 in.	332.5	128	3368	26.34	193,927	204	1516
c TS 0.95 B1 NK Off 2 10 in.	344.6	132	2689	20.27	193,927	199	1463
8a TS 0.95 B1 NK NO 10 in. S	425.1	164	2944	18.02	193,927	160	1186
b TS 0.95 B1 NK NO 10 in. I	1009.3	388	5307	13.68	193,927	68	499

---

* Number in inches is standoff distance
** Based on jackhammer efficiency = 65%
   Flame jet efficiency at 14 in. = 2%
                    at 10 in. = 3%

TS = Table speed in./sec
B1 = 1-1/2 in. cross bit
B2 = 2-1/4 in. cross bit
B3 = 1-3/4 in. button bit
B4 = 2 in. button bit

NK = No kerf
KA = Kerf A (1.2 in. wide x 0.3 in. deep
KB = Kerf B (1.6 in. wide x 0.2 in. deep)
NO = No offset
Off 1 = 1 in. offset
Off 2 = 2 in. offset
S = Simultaneous
I = Independent

132

speed was employed in the remainder of the preliminary test series. It was not necessarily the optimum speed for thermal weakening or fragmentation.

Flame Jet Standoff. Three standoff distances were employed, i.e., 14, 10, and 6 inches, with the heat transfer efficiency being approximately 2, 3, and 7 percent, respectively, at those distances. The optimum speed for chipping after flame jet heating at 10 in. (test group 3) standoff was 0.95 in/sec. This also gave the lowest total specific energy (1186 j/cc) and the lowest chipping specific energy (160 j/cc). The best standoff (test group 6) was 6 in. requiring a total specific energy of 633 j/cc and a chipping energy of 86 j/cc. Thus, the chipping energy is reduced by a factor of 3+ for flame jet heat applied at 10 in. or 6 in. standoff. It should be noted that the flame jet was used for heating without a cooling water spray.

Shallow Kerfing. Shallow kerfing without heat at a traverse speed of 0.95 in/sec showed the lowest specific energy for narrow deeper kerfs (138 j/cc). With heat the total energy was 580 j/cc while the chipping energy was 79 j/cc.

Bit Characteristics. Only two sizes each of two types of bits were available for testing, cross bits of 1½ and 2¼ in. diameter, and button bits of 1-3/4 and 2 in. diameter. These were tested without heat and while the larger diameter button bit appeared to be the most effective, this type of bit could not be used effectively to traverse the rock. Hence, the majority of the preliminary and later tests were conducted with the smaller cross bit, which was most effective of the other three at the thrust and traverse rate which proved operable for the hard rocks tested.

Thrust. The maximum thrust was employed at which the drill bits would traverse the rock without being stopped in one position to drill a hole. This also required operating the jackhammer at No. 3 throttle setting.

Conclusions. In general it can be stated that the values of breakage energy calculated by means of K_r which vary from about 9 to 32 j/cc, are probably too low, because some of the very fine material produced in the drilling was lost.

The chipping energies both with and without heat are not optimum values. With improved techniques which would permit operation of the jackhammer at open throttle and optimum thrust the energy values could be improved considerably. Likewise, if a cooling spray of water were employed in conjunction with the flame jet, thermal weakening and fragmentation could well be improved.

Controlled Fragmentation Tests

Based upon observations made in the preliminary fragmentation tests, i.e., the large amount of -200 mesh material produced by the jackhammer, the table speed was increased to 4.5 in/sec for most of the final series of tests. On Missouri Red Granite the effect of increase in table speed (Table 10) was to decrease the jackhammer specific energy of rock removal (w/o heat)(Test No. 5) to 159 j/cc for one pass and 93 j/cc for three consecutive passes (Test No. 3).

Repeated passes (5) of the flame jet (Test No. 1) and 3 for the jackhammer reduced the jackhammer energy to 35 j/cc, while the values for the shallow kerfing tests (Tests No. 2 and 4) showed some advantage in the deeper kerf.

For Charcoal Grey Granite the heat from both the flame jet and a No. 5 weld torch appeared to have a detrimental effect rather than assisting in the fragmentation. One reason could be that the heat caused micro-fractures to form in the surface of the rock, thus decreasing the efficiency of transmission of energy from the drill bit into the rock. Shallow kerfing also showed no improvement over single passes with or without heat.

The pattern of behavior for Kitledge Pink Granite was similar to that of the Charcoal Grey Granite, but the amount of energy required for fragmentation was lower. The Kitledge Pink Granite appeared to be softer and easier to drill than the other rocks tested. For the Buena Gabbro the heat improved the jackhammer energy consumption for both six passes in the same groove and for the shallow kerfing test.

Table 10. Thermomechanical Fragmentation

Test No.	Rock	K_r	Specific Breakage Energy (j/cc)	Table Speed in./sec.	Flame Jet/Weld Torch S.O. in.	Flame Jet/Weld Torch No. Passes	J.H. No. Passes	Weight grams	Vol. cc	Specific Energy joules/cc JH	Specific Energy joules/cc JH & FJ
1	Missouri Red Granite Density - (2.60)	.0030	13.10	4.5	8	5	3	832	320	35	1054
2		.0030	22.64	"	8	20	20	2101	808	96	804**
3		"	16.55	*2.1	-	-	3	955	367	93	-
4		"	18.59	*2.1	6	5	5	825	317	173	1614
5		"	17.29	*2.1	-	-	1	196	75	159	-
6		"	16.34	*2.1	6	1	1	363	140	78	931
7	Charcoal Grey Granite (2.73)	.0044	30.68	4.5	-	-	6	893	327	69	-
8		"	24.14	"	6	6	6	849	311	72	846
9		"	25.90	"	6	19	19	2239	820	87	2045**
	(#5 Weld Torch)			2.25	-	7	8	1626	595	99	127**
				2.25	-	2	1	272	100	107	135
				4.5	-	7	8	759	92	98	126
10	Kitledge Pink Granite (2.60)	.0039	21.16	4.5	-	-	6	1152	442	50	-
11		"	24.79	"	6	6	6	1257	483	46	541
12		"	22.53	"	6	20	20	3314	1275	59	685**
13	Black Granite (Buena Gabbro) (3.10)	.0042	29.40	4.5	-	-	6	515	166	131	-
14		"	27.97	"	6	6	6	605	195	115	1150
15		"	30.23	"	6	20	20	2356	759	98	1163**
16	(#5 Weld Torch)	"	34.58	"	-	8	7	678	219	139	174
17	Sioux Quartzite (2.64)	.0040	26.25	4.5	-	-	6	644	244	92	-
18		"	26.86	"	8	6	6	961	364	62	535
19		"	20.30	4.5	8	20	20	3592	1360	55	391**
20	Dresser Basalt (2.97)	.0127	43.01	4.5	-	-	6	589	198	113	-
21		"	43.17	"	6	6	6	551	185	120	1230
22		"	35.83	"	6	20	20	1847	622	119	1407**
23	(#5 Weld Torch)	"	56.49	"	-	8	7	188	265	84	105

*1½ in. bit. All other tests with 2½ in. bits

**Shallow Kerf test

The pattern was somewhat similar for Sioux Quartzite although the specific energy values were about one-half of those for the Buena Gabbro for the shallow kerfing test.

The results for Dresser Basalt showed no improvement with heat from the flame torch either in multiple passes or in shallow kerfing. A rather marked improvement was made, however, with heat from the No. 5 weld torch. Even with a high table speed of 4.5 in/sec, the flame jet may have caused melting or softening of the whole surface contact layer of minerals while the heat from the weld torch was concentrated along a narrow line, permitting the jackhammer to chip more efficiently.

The specific energy of breakage calculated from particle size distribution analyses utilizing Rittinger numbers determined by drop crushing show some interesting correlations. Within the series of tests for Missouri Red Granite, with the exception of Test No. 2, there is rough correlation between the calculated and jackhammer energies. The low values for Test No. 1 indicate that the multiple passes of the flame jet resulted in the formation of more large size particles.

Because of the variation in test conditions there is likewise only a rough correlation between jackhammer energy values and calculated values for the other types of rocks. Difference in grain size (large for Missouri Red Granite, small for Buena Gabbro) also has an influence on the energy required to fragment the rock.

Test results indicate, however, that for given test conditions the correlations would be much better, particularly if adjusted for the grain size and mineral content of the rock, i.e., the hardness and strength of the constituent minerals. Thus, the drop crushing test, or a modification of it, appears to have promise as a test to predict rock resistance to fragmentation.

137

Deep Kerfing

The minimum total specific energy required to remove rock (quartzite) by shallow kerfing was 391 j/cc. A series of deep kerfing tests was conducted on Charcoal Grey Granite, Sioux Quartzite, and Dresser Basalt (Tables 11 & 12). In the first test (No. 2) on quartzite the two slots were only 2 in. deep with a 6 in. ridge. The slots were cut using a jackhammer assisted with No. 5 weld torches. The ridge was then removed by focusing the flame tip along one of the slots causing a stress concentration at the bottom of the slot, which served as the initiating point for a fracture which removed the ridge at its base.

For all of the remaining tests the slots were cut with the jackhammer alone. In Test No. 3 four holes were drilled to serve as loci for breakage. On this test, however, the quartzite spalled to a wide kerf which rapidly reached a stable curved surface which required excessive heat for additional spallation. The other configurations are as shown in the footnote of Table 11. In test No. 4, the whole face of a 30 inch cube was split off by running the flame jet along the bottoms of the outside two slots. The major part of the energy required was for cutting the slots with the jackhammer. Also, more heat was used for the basalt than necessary because melting and solidification held the ridge in place after it had fractured. The figures in Table 11 were adjusted (Table 12) to give the energy required for simulated operational conditions, i.e., one slot cut per ridge removed with the heat applied to each slot.

For all of the rocks tested the coefficient of thermal expansion was adequate to cause fracture. None of the tests were designed to give optimum performance of either the jackhammer or the flame jet. It is estimated that the total energy required could be reduced by a factor of 3

Table 11
Deep Kerf Tests

Rock	Wt - JH grams	Vol - JH cc	Wt - FJ grams	Vol - FJ cc	Specific Energy j/cc		
					JH	FJ	JH + FJ
1. Grey Granite	19,600	7,180	43,549	15,952	120	5.6	41
2. Sioux Quartzite	5,695	2,157	29,318	11,105	387**	10.0	71**
3. Sioux Quartzite	2,142	811	20,828	7,889	219	12.3	32
4. Sioux Quartzite	25,220	9,553	162,200	61,439	210	2.1	31
5. Basalt	28,976	10,614	62,902	21,179	282	6.5	98

Test Geometry

1. two slots 5 in. deep by 30 in. long, 6 in. ridge
2. two slots 2 in. deep by 30 in. long, 6 in. ridge
3. four drill holes 1½ in. diam, 3¼ in. deep on 6 in. centers
4. three slots 5 in. deep, 33 in. long, 5 in. ridge
5. three slots 4 in. deep, 36 in. long, 4 in. ridge

**includes acetylene torch energy used in cutting grooves

Table 12
Deep Kerf - Energy Per Kerf

Rock	Wt - JH grams	Vol - JH grams	Wt - FJ grams	Vol - FJ cc	Specific Energy j/cc		
					JH	FJ	JH + FJ
*1. Grey Granite	9,000	3,590	43,549	15,952	120	5.2	31
2. Sioux Quartzite	2,848	1,078	29,318	11,105	387	10.0	43
4. Sioux Quartzite	8,407	3,184	40,550	15,359	210	2.1	38
5. Basalt	9,658	3,538	31,451	10,589	282	6.5	75

*See Table VI- for test geometry

139

for the granite and quartzite, and by a factor of 4 or 5 for the basalt by utilization of narrower and deeper kerfs, wider ridges, and by application of a mechanical pressure to wedge the ridges as thermal cracks begin to form.

CHAPTER VII

CONCLUSIONS AND RECOMMENDATIONS

The investigations conducted on the thermal-mechanical disintegration of hard rock dealt with the theory and measurement of temperature distribution and heat coupling of flame sources, induced thermal stresses, effects of impact indentors, fragmentation energy determination, and laboratory tests on fragmentation of large cubes of rock using a flame jet and a pneumatic hammer. Several important facts were disclosed by the research, leading to a concept for a thermal fragmentation rock breakage round for tunnel excavation. The concept is based upon a technique for thermal fracturing the rock similar to blasting with explosives, but using a minimum amount of heat to induce thermal stresses for fracture. Thermal processes for excavating rock which require melting of a significant portion, or even heating a large percentage of the rock removed, do not appear to be economically feasible.

Heat Coupling and Temperature Distribution. The complexity of known methods of evaluating mathematical solutions for temperature distribution equations in three dimensions for rock materials with moving heat sources make computer calculations impractical. An existing analytical solution for a moving (point) source for a one-dimensional problem was applied to basalt utilizing known thermal properties. The results showed extremely high temperature gradients in the rock directly beneath the heat source. Steady state solutions for a hemispherical source show that the highest temperature gradients are at the edge of the source.

Temperature measurements (for a flame jet source) at shallow depths in the rocks showed that the critical temperature gradients occurred within 1 mm

of the surface. Hence, fractures would be expected to originate within this depth, and spallation phenomena would be similar in many respects to that observed for thermal shock of brittle ceramic materials.

Because of the low conductivity of minerals and the consequent necessity of placing thermocouples very close to the surface, surface temperatures and near surface temperature gradients of the rock were difficult to measure. Approximations were made, however, indicating that the heat coupling of the flame jet could be within 6 to 18 percent, the lower figure being the most reasonable.

Thermal Stresses. The basic concepts of thermal stress analysis in elastic materials are well defined. Tractable mathematical equations have been derived for steady state conditions for several geometries, heat sources, and solid homogeneous bodies with temperature independent properties. The process of evaluating solutions becomes increasingly complex for two- and three-dimensional problems, for moving heat sources, for temperature dependent material properties, and for most types of heat sources which vary with time or distance.

While it was not possible to evaluate existing solutions of three-dimensional stress equations for a moving point source, or for temperature dependent properties, existing solutions for one- and two-dimensional problems were found to be useful in furnishing concepts of temperature distributions for the more complex problems. Thus, a moving point source on the edge of a plate indicates that the highest temperature gradients exist just in front of and under the leading edge of the heat source, giving the location of the highest stresses. Other configurations have similar characteristics.

In thermal shock processes the high thermal gradients usually exist near the front of the temperature change. These give rise to high tensile,

142

compressive, and shear stresses which will cause brittle materials to fail. Some investigators have described these types of thermal stress failure mathematically by means of the Griffith theory.

The nature of thermal stress fractures observed in Sioux quartzite indicate that most probably they originate at the (plane) surface and form spalls only when they intersect other fracture surfaces which allow a particle to be separated from the rock body. Otherwise, the cracks die out with depth or lateral extension.

In deep kerfing tests it was found that heating at the bottom of a kerf (slot) on one side of a ridge caused high local stress concentrations at the corners of the groove. When the stresses and stored thermal strain energy reached sufficiently high values a crack propagated to the bottom of the adjacent kerf, severing the ridge. The thermal energy consumption for removing such ridges was 2 to 5 joules/cc, and may be much smaller for more carefully controlled conditions and for deeper kerfs. Thus, large fracture propagation is not entirely due to very local high temperature gradients, but is due to other factors as well, such as the overall stress field created, the total strain energy, and heat dissipation in the rock. Therefore, a combination of thermal stresses and geometry for efficient fracture of large blocks of the rock is necessary. That is, small scale fragmentation from a plane or nearly plane surface represents an inefficient utilization of strain energy and requires heating of a large percentage of the rock. Residual heat represents wasted energy and large amounts of hot rock may cause environmental problems in a thermal excavation system.

The condition that thermal stresses may be localized without inducing excessive unwanted stresses, strain or strain energy in large portions

of an elastic body indicates a marked advantage may be achieved in controlling the fracture pattern and the resulting fragmentation. By contrast, the whole of a compressive specimen in a testing machine is strained before it ruptures. Likewise, in most blasting operations all of the blasted rock is subjected to large stresses and strains, resulting in a high degree of fragmentation.

The facts that the location of thermal stresses can be controlled with respect to a favorable geometry of the rock, and that geometries may be created which permit fracture control with low energy expenditures are the bases for the design of a thermal fragmentation tunnel round described later.

Mechanical Fragmentation. The effects of shapes of indentors and friction between the indentors and rock were investigated mathematically. It was found that the force required for penetration was least for sharp wedge-shaped indentors with no friction. Resistance to penetration increases rapidly for increased friction and bluntness of the nose of the wedge, as well as with the included angle of the indentor. Thus, the sharper the angle the easier penetration is achieved. However, sharp edges wear so rapidly that a compromise must be made between ease of penetration and the angle which will give optimum wear. For semicylindrical indentors, the force required for penetration increases rapidly with depth, but quickly levels off as the depth approaches a value of half of the radius of curvature of the indentor.

The slip-line hypothesis based upon the theory of plasticity gives an indication of why heat treated rocks may be more difficult to chip than solid rocks. That is, if near surface fractures are created by

144

heat, then the friction along the cracks may be less than that within the solid, thus restricting the area of plastic deformation, failure and possible chipping. Also, the existence of fractures in the surface impedes the transmission of stress waves which normally are responsible for some of the chip formation. Thus, for some rocks which have micro-fractures near the surface due to thermal stress, the minerals at the area of impact are pulverized, and small particles are produced rather than large fragments.

Further experimental studies of individual indentation processes will be required to check the applicability of the theory which has been developed.

Fragmentation Energy. Of the laws which have been proposed by re-searchers to represent the relationship between particle size distribution and specific fragmentation energy, Rittinger's hypothesis and its modi-fications appear to offer the best basis for evaluation of thermal-mechanical fragmentation processes. For some types of thermal fragmentation which produce only relatively large fragments, the flaws in the unbroken solid, and the manner in which fragmentation occurs have an effect upon the apparent energy distribution.

The technique of employing a drop crushing device to evaluate fragmentation energy furnishes a means of approximating the apparent particle size-energy relationship for calculation of an effective Rittinger constant, K_r. This in turn may be employed to calculate the approximate useful energy consumed in the thermal fragmentation process where the particle size distribution is similar. Because producing very fine material consumes so much energy, even small amounts of finer particles have a dominant effect in fixing the value of K_r, and particle shape factors

employed mostly for larger particles have a minor effect on calculations.

For the drop crushing and thermal-mechanical fragmentation tests conducted in this project is was found that 50 percent or more of the crushing energy was utilized in producing -200 mesh material. Thus, it will be profitable to develop rock fragmentation methods which will produce a minimum of fine material.

Also, the value of K_r gives an approximate measure of the energy required to break the rock. It is planned to standardize and refine the crushing test so that it can be used as a reliable index for measuring rock resistance to breakage.

Thermal-Mechanical Fragmentation. The controlled test results show that for some rocks thermal treatment with the flame jet made them more susceptible to surface mechanical fragmentation by a pneumatic hammer, while other rocks became more resistant. Both single pass and shallow kerf methods of fragmentation required relatively large amounts of heat from the flame jet, and smaller, but significant amounts from a #5 weld torch. Both types of tests required that the rock removed be heated to a critical temperature, and only part of the heat was utilized in fracture. The remaining residual heat is believed to represent a large percentage of the total heat transmitted to the rock.

Deep Kerfing. For deep kerfing tests much less heat per unit volume of rock removed was required, because only a small portion of the rock was heated. As previously described, for 5 in. deep kerfs and ridges 6 in. wide the total heat energy transferred into the rock was from 2 to 5 joules/cc. Thus, a combination of utilization of thermal strain energy with proper geometry to provide nuclei for crack initiation at the point of high thermal stress, plus guidance of the fracture to create large fragments, permits an

146

efficient use of the thermal energy.

Based upon the results of deep kerfing it is planned that the
feasibility of a thermal fragmentation round be investigated. As with
explosive energy, the most efficient usage of thermal energy for
fracturing for excavation purposes is obtained when the energy is re-
leased within the rock, and fracture processes are enhanced by the presence
of free faces which allow fracture propagation. That is, some of the
basic principles of rock breakage by explosives may be applied to the
design of a thermal fragmentation round.

Since the energy required for pneumatic drilling varies from 75 to
200 joules/cc for medium hard to hard rocks, an optimum design of a round
will require a minimum of mechanical removal of rock for forming a kerf
and drilling holes for placement of heating elements. This may be
accomplished by means of a shallow round utilizing the principle of a
burn cut round.

One concept provides that the "cut" portion of the round may be a
vertical or horizontal slot near the bottom a tunnel face with holes
drilled adjacent thereto, the breakage proceeding outward therefrom. The
depth of the round will be determined by the size of blocks which can be
handled by the muck removal system. The spacing of holes also will be
governed by the size of blocks desired, the amount of heat required versus
spacing and depth, and the properties of the rock. The required hole
diameter is a factor related to the critical size of heating elements,
the heat flux and the heat transfer properties of the rock. The frag-
mentation sequence contemplated is similar to an explosive round. If the
round is relatively shallow, most of the broken rock will fall onto a
conveyor or within reach of a simple mucking machine.

147

Laboratory feasibility studies are planned on three to four foot cubes of three or four types of hard rock, including basalt, granite, and quartzite. Heating elements of the electrical resistance type have furnished sufficient heat to fracture small blocks in preliminary tests. The kerf can be cut readily and holes drilled with a pneumatic hammer.

Problems expected are in the design of structurally strong heating elements which will stand up under both laboratory and field conditions. For initial field tests in a subsequent phase of the research program jackhammers and electric elements may be mounted on separate arms of available automated jumbos.

Recommendations. In view of the findings of the investigations described in this report the following are deemed to be areas worthy of additional research:

1. Continue theoretical investigations of thermal shock, heat transfer, temperature distribution, stress distribution, and partitioning of thermal energy between strain energy, residual energy, and other means of absorption.

2. Continue studies of evaluation of fragmentation energy of rocks by thermal and mechanical means, including further refinements of the "drop crushing" technique to provide a measure of rock resistance to fragmentation.

3. Continue studies of rock fragmentation by thermal, mechanical and by a combination of the two processes, utilizing in line acetylene heaters, infrared heat, quenching, and roller type cutters and cones.

4. Make a study of the basic thermal and mechanical properties of minerals and rocks which affect their resistance to different techniques for fragmentation.

5. Assess other means of exploiting the surface microfracturing of rock caused by heating.

6. Investigate the feasibility of a thermal fragmentation round for a tunnel in hard rock as outlined under Thermal-Mechanical Fragmentation.

REFERENCES

1. Clark, George B., et al., "Review of Effects of Hypervelocity Jets and Projectiles on Rock," Office of High Speed Ground Transportation, Washington, D.C., Final Rept., Contract No. DC7-35511, June 1968.

2. Clark, George B., et al., "Rock Properties Affecting Fracture in Rapid Excavation Processes," Office of High Speed Ground Transportation, Washington, D.C., Final Rept., Contract No. 3-0143, January 1969.

3. Clark, George B., "Blasting and Dynamic Rock Mechanics," 8th Symposium on Rock Mechanics, Minneapolis, Minnesota, 1966.

4. Maurer, Wm. C., Novel Drilling Techniques, Pergamon Press, New York, 1968.

5. Carstens, J.P., et al., "Feasibility of Flame-Jet Tunneling," Vol. II, Systems Analysis and Experimental Investigations, Rept. G-910560-10, May 1968.

6. Geller, L.B., et al., "Jet Piercing Research Project," Dept. of Mines and Mineral Surveys, Mines Branch, IR 62-27, 1962.

7. Conference on Rapid Excavation, Deerfield, Mass., July 20-25, 1969.

8. Gross, J., and Zimmerly, S.R., "Relation of Work Input to Surface Produced in Crushing Quartz," AIME Trans., Vol. 87, p. 35, 1930.

9. Browning, J.A., et al., "Recent Advances in Flame Jet Working of Minerals," VII Symp. on Rock Mech., pp. 281-311, June 1965.

10. Anderson, J.E., et al., "Heat Transfer from Flames Impinging on Flat and Cylindrical Surfaces," Jl. of Heat Transfer, pp. 49-54, 1961.

11. Stolz, G., Jr., "Numerical Solutions to an Inverse Problem of Heat Conduction for Simple Shapes," Trans. of ASME, pp. 20-26, 1960.

12. Sparrow, E.M., et al., "The Inverse Problem in Transient Heat Conduction," Jl. of Appl. Mech., pp. 369-375, 1964.

13. Burggraf, O.R., "An Exact Solution of the Inverse Problem of Heat Conduction Theory and Applications," Jl. of Heat Transfer, pp. 373-382, 1964.

14. Nestor, D.H., et al., "Numerical Methods for Reducing Line and Surface Probe Data," SIAM Review, Vol. 2, No. 3, pp. 200-207, 1960.

15. Beck, J.V., "Surface Heat Flux Determination Using an Integral Method," Nuclear Eng. and Design, pp. 170-178, 1968.

16. Beck, J.V., "Nonlinear Estimation Applied to the Nonlinear Inverse Heat Conduction Problem," Jl. of Heat; Mass Transfer, Vol. 13, pp. 703-716, 1970.

References (continued)

17. Stakgold, Ivor, _Boundary Value Problems of Mathematical Physics_, Vol. 2, MacMillan Co., New York, p. 228, 1971.

18. Metzger, D.E., "Spot Cooling and Heating of Surfaces with High Velocity Impinging Air Jets," TR No. 52 for NONR 225(13), Stanford Univ., April 1962.

19. Carstens, J.P., et al., "Heat Assisted Tunnel Boring Machines," UARL Rept. J-970802-12, September 1970.

20. Rosenthal, D., "The Theory of Moving Sources of Heat and Its Application to Metal Treatments," Trans. ASME 68, pp. 849-866, 1946.

21. Thirumalai, K., "The Process of Thermal Spalling in Rocks-An Exploratory Study, 11th Symp. on Rock Mech., Berkeley, Calif., June 1969.

22. Lindroth, D.P., et al., "Heat Content and Specific Heat of Six Rock Types at Temperatures to 1000°C," Bur. Mines RI 7503, 1971.

23. Marovelli, R.L., et al., "Thermal Conductivity of Rock: Measurement by the Transient Line Source Method," Bur. Mines RI 6604, 1965.

24. Carslaw, H.S., et al., _Conduction of Heat in Solids_, 2nd ed., Oxford Univ. Press, London, 1959.

25. Crank, J., _The Mathematics of Diffusion_, Oxford Univ. Press, London, 1956.

26. Ames, W.F., _Nonlinear Partial Differential Equations in Engineering_, Academic Press, New York, 1965.

27. Luikov, A.V., "Methods of Solving the Nonlinear Equations of Unsteady-state Heat Conduction," Heat Transfer-Soviet Research, Vol. 3, No. 3, pp. 1-51, May-June 1971.

28. Bio, M.A., _Variational Principles in Heat Transfer_, Oxford Univ. Press, 1970.

29. Grosh, R.F., et al., "Temperature Distribution in Solids of Variable Thermal Properties Heated by Moving Heat Sources," Qtly. Appl. Math., Vol. 13, 1955.

30. Thomas, P.H., "Some Conduction Problems in the Heating of Small Areas on Large Solids," Qtly. Jl. Mech. Appl. Math., Vol. 10, pp. 482-493, 1957.

31. Hays, D.F., et al., "Heat Conduction in Solids: Temperature-Dependent Thermal Conductivity," Intl. Jl. Heat Mass Transfer, Vol. 11, pp. 285-295, 1968.

32. Cobble, M.H., "Finite Transform Solution of the Temperature of a Plate Heated by a Moving Discrete Source," Intl. Jl. Heat Mass Trans., 10, pp. 1281-1289, 1967.

33. Cobble, M.H., "The Temperature of a Plate Heated by a Source of Arbitrary Motion and Strength," Intl. Jl. Heat Mass Trans., pp. 1831-1835, 1968.

34. Birch, F., et al., "The Thermal Conductivity of Rocks and its Dependence upon Temperature and Composition," Am. Jl. Science, Vol. 238, pp. 529-558, Aug. 1940, and pp. 613-635, Sept. 1940.

35. Wingquist, C.F., "Elastic Moduli of Rock at Elevated Temperatures," Bur. Mines RI 7269, June 1969.

36. Bornefeld, H., "Temperature Measurements in Fusion Welding," (in German), Technische Zentrolblatt fur Prakische Metalbearbeitung, Vol. 43, pp. 14-18, 1933.

37. Thirumalai, K., "The Process of Thermal Spalling Behavior in Rocks-An Exploratory Study," Rock Mechanics-Theory and Practice, Ed. W.H. Somerton, Proc. 11th Symp. Rock Mech., pp. 705-727, 1970.

38. Smith, G.D., Numerical Solution of Partial Differential Equations, Oxford Univ. Press, 1965.

39. von Rosenberg, D.B., Methods for the Numerical Solution of Partial Differential Equations, American Elsevier Publishing Co., Inc., New York, 1969.

40. Crank, J., et al., "A Practical Method for Numerical Evaluation of Solutions of Partial Differential Equations of the Heat Conduction Type," Proc. Camb. Phil. Soc., 1947.

41. Douglas, J., Jr., "Alternating Direction Methods for Three Space Variables," Numerische Mathematik, Vol. 4, pp. 41-63, 1962.

42. Brian, P.L.T., "A Finite-Difference Method of High Order Accuracy for the Solution of Three-Dimensional Transient Heat Conduction Problems," AIChE Jl., Vol. 7, pp. 367-370, Sept. 1961.

43. Peaceman, D.W., et al., "The Numerical Solution of Parabolic and Elliptic Differential Equations," Jl. Soc. Indust. Appl. Math., pp. 28-41, March 1955.

44. Douglas, J., Jr., et al., "On the Numerical Solution of Heat Conduction Problems in Two and Three Space Variables," Trans. Am. Math. Soc., Vol. 82, pp. 421-439, 1956.

45. Love, A.E.H., Mathematical Theory of Elasticity, 4th ed., Cambridge Univ. Press, 1927.

46. Timoshenko, S.P., et al., Theory of Elasticity, 3rd ed., McGraw-Hill, Inc., 1970.

References (continued)

47. Lekhnitskii, S., _Theory of Elasticity of an Anisotropic Elastic Body_, trans. by P. Fern, Holden-Day, San Francisco, 1963.

48. Kupradge, V.D., "Potential Methods in the Theory of Elasticity," Trans. from Russian by H. Gutfreund, Israel Program of Scientific Translations, Jerusalem, 1965.

49. Nowacki, W., _Thermoelasticity_, Addison-Wesley Publishing Co., Inc. 1962.

50. Boley, B.A., et al., _Theory of Thermal Stresses_, John Wiley & Sons, Inc., 1960.

51. Atsumi, A., et al., "Transient Thermoelastic Problem of Transversely Anisotropic Sphere with Temperature Dependent Properties," Japan Soc. Mech. Engrs., Bull. 12, No. 5, June 1969.

52. Hilton, H.H., "Thermal Stresses in Bodies Exhibiting Temperature Dependent Properties," Jl. Appl. Mech., 1952.

53. Nowinski, J., "Thermoelasticity Problem for an Isotropic Sphere with Temperature Dependent Properties," Z.A.M.P., Vol. 10, 1959.

54. Sokolowski, M., "One-Dimensional Problems for Elastic Bodies with Material Constants Dependent on Temperature," Bull. Acad. Polon. Sci., Vol. 8, 1960.

55. System/360 Scientific Subroutine Package, (360-CM-03X) Version III, Programmer's Manual, IBM, Tech. Publ. Dept., New York, pp. 291-292, 1968.

56. Senol, V., et al., "ELAS-A General Purpose Computer Program for the Equilibrium Problems of Linear Structures," Jet Propulsion Laboratory, CIT, Pasadena, 1968.

57. Sternberg, E., et al., "On the Steady-State Thermoelastic Problem for the Half-Space," Qtly. Appl. Math., pp. 381-398, 1957.

58. Manson, S.S., _Thermal Stress and Low Cycle Fatigue_, McGraw-Hill, 1966.

59. Newman, R.L., "An Approach to Prediction of Thermal Shock Resistance During Very High Heating Rates," General Motors Corp., DDA Div., RN70-84, Oct. 1970.

60. Norton, F.H., _Refractories_, McGraw-Hill, Inc., 1949.

61. Weibull, W., "Statistical Theory of Strength of Materials," Proc. Roy. Acad. Eng. Sci., No. 151, 1939.

62. Sih, G.C., et al., "Mathematical Theories of Brittle Fracture," Chap. 2, Vol. II, _Fracture_, Acad. Press, 1968.

63. Erdogan, F., "Crack Propagation Theories," Chap. 5, _Fracture_, Vol. II, Acad. Press, 1968.

References (continued)

64. Hill, R., The Mathematical Theory of Plasticity, Clarendon Press, Oxford, 1950.

65. Johnson, Sowerby, and Haddow, Plane-Strain Slip-line Fields, American Elsevier Publishing Company, Inc., New York, 1970.

66. Courant, R., et al., Supersonic Flow and Shock Waves, Wiley Interscience, New York, 1948.

67. Cheatham, J.B., "An Analytical Study of Rock Penetration by a Single Bit Tooth," Eighth Annual Drilling and Blasting Symposium, Oct. 2, 1958.

68. Pariseau, W.G., et al., "The Force-Penetration Characteristic for Wedge Penetration into Rock," Intl. Jl. Rock Mech. & Min. Sci., Vol. 4, No. 2, pp. 165-180.

69. Charles, R.J., "Energy-Size Reduction Relationships in Comminution," Trans. AIME, Vol. 9, No. 1, January 1957.

70. Gilvarry, J.J., "Fracture of Brittle Solids, I. Distribution Function for Fragment Size in Single Fracture (Theoretical)," Jl. of Appl. Phys., Vol. 32, No. 2, March 1961.

71. Thirumalai, K., et al., "A Study of a New Concept of Thermal Hard Rock Crushing," Preprint, 14th Symp. on Rock Mech., Penn State Univ., June 1972.

72. Dallavalle, J.M., Micromeritics-The Technology of Fine Particles, Pitman Publishing Corporation, 1948.

73. Ralston, A., A First Course in Numerical Analysis, McGraw-Hill, Inc., 1965.

74. Pflieder, E.P., et al., "Higher Air Pressure for Down-the-Hole Percussive Drills," Min. and Quarry Eng., Pt. I, pp. 463-468, Oct. 1961, and Pt. 2, pp. 496-501, Nov. 1961.

75. Fenton, Gary E., "Design and Preliminary Testing of a Thermo-mechanical Rock Fragmentation Apparatus," M.S. thesis, University of Missouri-Rolla, 1971.

76. Lundquist, R.G., and Anderson, C.F., "Energetics of Percussive Drills-Longitudinal Strain Energy," Bureau of Mines RI 7329, December 1969.

APPENDIX A

ROCK PROPERTIES

Table A-1. Rock Properties - Summary

Rock	ρ[1]	IH[2]	RD[3]	σ_c[4]	σ_t[5]	E[6]	α[7]	k[8]	C_p[9]	V_e[10]	AP[11]
Missouri Red Granite	2.60	53	9	1.62	.099	584.0	12.7	-	-	.452	0.40
Charcoal Grey Granite	2.73	91	-	2.34	.1245	788.0	6.2	3150.0	.293	-	0.77
Kitledge Pink Granite	2.60	53	7	1.71	.112	406.0	-	-	-	.329	0.80
Black Granite (Buena Gabbro)	3.10	64	6	2.28	.167	753.0	8.20	-	-	.547	0.30
Sioux Quartzite	2.64	57	8	3.42	.256	810.0	11.3	-	-	.545	0.50
Dresser Basalt	2.97	79	-	3.04	.1545	1025.0	9.6	4200.0	.293	-	0.20

[1] ρ = Density (g/cm^3)

[2] IH = Impact Hardness

[3] RD = Relative Drillability

[4] σ_c = Compressive Strength (10^6 gm/cm^2)

[5] σ_t = Tensile Strength (10^6 gm/cm^2)

[6] E = Modulus of Elasticity (10^6 gm/cm^2)

[7] α = Coefficient of Thermal Expansion @ 100°C (10^{-6} cm/cm°C)

[8] k = Thermal Conductivity (10^{-6} cal/cm sec°C)

[9] C_p = Specific Heat (cal/gm°C)

[10] V_e = Compression Wave Velocity (cm/sec)

[11] AP = Apparent Porosity (Percent)

A-1

Table A-2. Rock Composition

Rock	Composition (percent by volume)	
Missouri Red Granite	Quartz	32.5
	Potash feldspar	42.5
	Plagioclase feldspar	25.0
	Hornblende	trace
	Hypersthene	trace
	Magnetite	trace
Charcoal Grey Granite	Feldspar, plagioclase (sodic end) and microcline	63.0
	Quartz	16.0
	Hornblende	17.0
	Biotite	3.0
	Clays, Zircon, Apatite, Sphene	1.0
Kitledge Pink Granite	- - -	- -
Black Granite (Buena Gabbro)	Labradorite	45.0
	Augite	40.0
	Olivine	15.0
Sioux Quartzite	Quartz	99.0
	Chert	0.5
	Mica	0.5
Dresser Basalt	Feldspar (Labradorite), microcline	50.0
	Augite	40.0
	Magnetite	8.0

APPENDIX B

TEMPERATURE DISTRIBUTION CURVES
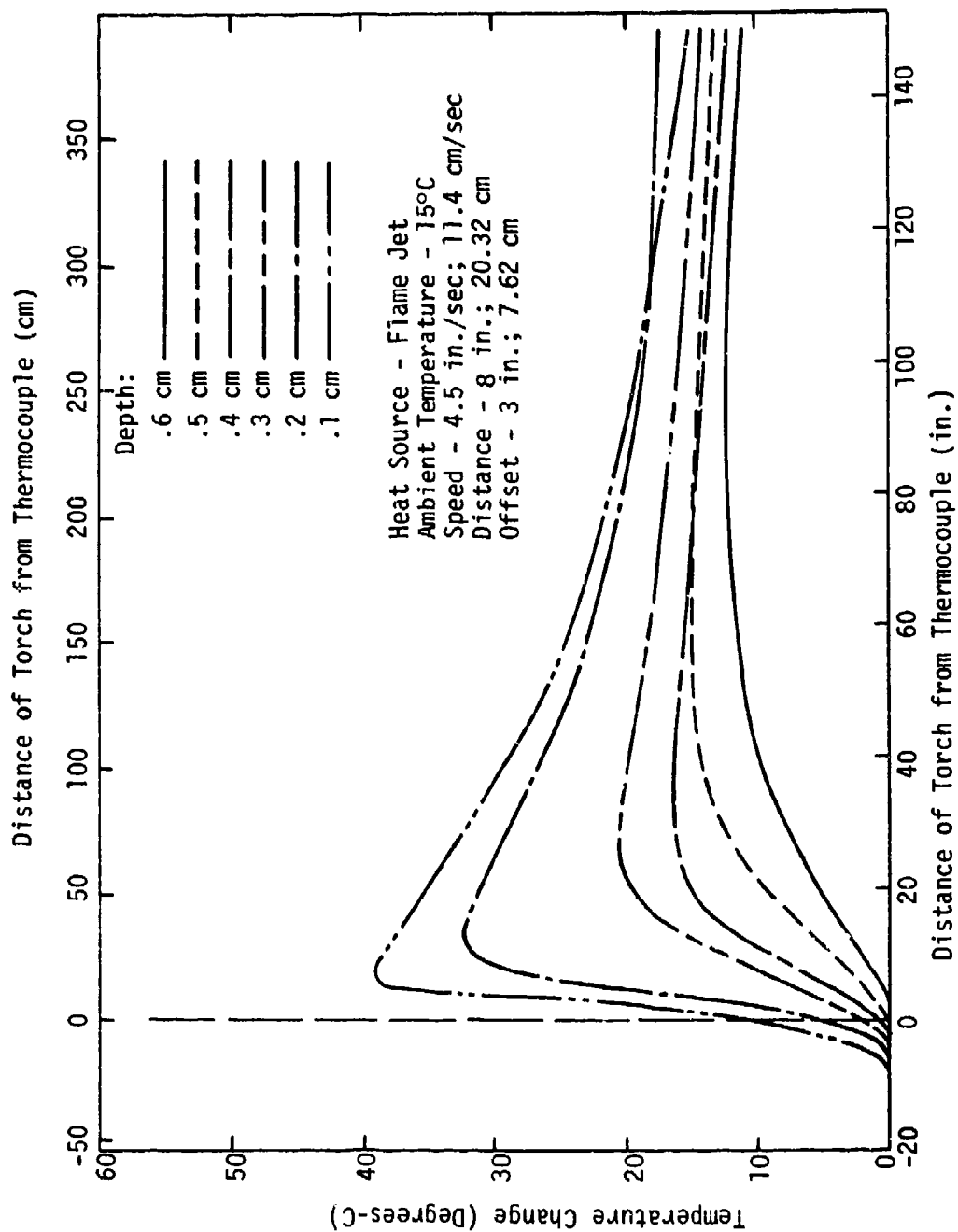
Fig. B-1. Subsurface Temperature Measurements - Dresser Basalt

B-1
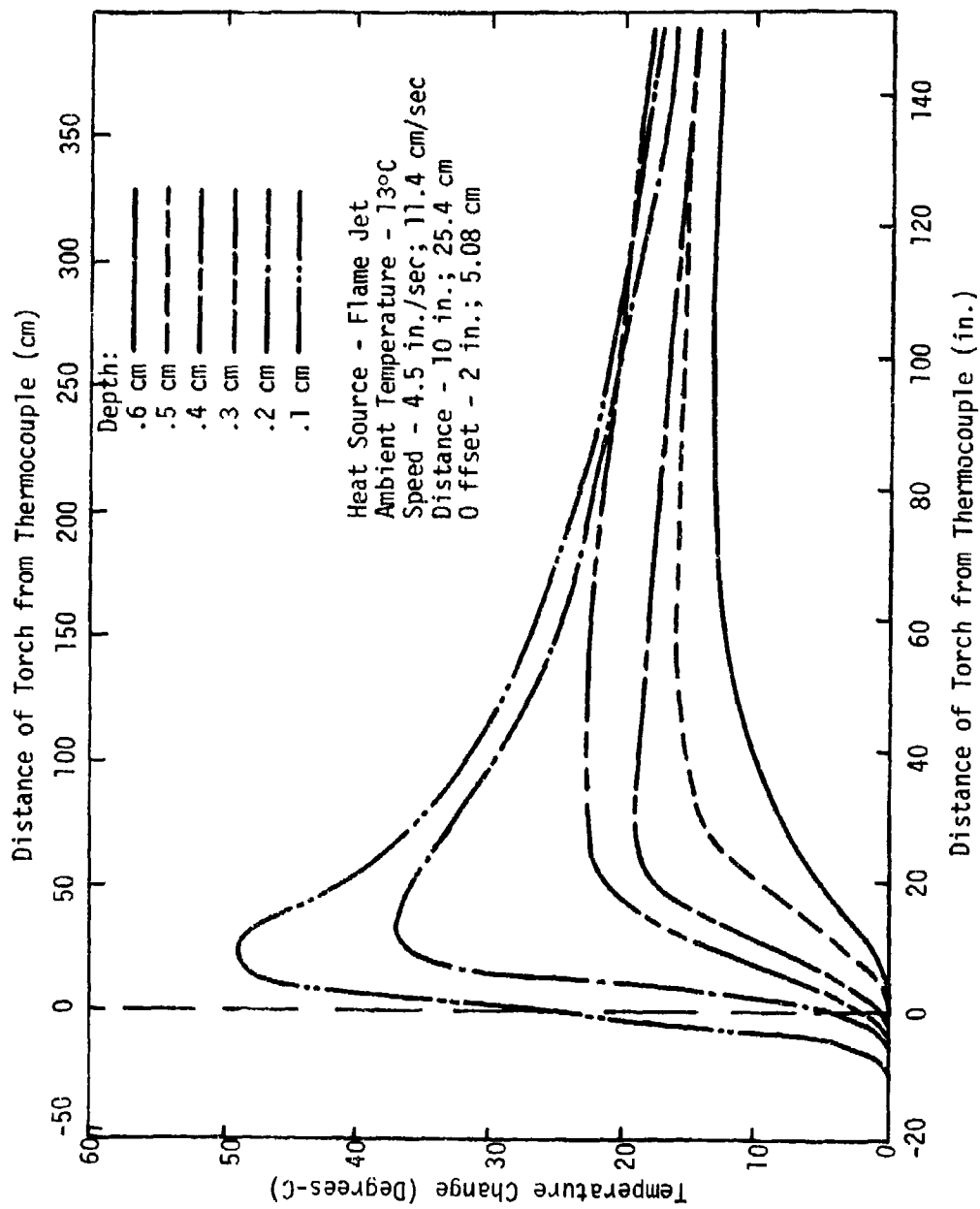
Fig. B-2. Subsurface Temperature Measurements - Dresser Basalt
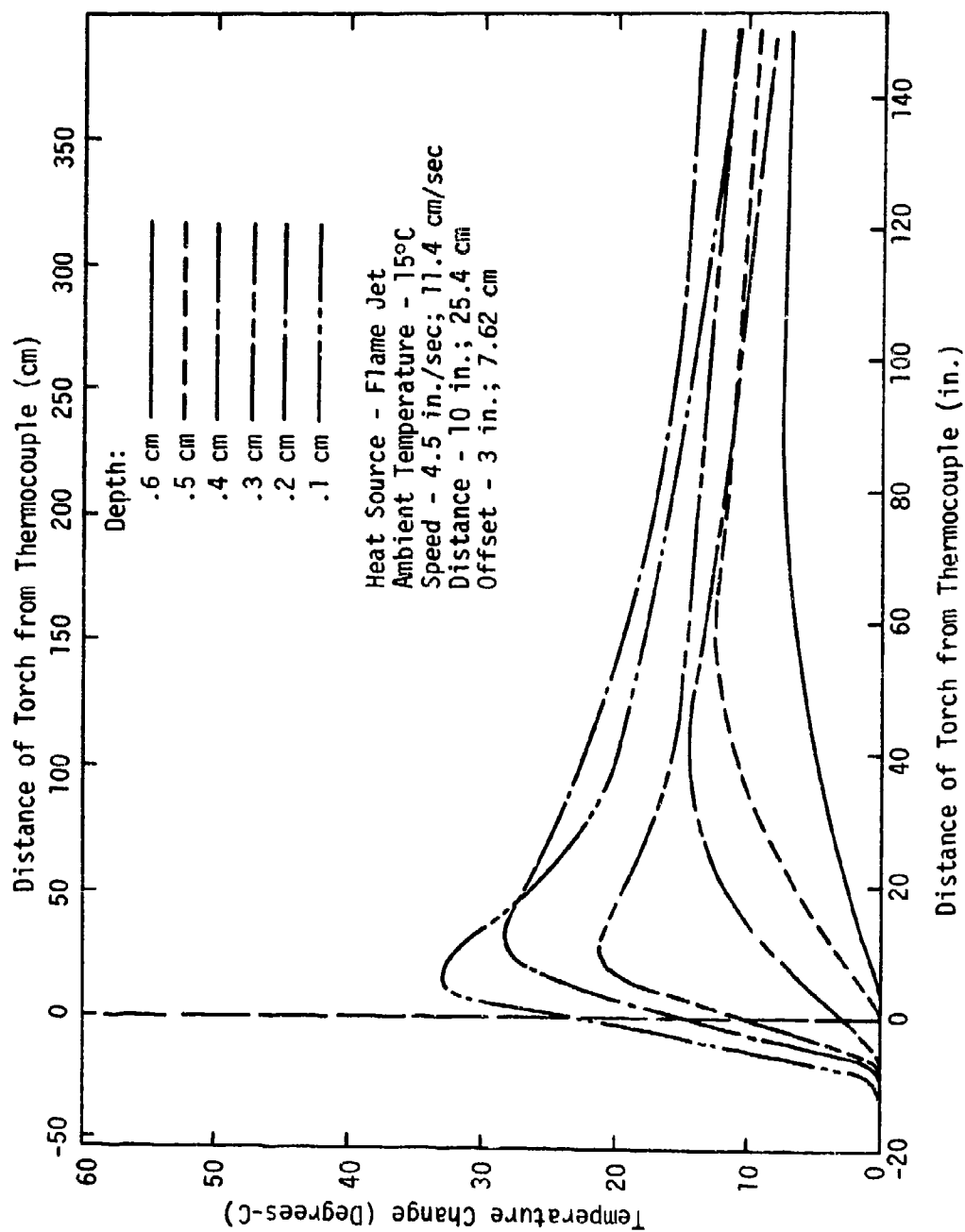
Fig. B-3. Subsurface Temperature Measurements - Dresser Basalt

B-3
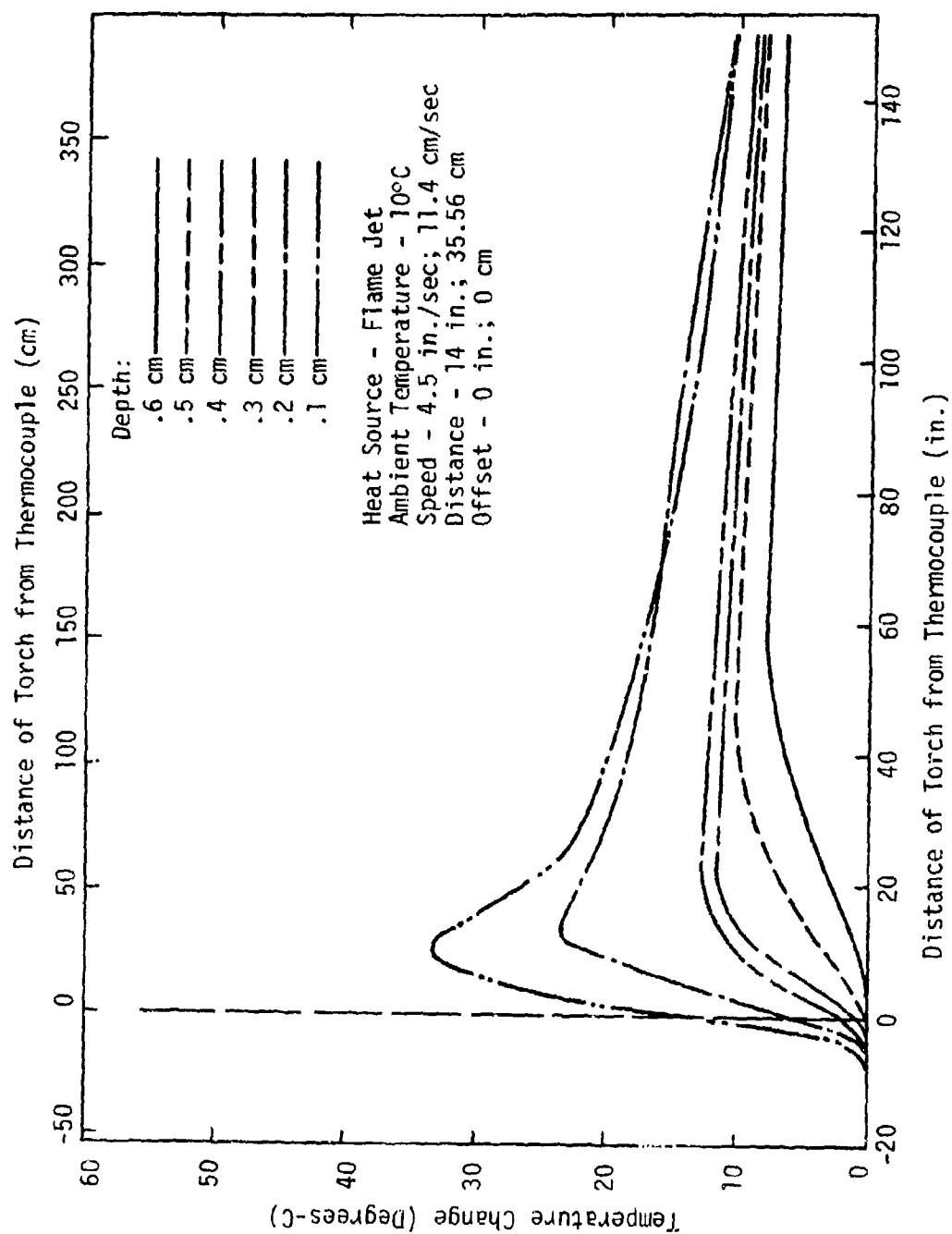
Fig. B-4. Subsurface Temperature Measurements - Dresser Basalt

B-4
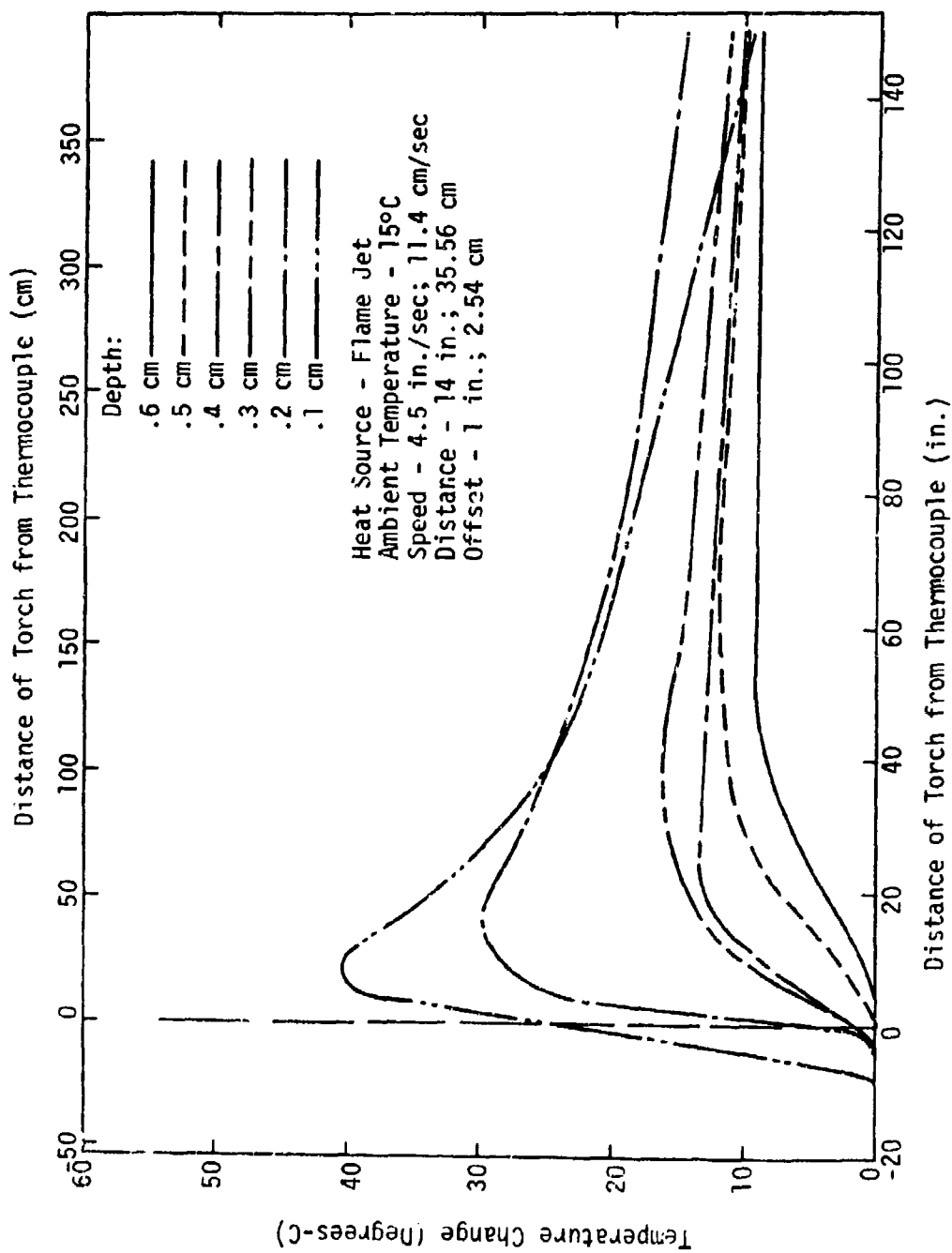
Fig. 8-5. Subsurface Temperature Measurements - Dresser Basalt
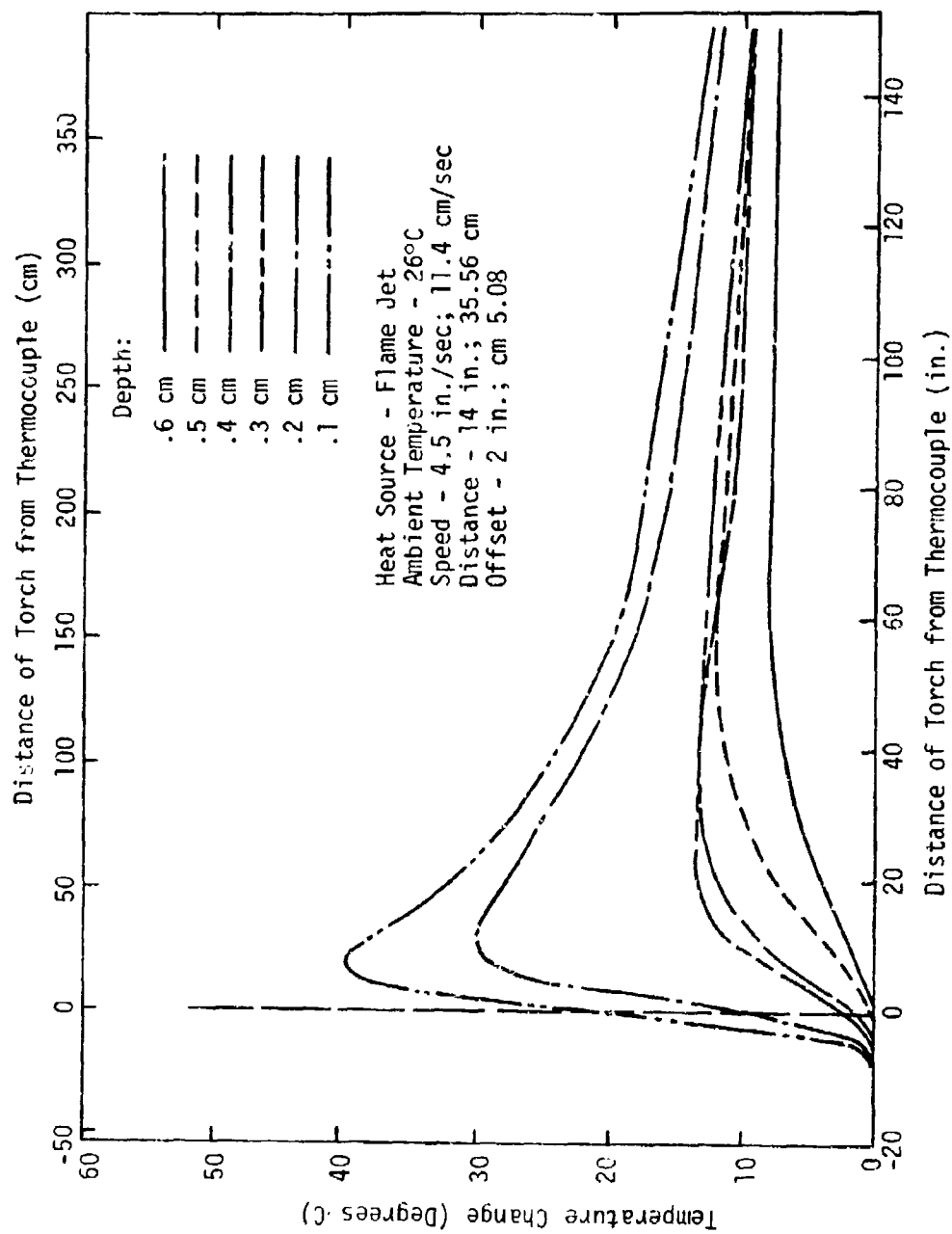
Fig. B-6. Subsurface Temperature Measurements - Dresser Basalt

Fig. B-7. Subsurface Temperature Measurements – Dresser Basalt

The figure shows temperature change (Degrees-C) versus distance of torch from thermocouple (in cm and in.). Plot parameters:

Depth:
— .6 cm
— — .5 cm
— · — .4 cm
— ·· — .3 cm
— ··· — .2 cm
— ···· — .1 cm

Heat Source – Flame Jet
Ambient Temperature – 14°C
Speed – 4.5 in./sec; 11.4 cm/sec
Distance – 14 in.; 35.56 cm
Offset – 3 in.; 7.62 cm
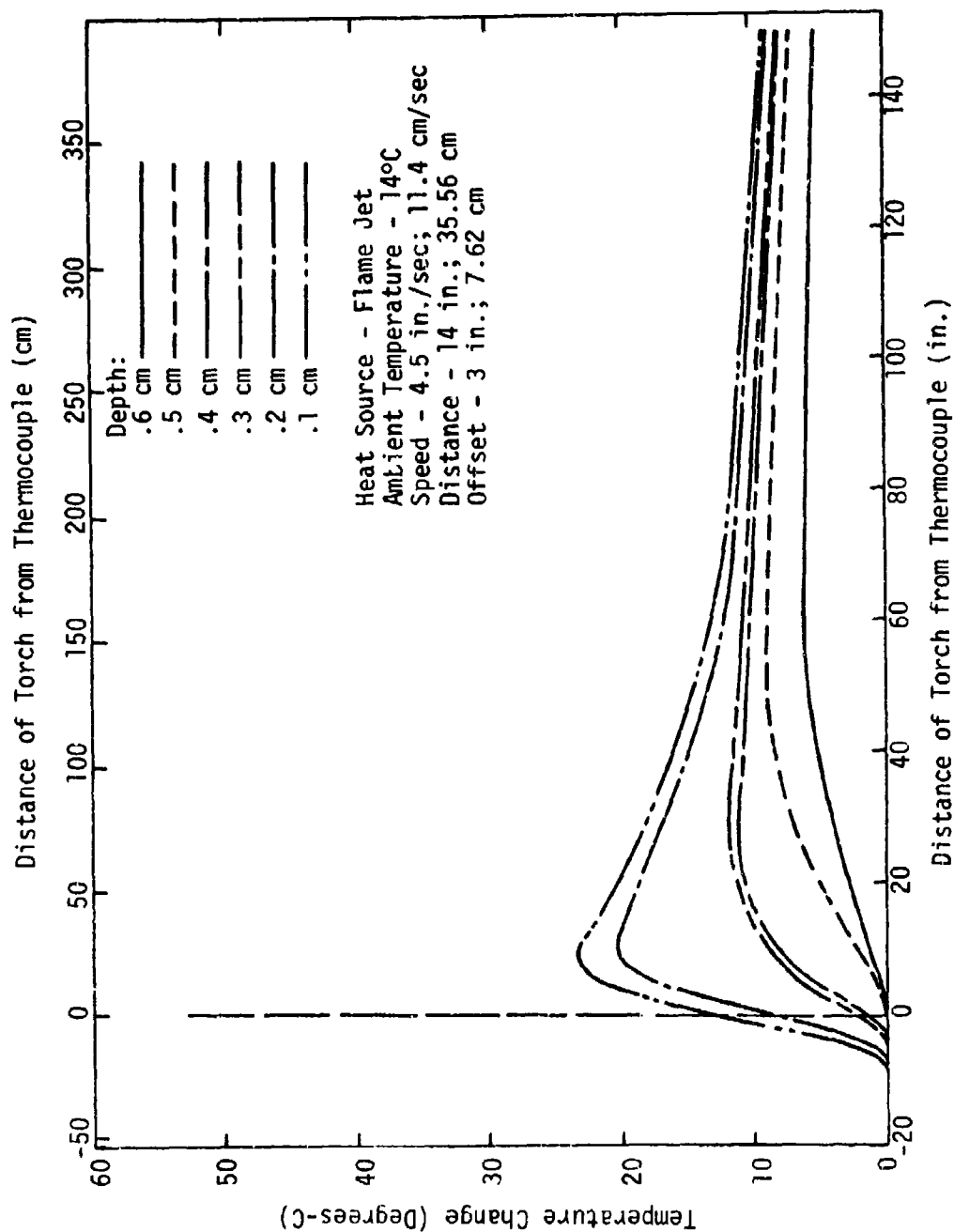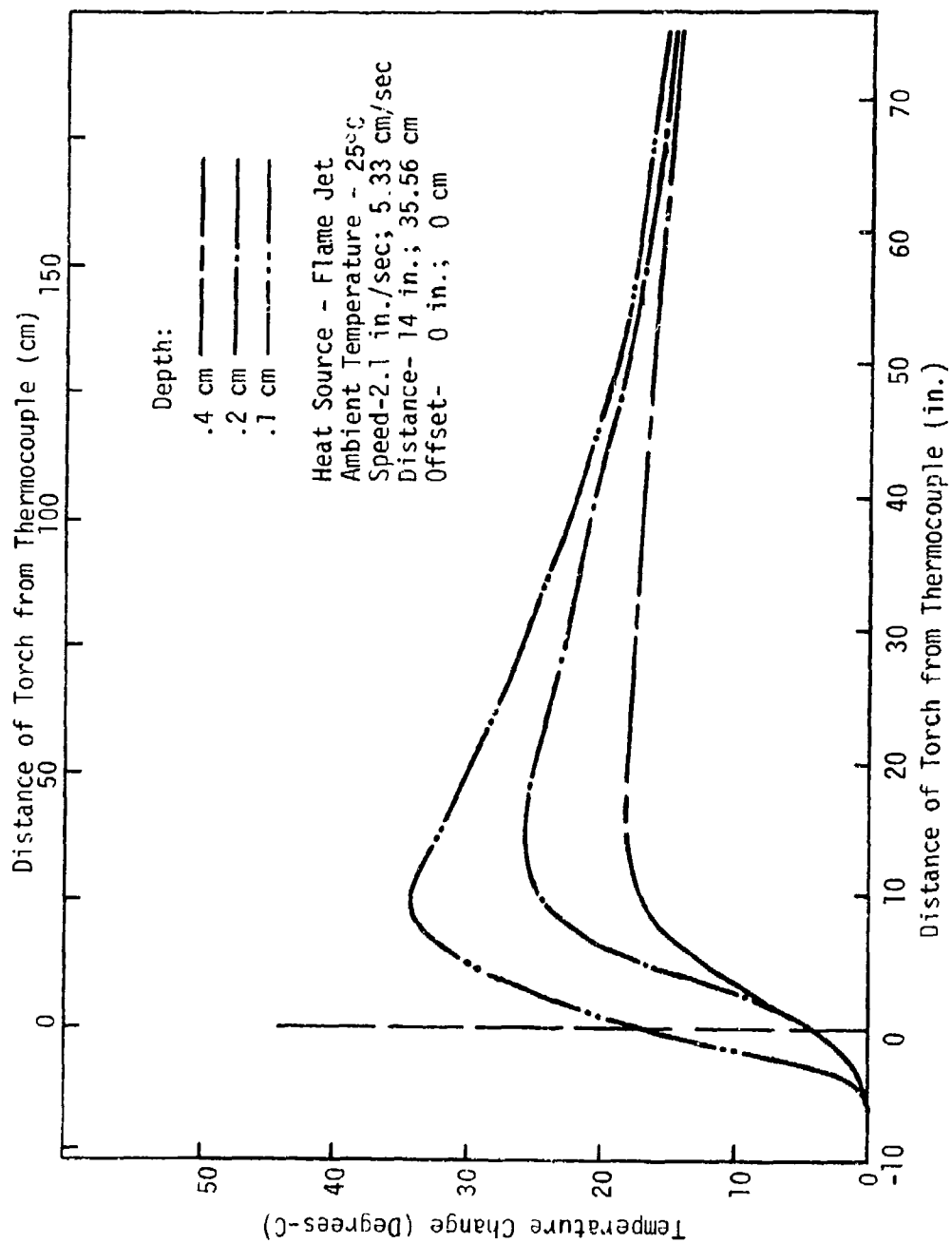
Fig. B-8. Subsurface Temperature Measurements - (Mo. Red Granite)
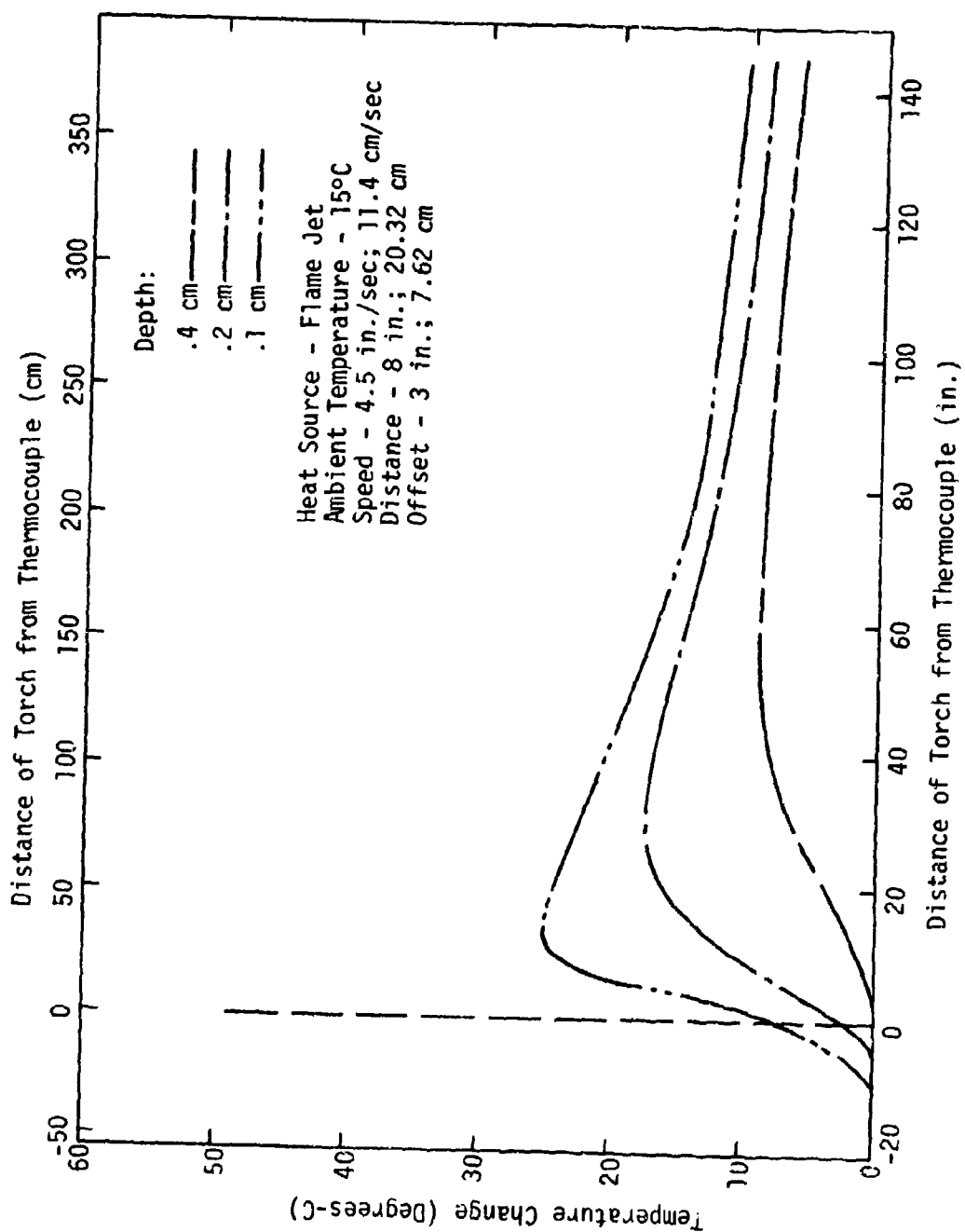
Fig. B-9. Subsurface Temperature Measurements - (Mo. Red Granite)
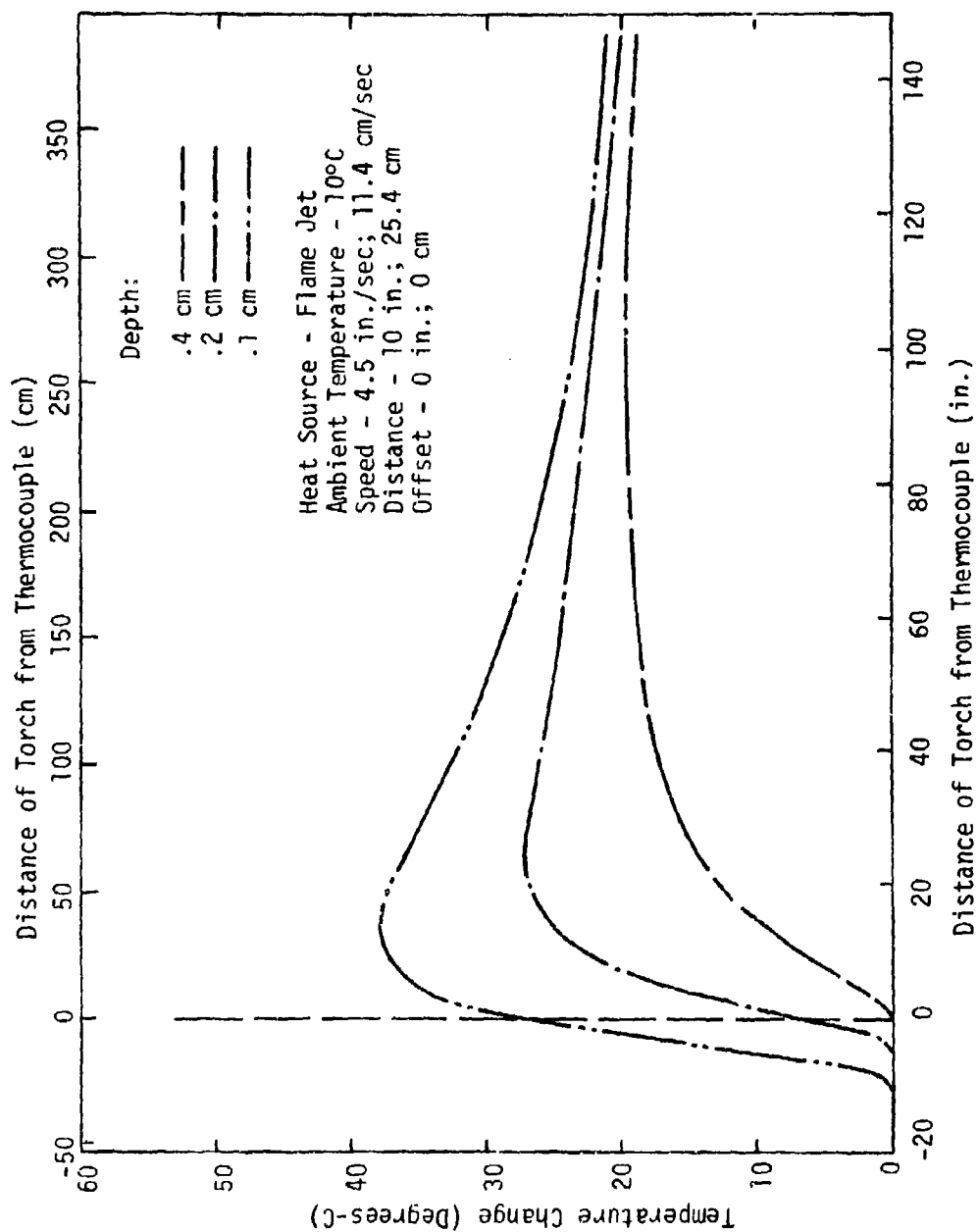
Fig. B-10. Subsurface Temperature Measurements - (Mo. Red Granite)
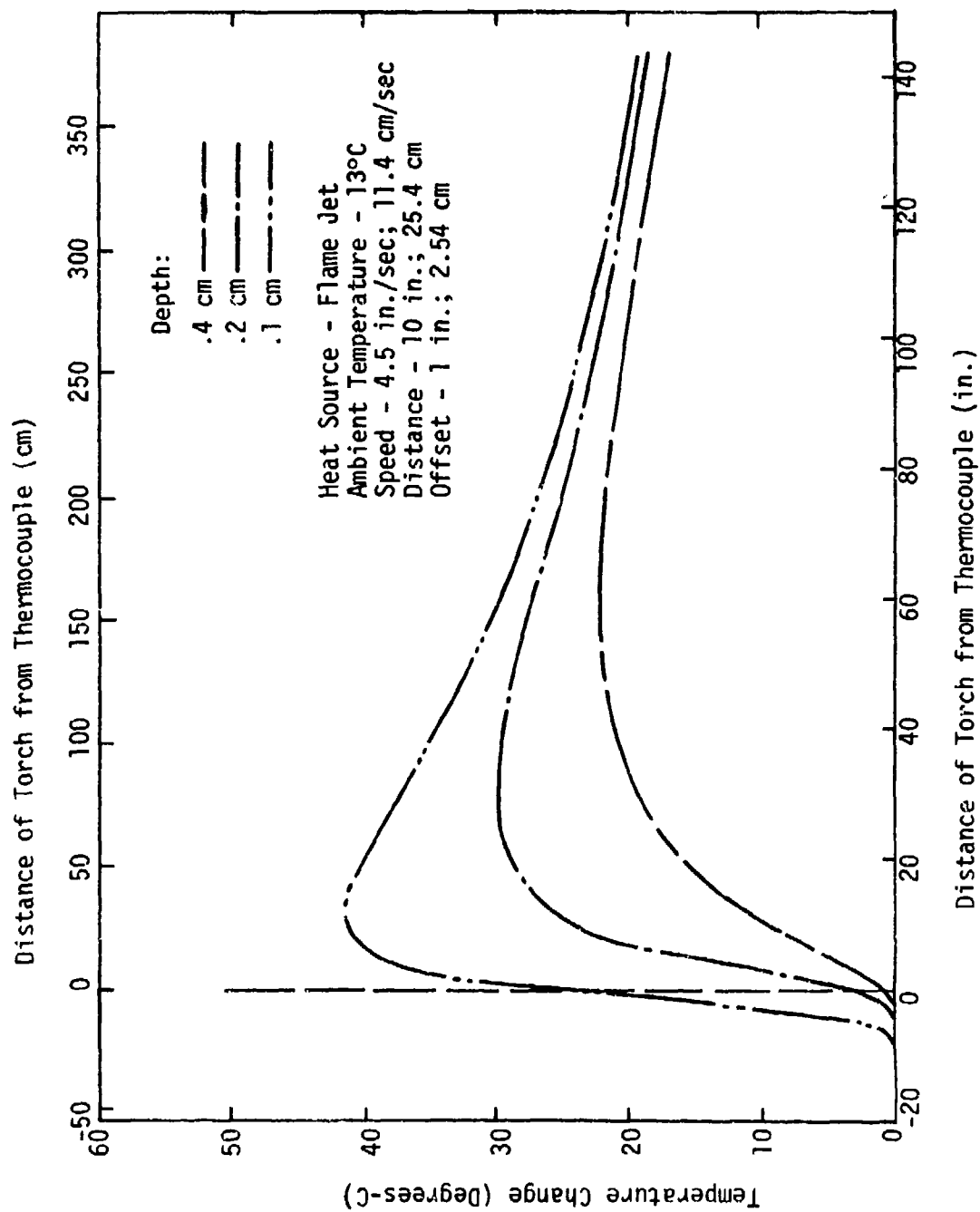
Fig. B-11. Subsurface Temperature Measurements - (Mo. Red Granite)
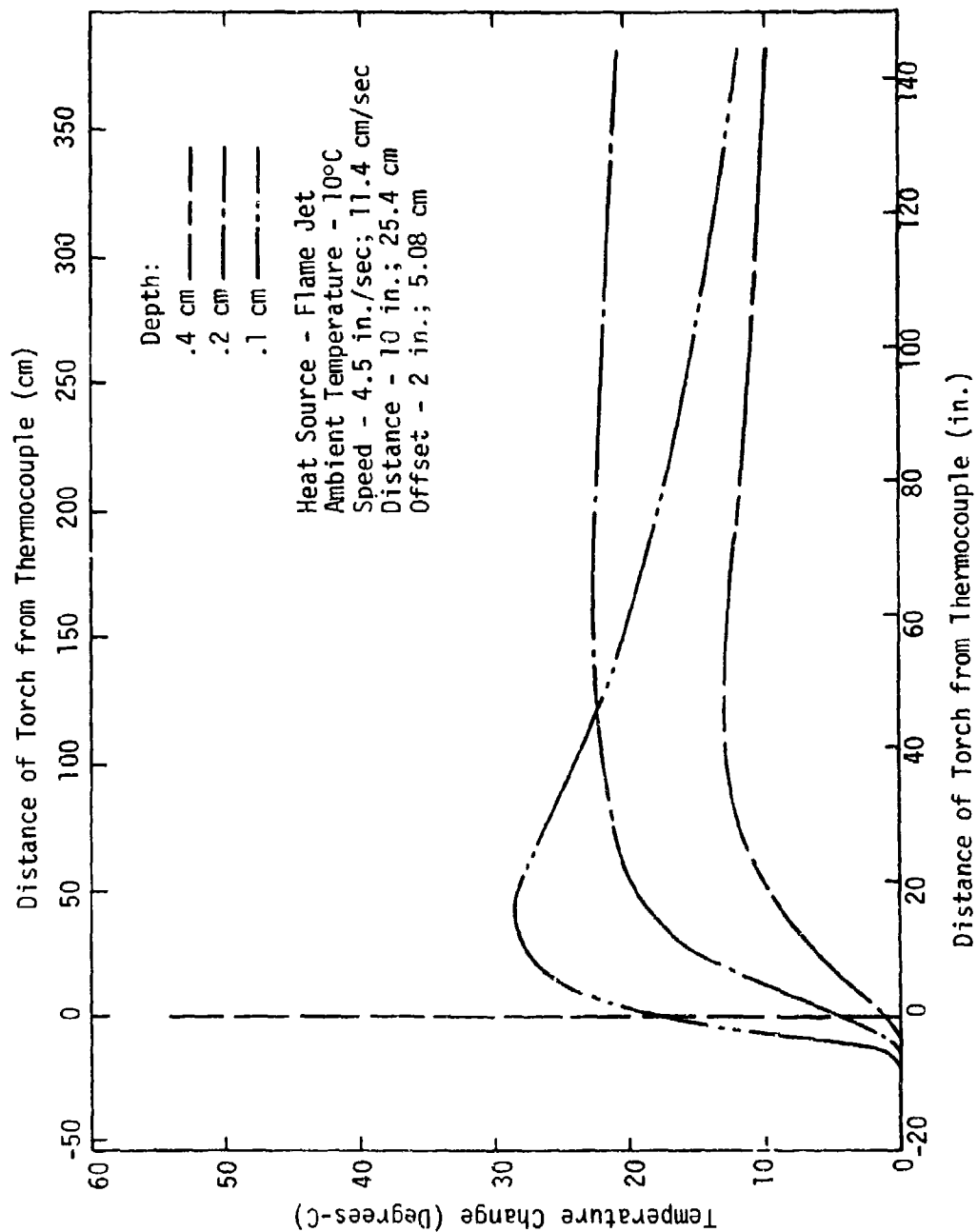
Fig. B-12. Subsurface Temperature Measurements – (Mo. Red Granite)
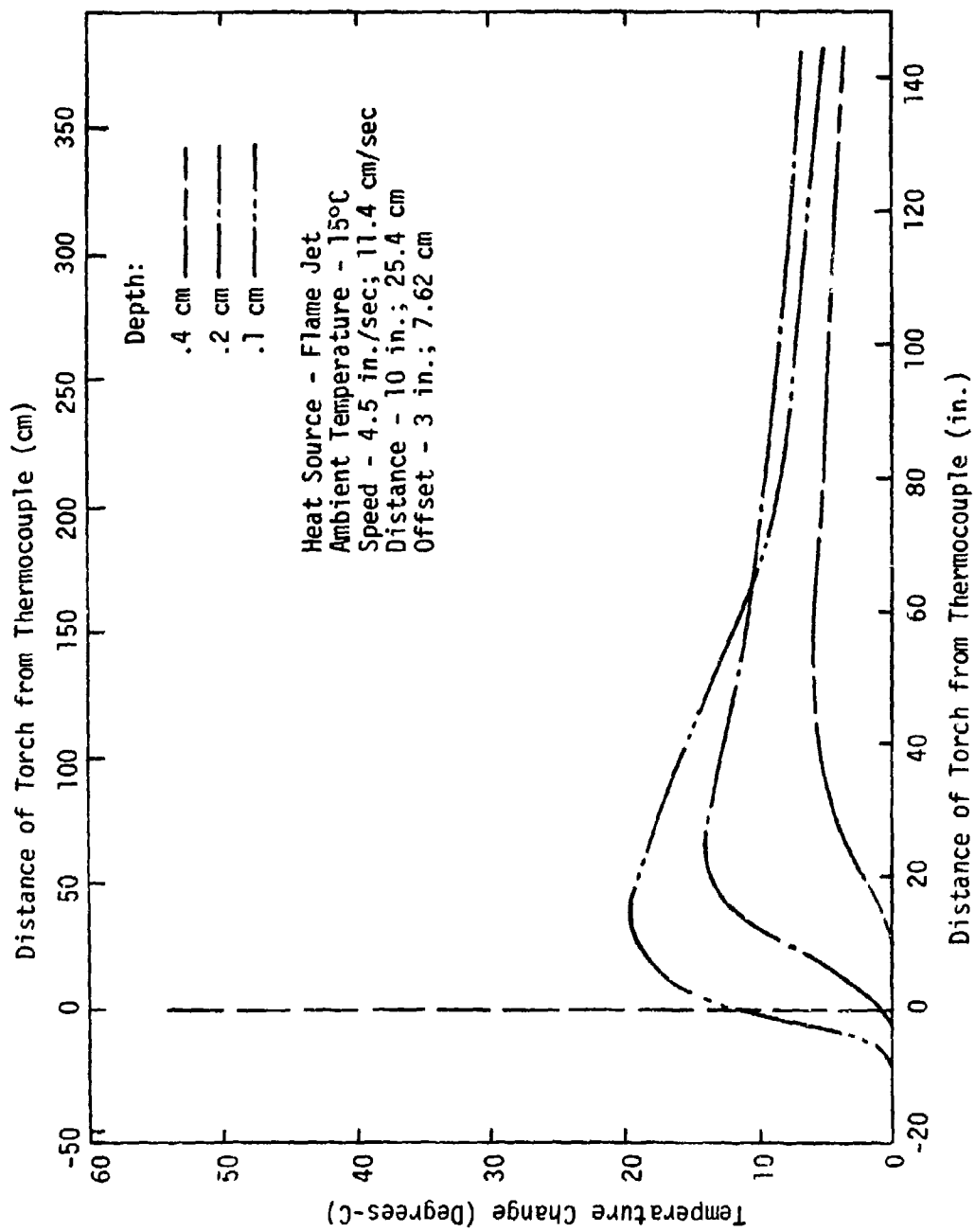
Fig. B-13. Subsurface Temperature Measurements – (Mo. Red Granite)

Fig. B-14.   Subsurface Temperature Measurements - (Mo. Red Granite)

Heat Source - Flame Jet
Ambient Temperature - 10°C
Speed - 4.5 in./sec; 11.4 cm/sec
Distance - 14 in.; 35.56 cm
Offset - 0 in.; 0 cm

Depth:
.4 cm
.2 cm
.1 cm
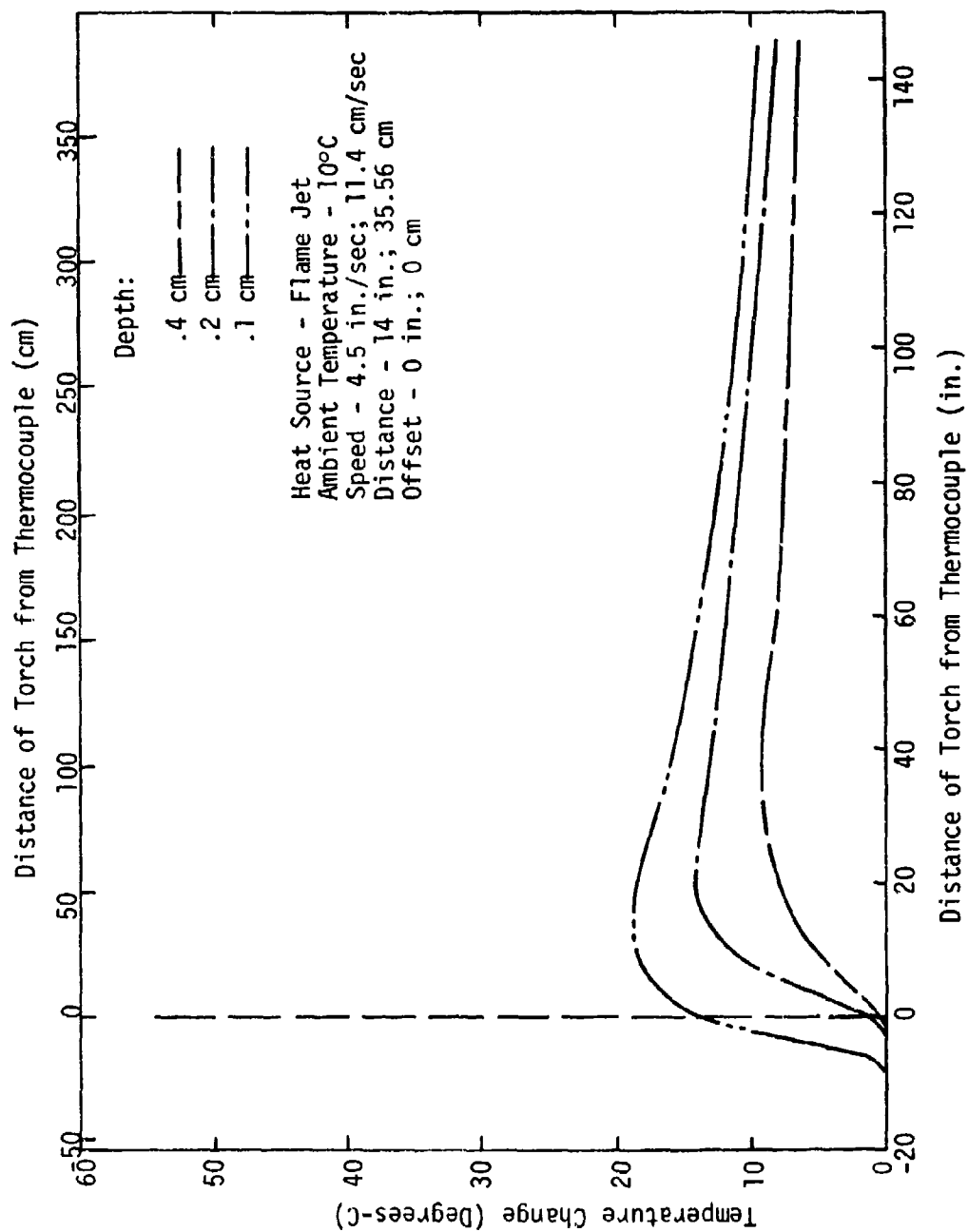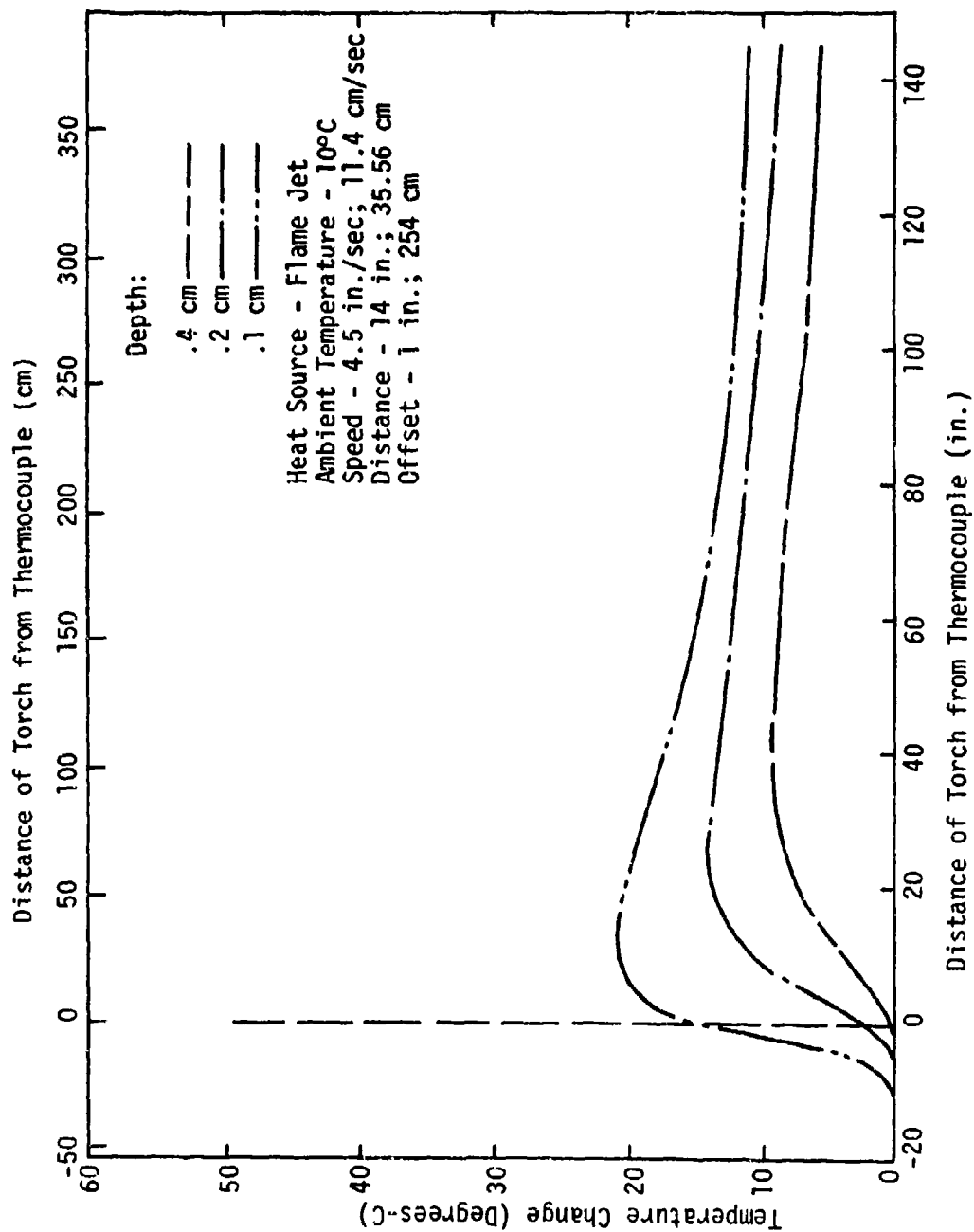
Fig. B-15. Subsurface Temperature Measurements - (Mo. Red Granite)
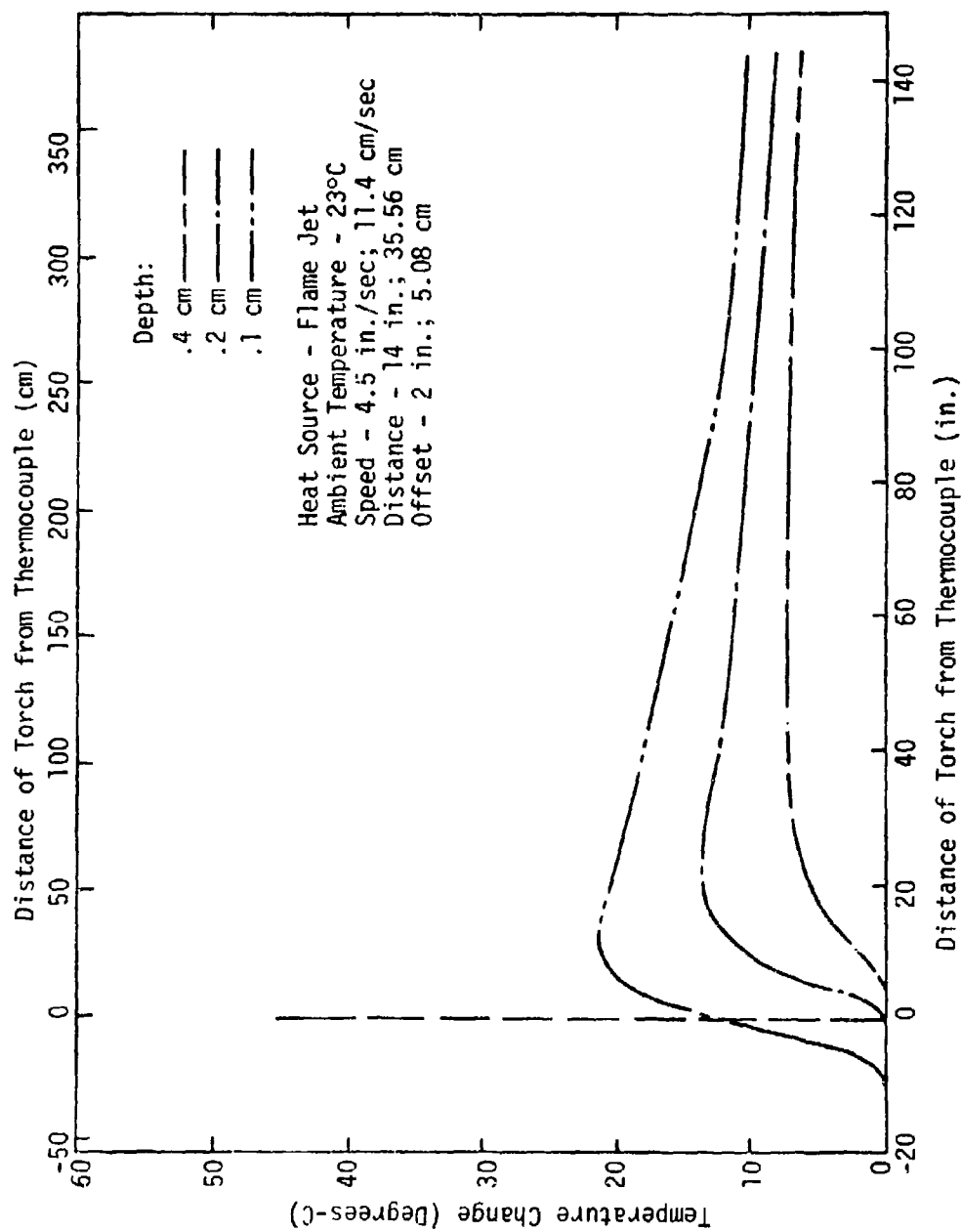
Fig. B-16. Subsurface Temperature Measurements – (Mo. Red Granite)

Fig. B-17. Subsurface Temperature Measurements - (Mo. Red Granite)

The figure shows a plot with axes labeled "Distance of Torch from Thermocouple (cm)" and "Distance of Torch from Thermocouple (in.)" versus "Temperature Change (Degrees-C)".

Depth:
.4 cm
.2 cm
.1 cm

Heat Source - Flame Jet
Ambient Temperature - 25°C
Speed - 4.5 in./sec; 11.4 cm/sec
Distance - 14 in.; 35.56 cm
Offset - 2 in.; 5.08 cm
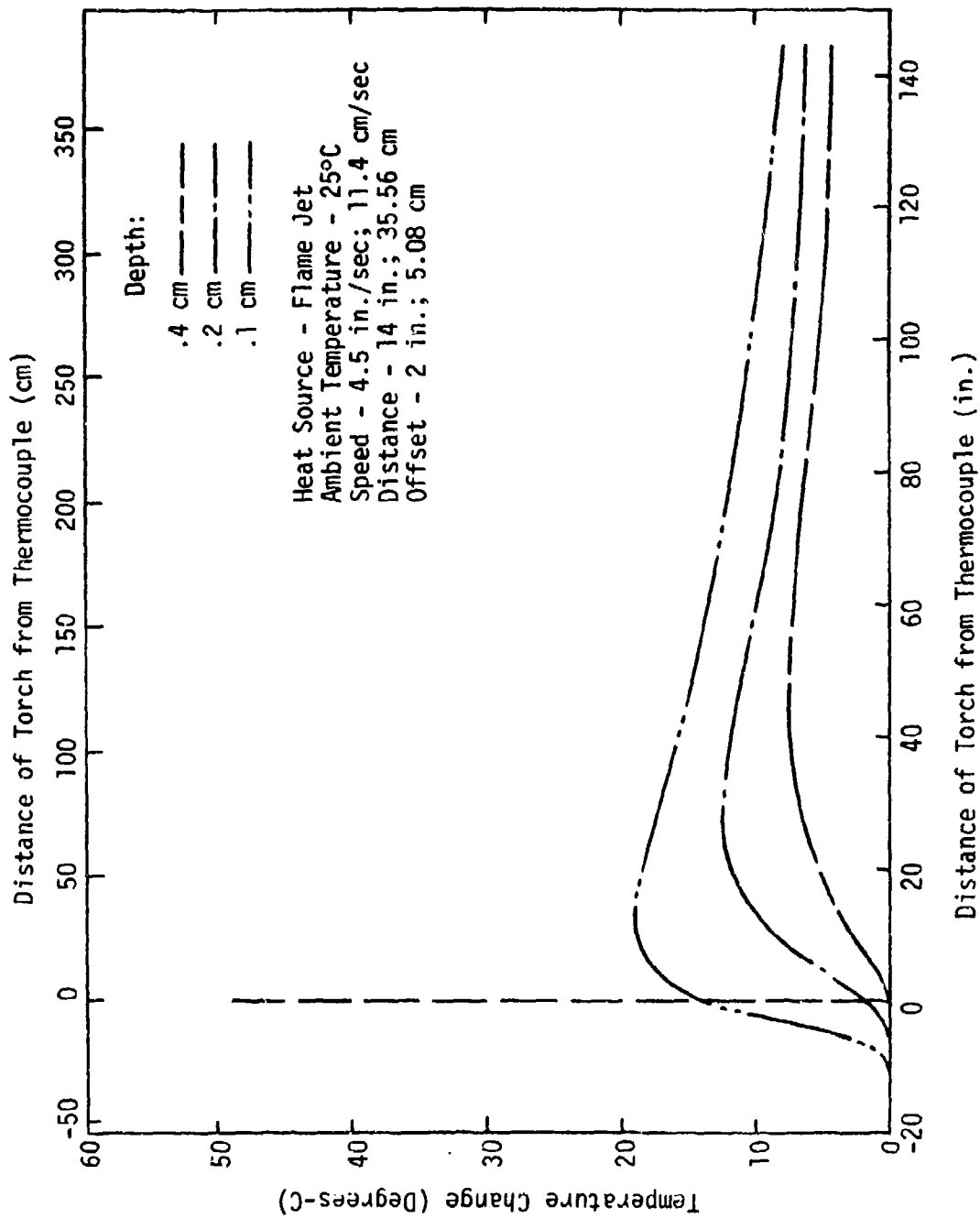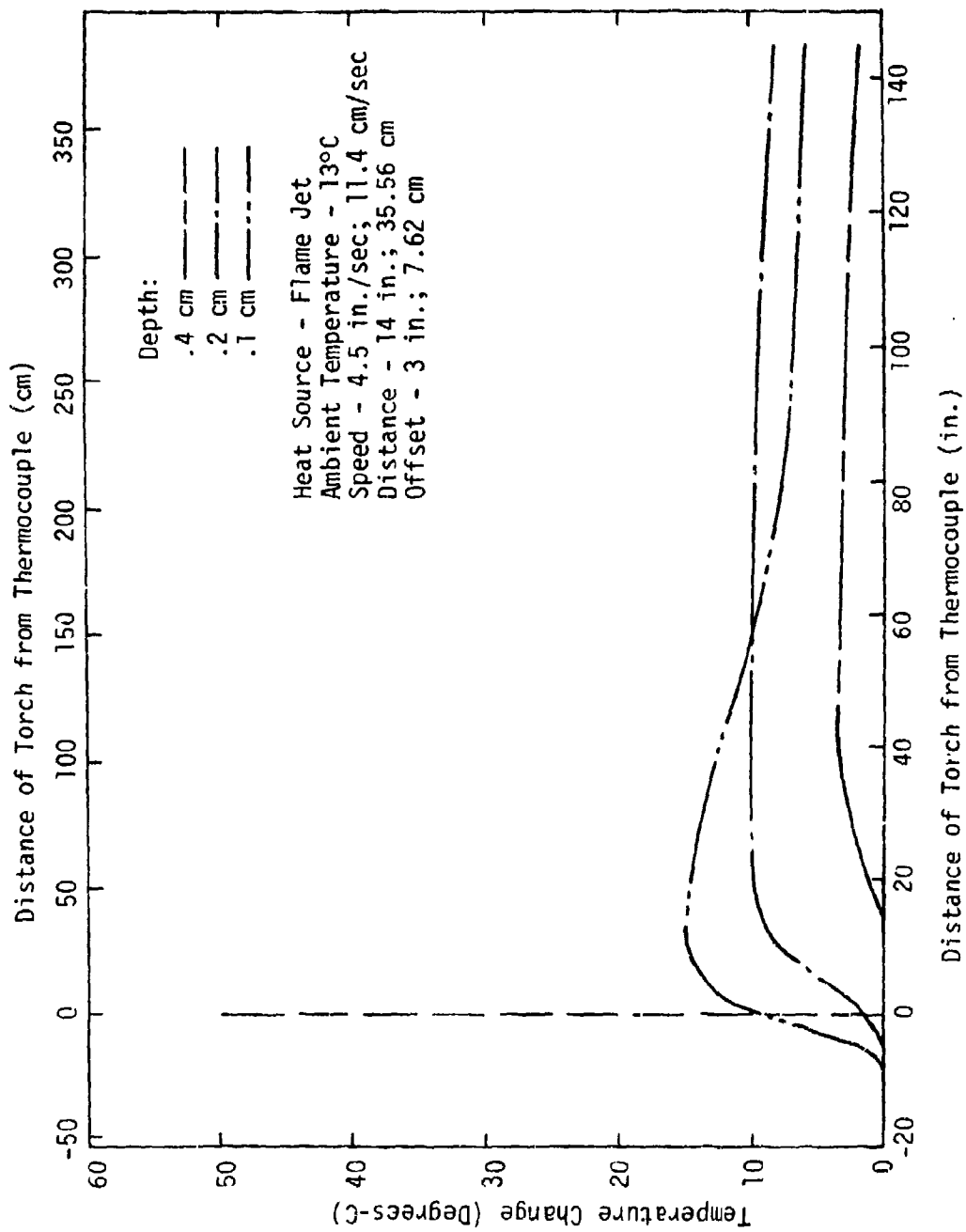
Fig.B-18. Subsurface Temperature Measurements - (Mo. Red Granite)

B-18
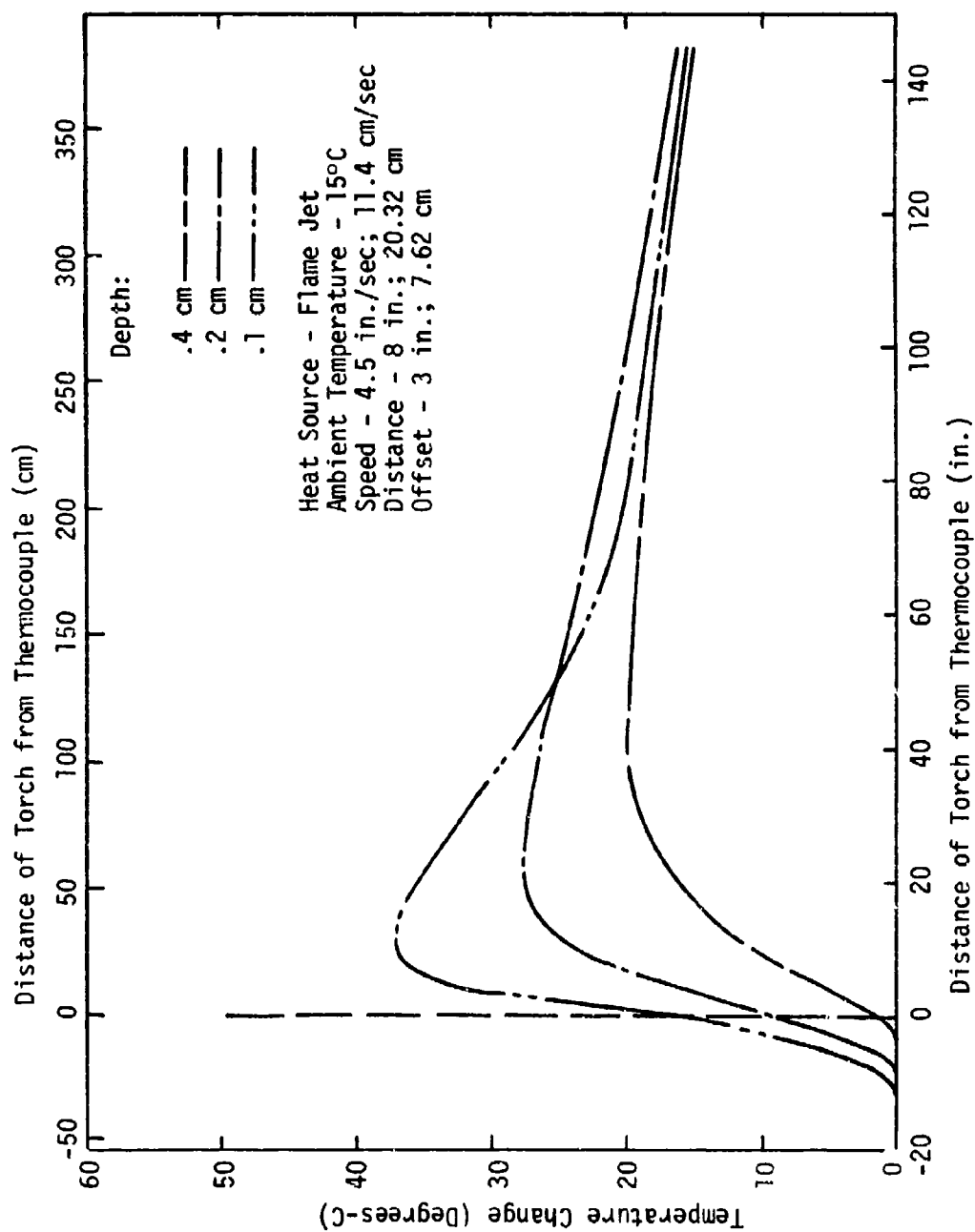
Fig. B-19. Subsurface Temperature Measurements - Buena Gabbro

Fig. B-20. Subsurface Temperature Measurements – Buena Gabbro

The chart shows:
- Distance of Torch from Thermocouple (cm) on top axis
- Distance of Torch from Thermocouple (in.) on bottom axis
- Temperature Change (Degrees-C) on vertical axis

Depth:
- .4 cm
- .2 cm
- .1 cm

Heat Source – Flame Jet
Ambient Temperature – 11°C
Speed – 4/5 in./sec; 11.4 cm/sec
Distance – 10 in.; 25.4 cm
Offset – 0 in.; 0 cm
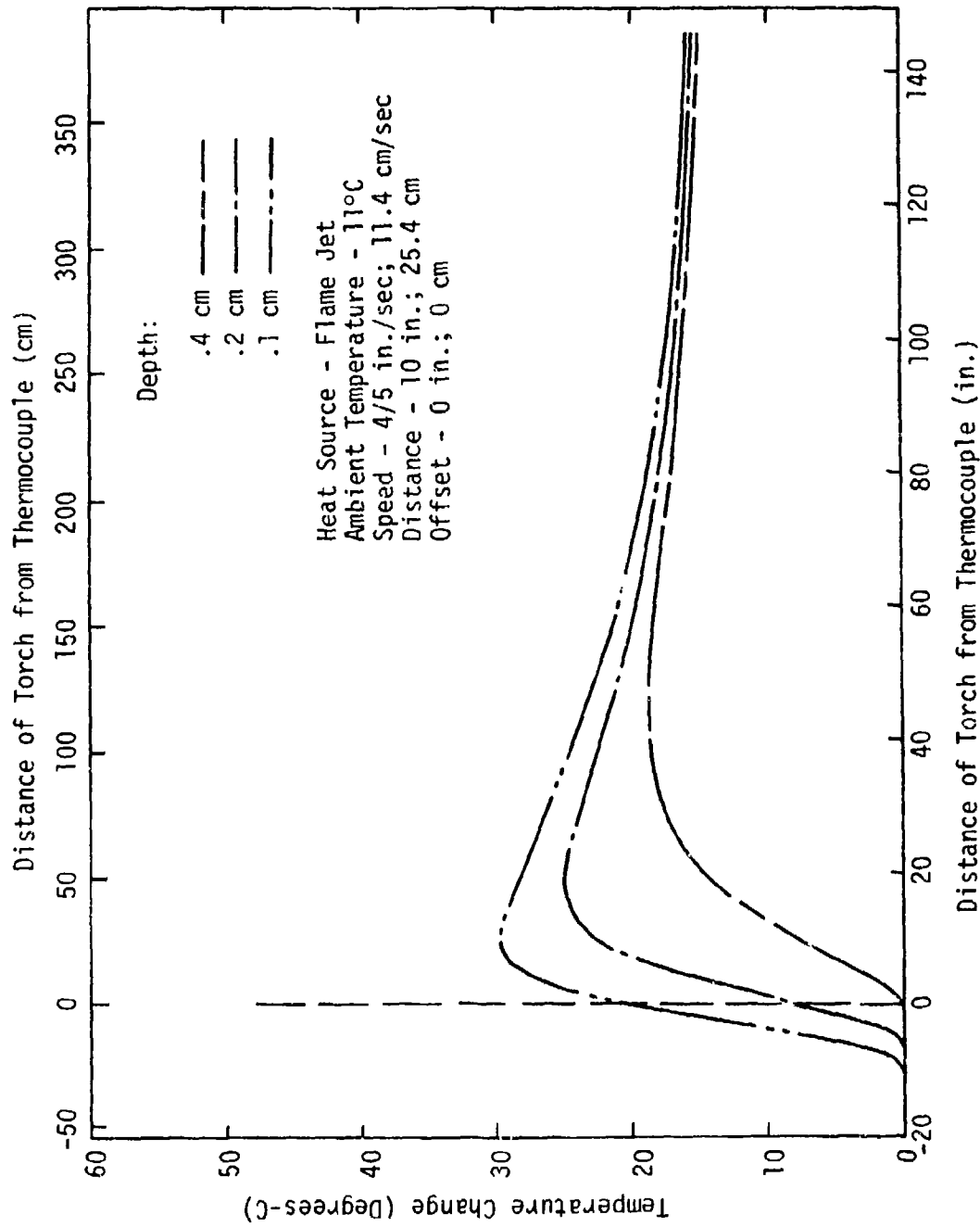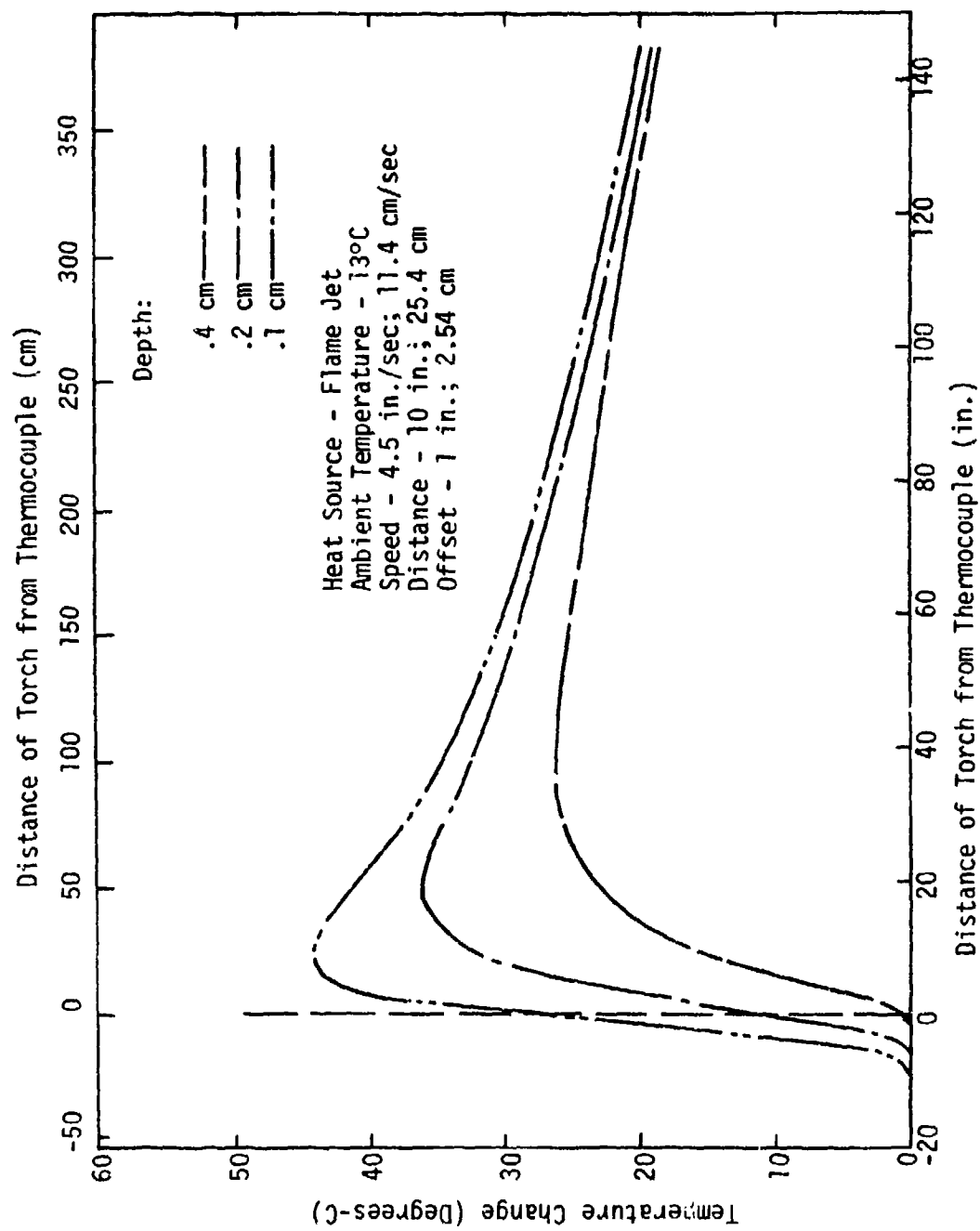
Fig. B-21. Subsurface Temperature Measurements - Buena Gabbro
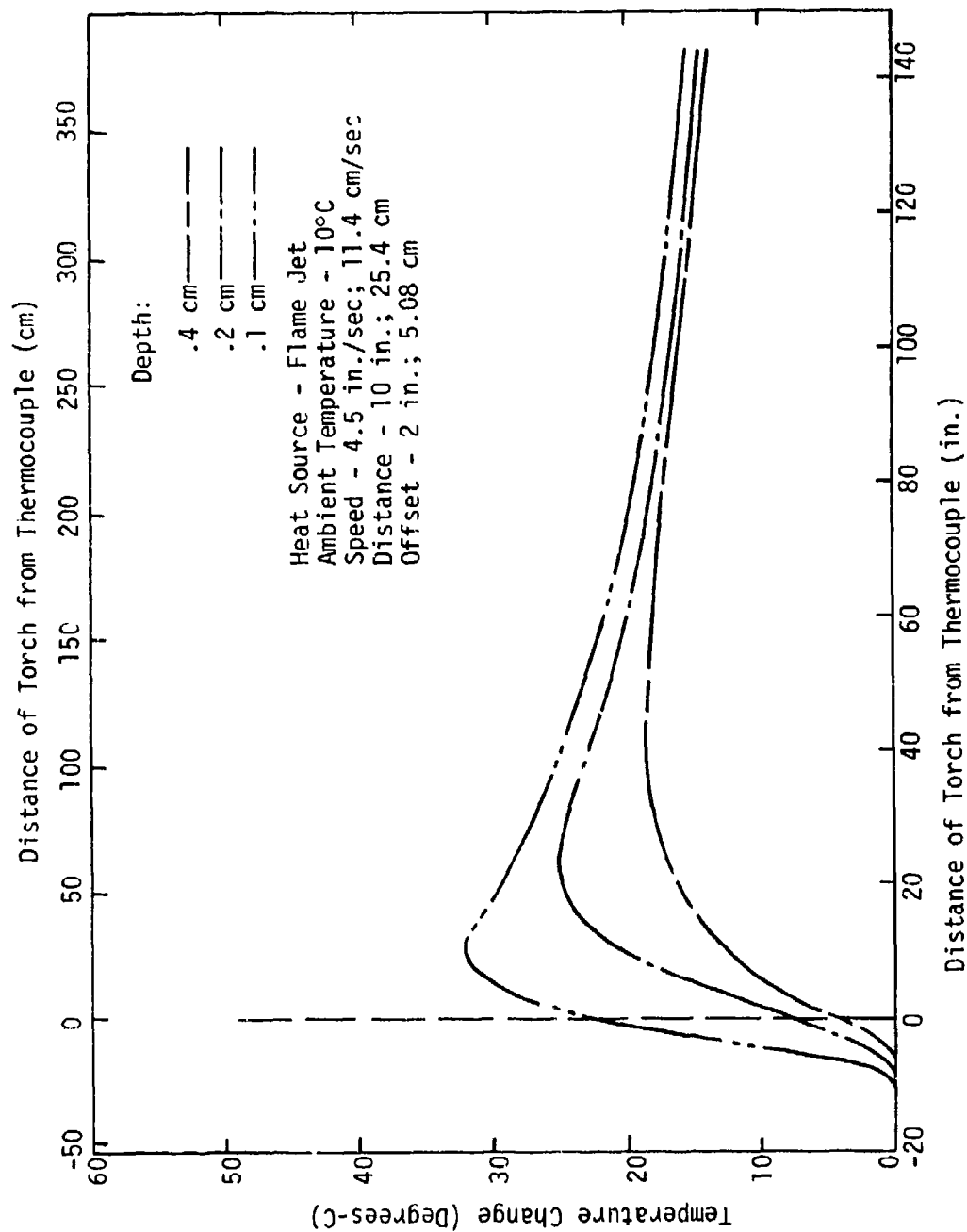
Fig. B-22. Subsurface Temperature Measurements – Buena Gabbro
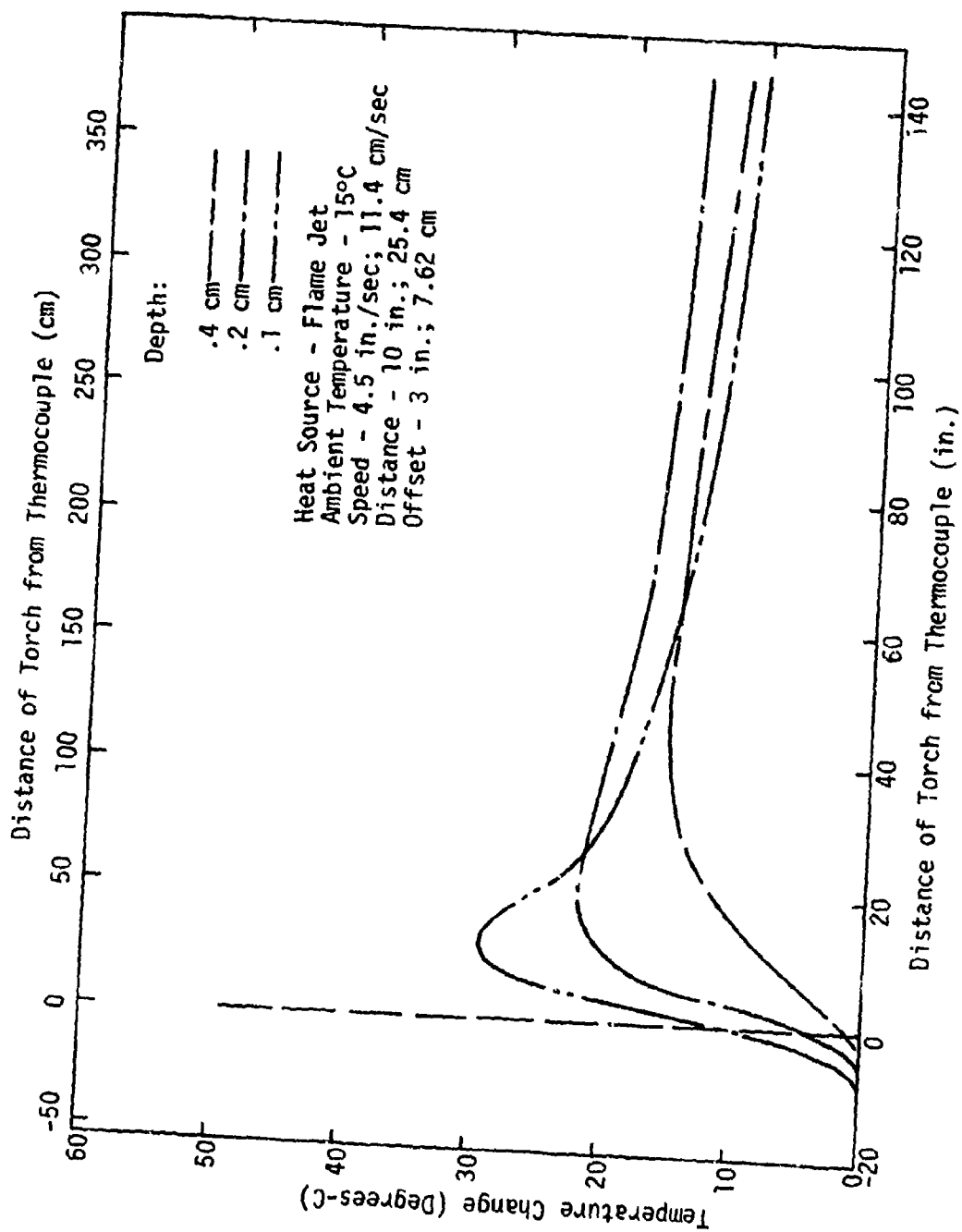
Fig. B-23. Subsurface Temperature Measurements - Buena Gabbro
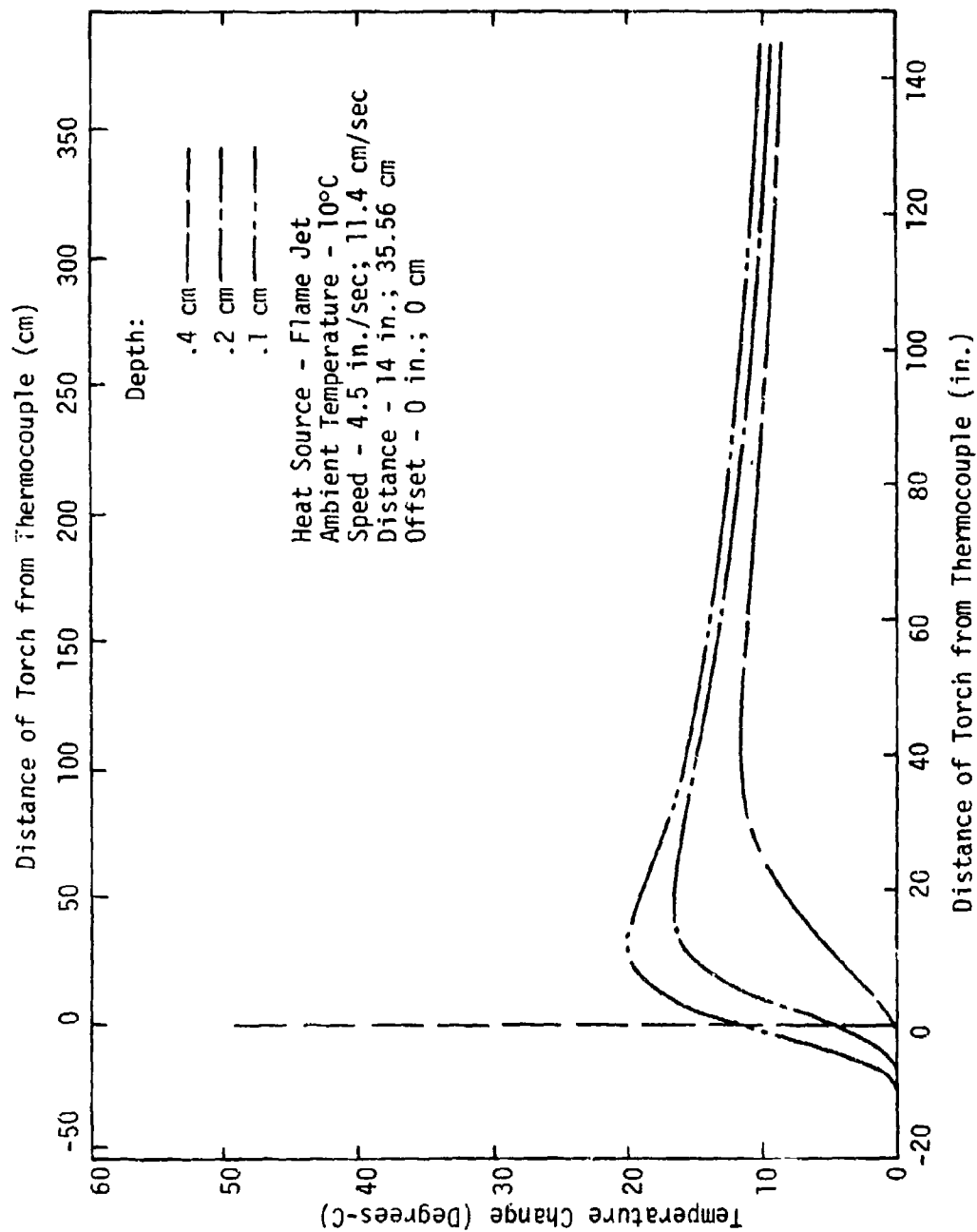
Fig. B-24.   Subsurface Temperature Measurements - Buena Gabbro
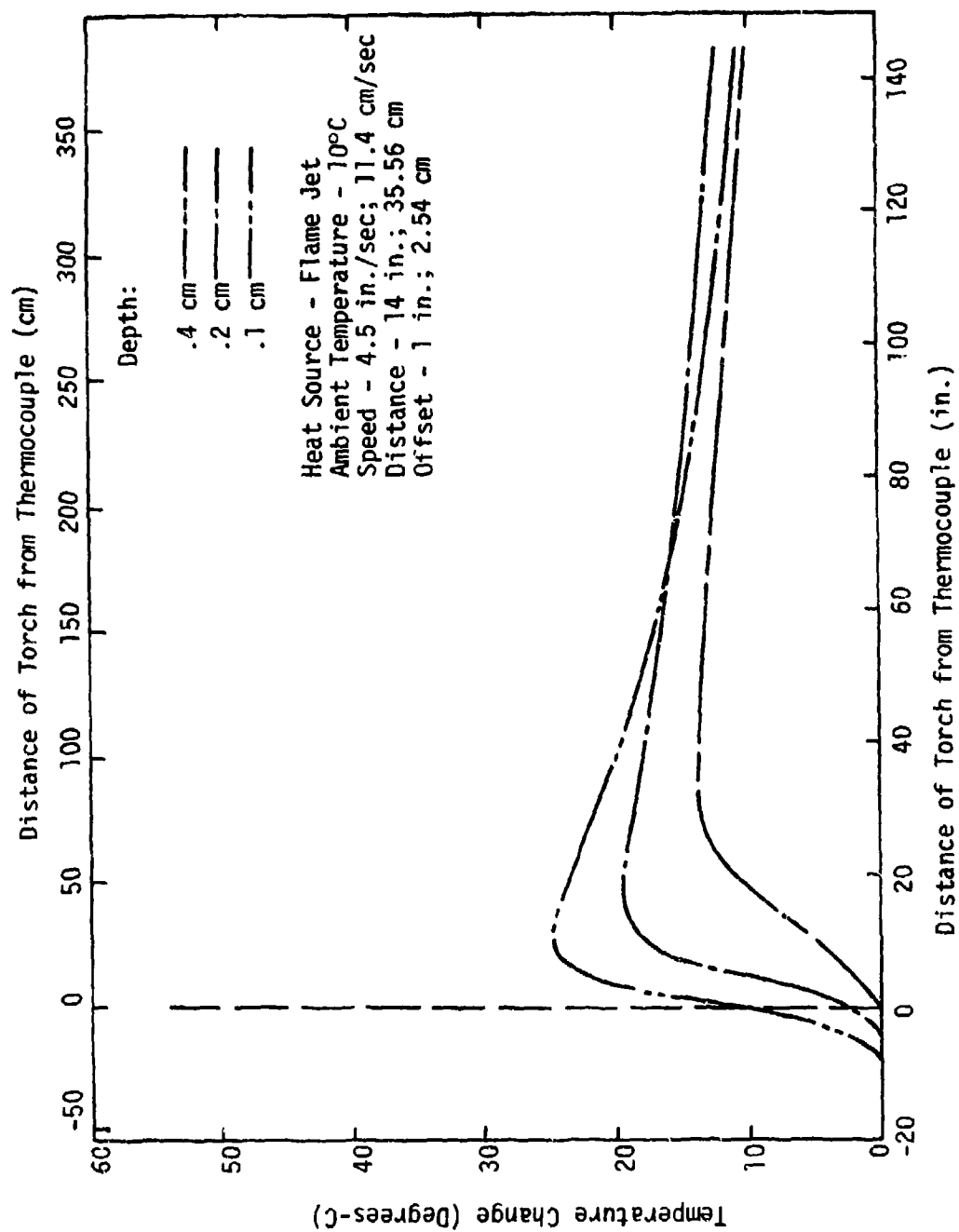
Fig. B-25. Subsurface Temperature Measurements – Buena Gabbro
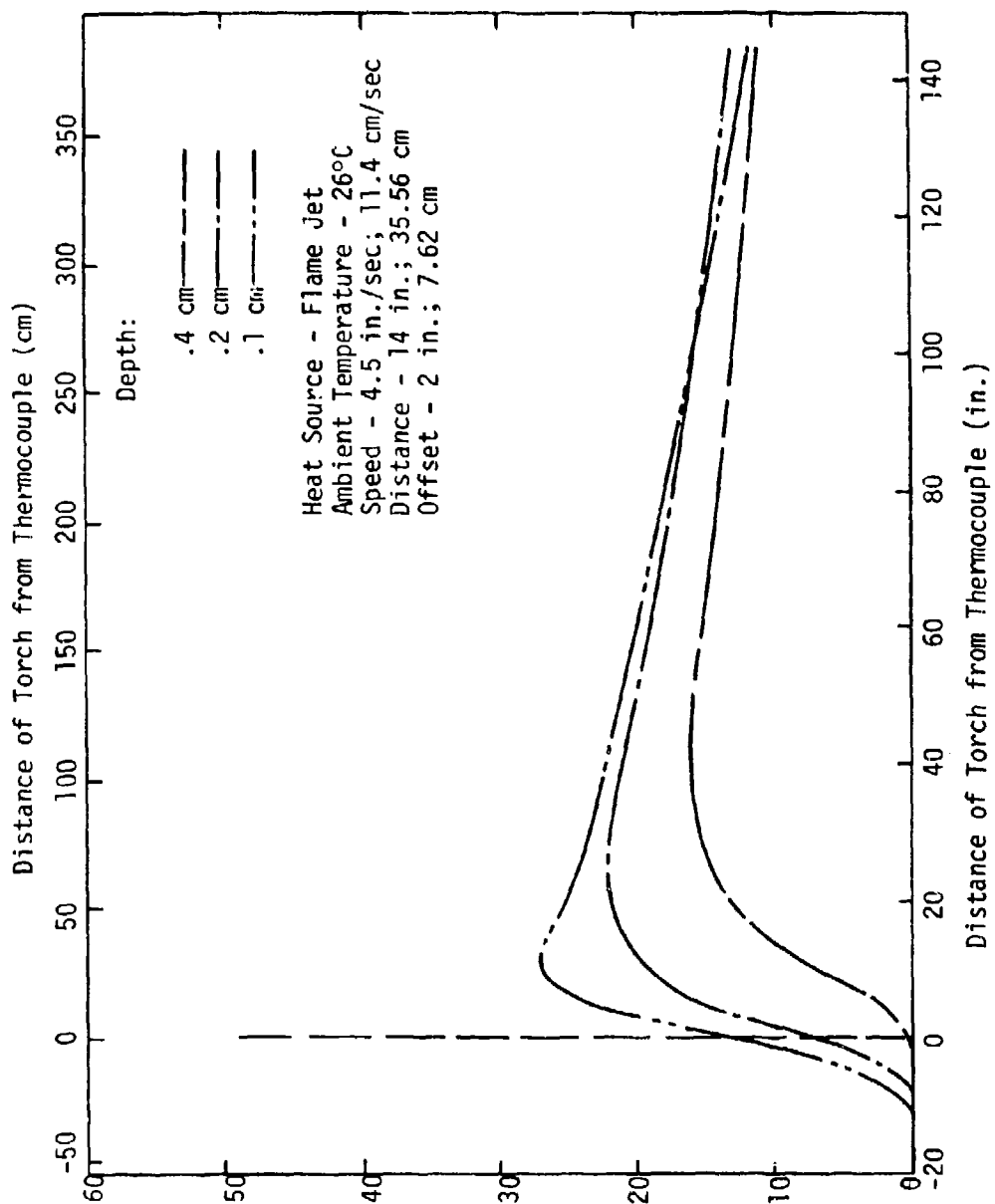
Fig. B-26. Subsurface Temperature Measurements - Buena Gabbro
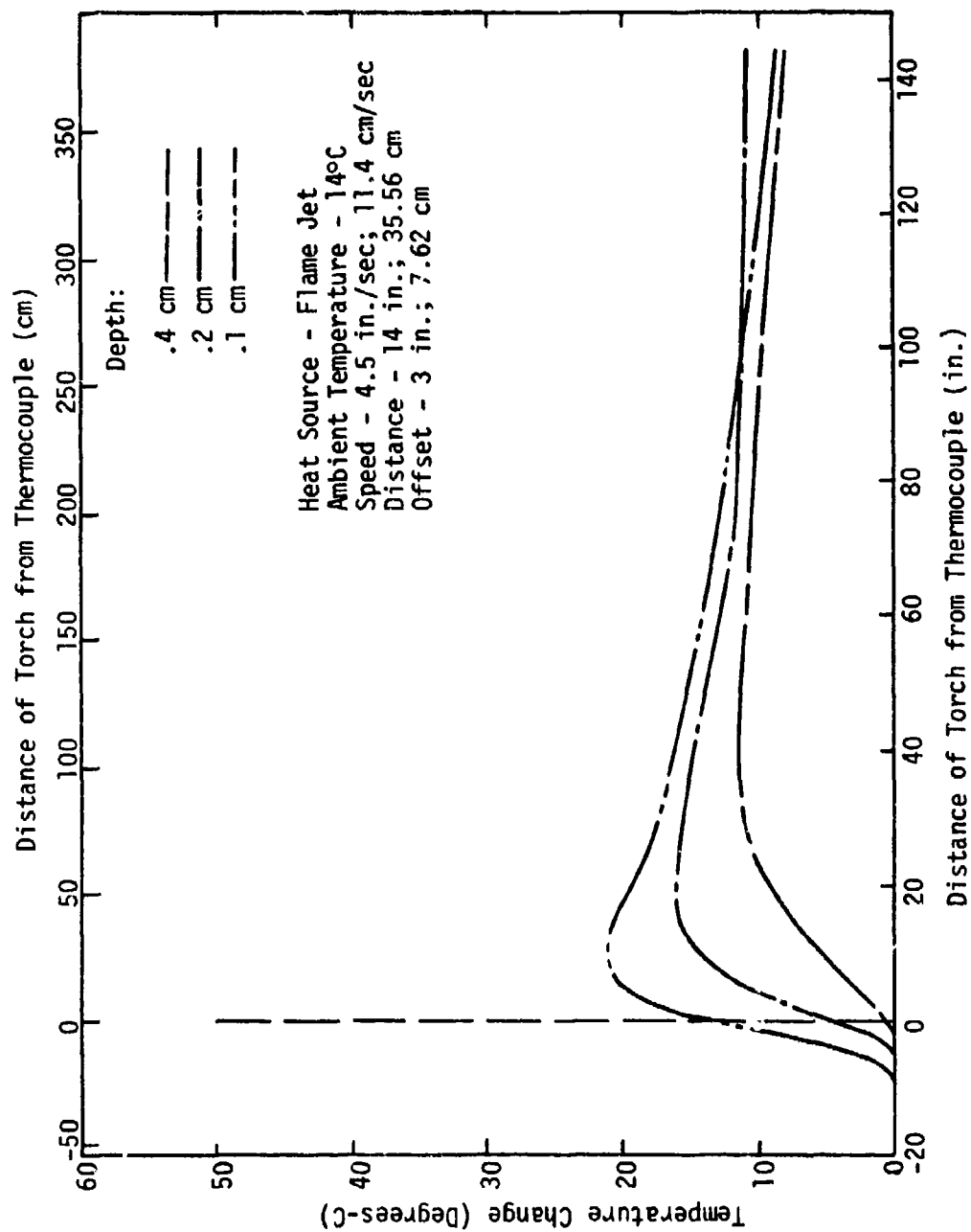
Fig. B-27. Subsurface Temperature Measurements - Buena Gabbro

APPENDIX C

NOWACKI'S SOLUTION FOR HALF-SPACE

APPENDIX C

Nowacki's Solution for Half-Space

Suppose that on the plane $\xi_3 = 0$ which bounds the elastic semi-space, a concentrated heat source of unit intensity is moving in the origin of the coordinate system ξ_r, in the direction of the ξ_1 axis. It is assumed that the plane $\xi_3 = 0$ is thermally insulated and free of traction.

The heat conduction equation for this case is

$$\nabla^2 + 2\sigma \frac{\partial}{\partial \xi_1} \, T(\xi_r) = -\frac{Q^*(\xi_r)}{\kappa} \tag{C-1}$$

where

$$\sigma = \frac{v}{2\kappa} \, ,$$

$$\kappa = \frac{k}{\rho c} \, , \text{ the diffusivity, and}$$

$$Q^*(\xi_r) = \delta(\xi_1)\delta(\xi_2)\delta(\xi_3)$$

The solution of equation (C-1) for this problem is known

$$T(\xi_r) = \frac{1}{4\pi\kappa R} \, e^{-\sigma(\xi_1 + R)}$$

$$\tag{C-2}$$

$$R = (\xi_1^2 + \xi_2^2 + \xi_3^2)^{\frac{1}{2}}$$

Solution to the stress problem is obtained in the form of a sum of two solutions, $\bar{s}$ and $\bar{\bar{s}}$. The solution $\bar{s}$ is that for the action of a moving heat source in the infinite space and is given by

$$\bar{\sigma}_{11} = -K \frac{1}{\sigma R(\xi_1+R)} \left\{ e^{-\sigma(\xi_1+R)} \left[2 - \frac{r^2}{R^2}\left(1 + \sigma R + \frac{R}{\xi_1+R} \right) \right] - \right.$$

$$\left. - \left[2 - \frac{r^2}{R^2}\left(1 + \frac{R}{\xi_1+R} \right) \right] \right\}$$

$$\bar{\sigma}_{22} = -K \frac{1}{\sigma R(\xi_1+R)} \left\{ e^{-\sigma(\xi_1+R)} \left[1 - \frac{\xi_3^2}{R^2}\left(1 + \sigma R + \frac{R}{\xi_1+R} \right) - \right. \right.$$

$$\left. - \frac{\xi_1+R}{R}\left(\frac{\xi_1}{R} + \sigma(\xi_1+R) \right) \right] - \left[1 - \frac{\xi_3^2}{R^2}\left(1 + \frac{R}{\xi_1+R} \right) - \right.$$

$$\left. \left. - \frac{\xi_1(\xi_1+R)}{R^2} \right] \right\}$$

$$\bar{\sigma}_{33} = -K \frac{1}{\sigma R(\xi_1+R)} \left\{ e^{-\sigma(\xi_1+R)} \left[1 - \frac{\xi_2^2}{R^2}\left(1 + \sigma R + \frac{R}{\xi_1+R} \right) - \right. \right. \qquad \text{(C-3)}$$

$$\left. - \frac{\xi_1+R}{R}\left(\frac{\xi_1}{R} + \sigma(\xi_1+R) \right) \right] - \left[1 - \frac{\xi_2^2}{R^2}\left(1 + \frac{R}{\xi_1+R} \right) - \right.$$

$$\left. \left. - \frac{\xi_1(\xi_1+R)}{R^2} \right] \right\}$$

$$\bar{\sigma}_{13} = K \frac{\xi_3}{\sigma R^3} \left[(1+\sigma R)e^{-\sigma(\xi_1+R)} - 1 \right]$$

$$\bar{\sigma}_{12} = K \frac{\xi_2}{\sigma R^3} \left[(1+\sigma R)e^{-\sigma(\xi_1+R)} - 1 \right]$$

$$\bar{\sigma}_{23} = K \frac{\xi_2 \xi_3}{\sigma R^3(\xi_1+R)} \left[\left(1 + \sigma R + \frac{R}{\xi_1+R} \right)e^{-\sigma(\xi_1+R)} - \right.$$

$$\left. - \left(1 + \frac{R}{\xi_1+R} \right) \right]$$

Here

σ_{ij} is the stress tensor

$r = (\xi_2^2 + \xi_3^2)^{\frac{1}{2}}$

$K = \dfrac{\mu m}{4\pi\kappa}$

$\mu = G$, the shear modulus

$m = \dfrac{1+\nu}{1-\nu}\,\alpha$

ν = Poisson's ratio

α = coefficient of thermal expansion

Note that on the plane $\xi_3 = 0$, $\dfrac{\partial T}{\partial \xi_3} = 0$, $\bar{\sigma}_{13} = \bar{\sigma}_{23} = 0$. The only non-zero component of the stress tensor on this plane is $\bar{\sigma}_{33}(\xi_1, \xi_2, 0)$ $= -p(\xi_1, \xi_2)$. The solution $\bar{\bar{s}}$ is that for the elastic semi-space $\xi_3 > 0$ in which $T = 0$, the only loading being the normal traction $\bar{\sigma}_{33} = -p(\xi_1, \xi_2)$ on the plane $\xi_3 = 0$. Hence, the stresses $\bar{\bar{\sigma}}_{ij}$ are obtained from the integral expression

$$\bar{\bar{\sigma}}_{ij}(\xi_1, \xi_2, \xi_3) = \int\limits_{-\infty}^{\infty} \int\limits_{-\infty}^{\infty} p(\eta_1, \eta_2) \sum_{ij} (\xi_1, \xi_2, \xi_3; \eta_1, \eta_2, 0)\, d\eta_1 d\eta_2 \quad (C\text{-}4)$$

In this expression, $\sum_{ij}(\xi_1, \xi_2, \xi_3; \eta_1, \eta_2, 0)$ denote the stresses at the point (ξ_r) due to the action of a concentrated unit force situated at the point $(\eta_1, \eta_2, 0)$ on the plane bounding the semi-space, and are given by

$$\sum_{11} = -\frac{3}{2\pi R^3} \left[\frac{\xi_3(\xi_1-\eta_1)^2}{R^2} - \frac{1-2v}{3} \left(\frac{R^2+R\xi_3-\xi_3^2}{R-\xi_3} \right. \right.$$

$$\left. \left. - \frac{(\xi_1-\eta_1)^2(2R-\xi_3)}{(R-\xi_3)^2} \right) \right]$$

$$\sum_{22} = -\frac{3}{2\pi R^3} \left[\frac{\xi_3(\xi_2-\eta_2)^2}{R^2} - \frac{1-2v}{3} \left(\frac{R^2+R\xi_3-\xi_3^2}{R-\xi_3} \right. \right.$$

$$\left. \left. - \frac{(\xi_2-\eta_2)^2(2R-\xi_3)}{(R-\xi_3)^2} \right) \right]$$

$$\sum_{33} = -\frac{3\xi_3^3}{2\pi R^5} \tag{C-5}$$

$$\sum_{12} = -\frac{3}{2\pi R^3} (\xi_1-\eta_1)(\xi_2-\eta_2) \left(\frac{\xi_3}{R^2} + \frac{1-2v}{3} \frac{2R-\xi_3}{(R-\xi_3)^2} \right)$$

$$\sum_{13} = -\frac{3}{2\pi R^5} \xi_3^2(\xi_1-\eta_1)$$

$$\sum_{23} = -\frac{3}{2\pi R^5} \xi_3^2(\xi_2-\eta_2)$$

$$R = [(\xi_1-\eta_1)^2 + (\xi_2-\eta_2)^2 + \xi_3^2]^{\frac{1}{2}}$$

The stresses in the semi-space due to the action of a source moving
on the bounding plane $\xi_3 = 0$ are obtained by adding the stresses given
by equation (C-3) and (C-4) as

$$\sigma_{ij} = \bar{\sigma}_{ij} + \bar{\bar{\sigma}}_{ij}$$

C-4

APPENDIX D

STRESS AND FORCE SOLUTIONS FOR FOUR INDENTORS

APPENDIX D

STRESS AND FORCE SOLUTIONS FOR FOUR INDENTORS

I. Indentor No. 1

A. Smooth Surface (Fig. III-4(A))

1. Maximum shear theory: $0 < \beta < \frac{\pi}{2}$, $\eta = \frac{\pi}{4}$

$$\sigma_n = 2K(1+\psi)$$

$$\tau_n = 0$$

$$F = 2AB\sigma_n \sin\beta \quad \text{(force/unit length)}$$

2. Internal friction theory

$$\sigma_n = \frac{2K(1+\sin\phi)^2}{\cos\phi} \exp(2\psi\tan\phi) - K\cot\phi$$

$$\tau_n = 0$$

$$F = 2AB\sigma_n \sin\beta$$

B. Rough Surface (Fig. III-4(B))

1. Maximum shear theory: $0 < \beta < \frac{\pi}{2}$, $\eta = 0$

$$\sigma_n = K(1+2\psi)$$

$$\tau_n = K$$

$$F = 2AB(\sigma_n \sin\Theta + \tau_n \sin\Theta)$$

where $\Theta = \beta$, if $\beta \leq \frac{\pi}{4}$

$\frac{\pi}{4}$, if $\beta > \frac{\pi}{4}$

AB = Edge of Indentor, if $\beta \leq \frac{\pi}{4}$

Edge of False Nose, if $\beta > \frac{\pi}{4}$

2. Internal friction theory: $0 < \beta < \frac{\pi}{2}$, $\eta = 0$

$$\sigma_n = K\cos\phi[(1+\sin\phi)\exp(2\psi\tan\phi)-1]$$

$$\tau_n = K(1+\sin\phi)\exp(2\psi\tan\phi)$$

$$F = 2AB(\sigma_n \sin\Theta + \tau_n \cos\Theta)$$

where $\theta = \beta$, if $\beta \leq \dfrac{\pi}{4} - \dfrac{\phi}{2}$

$\dfrac{\pi}{4} - \dfrac{\phi}{2}$, if $\beta \geq \dfrac{\pi}{4} - \dfrac{\phi}{2}$

AB = Edge of Indentor, if $\beta \leq \dfrac{\pi}{4} - \dfrac{\phi}{2}$

Edge of False Nose, if $\beta > \dfrac{\pi}{4} - \dfrac{\phi}{2}$

C. Frictional Surface (Fig. III-4(A))

1. Maximum shear theory: $0 < \beta \leq \dfrac{\pi}{4}$, $0 \leq \eta \leq \dfrac{\pi}{4}$.

$\sigma_n = K(1+2\psi+\sin 2\eta)$

$\tau_n = K\cos 2\eta$

$F = 2AB(\sigma_n \sin\beta + \tau_n \cos\beta)$

2. Internal friction theory: $0 < \beta \leq \dfrac{\pi}{4} - \dfrac{\phi}{2}$, $0 \leq \eta \leq \dfrac{\pi}{4} + \dfrac{\phi}{2}$

$\sigma_n = \dfrac{K(1+\sin\phi)}{s\phi}[\dfrac{1}{\sin\phi} - \sin(\phi-2\eta)]\exp(2\psi\tan\phi) - K\cot\phi$

$\tau_n = \dfrac{K(1+\sin\phi)}{\cos\phi}\cos(\phi-2\eta)\exp(2\psi\tan\phi)$

$F = 2AB(\sigma_n \sin\beta + \tau_n \cos\beta)$

II. Indentor No. 2

The stress and force equations for indentor No. 1 can be used for this indentor with the following modifications.

A. Smooth Surface (Fig. III-4(C))

1. Along BC - the same as I-A, except $\psi = \psi_1$, and AB=BC.

2. Along AB - the same as I-B, except $\psi = \psi_1 + \psi_2$.

B. Rough Surface

1. $\beta < \dfrac{\pi}{4} - \dfrac{\phi}{2}$ (Fig. III-4(C)) (Note: for maximum shear theory $\phi=0$.)

(a) Along BC - the same as I-B, except $\psi = \psi_1$, and AB=BC.

(b) Along AB - the same as I-B, except $\psi = \psi_1 + \psi_2$.

2. $\beta \geq \dfrac{\pi}{4} - \dfrac{\phi}{2}$ (Fig. III-4(D))

The same as I-B

C. Frictional Surface (Fig. III-4(C): $\beta \leq \frac{\pi}{4} - \frac{\phi}{2}$)

    1. Along BC - the same as I-C, except $\psi = \psi_1$ and $AB = \delta C$.

    2. Along AB - the same as I-B, except $\psi = \psi_1 + \psi_2$.

III. Indentor No. 3 $(r = 1)$

    A. Smooth Surface (Fig. III-5(A), AB=0)

        1. Maximum shear theory: $0 < \alpha < \pi/2$, $n = \frac{\pi}{4}$.

$$\sigma_n = 2K(1+\psi+\Theta) \quad \text{where } 0 \leq \Theta \leq \alpha$$

$$\tau_n = 0$$

$$F = 4 \int_0^\alpha \sigma_n \cos(\alpha-\Theta)d\Theta$$

        2. Internal friction theory: $0 < \alpha < \frac{\pi}{2}$, $n = \frac{\pi}{4} + \frac{\phi}{2}$

$$\sigma_n = \frac{(1+\sin\phi)^2}{\sin 2\phi} \exp[2(\psi+\Theta)\tan\phi] - K\cot\phi, \text{ where } 0 \leq \Theta \leq \alpha$$

$$\tau_n = 0$$

$$F = 4 \int_0^\alpha \sigma_n \cos(\alpha-\Theta)d\Theta$$

    B. Rough Surface (Fig. III-5(B)

        1. Maximum shear theory: $0 < \alpha < \frac{\pi}{2}$, $n = 0$.

           (a) Along BC $(\alpha \geq \frac{\pi}{4})$

$$\sigma_n = K[1+2(\psi+\Theta)], \text{ where } 0 \leq \Theta \leq \alpha - \frac{\pi}{4}$$

$$\tau_n = K$$

$$F = 2 \int_0^{\alpha-\frac{\pi}{4}} [\sigma_n \cos(\alpha-\Theta)+\tau_n \sin(\alpha-\Theta)]d\Theta$$

           (b) Along AB

$$\sigma_n = K[1+2(\psi+\Theta)] \text{ , where } \Theta = \begin{cases} \alpha - \frac{\pi}{4} \text{ , if } \alpha > \frac{\pi}{4} \\ 0 \text{ , if } \alpha \leq \frac{\pi}{4} \end{cases}$$

$$\tau_n = K$$

$$F = \sqrt{2} \, AB(\sigma_n + \tau_n)$$

        2. Internal friction theory: $0 < \alpha < \frac{\pi}{2}$, $n = 0$.

(a) Along BC $(\alpha \geq \frac{\pi}{4} + \frac{\phi}{2})$

$$\sigma_n = K \cot\phi\{(1+\sin\phi)\exp[2(\psi+\Theta)\tan]-1\}$$

$$\tau_n = K(1+\sin\phi)\exp[2(\psi+\Theta)\tan\phi]$$

where $0 \leq \Theta \leq \alpha \quad \frac{\pi}{4} - \frac{\phi}{2}$

$$F = 2 \int_0^{\alpha - \frac{\pi}{4} - \frac{\phi}{2}} [\sigma_n \cos(\alpha-\Theta)+\tau_n \sin(\alpha-\Theta)]d\Theta$$

(b) Along **AB**

$$\sigma_n = K\cot\phi\{(1+\sin\phi)\exp[2(\psi+\Theta)\tan\phi]-1\}$$

$$\tau_n = K(1+\sin\phi)\exp[2(\psi+\Theta)\tan\phi]$$

where $\Theta = \int_0^{\alpha - \frac{\pi}{4} - \frac{\phi}{2}}$, if $\alpha \geq \frac{\pi}{4} + \frac{\phi}{2}$

 , if $\alpha \leq \frac{\pi}{4} + \frac{\phi}{2}$

$$F = 2AB \left[\sigma_n \sin(\frac{\pi}{4} - \frac{\phi}{2}) + \tau_n \cos(\frac{\pi}{4} - \frac{\phi}{2})\right]$$

C. Frictional Surface (Fig. III-5(A))

1. Maximum shear theory: $0 < \alpha < \frac{\pi}{2}$, $0 \leq \eta \leq \frac{\pi}{4}$.

   (a) Along BC

   $$\sigma_n = K[1+2(\psi+\Theta)1+\sin 2\eta], \text{ where } 0 \leq \Theta \leq \alpha + \eta - \frac{\pi}{4}$$

   $$\tau_n = K\cos 2\eta$$

   $$F = 2 \int_0^{\alpha+\eta-\frac{\pi}{4}} [\sigma_n\cos(\alpha-\Theta)+\tau_n\sin(\alpha-\Theta)]d\Theta$$

   (b) Along AB

   $$\sigma_n = K\cot\phi\{(1+\sin\phi)\exp[2(\psi+\Theta)\tan\phi]-1\}$$

   $$\tau_n = K(1+\sin\phi)\exp[2(\psi+\Theta)\tan\phi]$$

where $\Theta = \begin{cases} \alpha+\eta-\frac{\pi}{4}, & \text{if } \alpha \geq \frac{\pi}{4}-\eta \\ 0, & \text{if } \alpha < \frac{\pi}{4}-\eta \end{cases}$

$$F = \sqrt{2}\ AB\ (\sigma_n+\tau_n)$$

2. Internal friction theory: $0 < \alpha < \frac{\pi}{2}$, $0 \leq \eta \leq \frac{\pi}{4}+\frac{\phi}{2}$.

(a) Along BC

$$\sigma_n = \frac{K(1+\sin\phi)}{\cos\phi}\left[\frac{1}{\sin\phi} - \sin(\phi-2\eta)\right]\exp[2(\psi+\Theta)\tan\psi]-K\cot\psi$$

$$\tau_n = \frac{K(1+\sin\phi)}{\cos\phi}\cos(\phi-2\eta)\exp[2(\psi+\Theta)\tan\phi]$$

where $0 \leq \Theta \leq \alpha+\eta - \frac{\pi}{4} - \frac{\phi}{2}$.

$$F = 2\int_{0}^{\alpha+\eta-\frac{\pi}{4}-\frac{\phi}{2}}[\sigma_n\cos(\alpha-\Theta)+\tau_n\sin(\alpha-\Theta)]d\Theta$$

(b) Along AB

$$\sigma_n = K\cot\{(1+\sin\phi)\exp[2(\psi+\Theta)\tan\phi]-1\}$$

$$\tau_n = K(1+\sin\phi)\exp[2(\psi+\Theta)\tan\phi]$$

where $\Theta = \begin{cases} \alpha+\eta-\frac{\pi}{4}-\frac{\phi}{2}, & \text{if } \alpha \geq \frac{\pi}{4}+\frac{\phi}{2}-\eta \\ 0, & \text{if } \alpha < \frac{\pi}{4}+\frac{\phi}{2}-\eta \end{cases}$

$$F = 2AB[\sigma_n\sin(\frac{\pi}{4}-\frac{\phi}{2}) + \tau_n\cos(\frac{\pi}{4}-\frac{\phi}{2})]$$

IV. Indentor No. 4

The stress and the force equations for indentors no. 1 and no. 3 can be used for this indentor with the following modifications:

A. Smooth Surface (Fig. III-5(C), AB=0)

1. Along CD - the same as I-A, except AB=CD.

2. Along ABC - the same as III-A, except $\beta = \frac{\pi}{2} - \alpha$

B. Rough Surface

    1. $\beta \leq \frac{\pi}{4} - \frac{\phi}{2}$ (Fig. III-5(D))

        (a) Along CD - the same as I-B, except AB=CD.

        (b) Along ABC - the same as III-B, except $\beta = \frac{\pi}{2} - \alpha$.

    2. $\beta > \frac{\pi}{4} - \frac{\phi}{2}$ (Fig. III-5(C), $\eta = 0$)

        The same as I-B, except AB=AD (AD is the edge of the false nose,

                                   not shown in Fig. III-5(C)).

C. Frictional Surface (Fig. III-5(C), $\beta \leq \frac{\pi}{4} - \frac{\phi}{2}$)

    1. Along CD - the same as I-C, except AB=CD.

    2. Along ABC - the same as III-C, except $\beta = \frac{\pi}{2} - \alpha$

APPENDIX E

PARTICLE SIZE ANALYSIS

DROP CRUSHING TESTS

Fig. E-1. Particle Size Analysis – Drop Crushing – Missouri Red Granite

Test No.: 1
Rock: Missouri Red Granite
Drops: 1-5 ft
Weight: 171 lb.
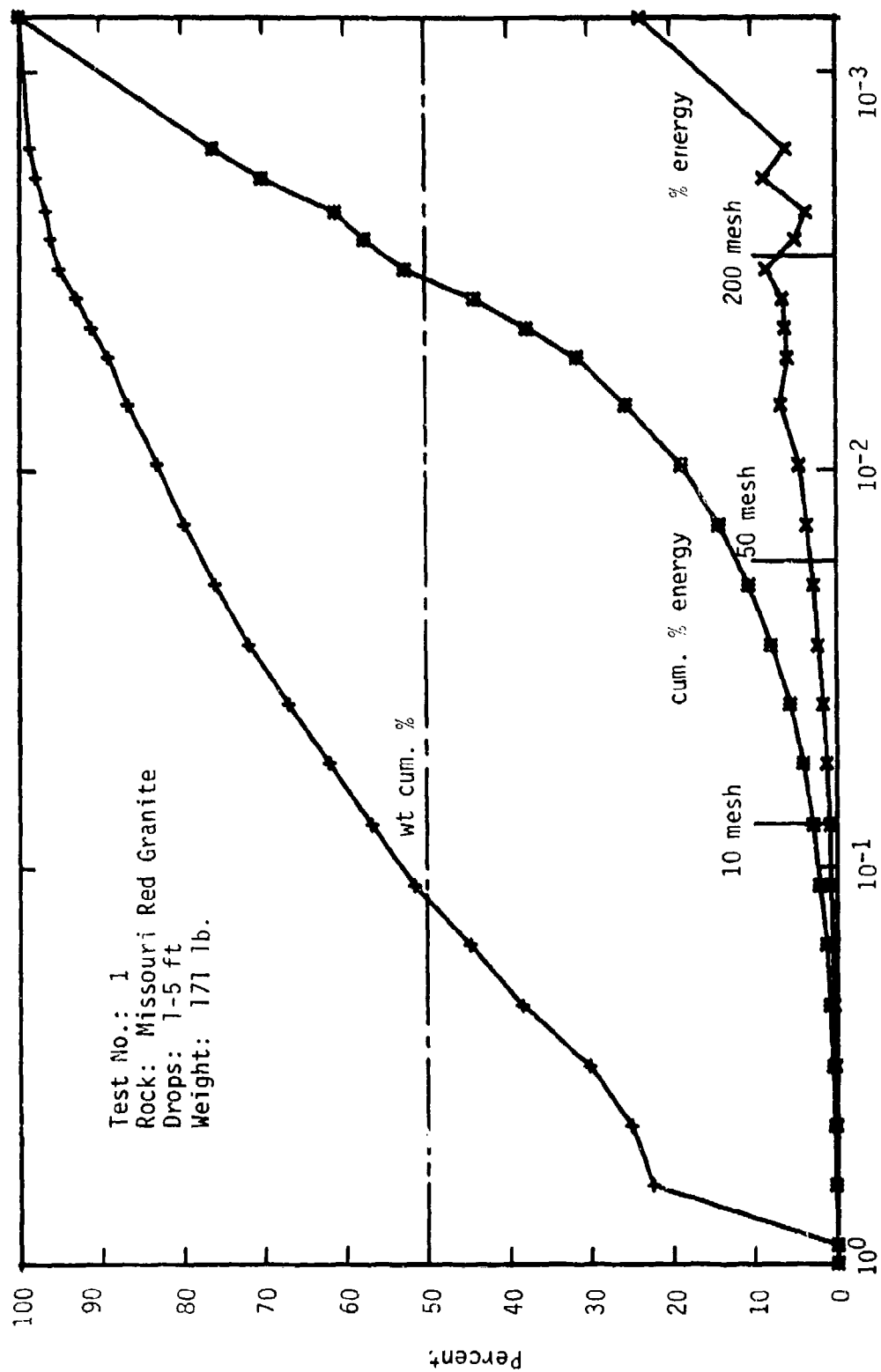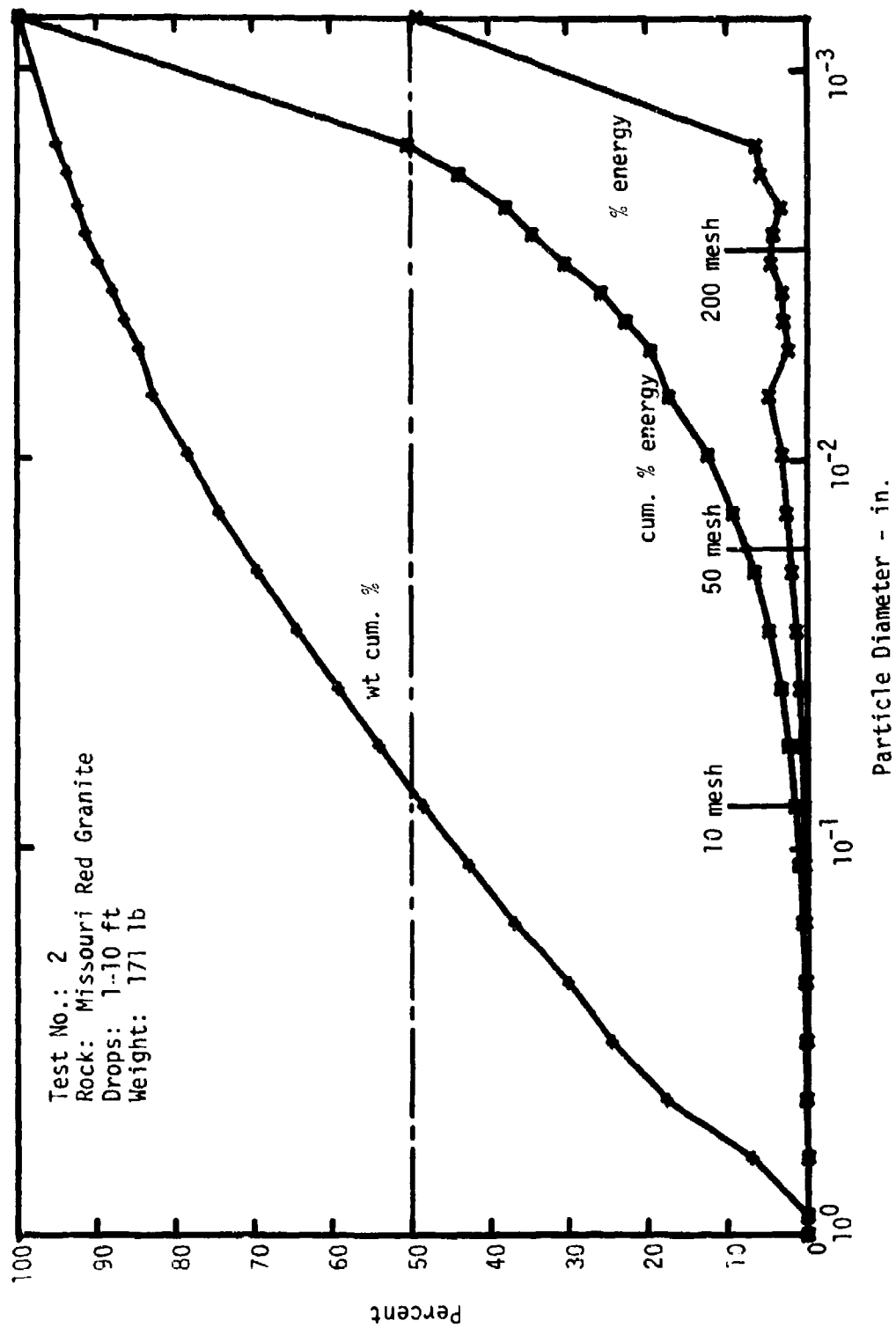
Fig. E-2. Particle Size Analysis – Drop Crushing – Missouri Red Granite

Fig. E-3. Particle Size Analysis - Drop Crushing - Missouri Red Granite

Test No.: 3
Rock: Missouri Red Granite
Drops: 2-1 ft
Weight: 171 lb

wt cum. %

cum. % energy

% energy

10 mesh

50 mesh

200 mesh

Particle Diameter - in.

Percent

Fig. E-4. Particle Size Analysis – Drop Crushing – Missouri Red Granite

Test No.: 4
Rock: Missouri Red Granite
Drops: 2-3 ft
Weight: 171 lb

Particle Diameter – in.

Percent

wt cum. %

cum. % energy

% energy

10 mesh

50 mesh

200 mesh

E-4

Fig. E-5. Particle Size Analysis – Drop Crushing – Missouri Red Granite

Fig. E-6. Particle Size Analysis – Drop Crushing – Missouri Red Granite

Fig. E-7. Particle Size Analysis - Drop Crushing - Missouri Red Granite

Test No.: 7
Rock: Missouri Red Granite
Drops: 1-4 ft
Weight: 171 lb.

E-7
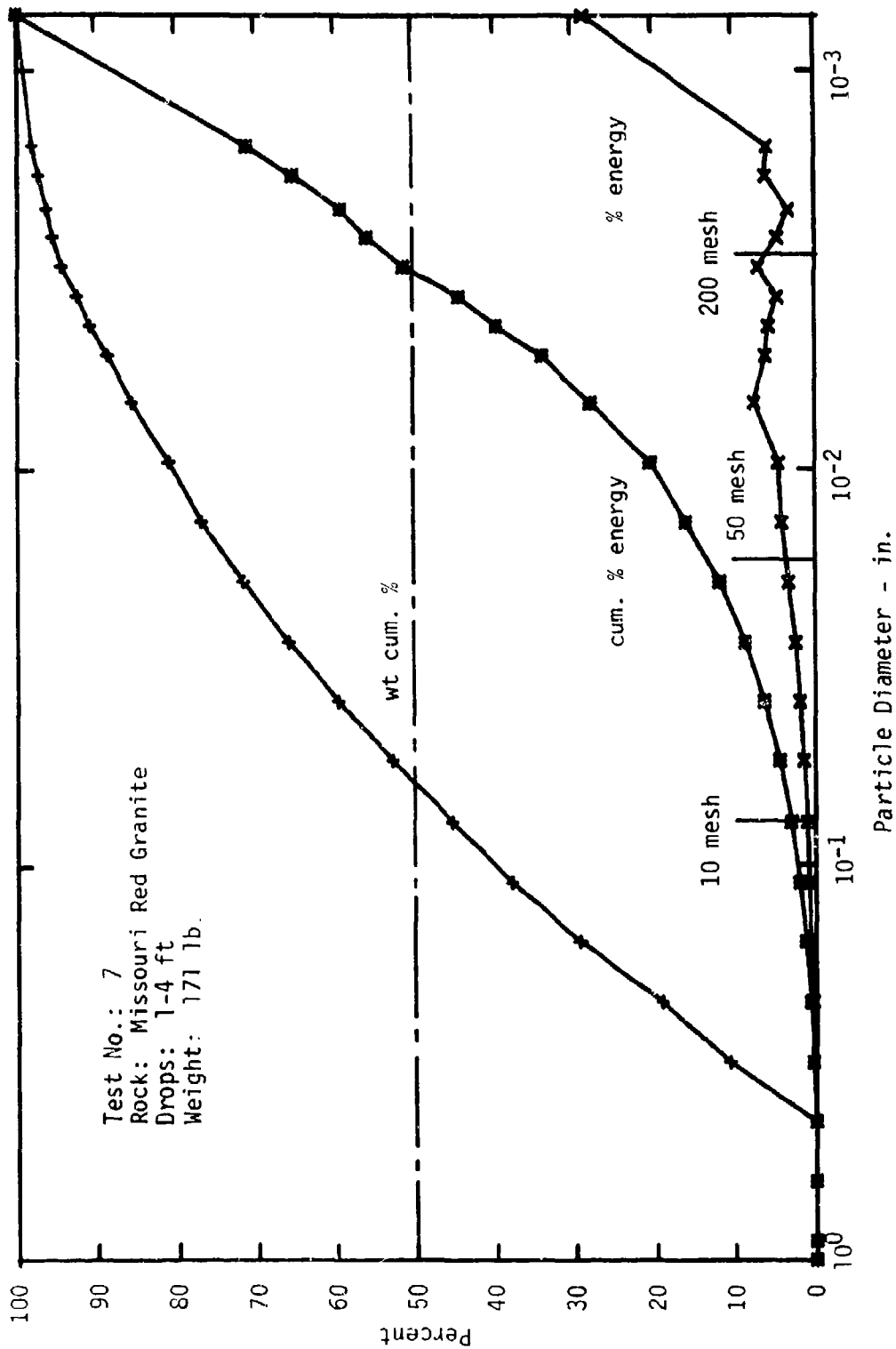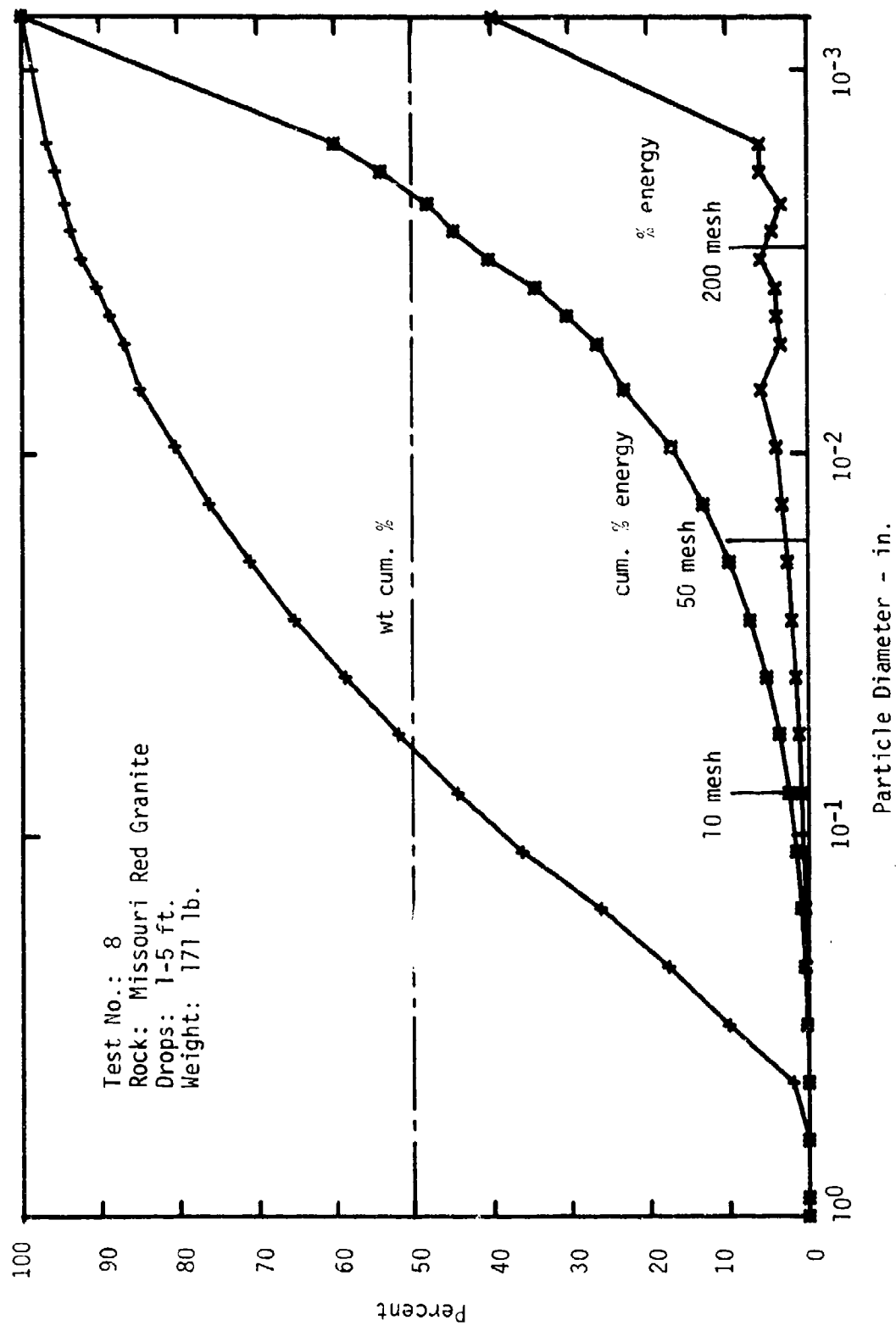
Fig. E-8. Particle Size Analysis – Drop Crushing – Missouri Red Granite

E-8

Fig. E-9. Particle Size Analysis - Drop Crushing - Missouri Red Granite

Particle Diameter - in.

Percent

Test No.: 9
Rock: Missouri Red Granite
Drops: 1-10 ft
Weight: 171 lb.

wt cum. %

cum. % energy

% energy

10 mesh

50 mesh

200 mesh
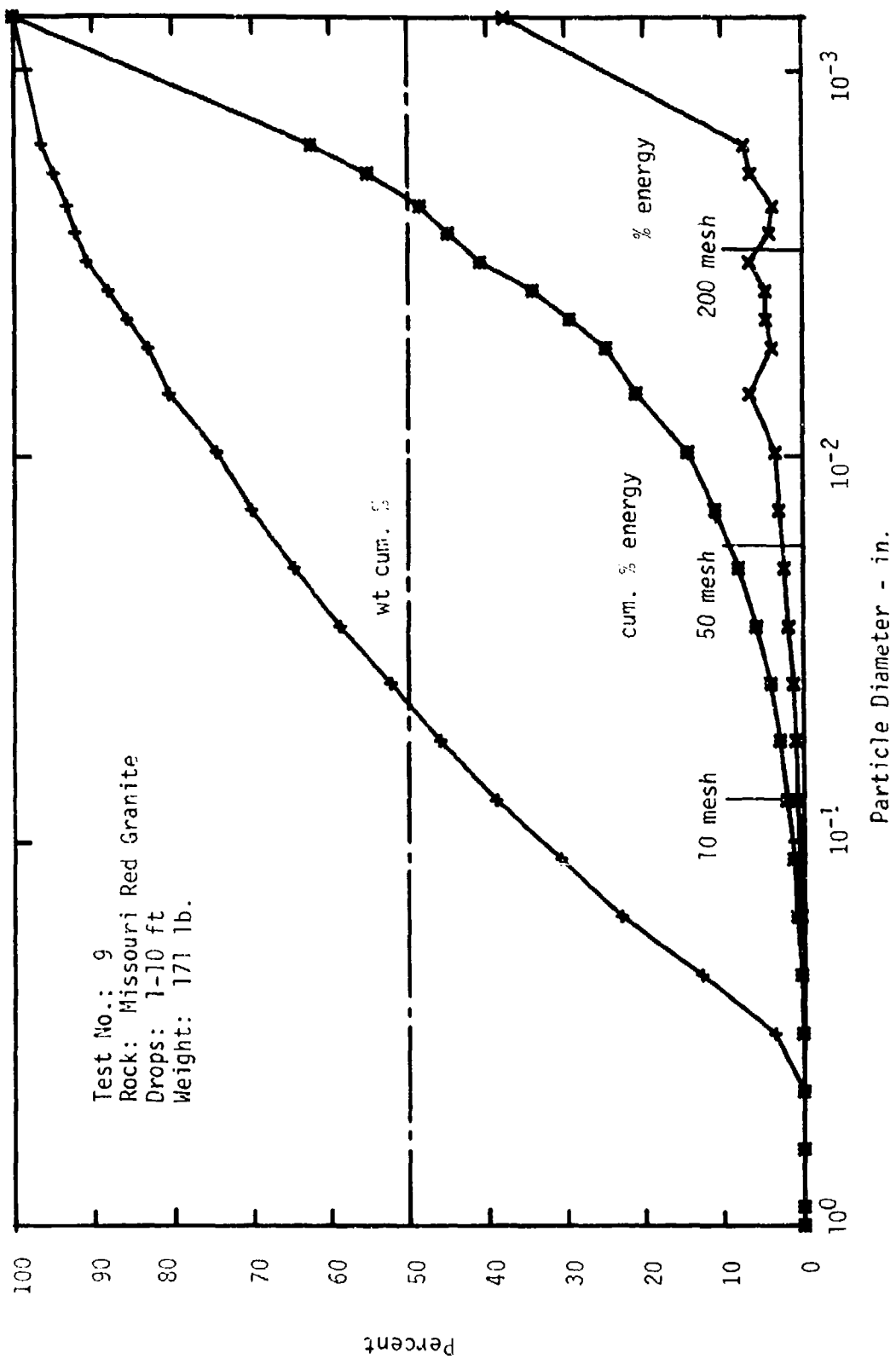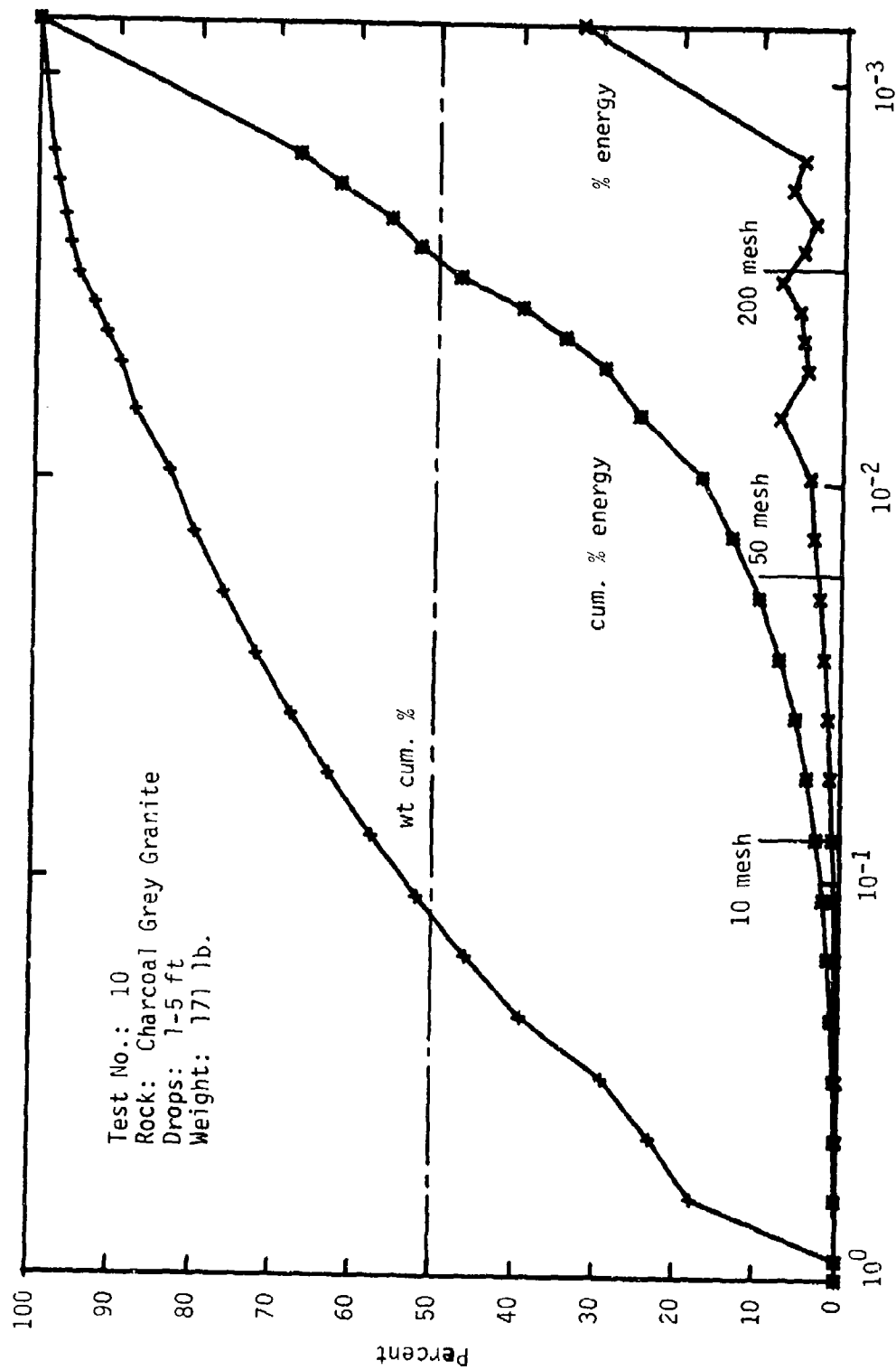
Fig. E-10. Particle Size Analysis – Drop Crushing – Charcoal Grey Granite

E-10

Fig. E-11. Particle Size Analysis - Drop Crushing - Charcoal Grey Granite
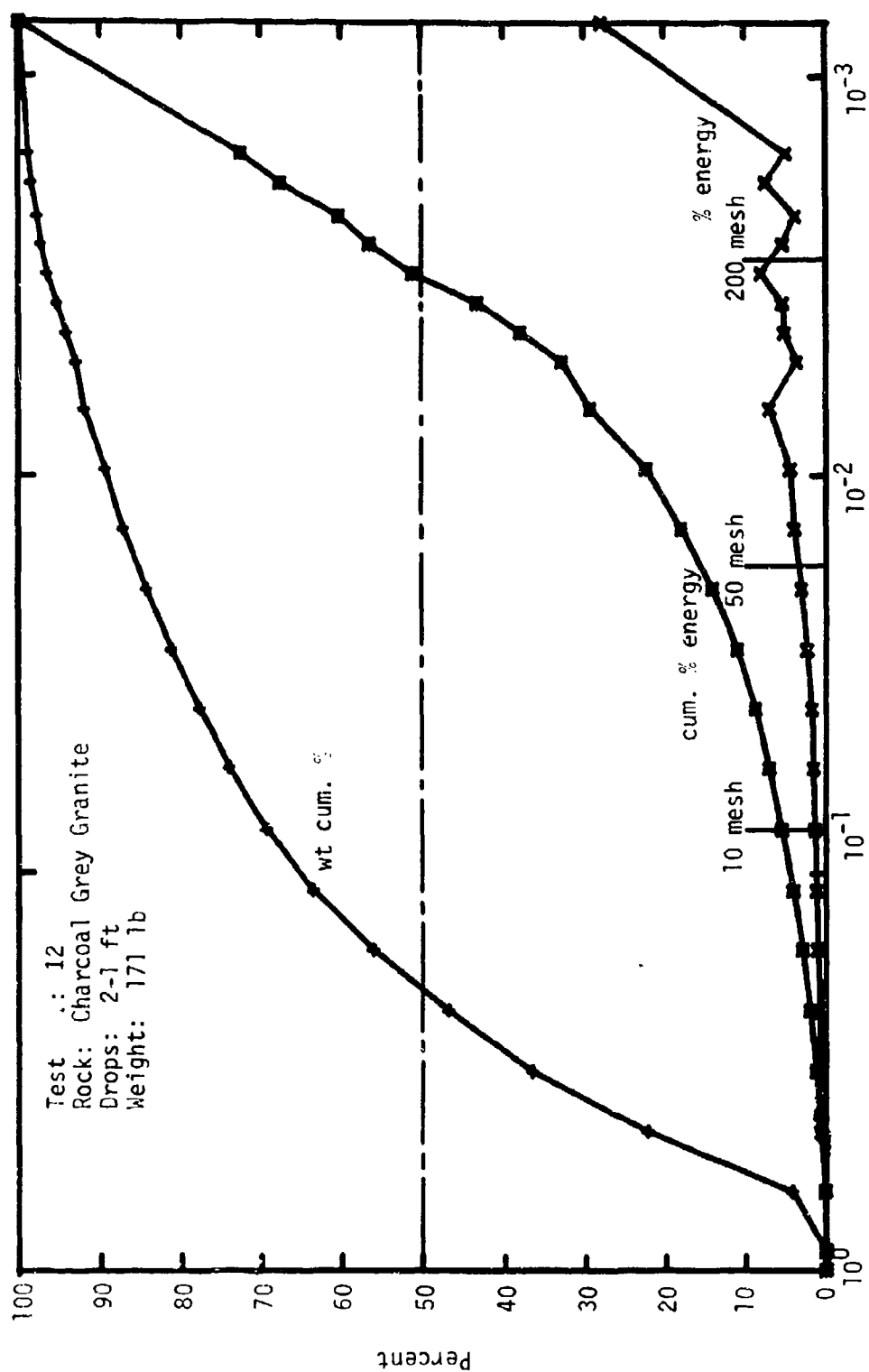
Test No.: 11
Rock: Charcoal Grey Granite
Drops: 1-10 ft
Weight: 171 lb

Fig. E-12 Particle Size Analysis - Drop Crushing - Charcoal Grey Granite

Test   .: 12
Rock: Charcoal Grey Granite
Drops: 2-1 ft
Weight: 171 lb

Fig. E-13. Particle Size Analysis – Drop Crushing – Charcoal Grey Granite

Test No.: 13
Rock: Charcoal Grey Granite
Drops: 1-2 ft
Weight: 171 lb

Fig. E-14. Particle Size Analysis – Drop Crushing – Charcoal Grey Granite

Test No.: 14
Rock: Charcoal Grey Granite
Drops: 1-4 ft.
Weight: 171 lb.

Fig. E-15. Particle Size Analysis - Drop Crushing - Charcoal Grey Granite

Test No.: 15
Rock: Charcoal Grey Granite
Drops: 1-5 ft.
Weight: 171 lb.

Fig. E-16. Particle Size Analysis - Drop Crushing - Charcoal Grey Granite

Test No.: 16
Rock: Charcoal Grey Granite
Drops: 1-10 ft
Weight: 171 lb

Particle Diameter - in.

Percent

Fig. E-17. Particle Size Analysis - Drop Crushing - Kitledge Pink Granite

Test No.: 17
Rock: Kitledge Pink Granite
Drops: 1-5 ft
Weight: 171 lb.

Particle Diameter - in.

Percent

Fig. E-18. Particle Size Analysis - Drop Crushing - Kitledge Pink Granite

Test No.: 18
Rock: Kitledge Pink Granite
Drops: 1-10 ft
Weight: 171 lb
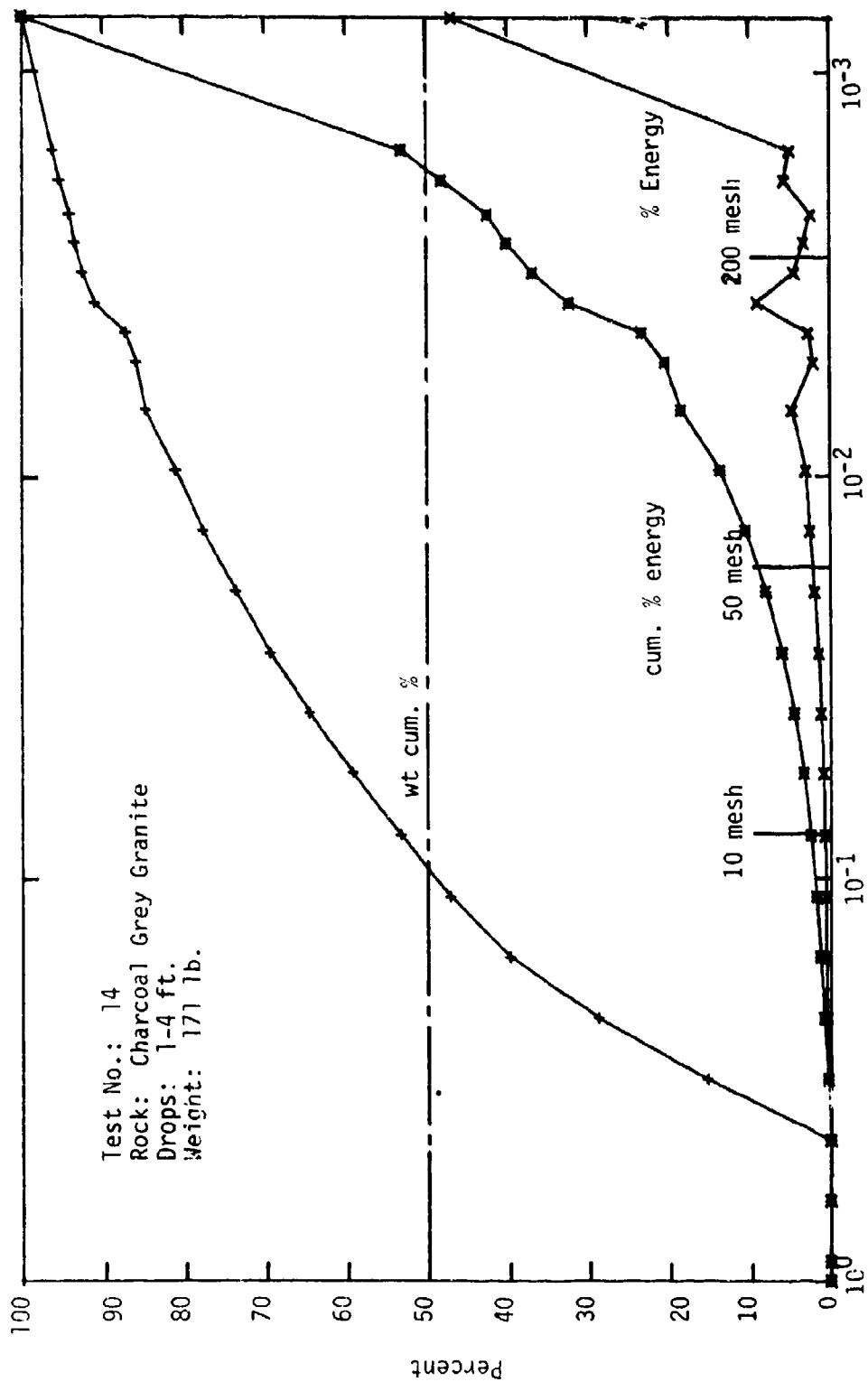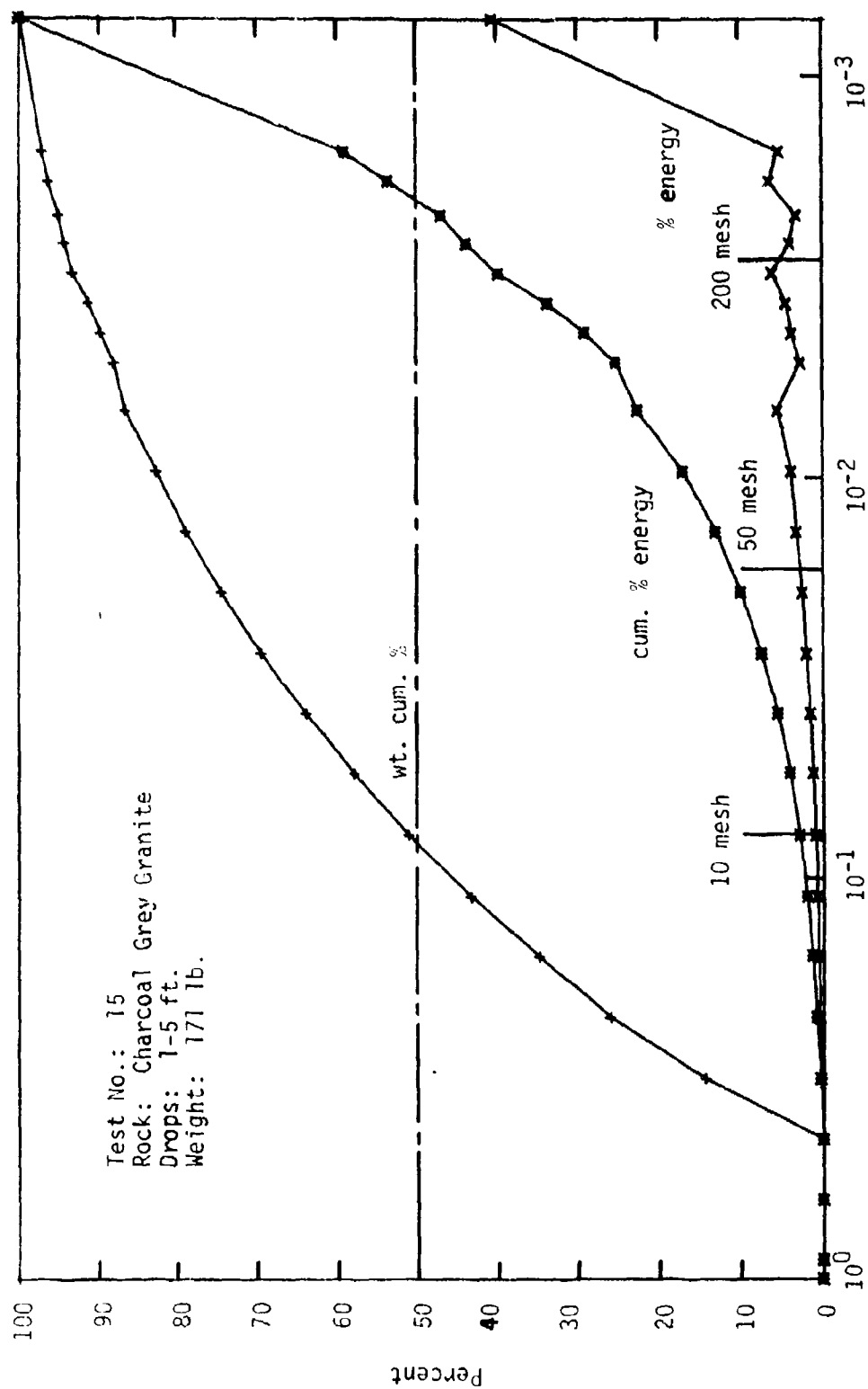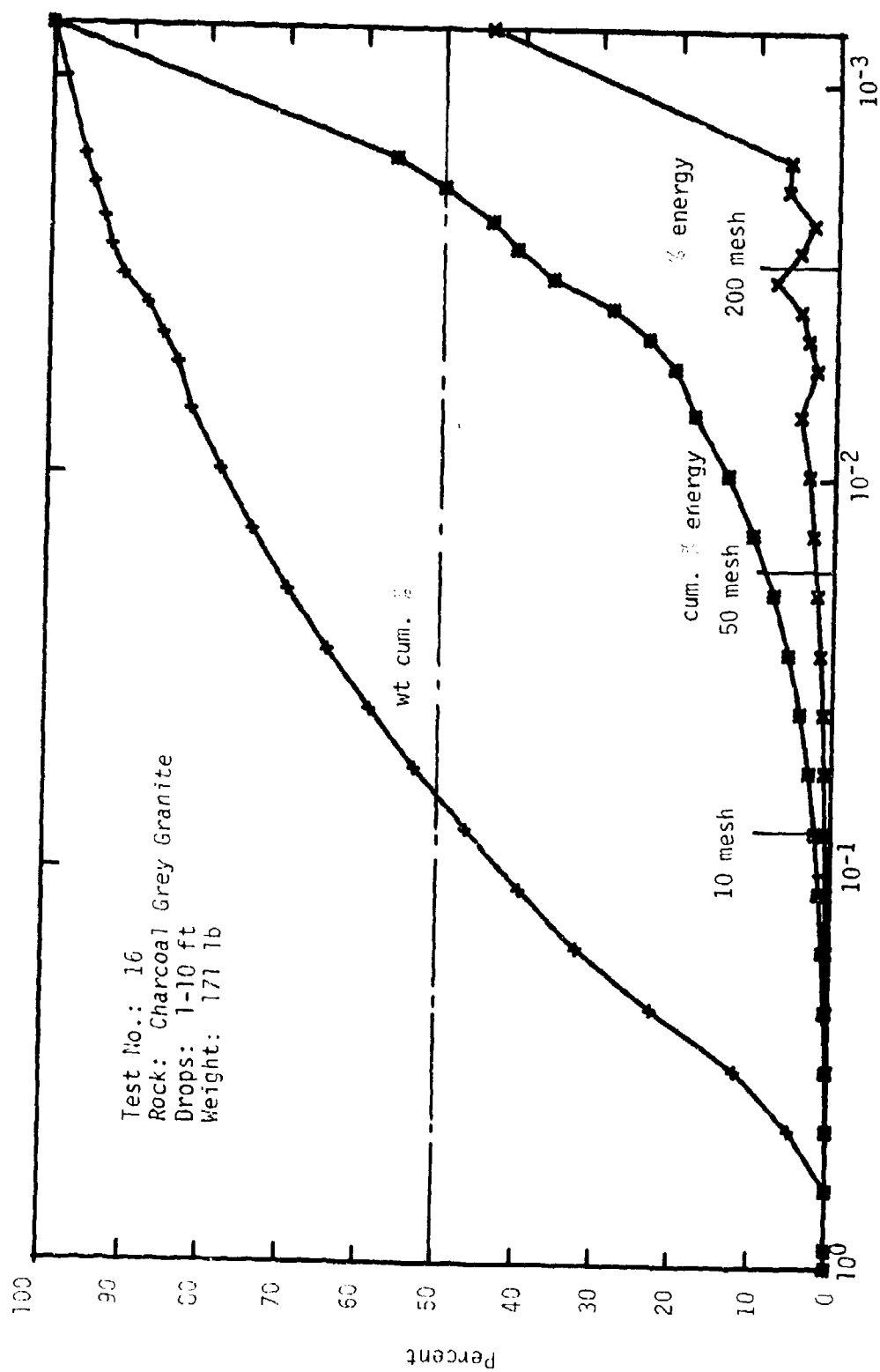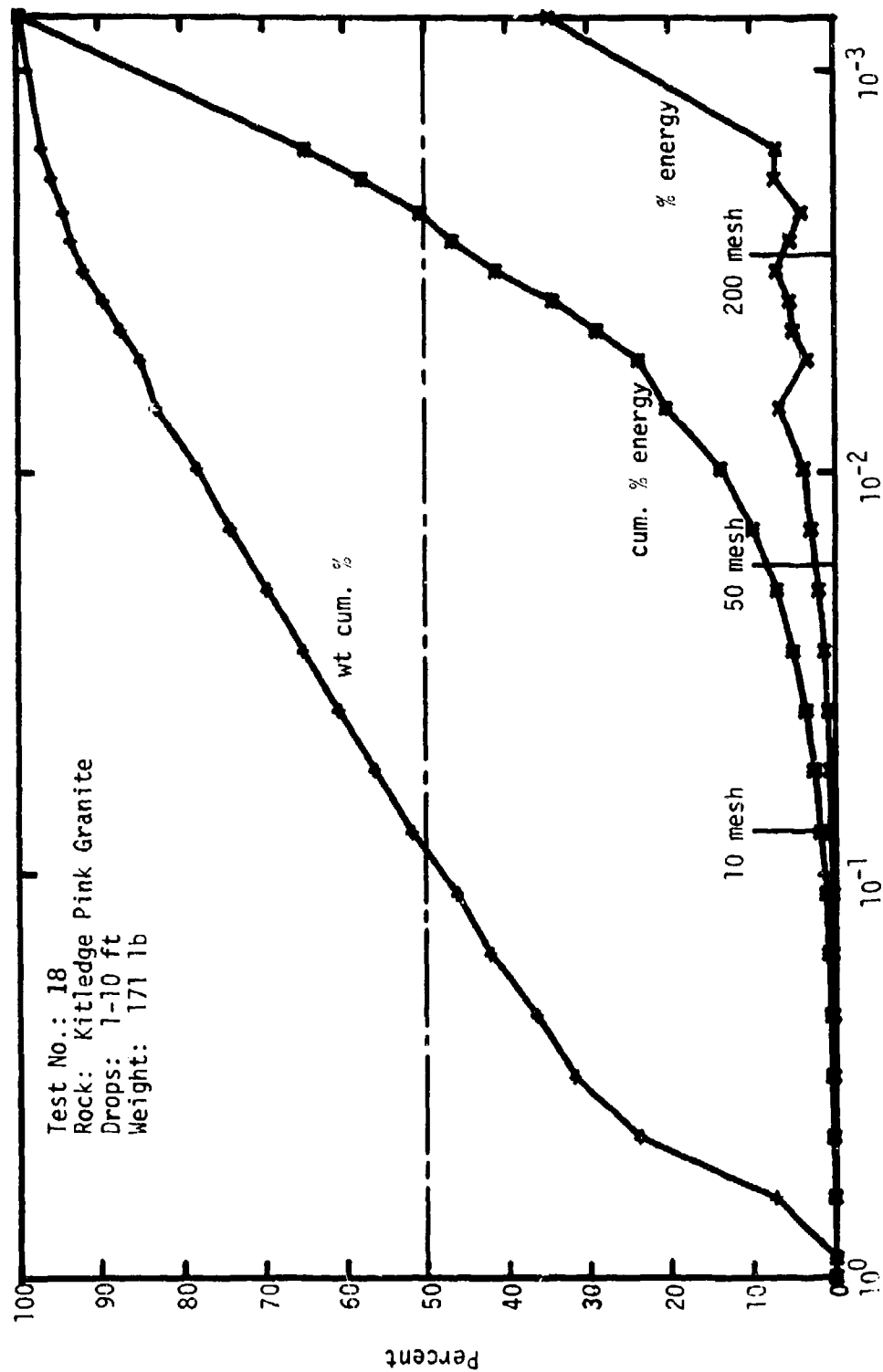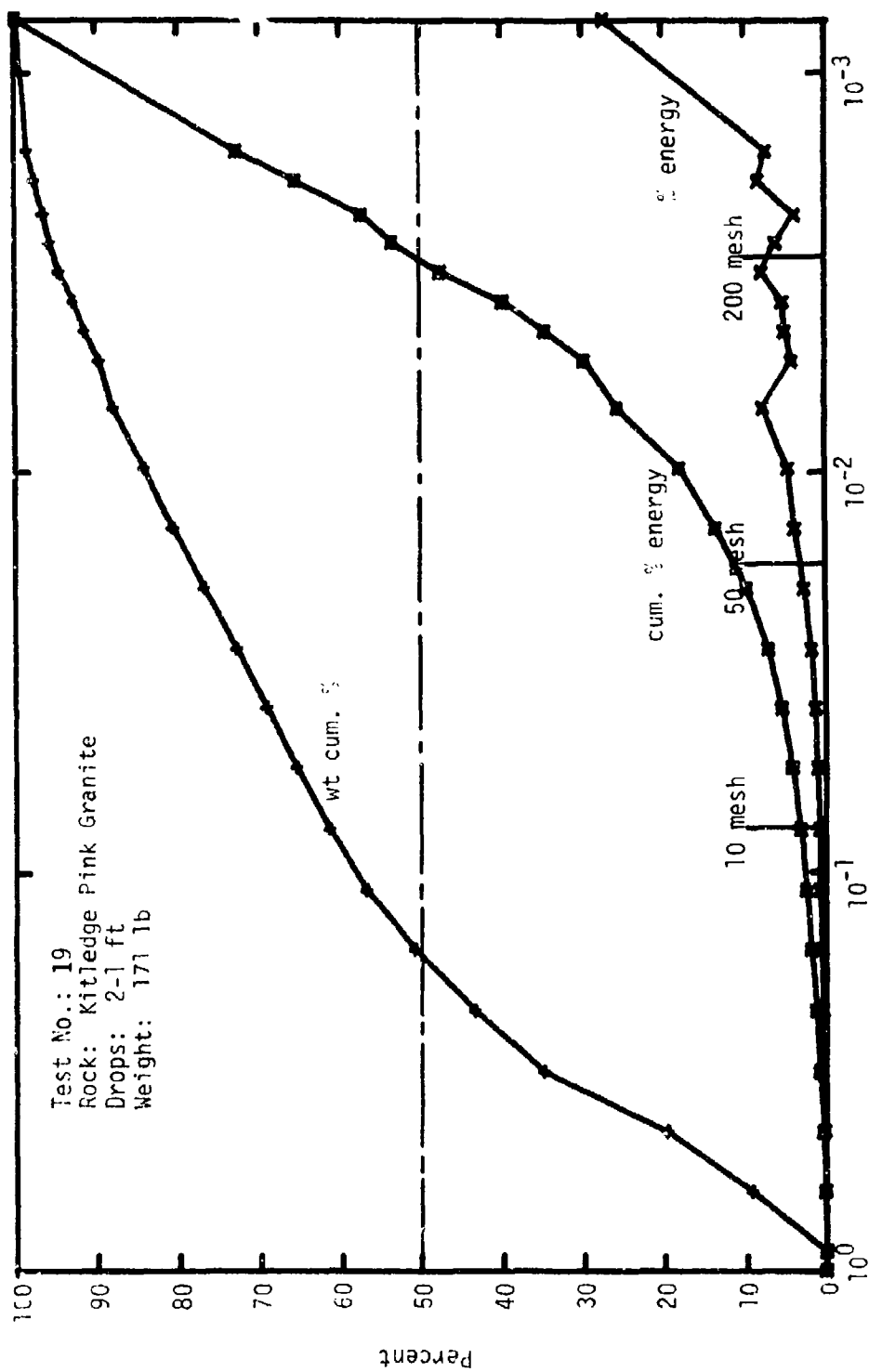
Fig. E-19. Particle Size Analysis – Drop Crushing – Kitledge Pink Granite

Fig. E-20. Particle Size Analysis - Drop Crushing - Kitledge Pink Granite
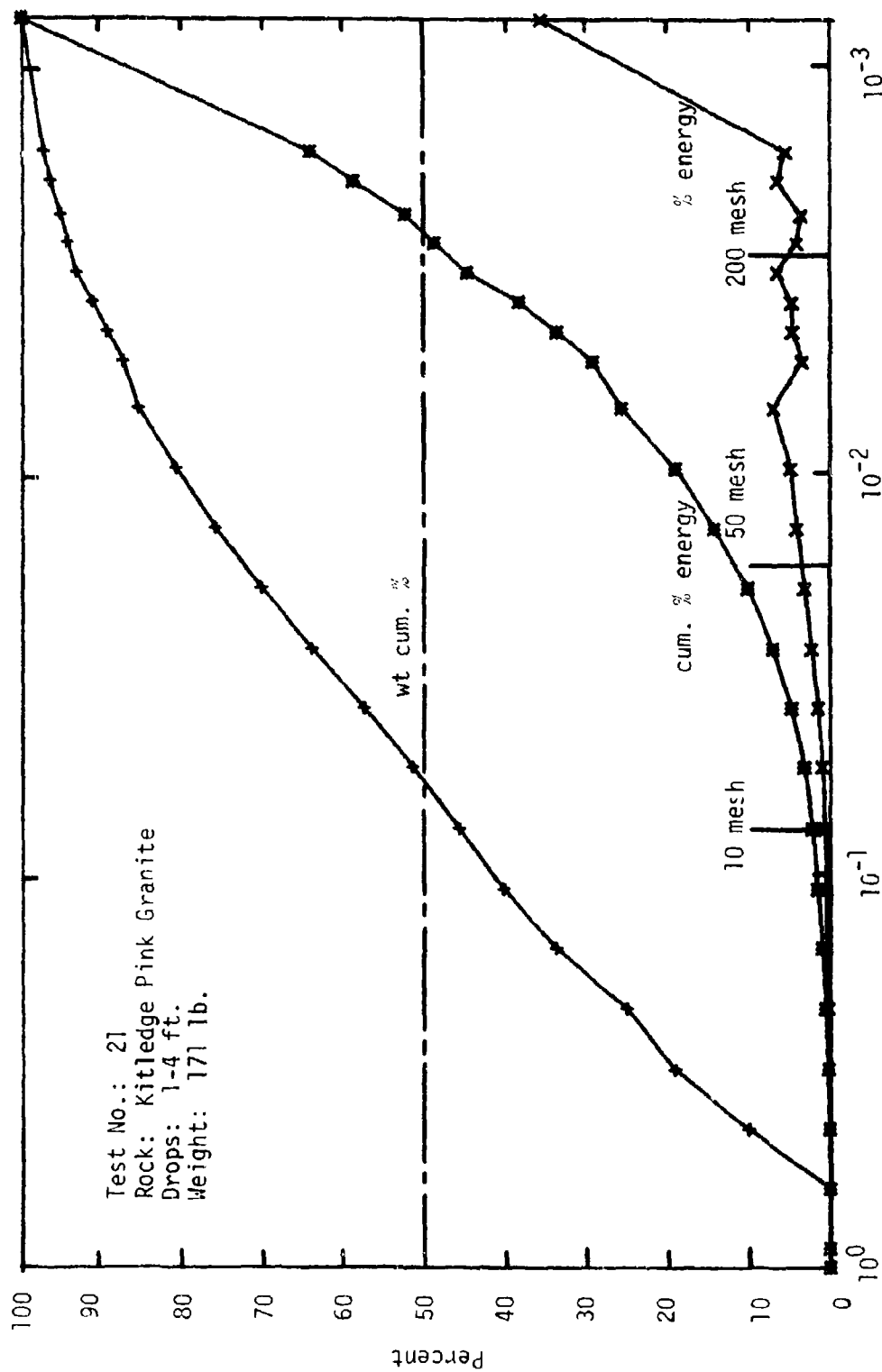
Test No.: 20
Rock: Kitledge Pink Granite
Drops: 1-2 ft.
Weight: 171 lb.

Fig. E-21. Particle Size Analysis - Drop Crushing - Kitledge Pink Granite

Test No.: 21
Rock: Kitledge Pink Granite
Drops: 1-4 ft.
Weight: 171 lb.
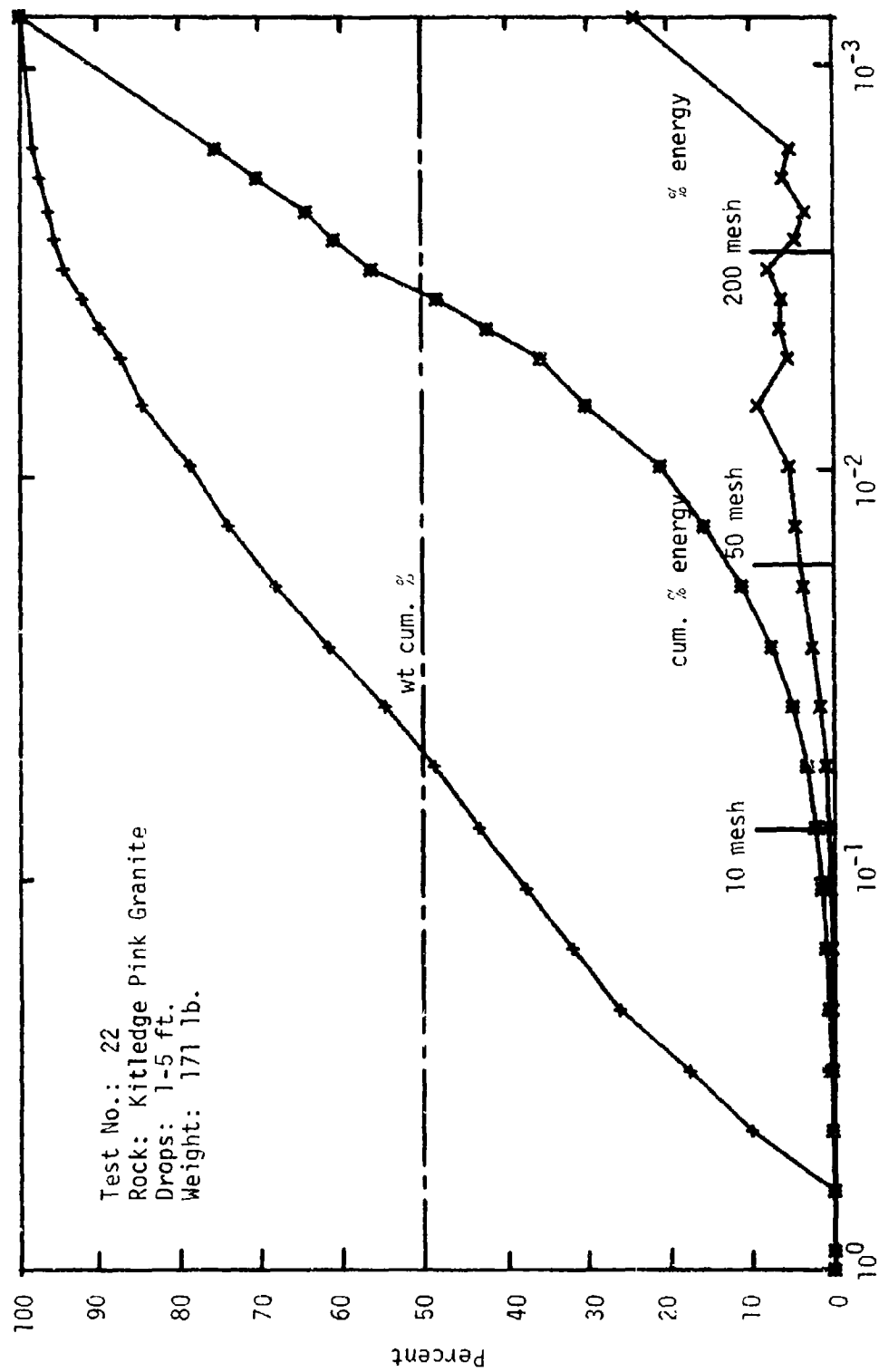
Fig. E-22. Particle Size Analysis - Drop Crushing - Kitledge Pink Granite
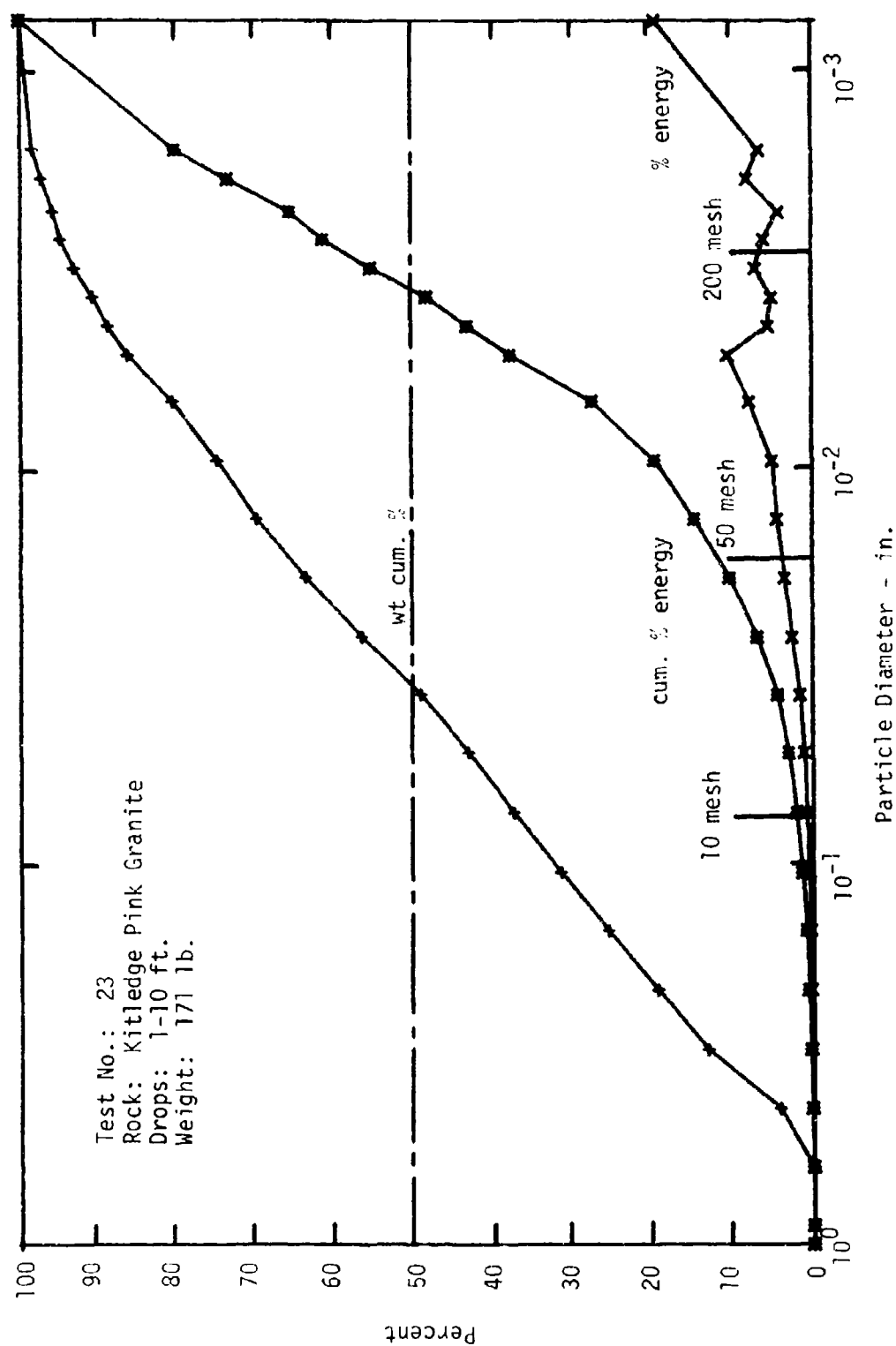
Fig. E-23. Particle Size Analysis - Drop Crushing - Kitledge Pink Granite
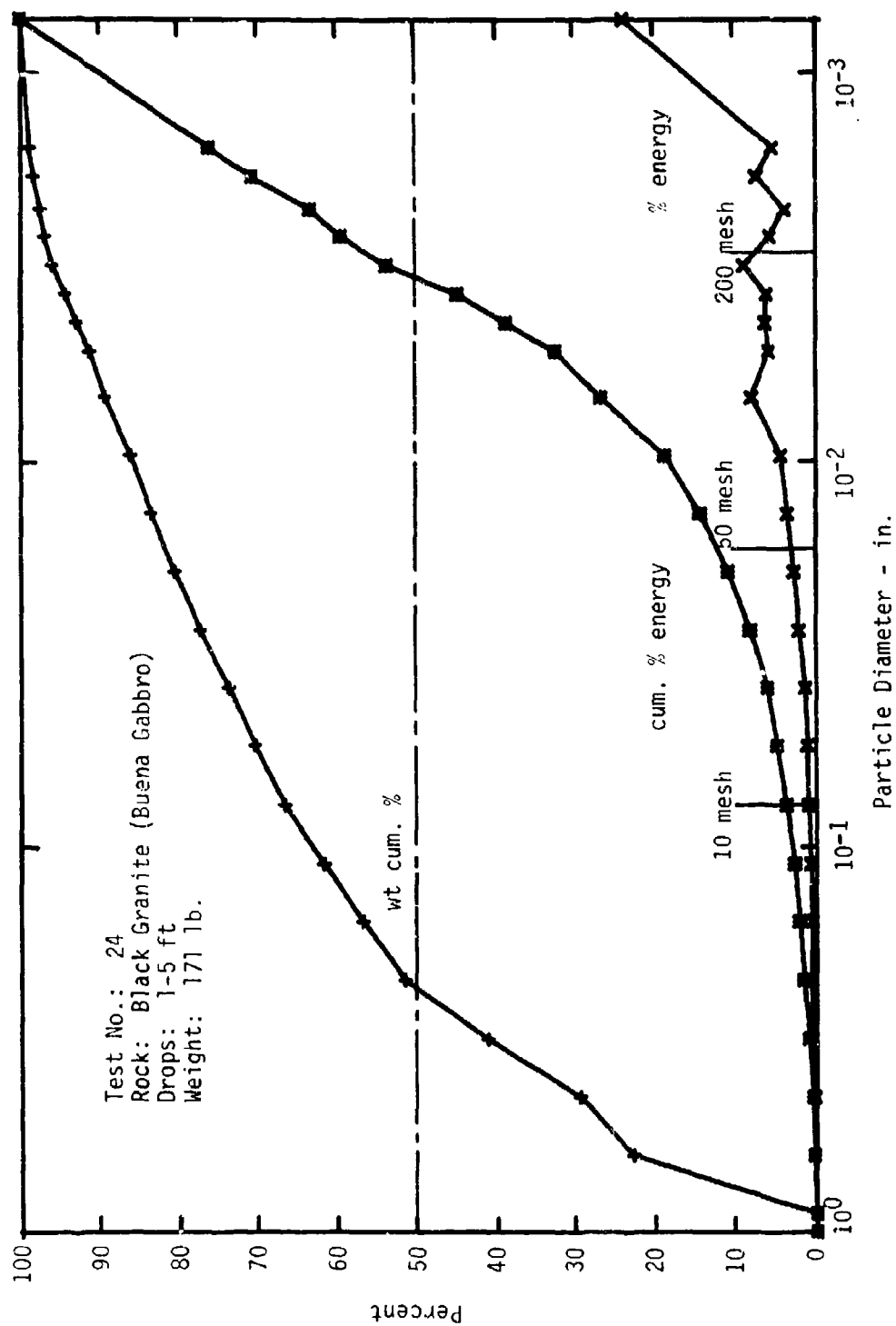
Fig. E-24. Particle Size Analysis - Drop Crushing - Black Granite (Buena Gabbro)

Test No.: 24
Rock: Black Granite (Buena Gabbro)
Drops: 1-5 ft
Weight: 171 lb.
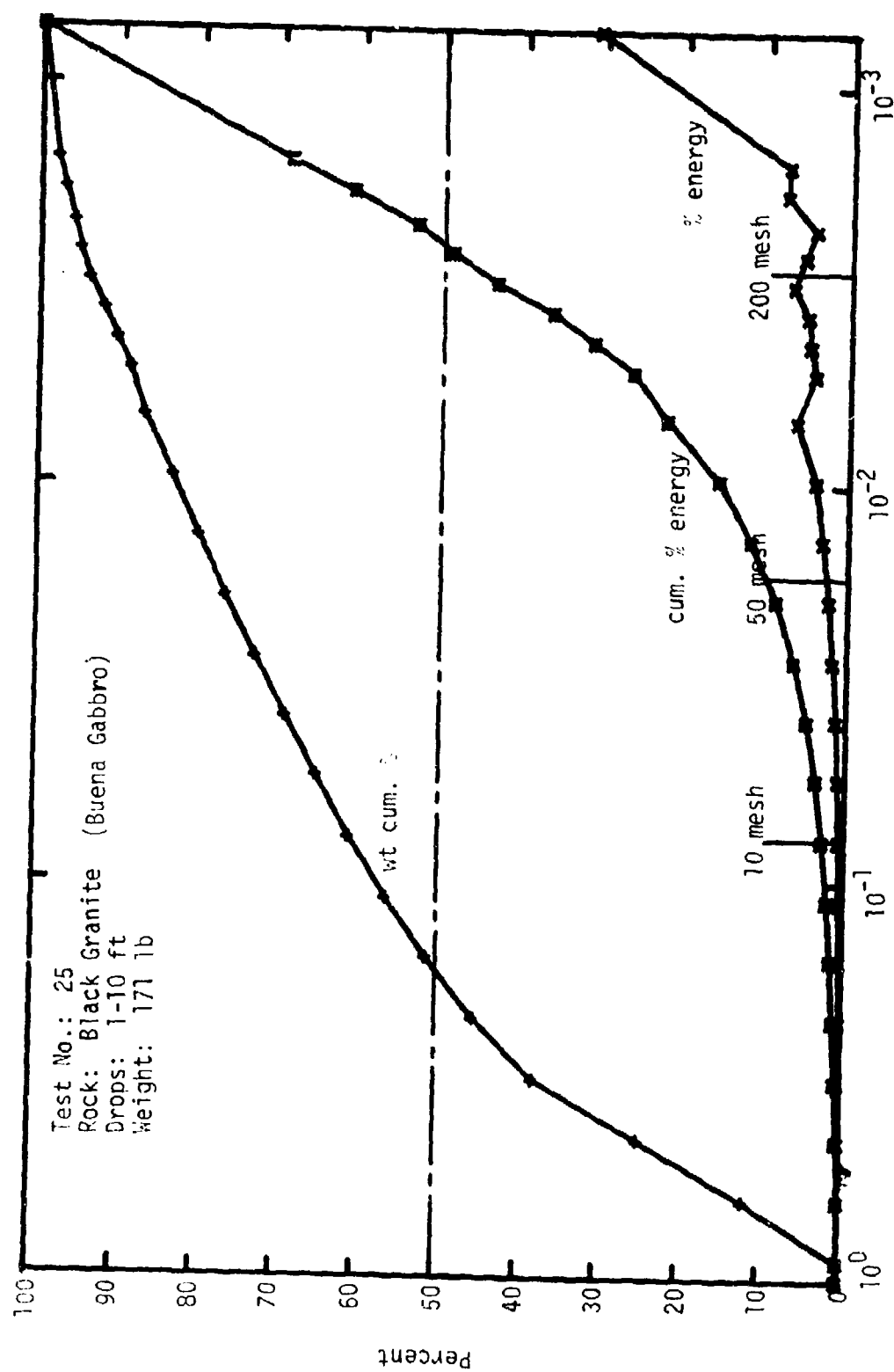
Fig. E -25. Particle Size Analysis - Drop Crushing - Black Granite (Buena Gabbro)

Fig. E-26. Particle Size Analysis – Drop Crushing – Black Granite (Buena Gabbro)
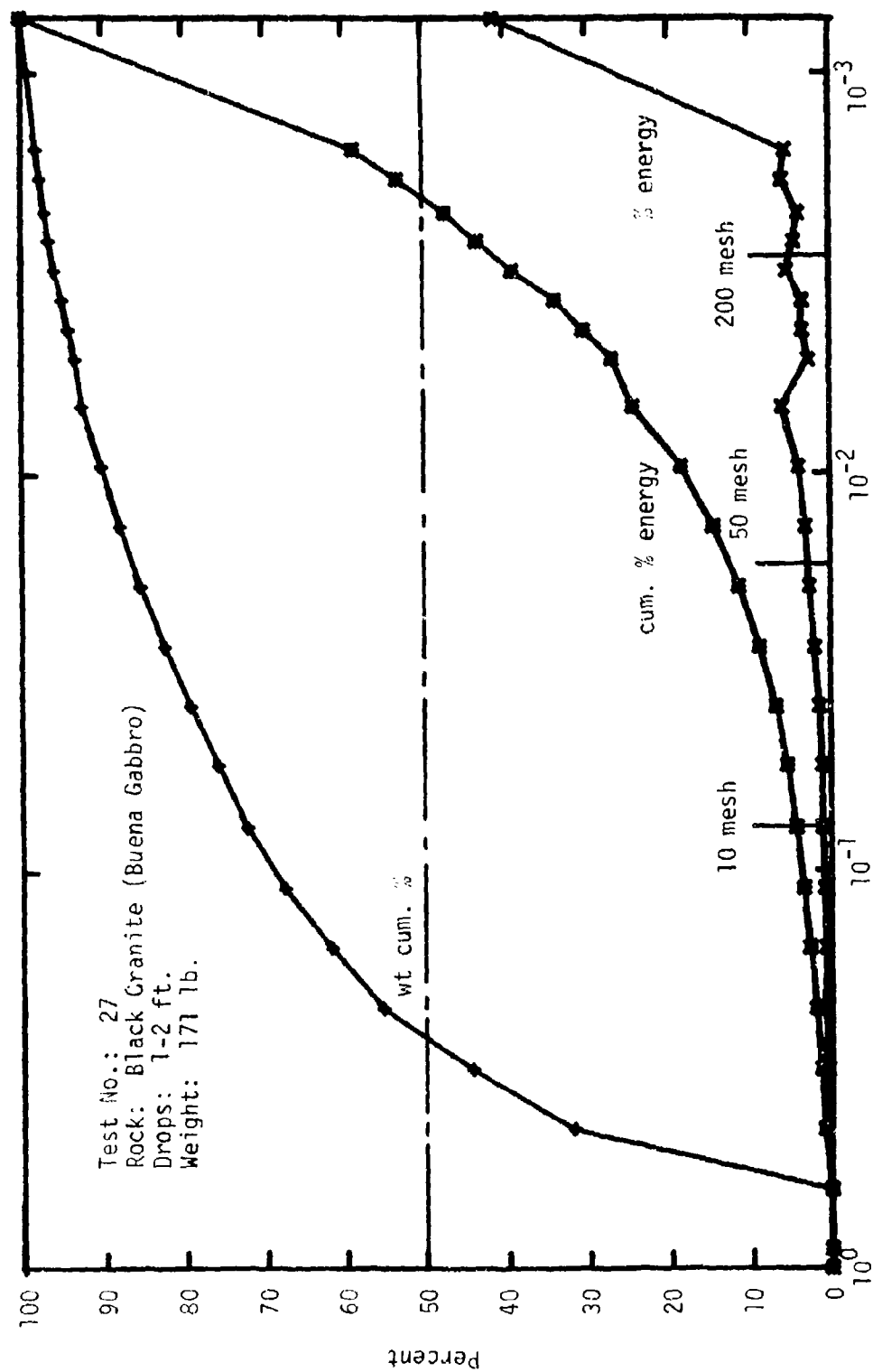
Test No.: 26
Rock: Black Granite (Buena Gabbro)
Drops: 2-1 ft
Weight: 171 lb

Particle Diameter – in.

Percent

Fig. E-27. Particle Size Analysis - Drop Crushing - Black Granite (Buena Gabbro)
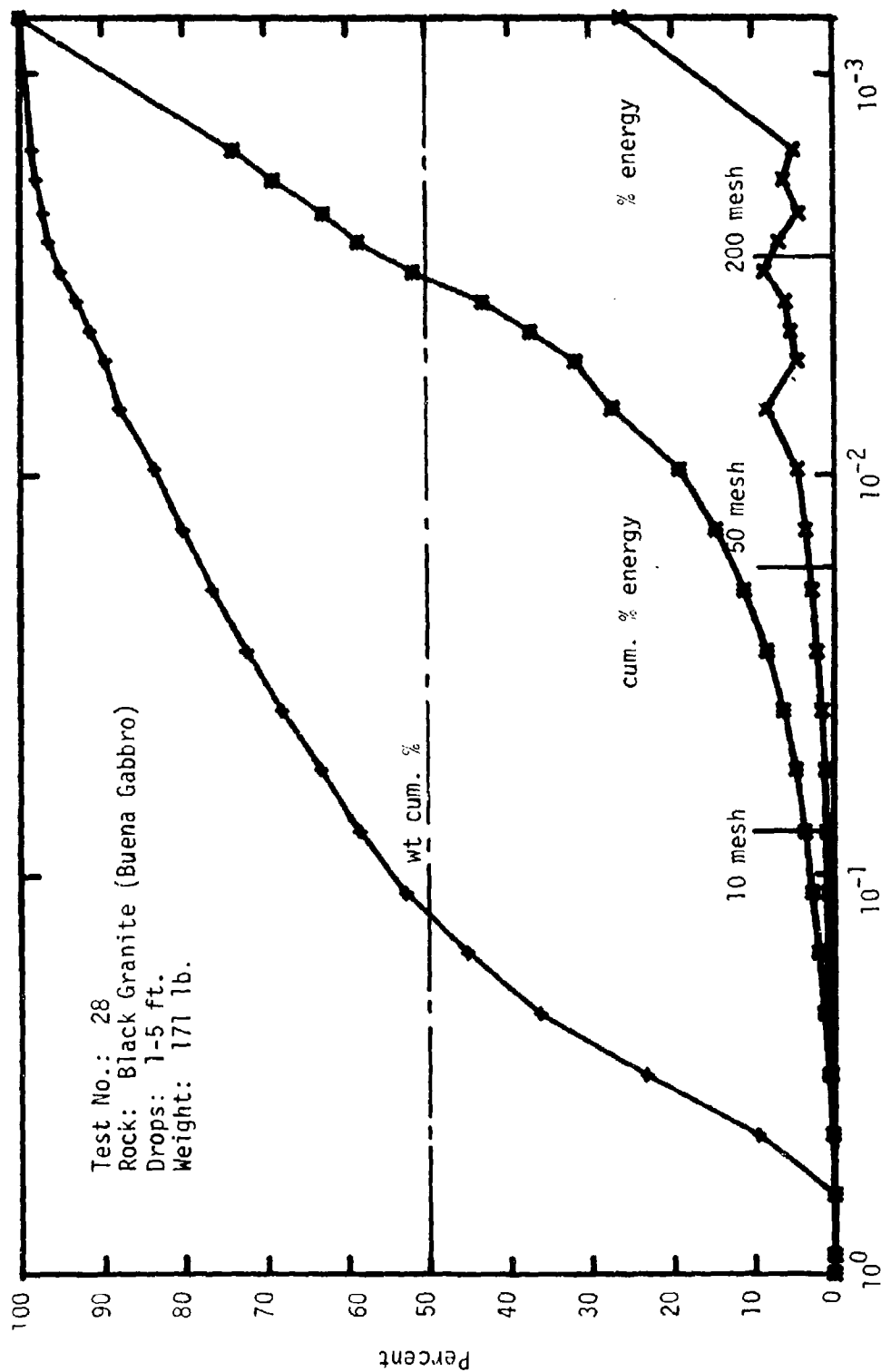
Test No.: 27
Rock: Black Granite (Buena Gabbro)
Drops: 1-2 ft.
Weight: 171 lb.

Particle Diameter - in.

Percent

Fig. E-28. Particle Size Analysis - Drop Crushing - Black Granite (Buena Gabbro)

Test No.: 28
Rock: Black Granite (Buena Gabbro)
Drops: 1-5 ft.
Weight: 171 lb.

Fig. E-29. Particle Size Analysis - Drop Crushing - Black Granite (Buena Gabbro)

Test No.: 29
Rock: Black Granite (Buena Gabbro)
Drops: 1-5 ft.
Weight: 171 lb.
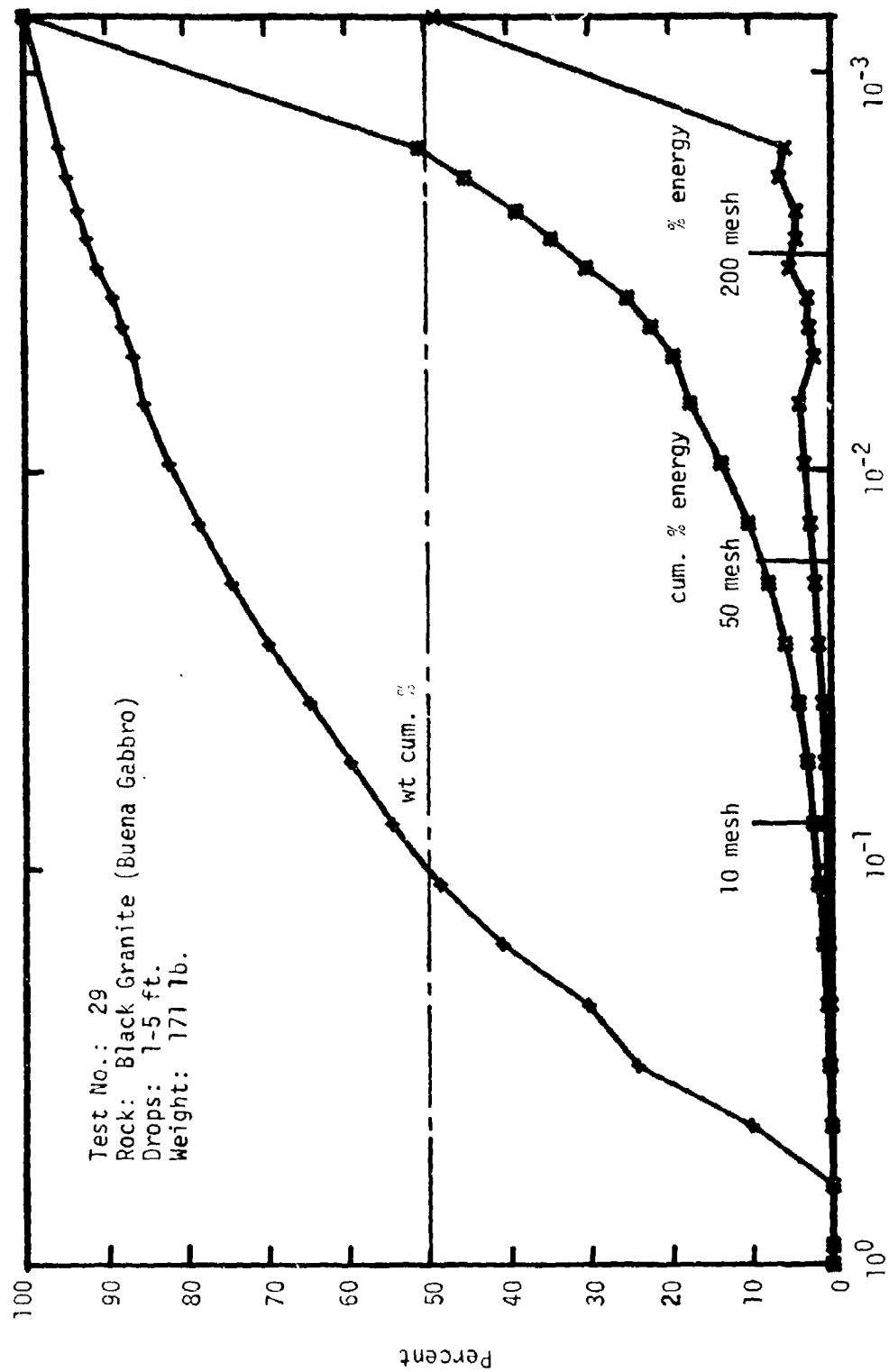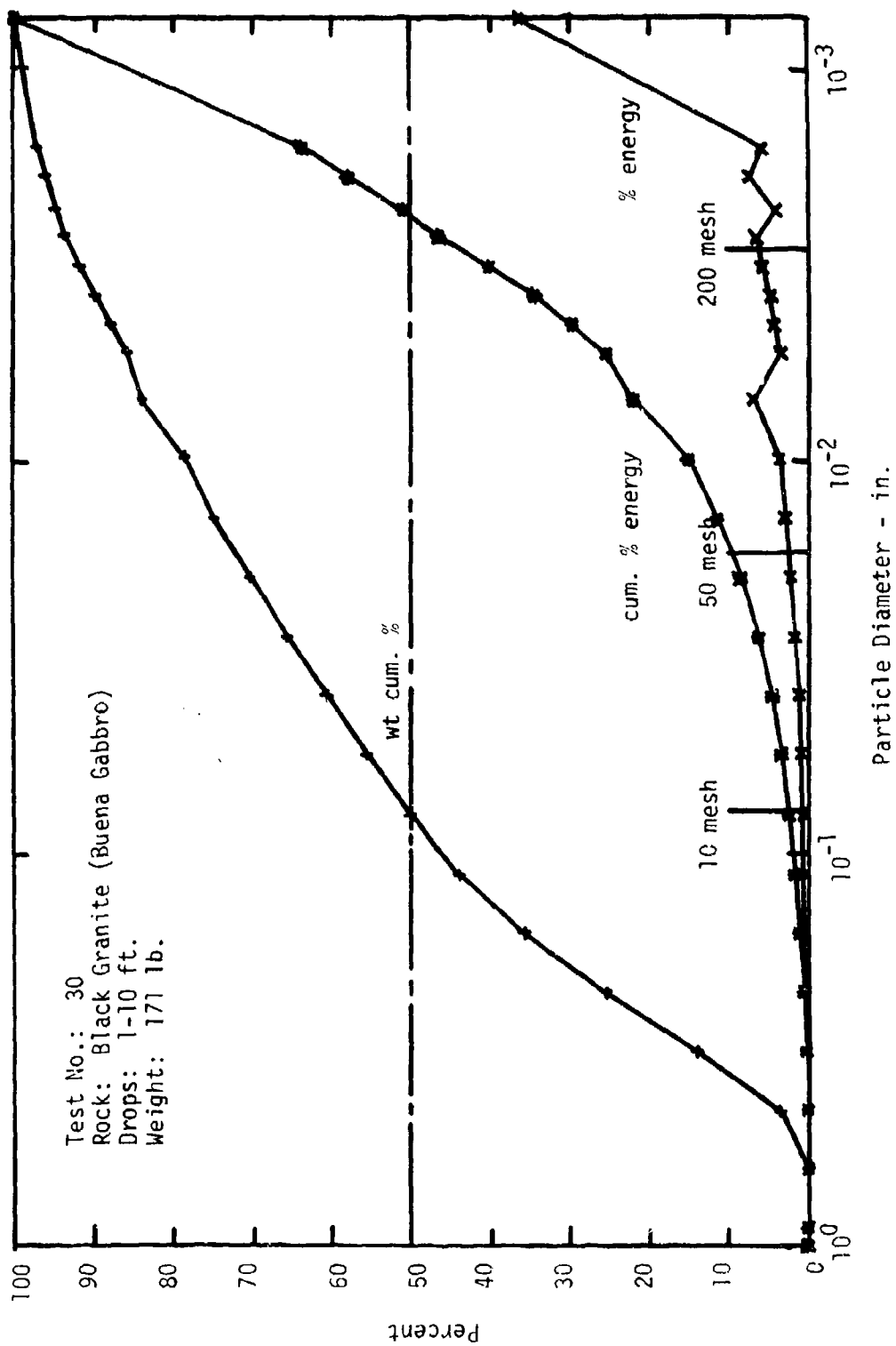
Fig. E-30. Particle Size Analysis – Drop Crushing – Black Granite (Buena Gabbro)

Test No.: 30
Rock: Black Granite (Buena Gabbro)
Drops: 1-10 ft.
Weight: 171 lb.
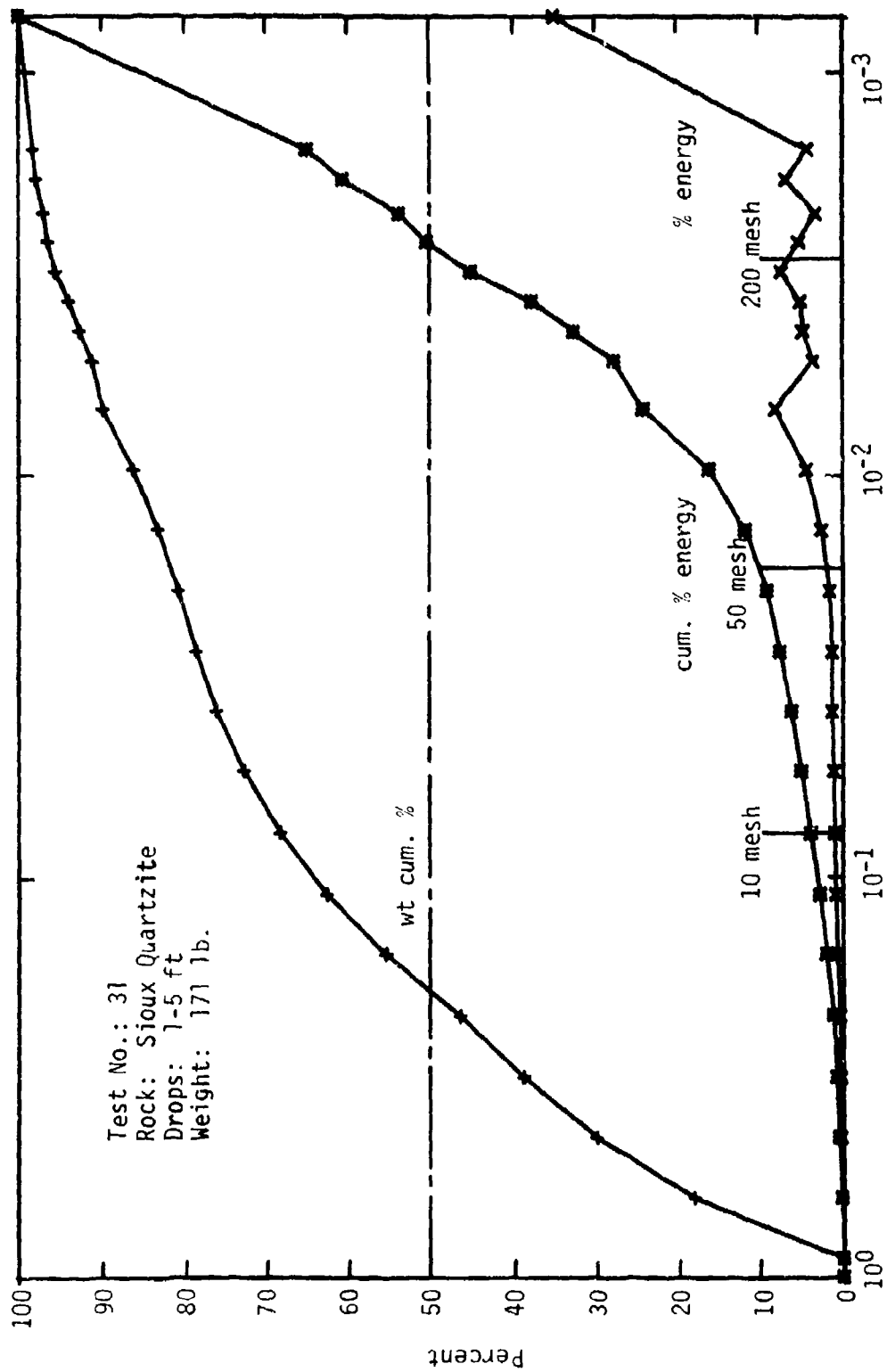
Fig. E-31. Particle Size Analysis - Drop Crushing - Sioux Quartzite

Test No.: 31
Rock: Sioux Quartzite
Drops: 1-5 ft
Weight: 171 lb.
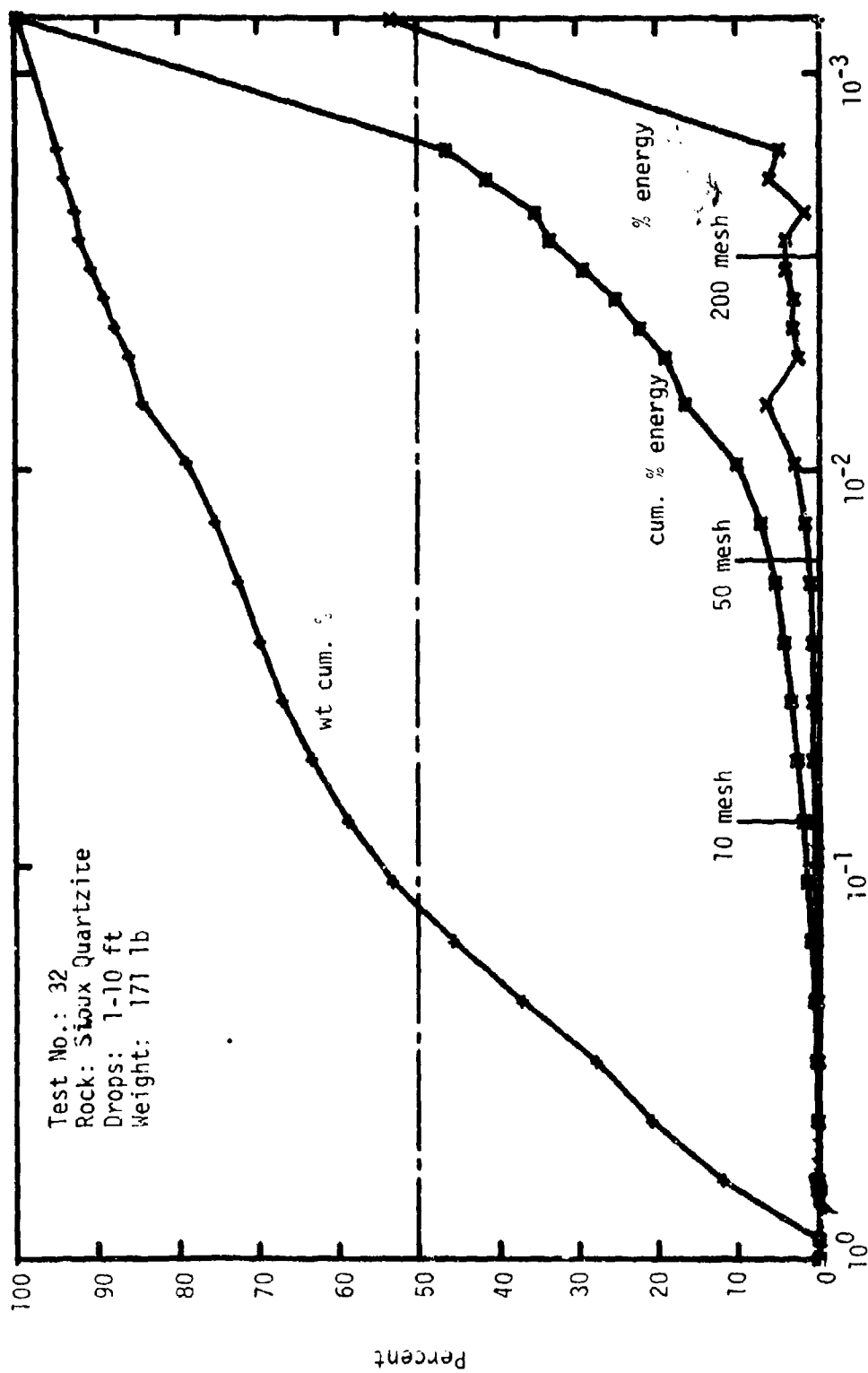
Fig. E-32. Particle Size Analysis - Drop Crushing - Sioux Quartzite

Fig. E-33. Particle Size Analysis - Drop Crushing - Sioux Quartzite

Particle Diameter - in.

Test No.: 33
Rock: Sioux Quartzite
Drops: 2-1 ft
Weight: 171 lb

wt cum. %

cum. % energy

% energy

10 mesh

50 mesh

200 mesh

Percent
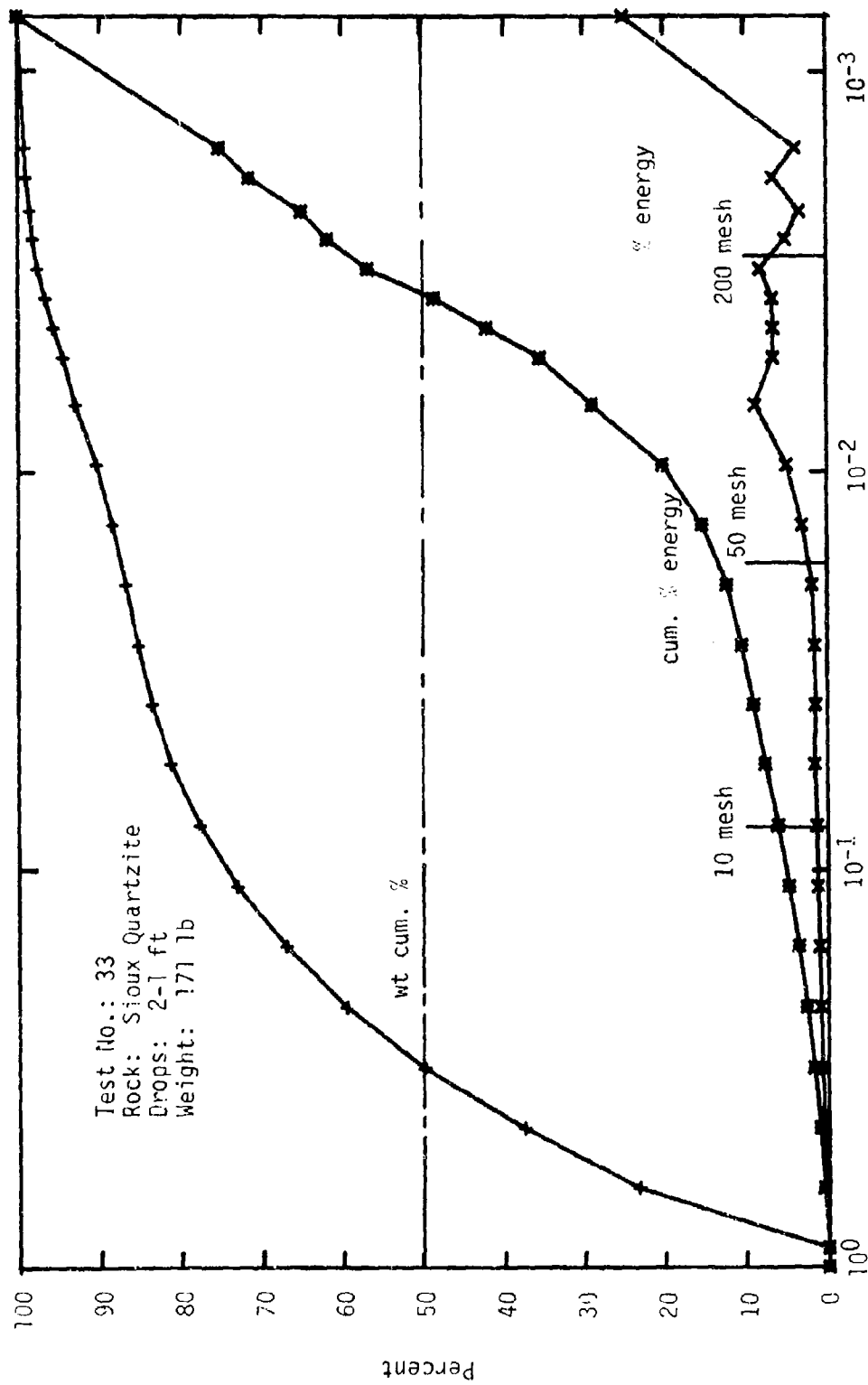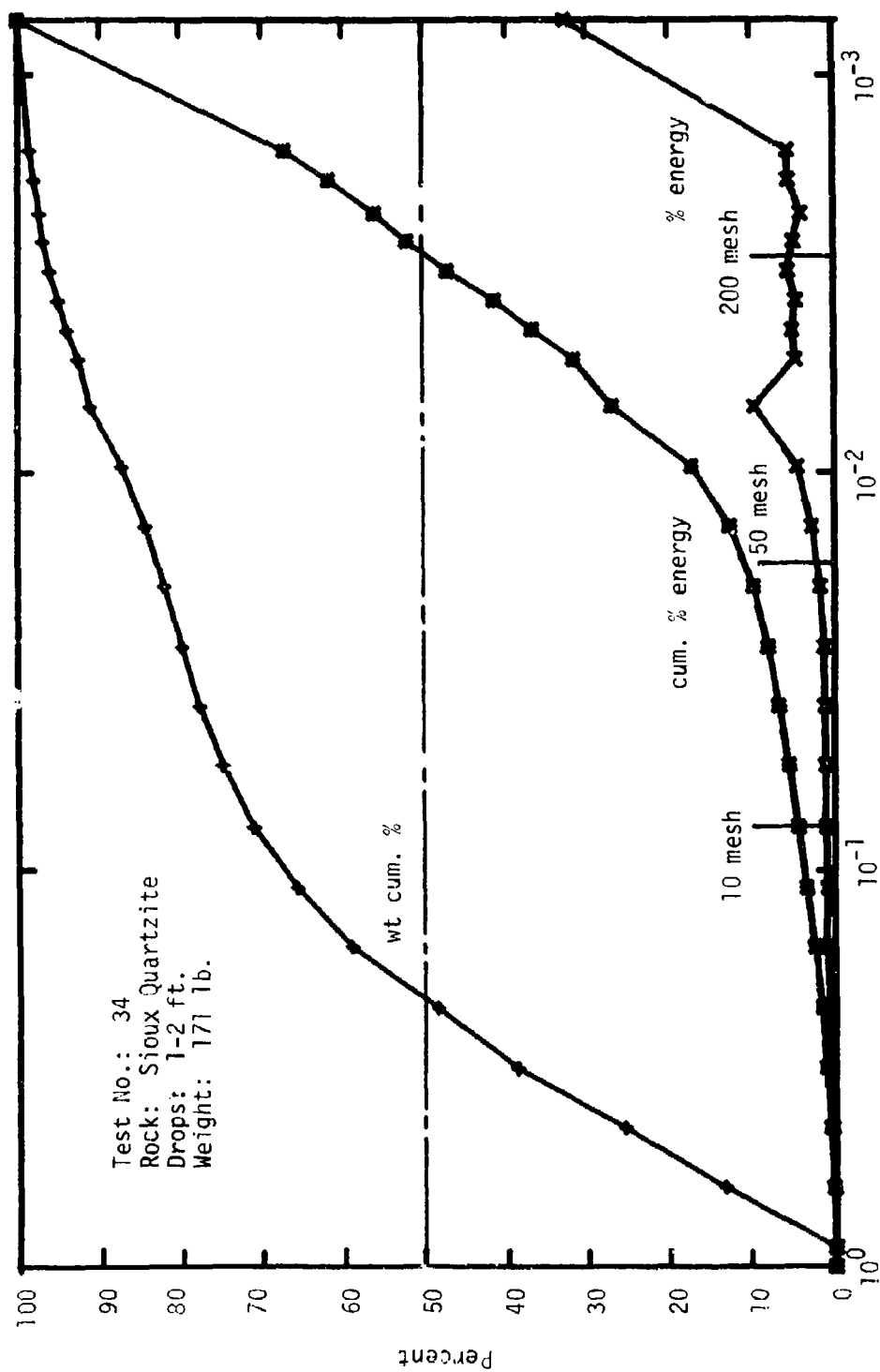
Fig. E-34. Particle Size Analysis - Drop Crushing - Sioux Quartzite
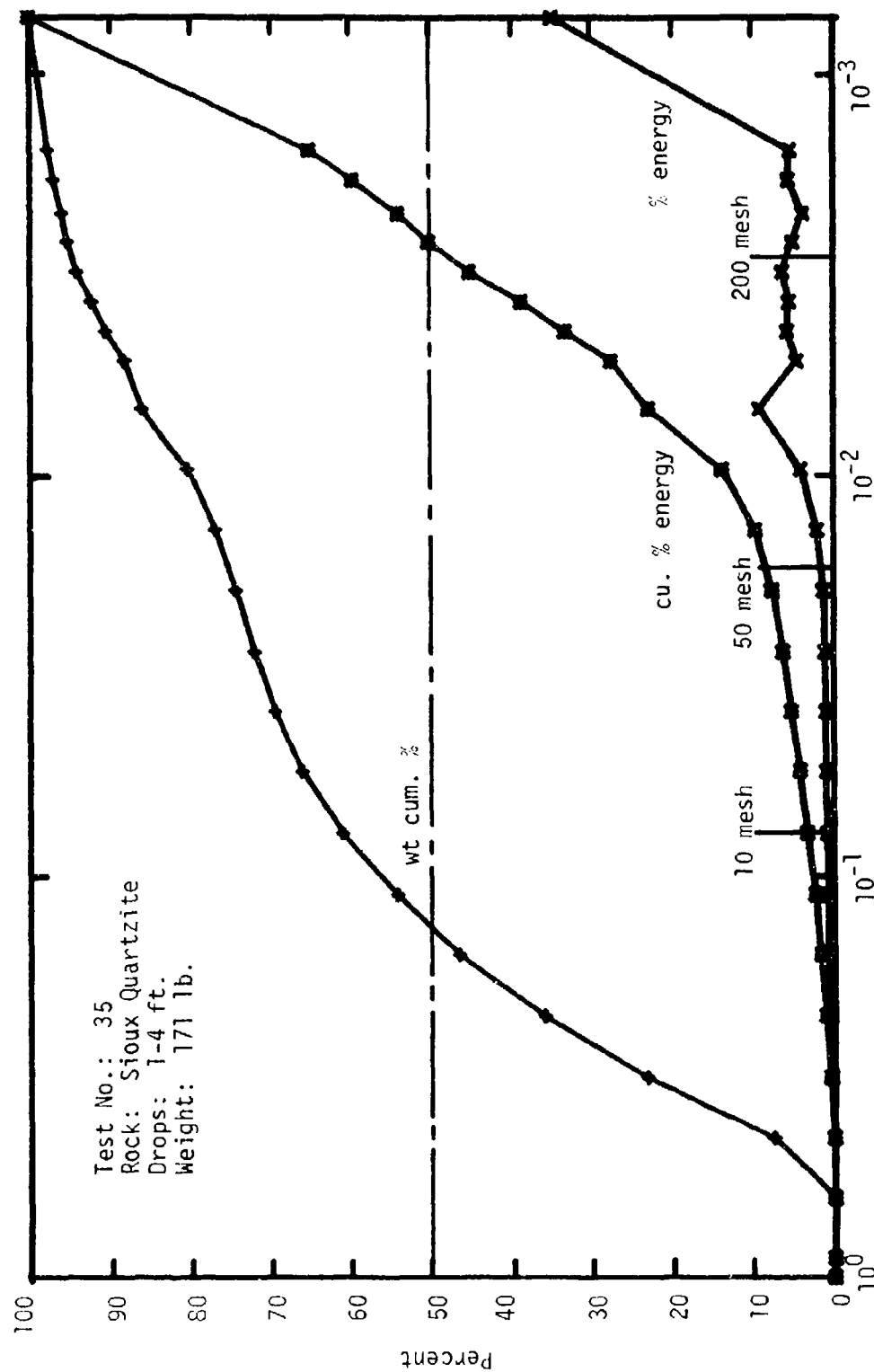
Fig. E-35. Particle Size Analysis - Drop Crushing - Sioux Quartzite
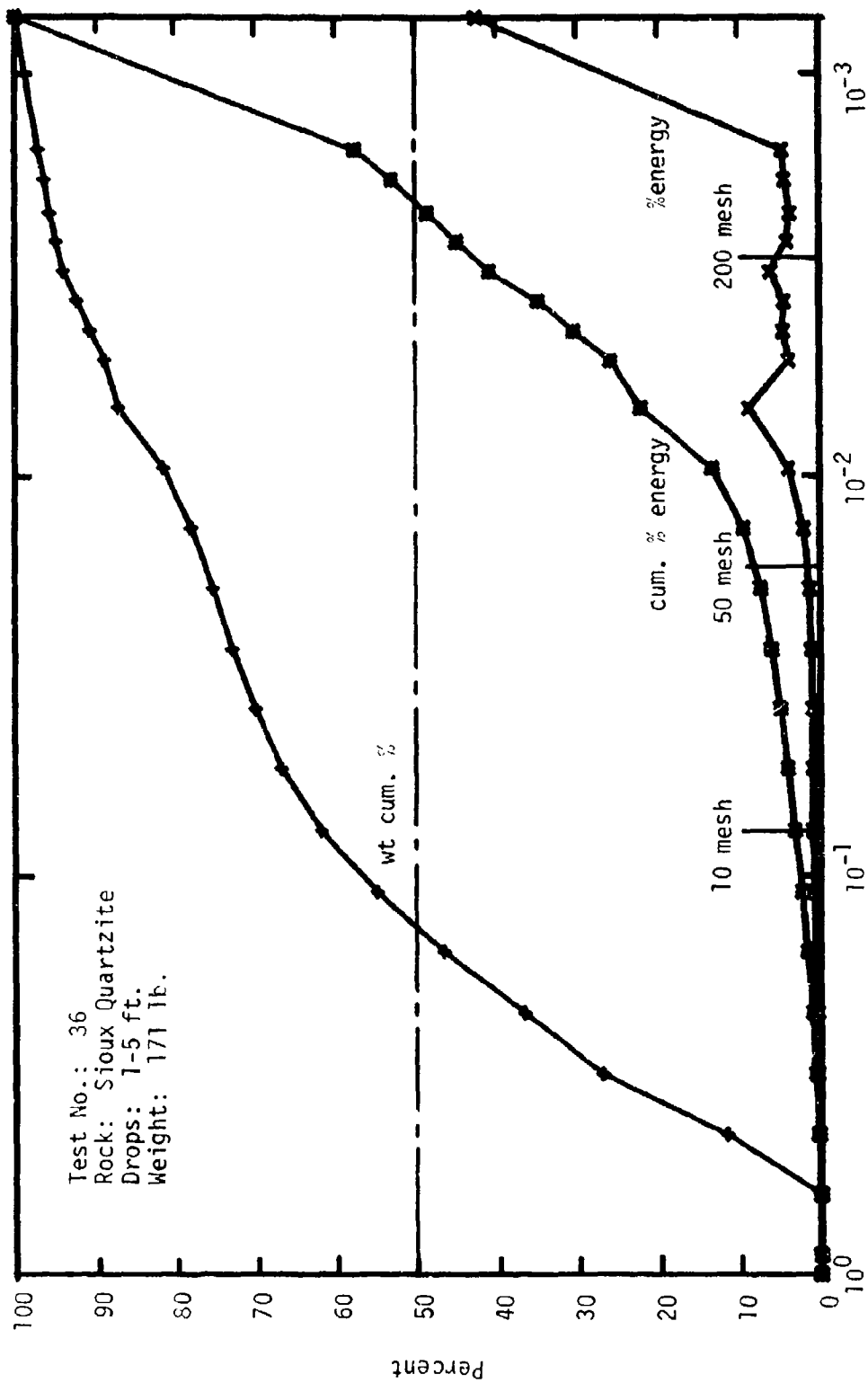
Fig. E-36. Particle Size Analysis - Drop Crushing - Sioux Quartzite
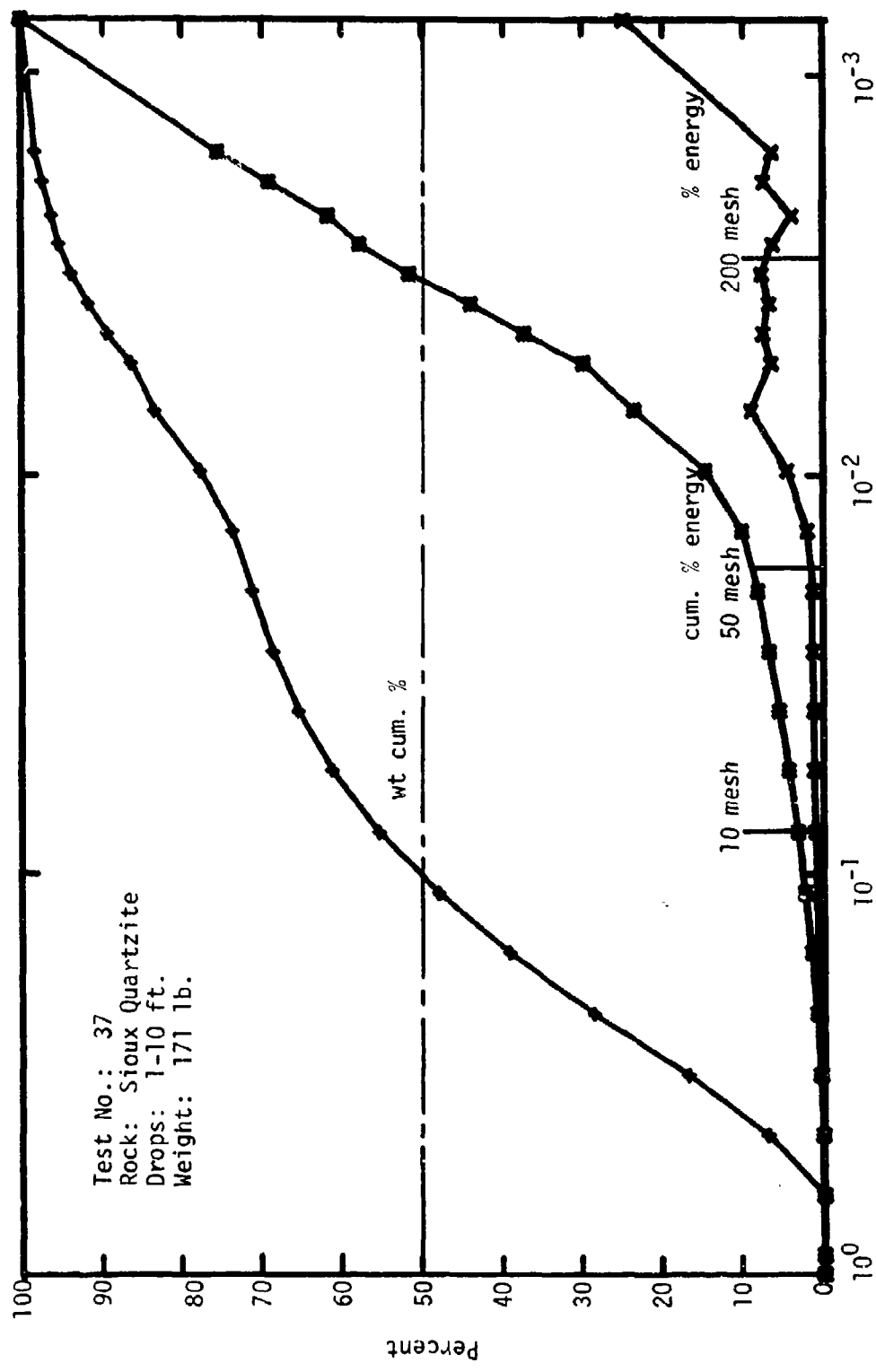
Test No.: 36
Rock: Sioux Quartzite
Drops: 1-5 ft.
Weight: 171 lb.

Particle Diameter - in.

Percent

Fig. E-37. Particle Size Analysis - Drop Crushing - Sioux Quartzite

Test No.: 37
Rock: Sioux Quartzite
Drops: 1-10 ft.
Weight: 171 lb.

Fig. E-38. Particle Size Analysis – Drop Crushing – Dresser Basalt

Test No.: 38
Rock: Dresser Basalt
Drops: 1–5 ft
Weight: 171 lb

Fig. E-39. Particle Size Analysis - Drop Crushing - Dresser Basalt

Test No.: 39
Rock: Dresser Basalt
Drops: 1-10 ft
Weight: 171 lb
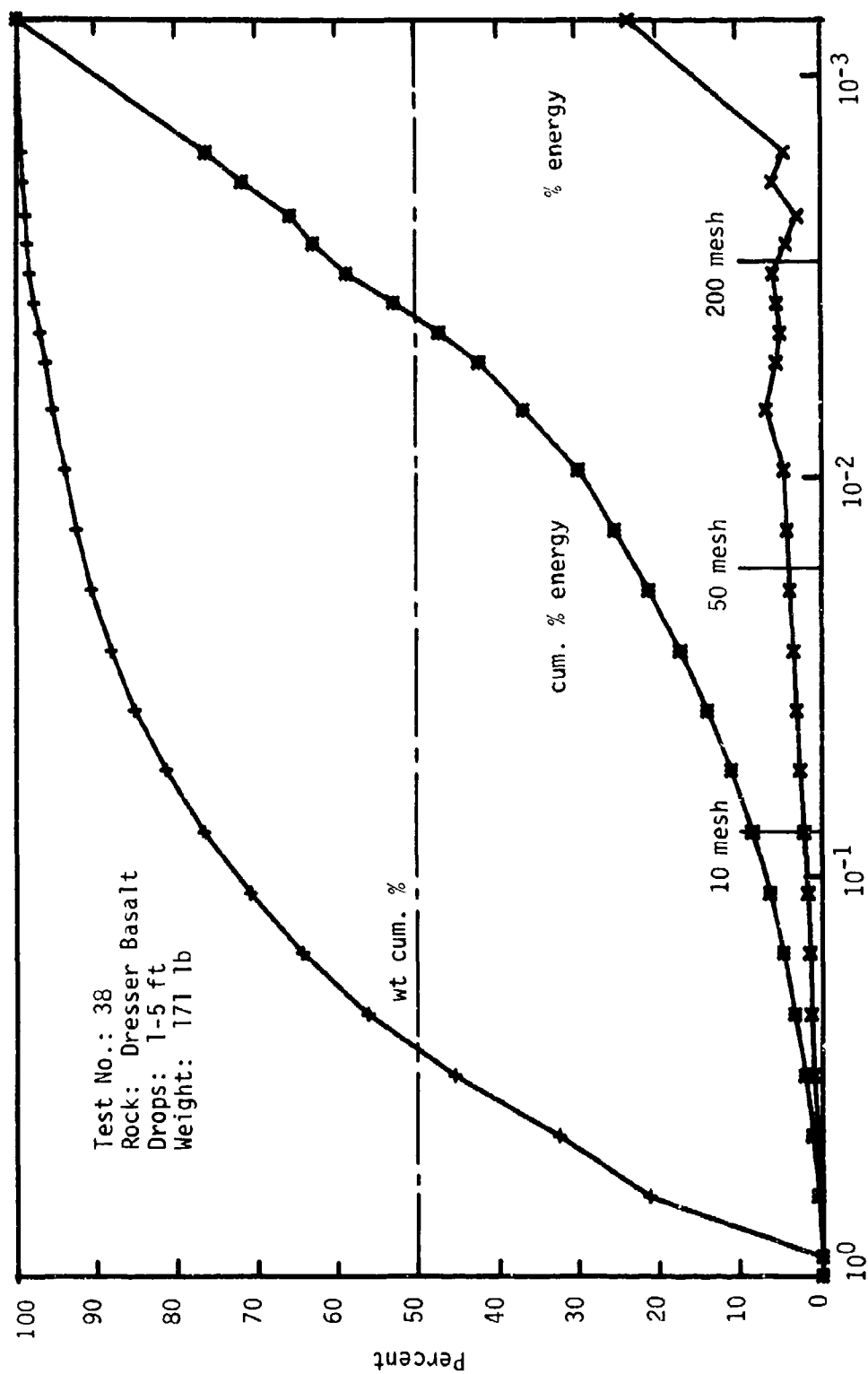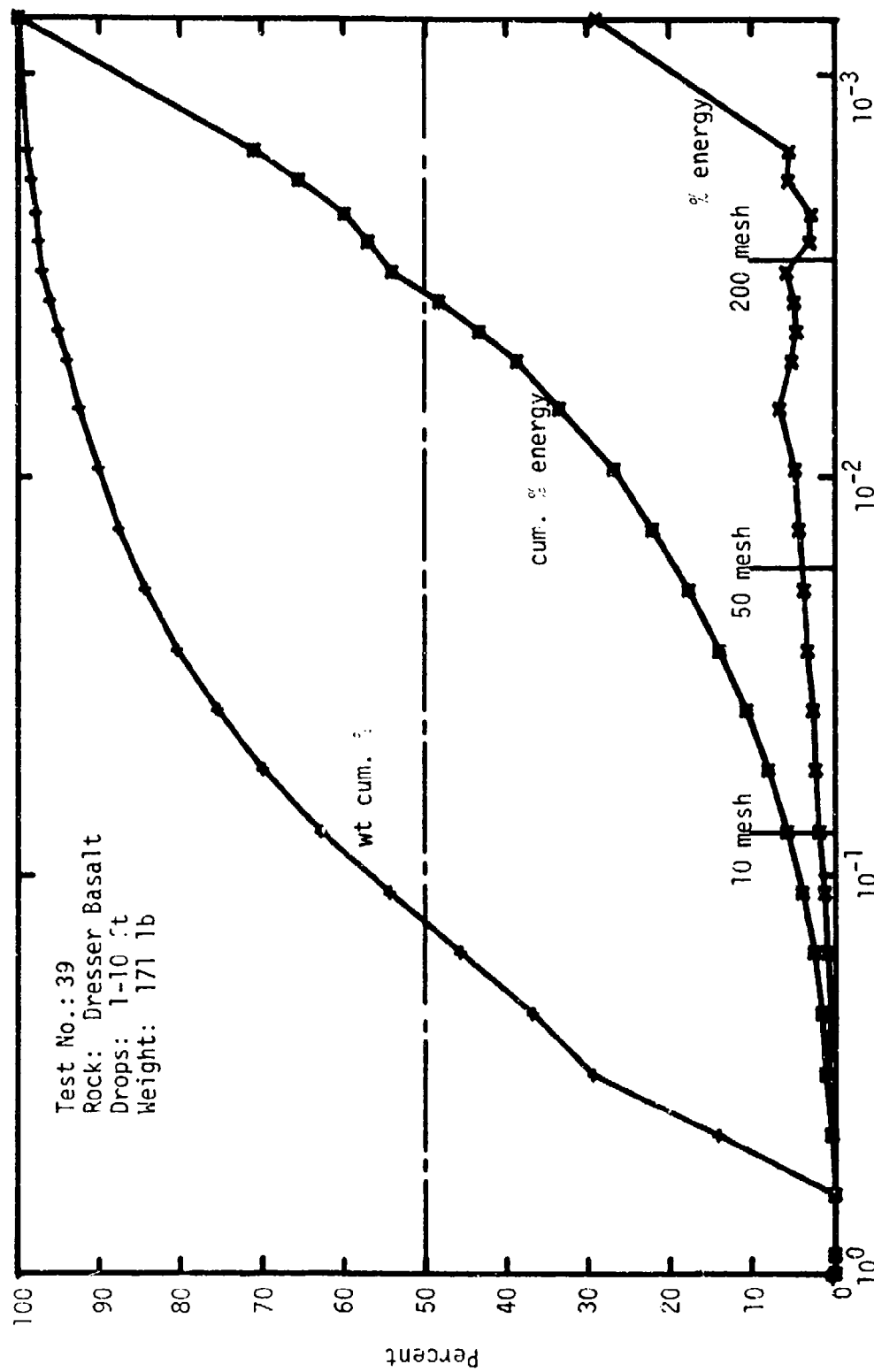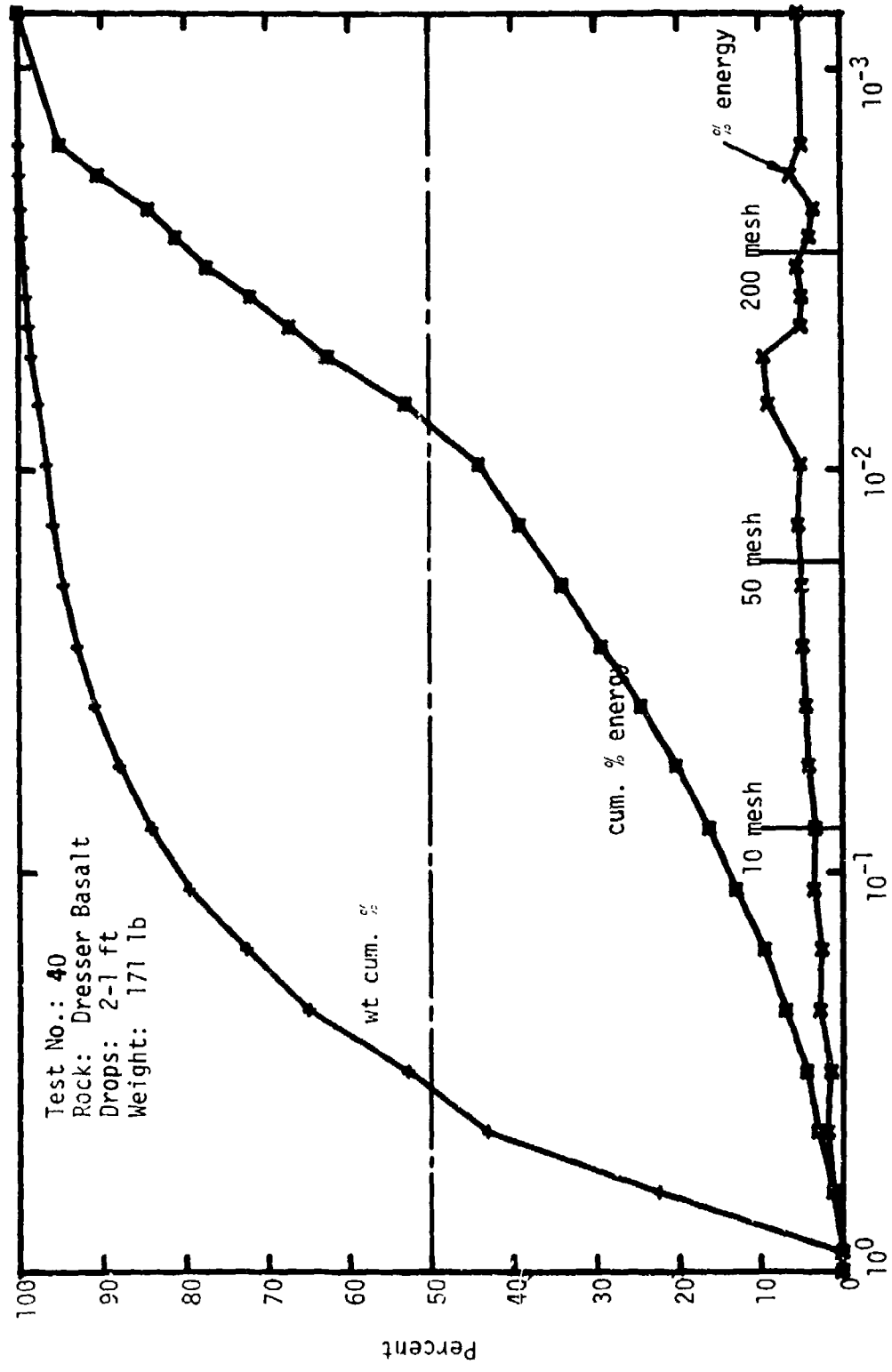
Fig. E-40. Particle Size Analysis – Drop Crushing – Dresser Basalt

Fig. E-41.   Particle Size Analysis - Drop Crushing - Dresser Basalt

Test No.:   41
Rock: Dresser Basalt
Drops: 1-2 ft.
Weight: 171 lb.
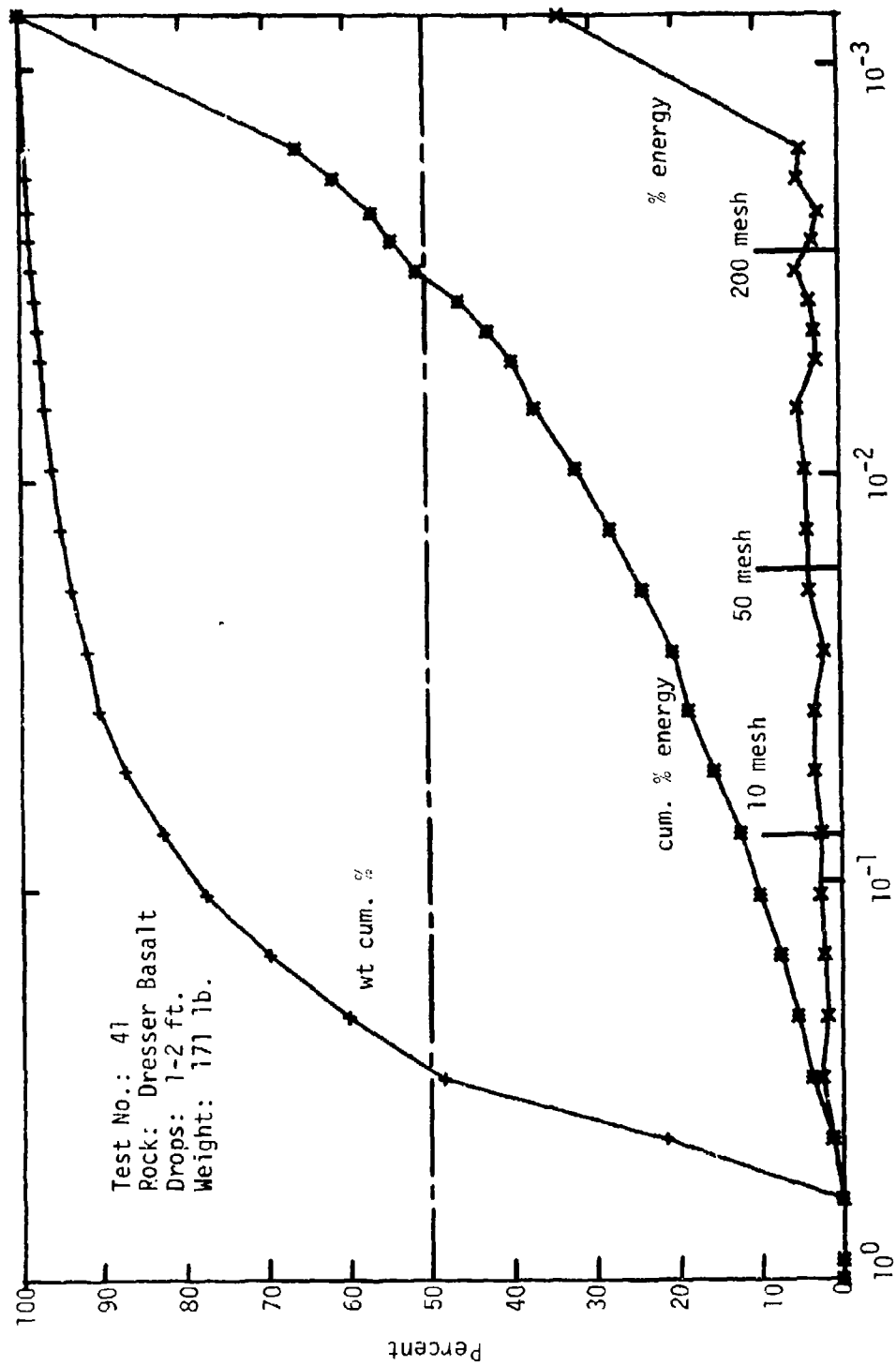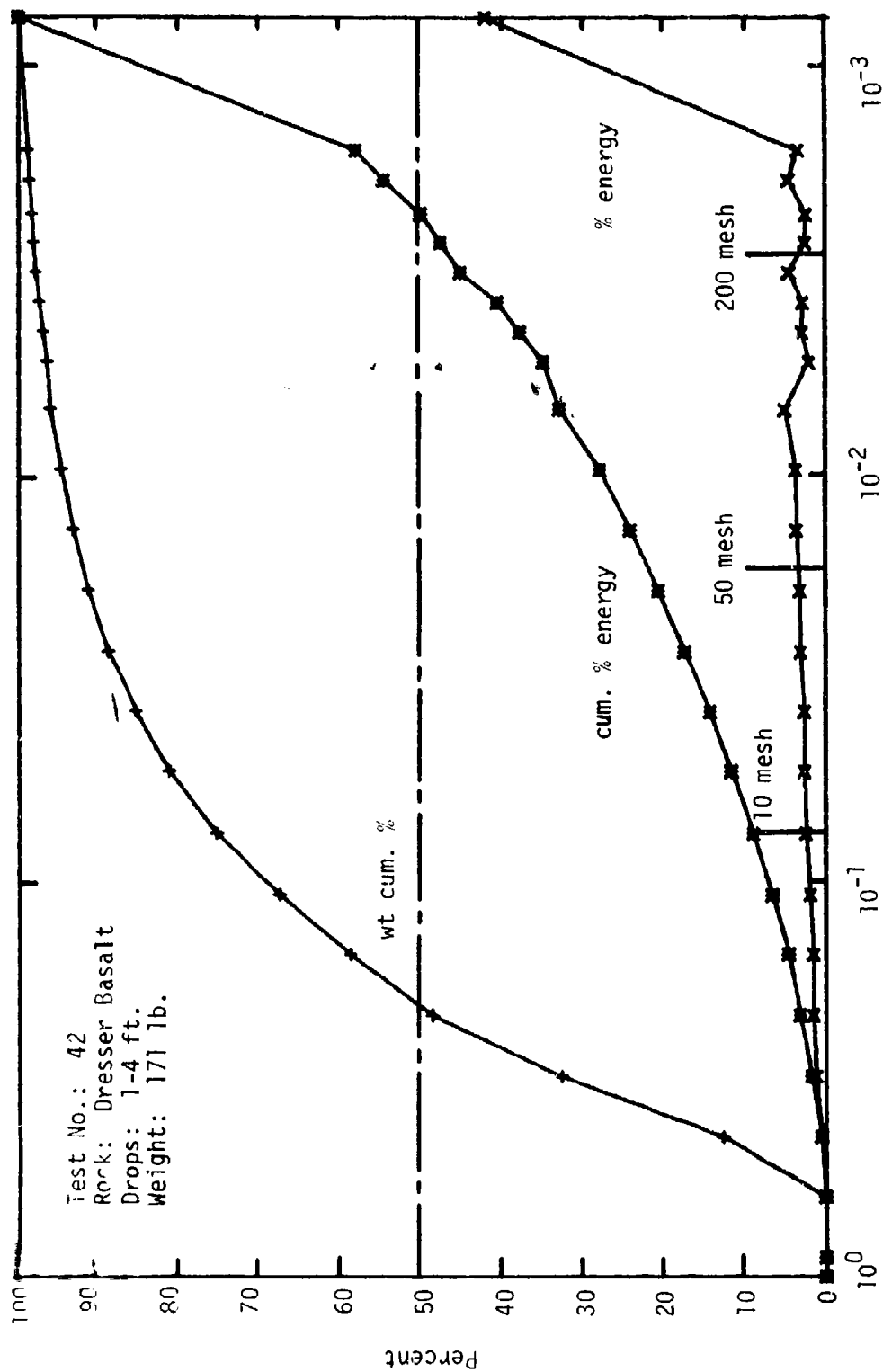
Fig. E-42. Particle Size Analysis - Drop Crushing - Dresser Basalt

Fig. E-43. Particle Size Analysis – Drop Crushing – Dresser Basalt

Test No.: 43
Rock: Dresser Basalt
Drops: 1-5 ft.
Weight: 171 lb.

Fig. E-44. Particle Size Analysis - Drop Crushing - Dresser Basalt

Test No.: 44
Rock: Dresser Basalt
Drops: 1-10 ft.
Weight: 171 lb.

E-44
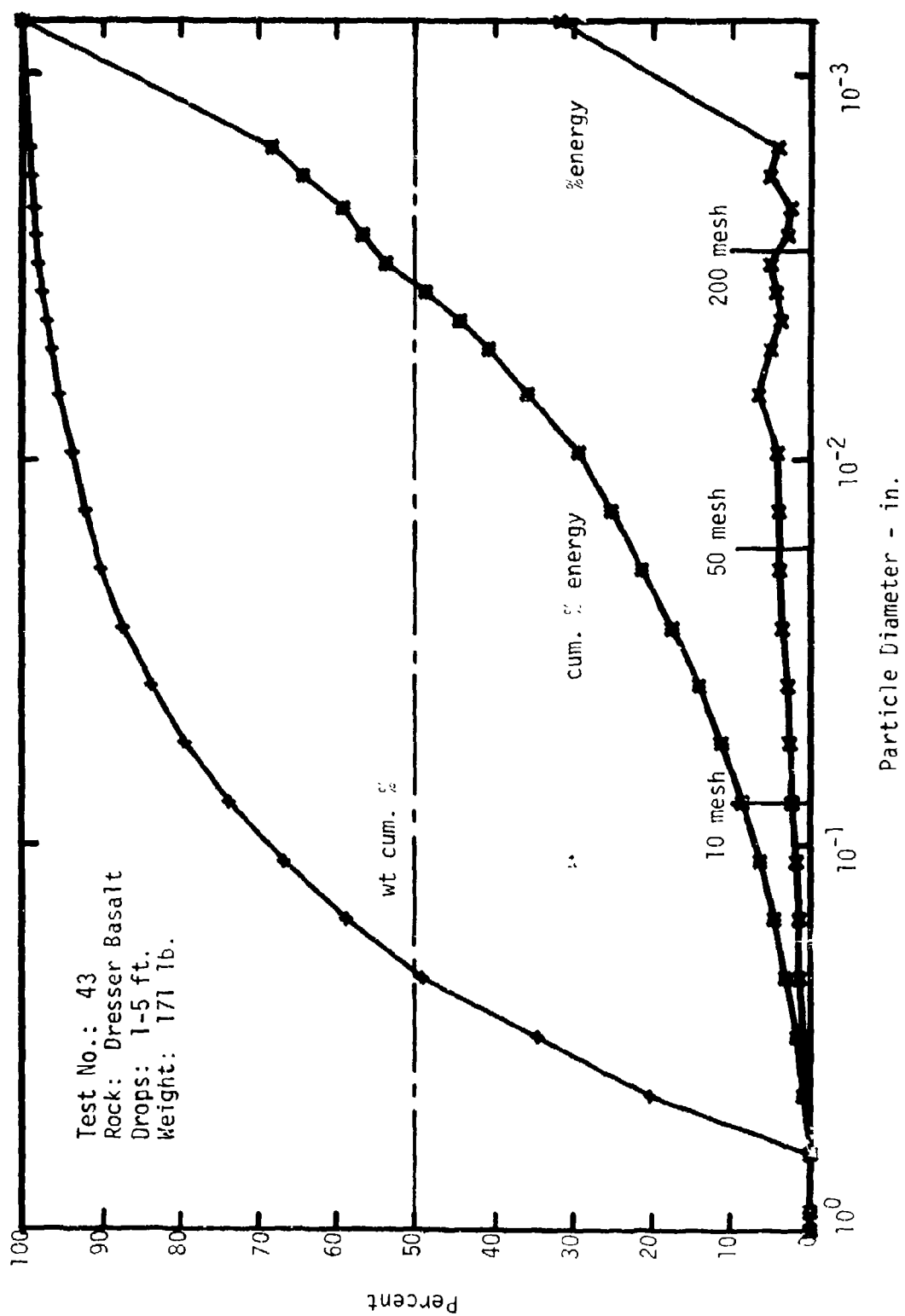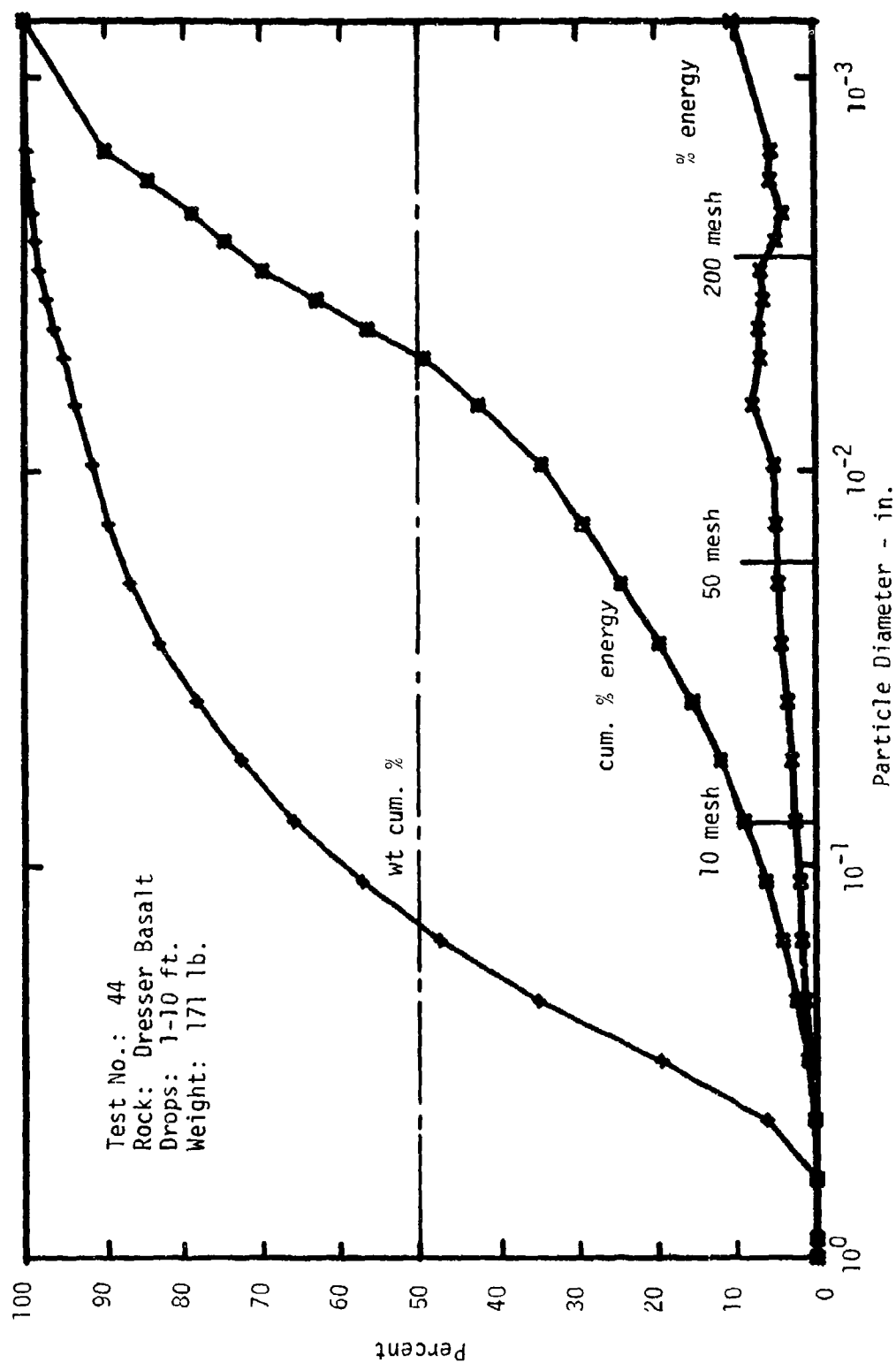
APPENDIX F

PARTICLE SIZE ANALYSIS

FRAGMENTATION TESTS
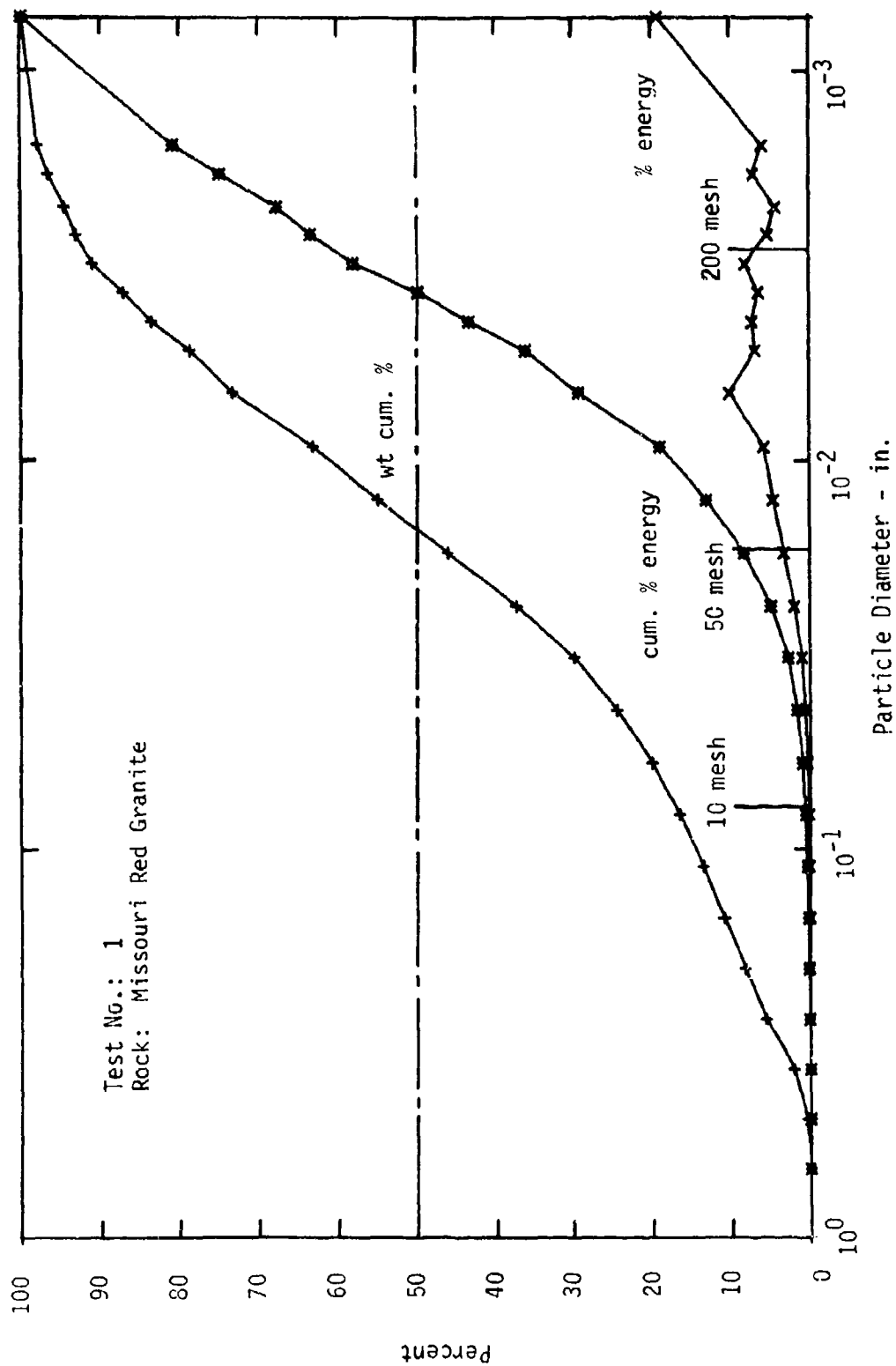
Fig. F-1. Particle Size Analysis - Fragmentation - Missouri Red Granite
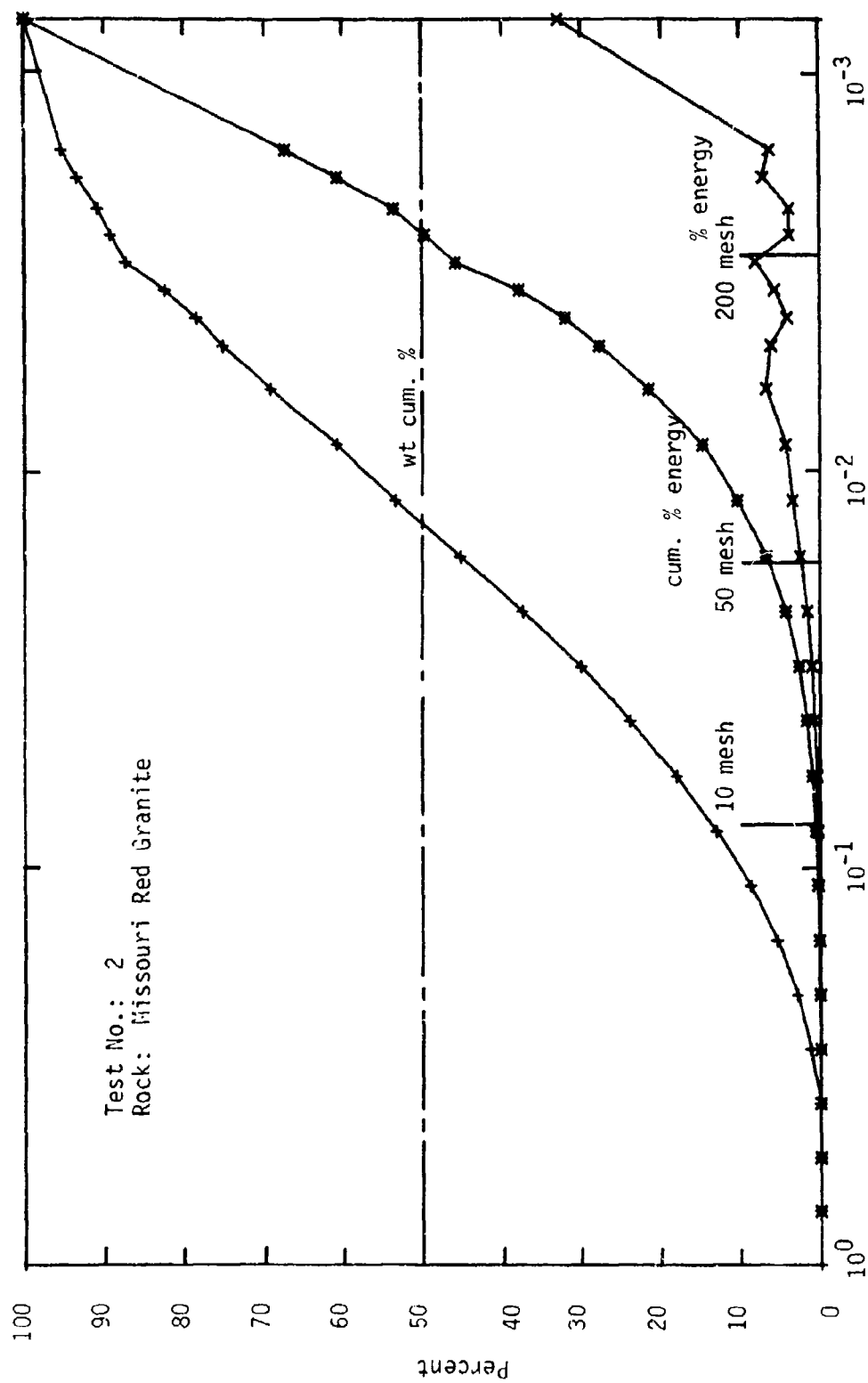
Fig. F-2. Particle Size Analysis - Fragmentation - Missouri Red Granite
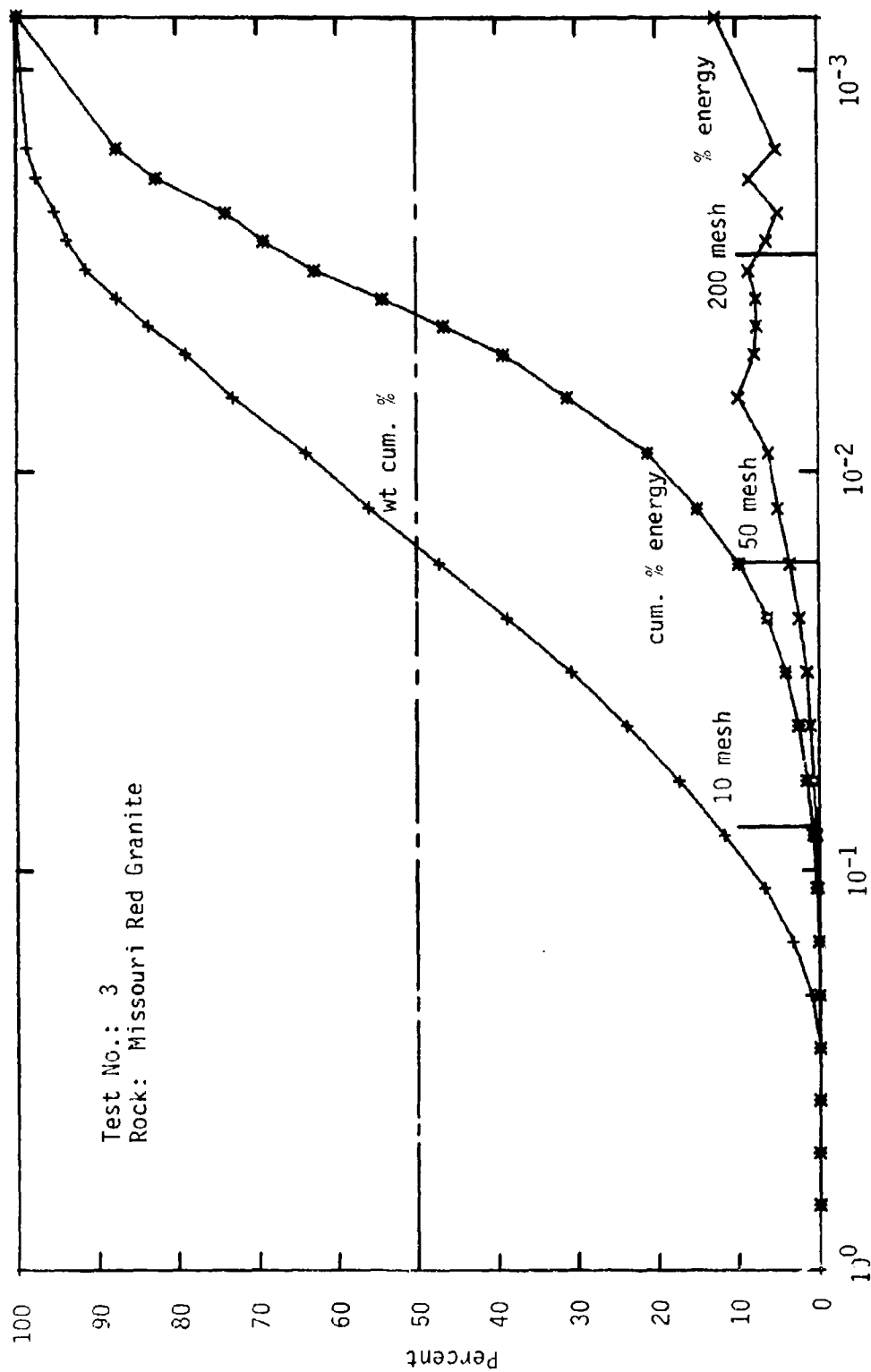
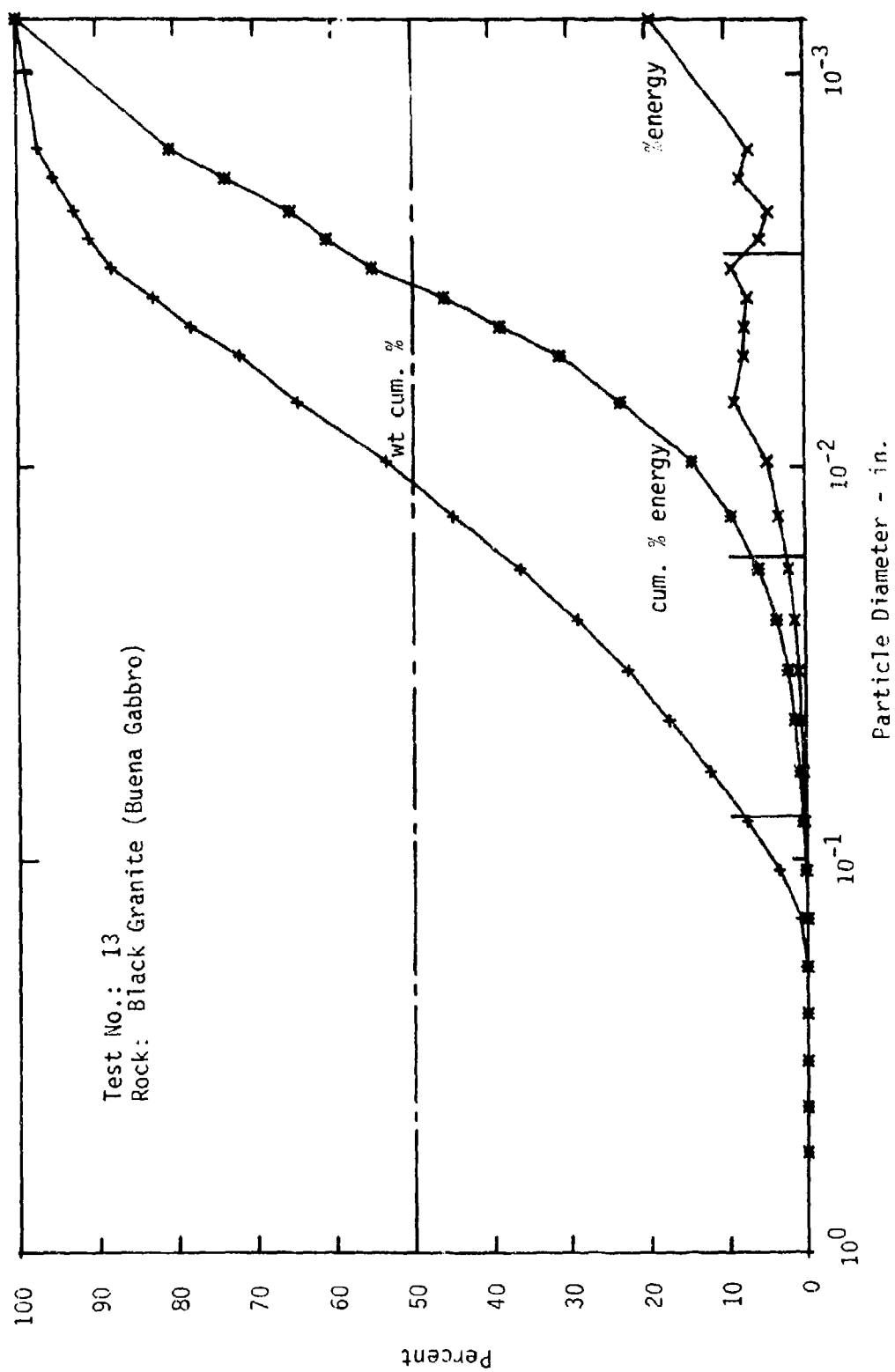Fig. F-3. Particle Size Analysis - Fragmentation - Missouri Red Granite
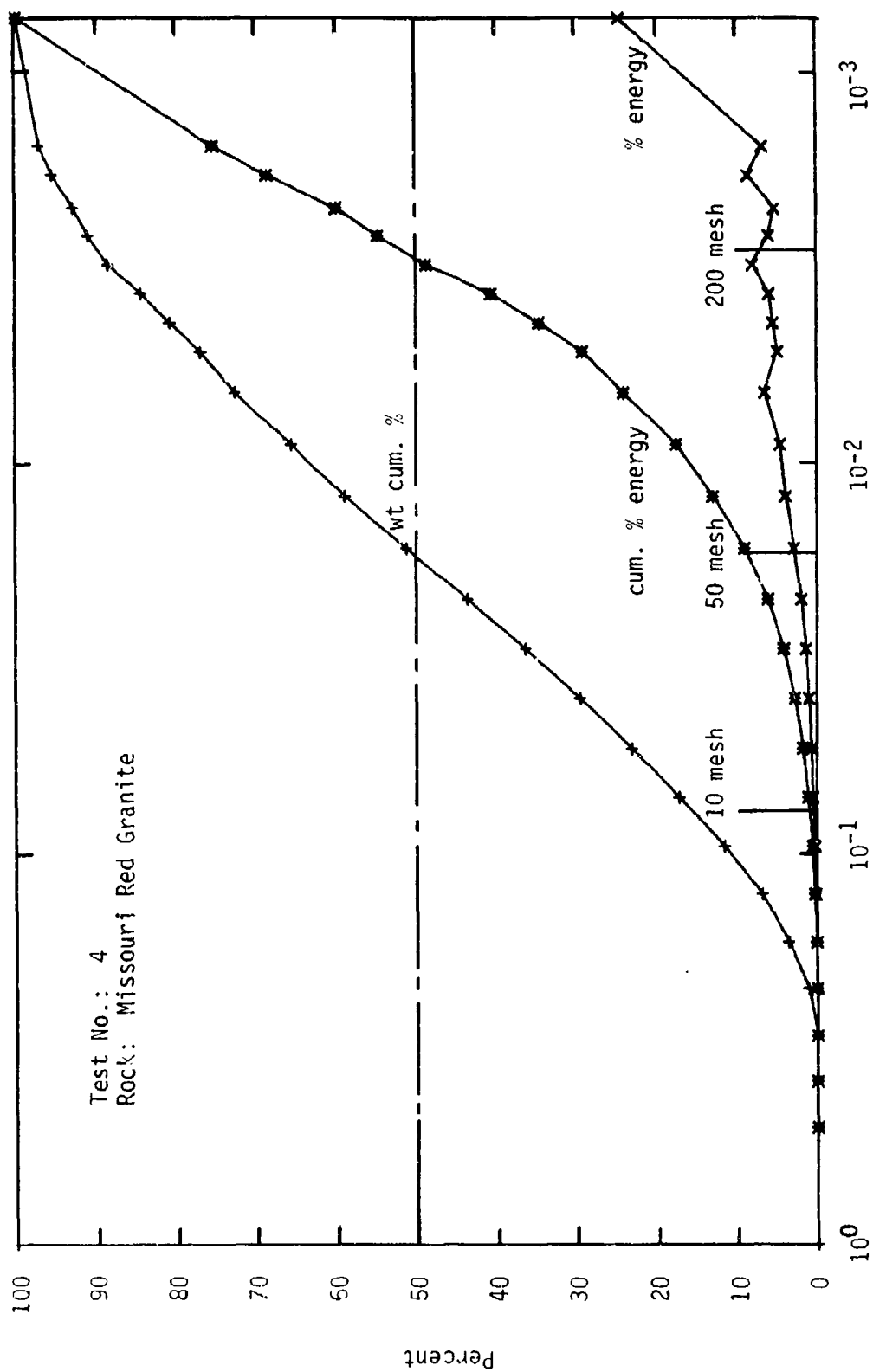
Fig. F-4. Particle Size Analysis - Fragmentation - Missouri Red Granite

Fig. F-5. Particle Size Analysis – Fragmentation – Missouri Red Granite
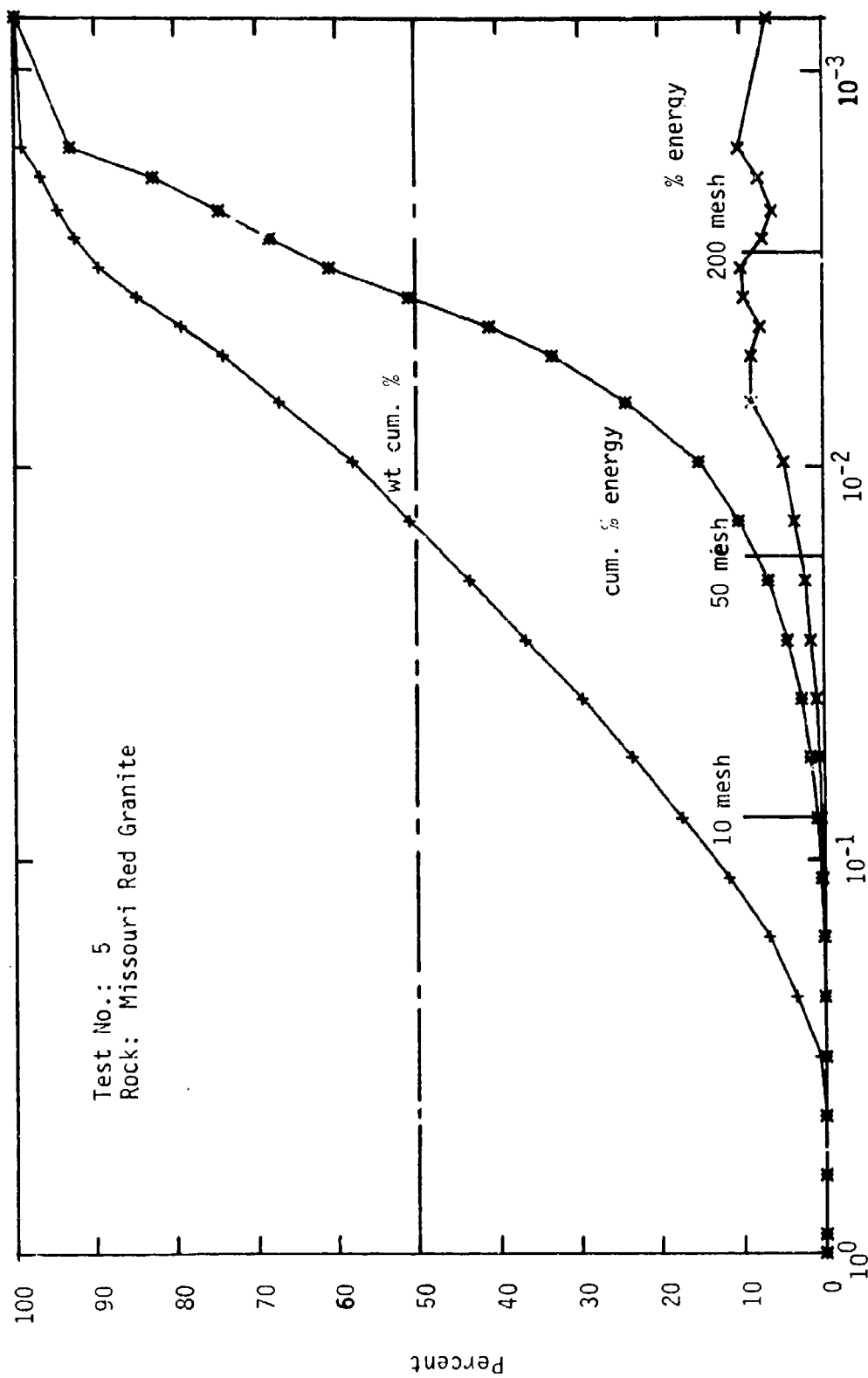
Test No.: 5
Rock: Missouri Red Granite
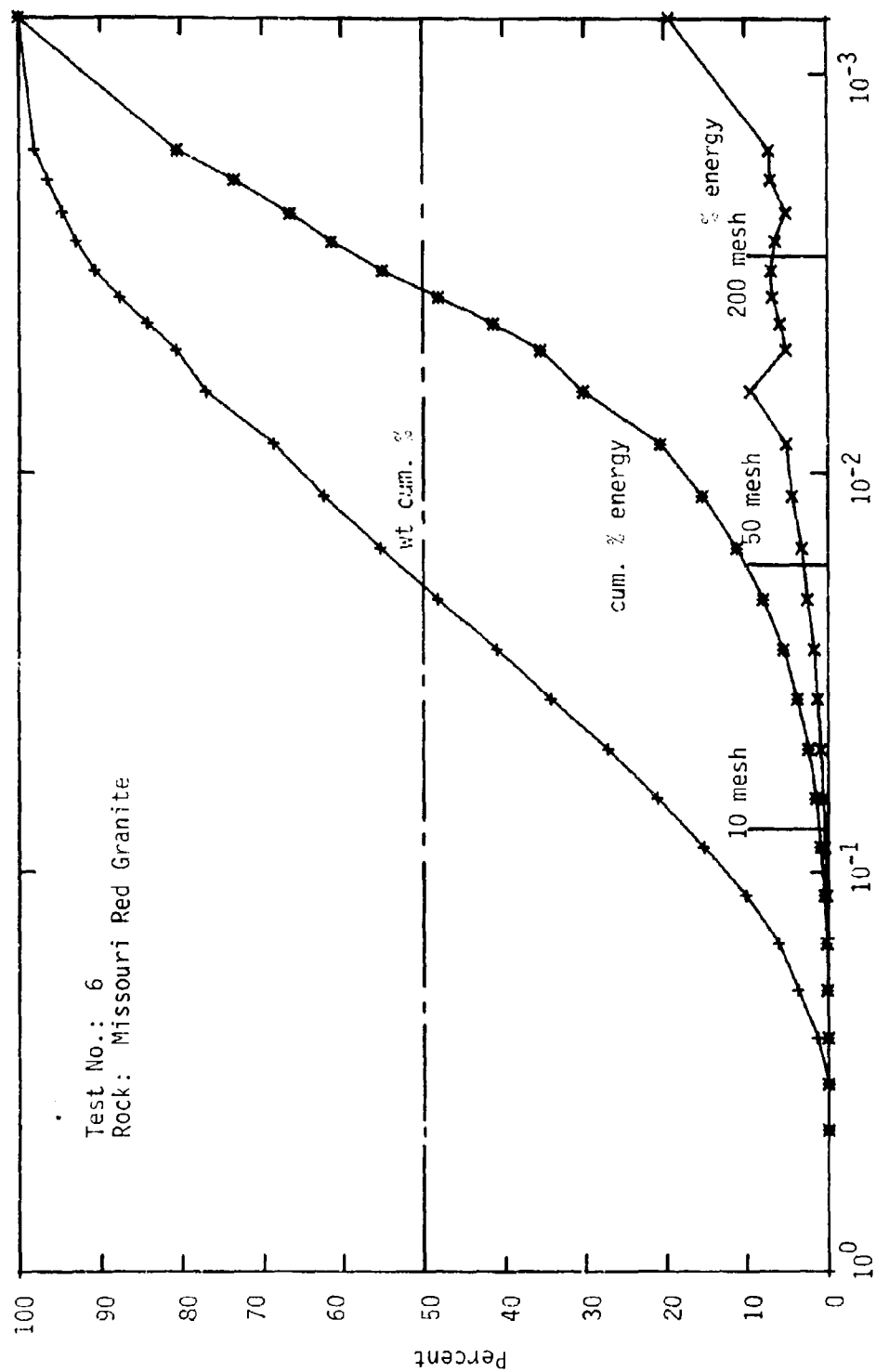
Fig. F-6. Particle Size Analysis - Fragmentation - Missouri Red Granite
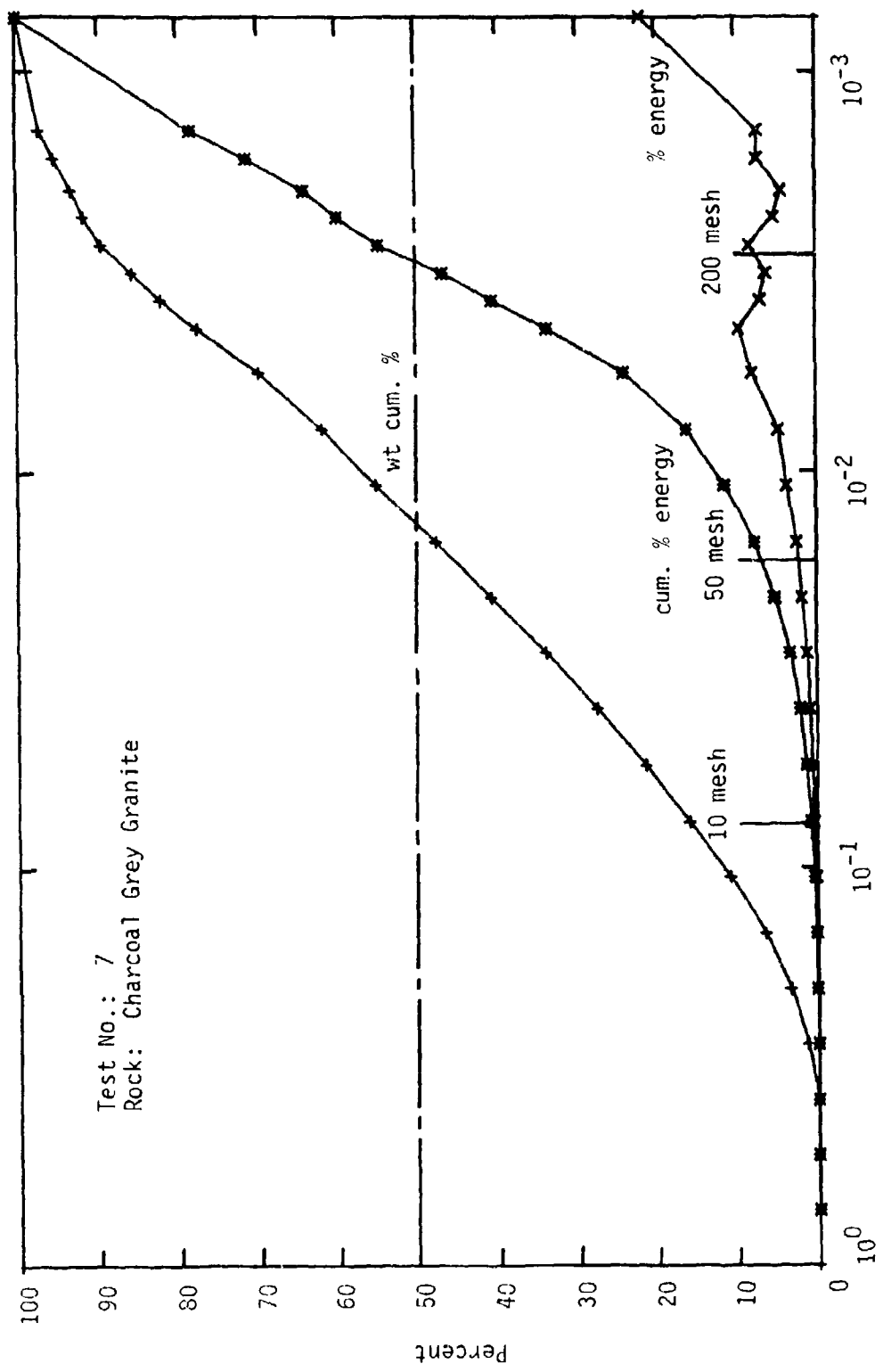
Fig. F-7. Particle Size Analysis - Fragmentation - Charcoal Grey Granite
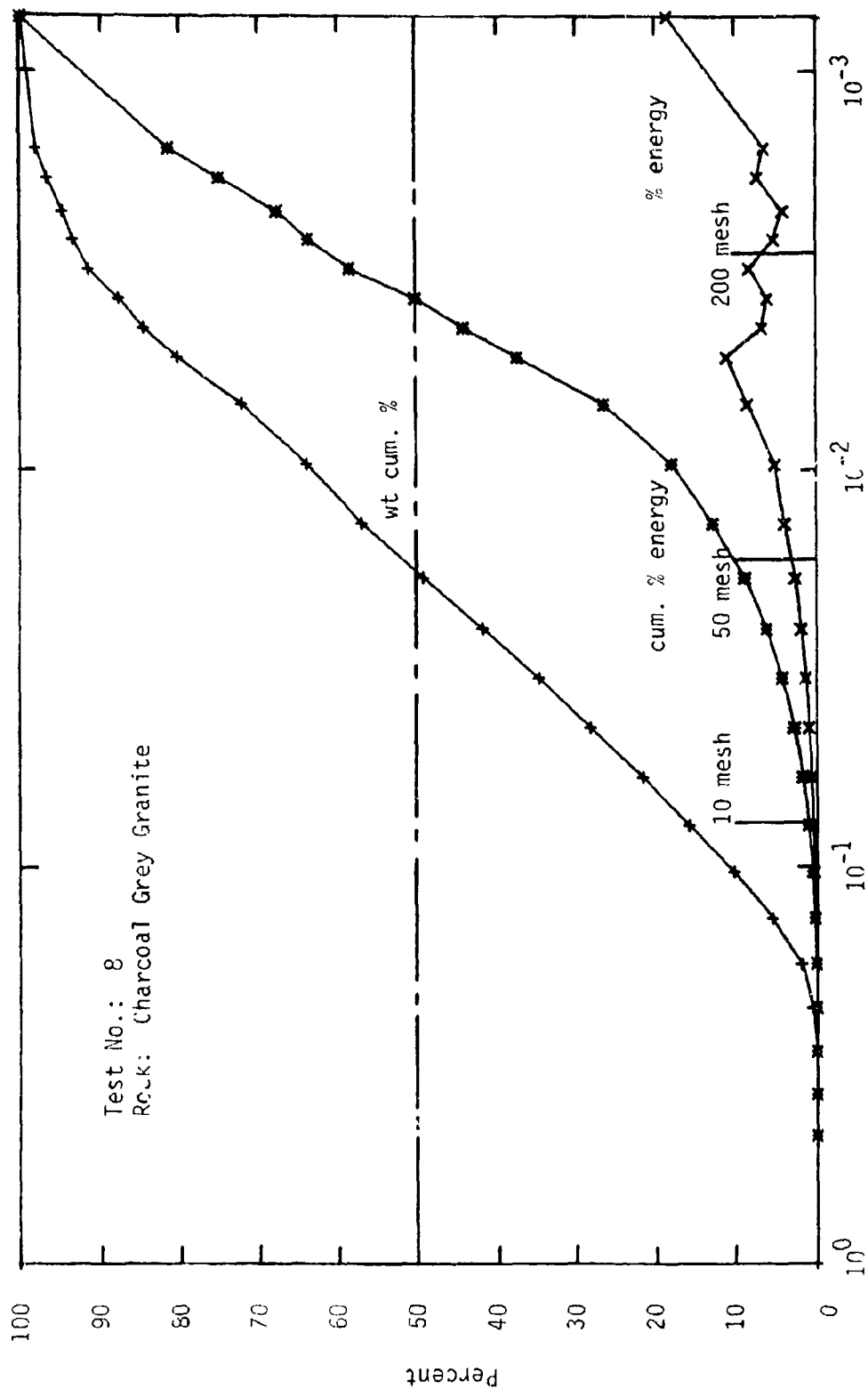
Fig. F-8. Particle Size Analysis - Fragmentation - Charcoal Grey Granite
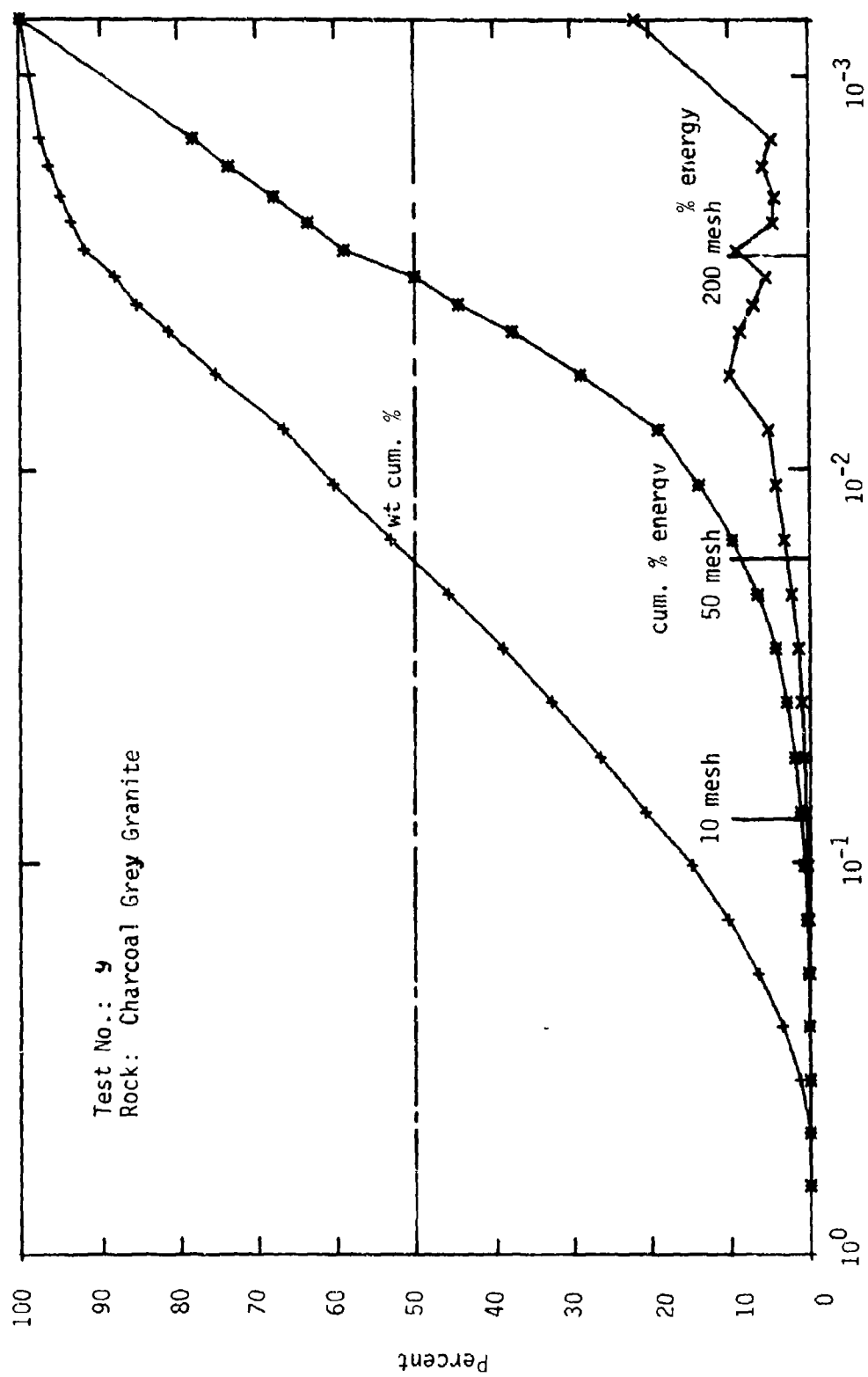
Fig. F-9. Particle Size Analysis - Fragmentation - Charcoal Grey Granite

Test No.: 9
Rock: Charcoal Grey Granite
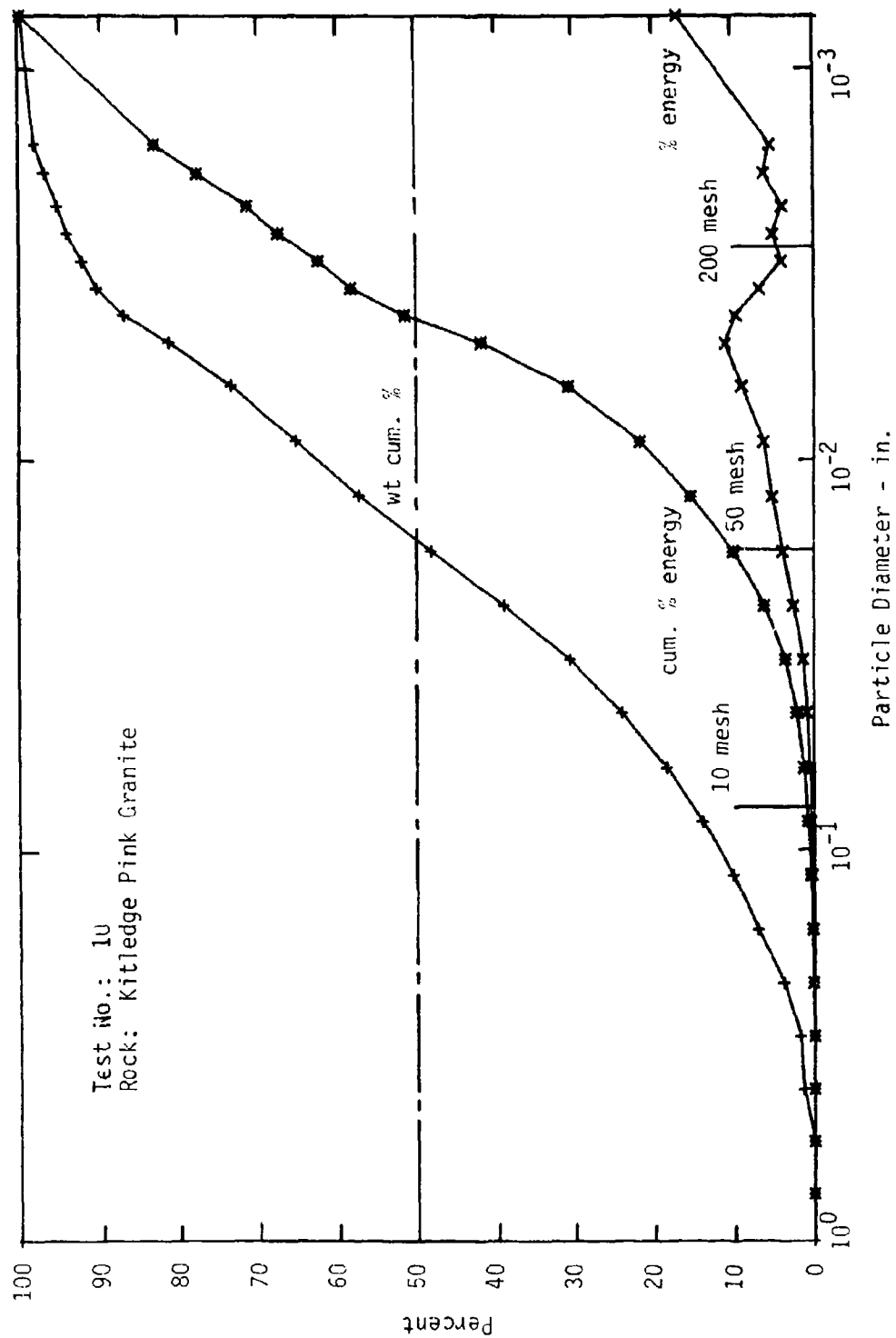
Fig. F-10. Particle Size Analysis - Fragmentation - Kitledge Pink Granite
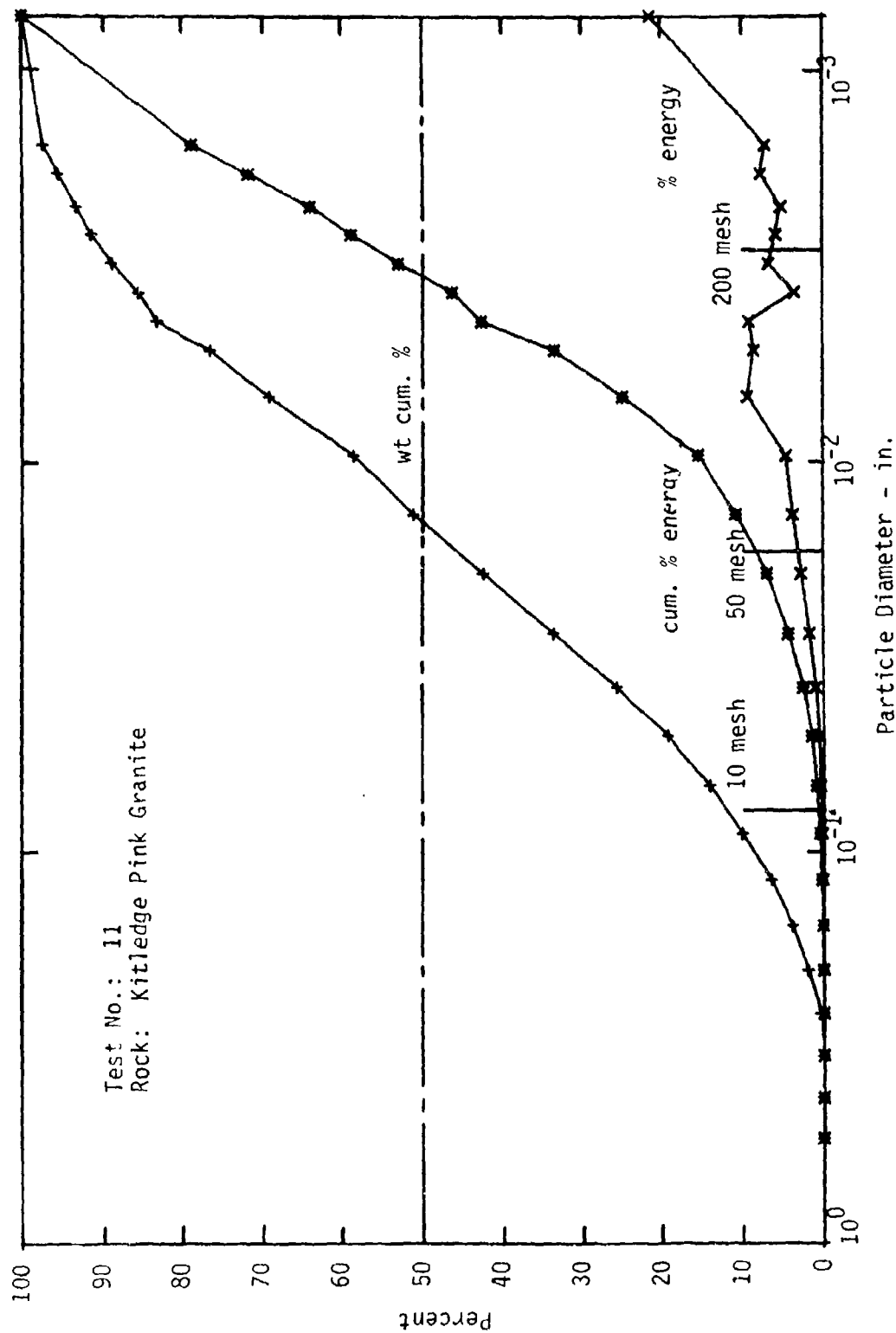
Fig. F-11. Particle Size Analysis - Fragmentation - Kitledge Pink Granite
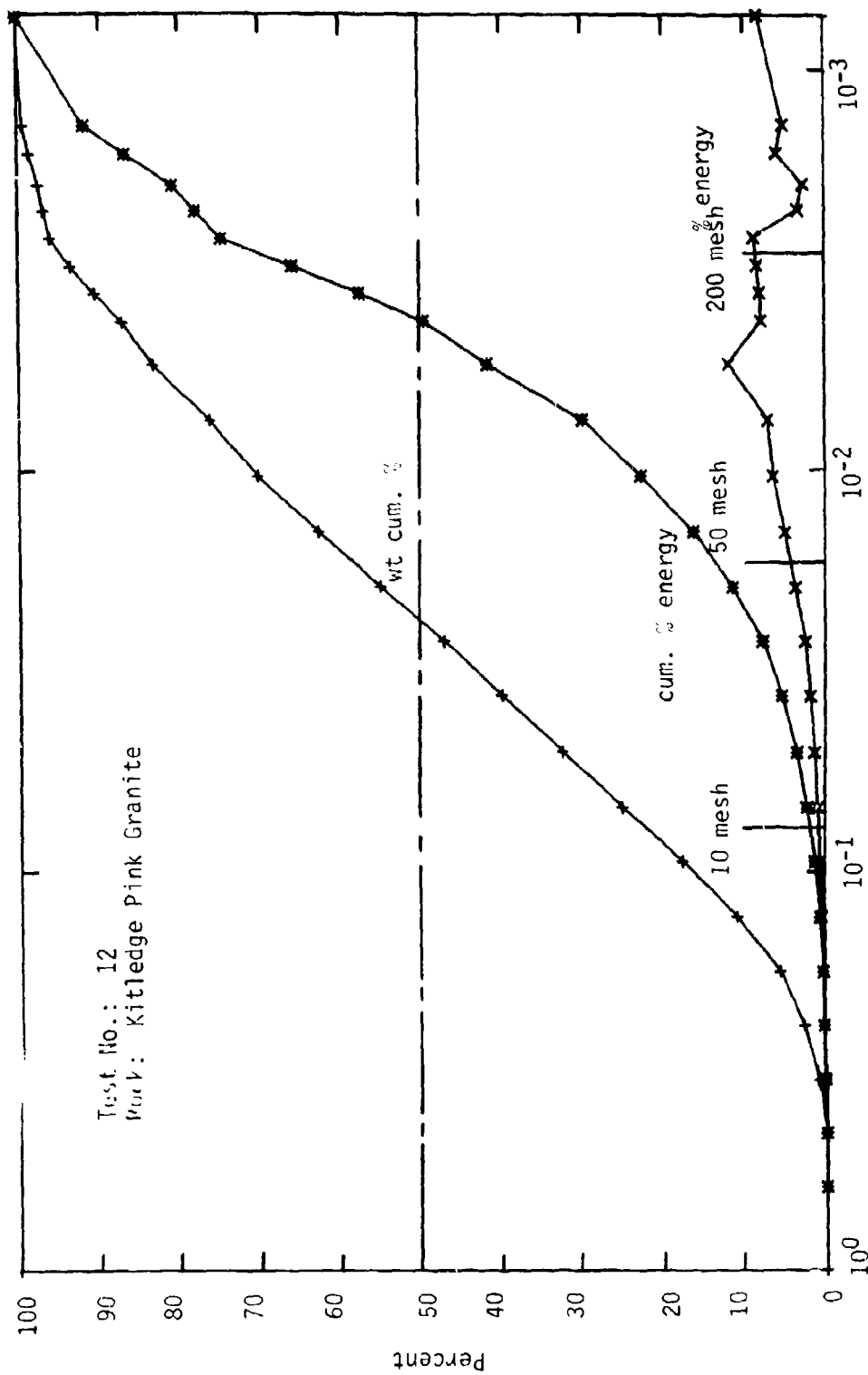
Fig. F-12. Particle Size Analysis - Fragmentation - Kitledge Pink Granite

Fig. F-13. Particle Size Analysis - Fragmentation - Black Granite (Buena Gabbro)
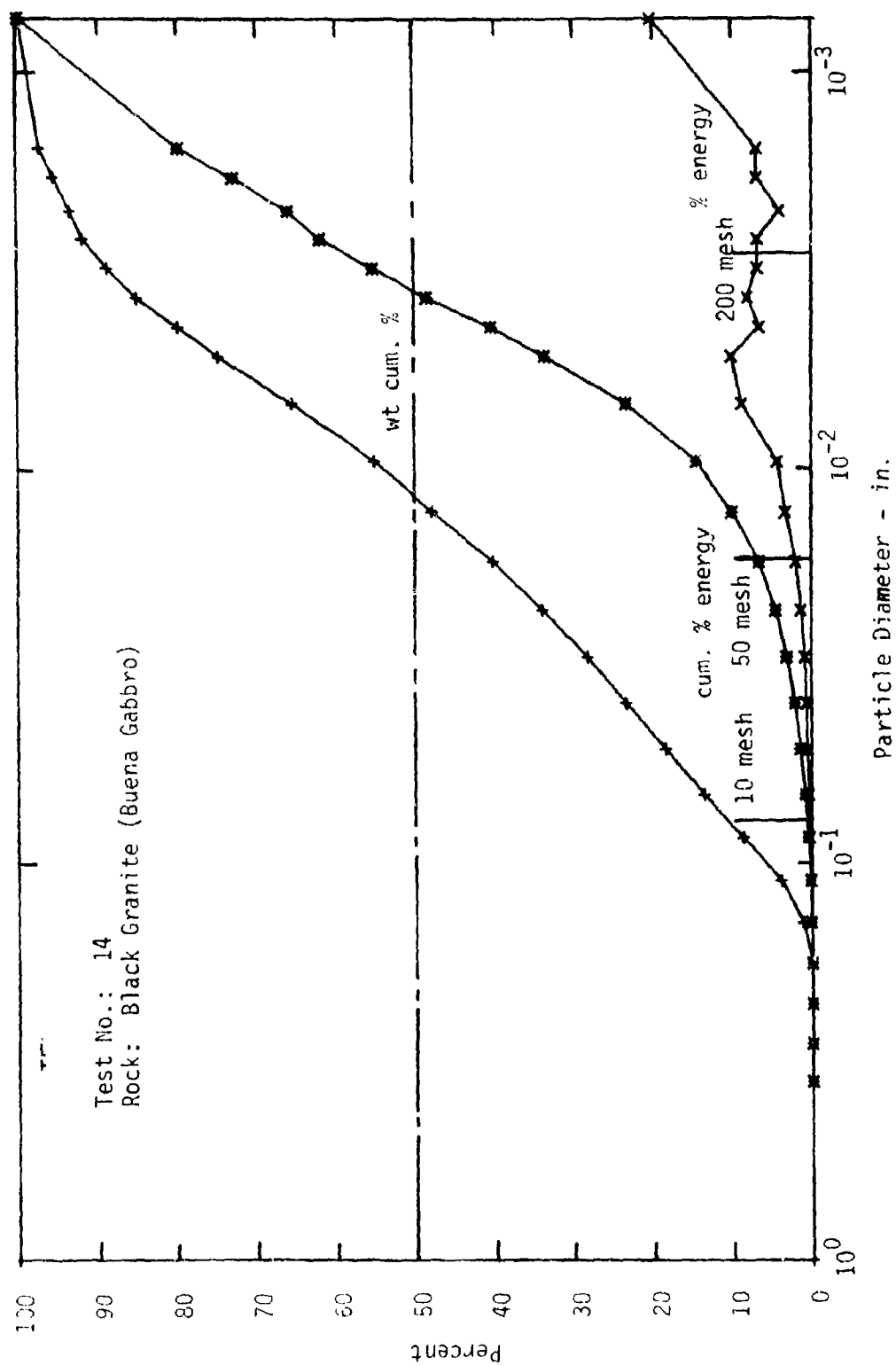
Fig. F-14. Particle Size Analysis – Fragmentation – Black Granite (Buena Gabbro)
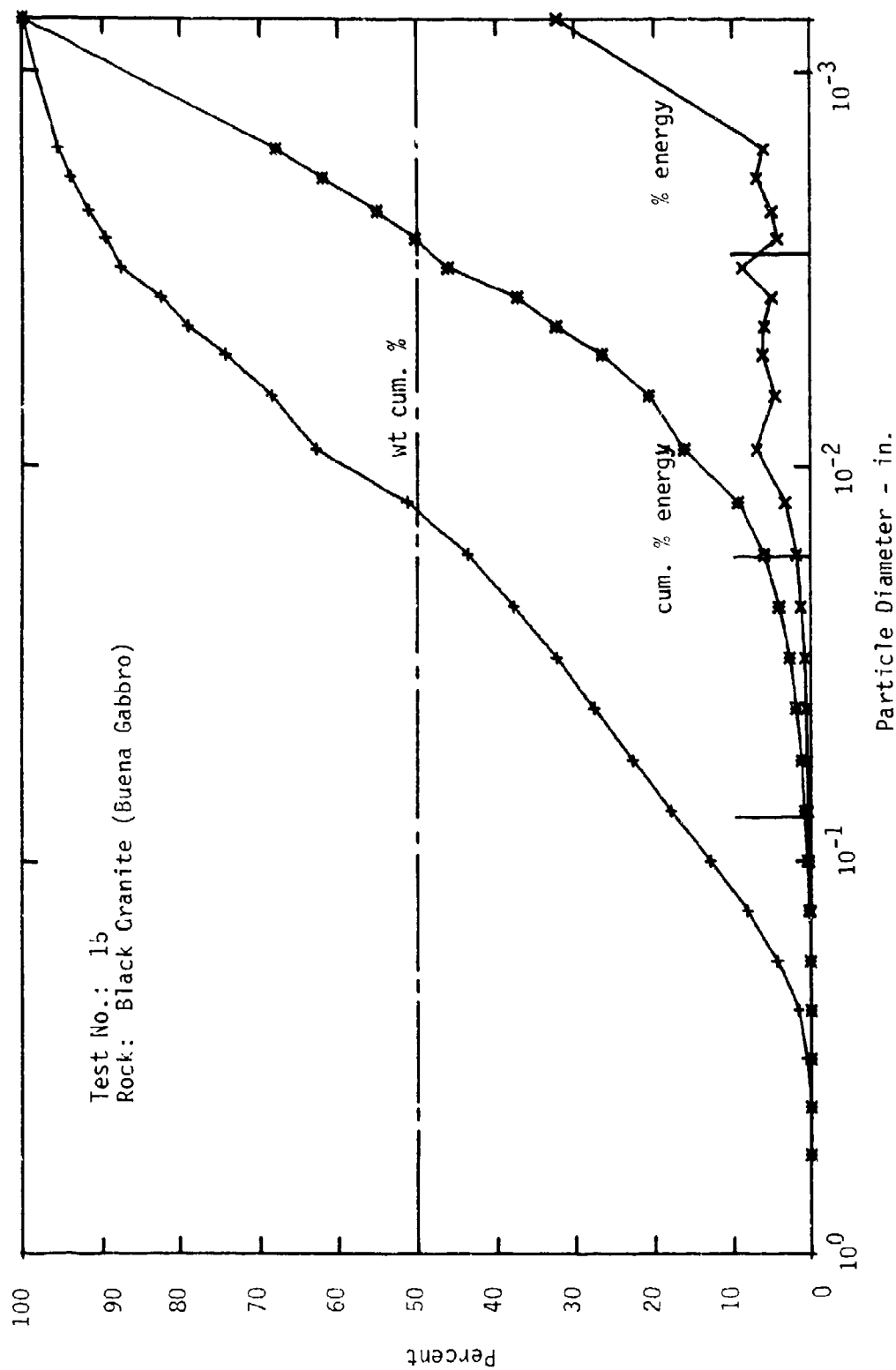
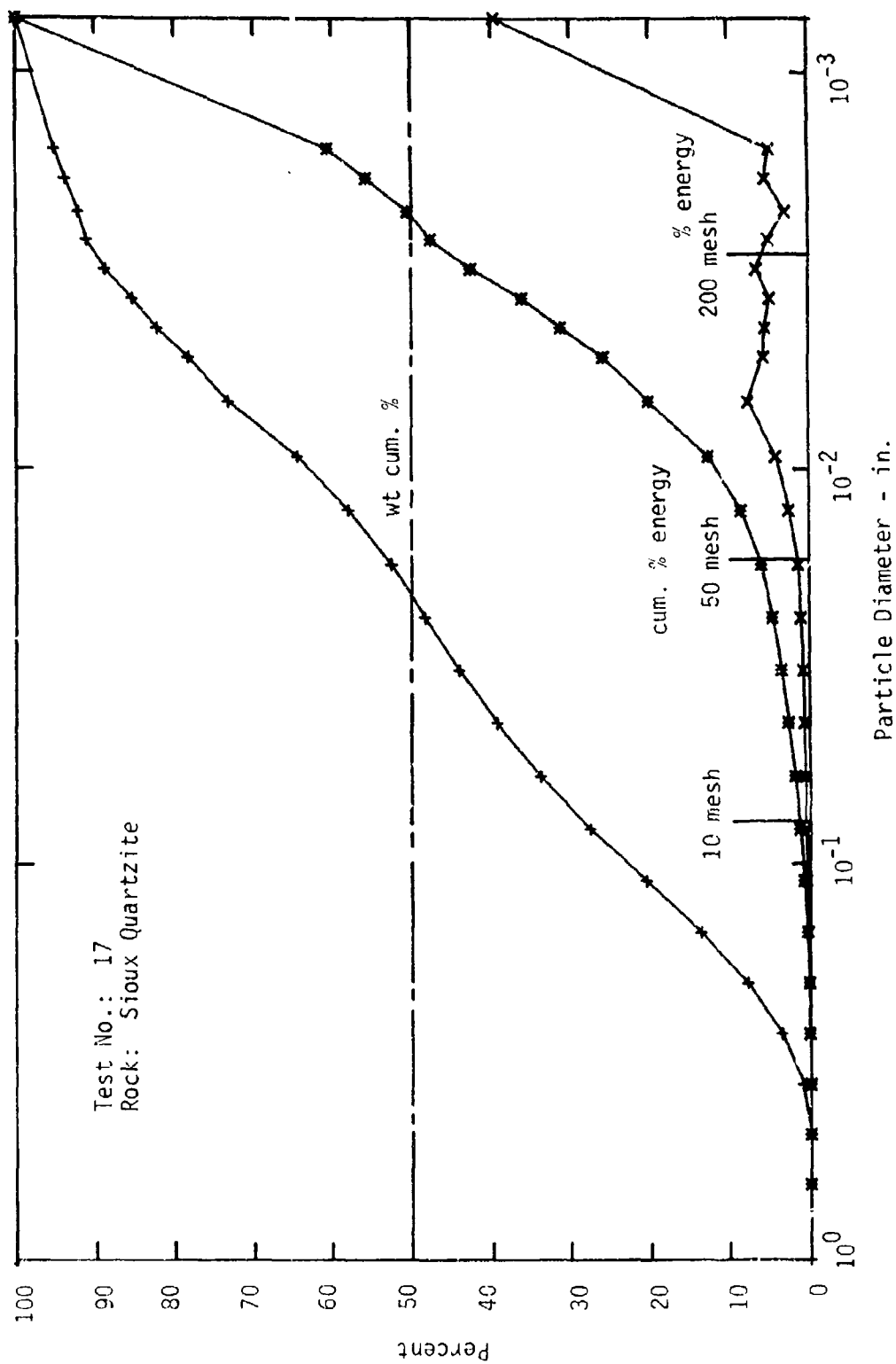Fig. F-15. Particle Size Analysis - Fragmentation - Black Granite (Buena Gabbro)
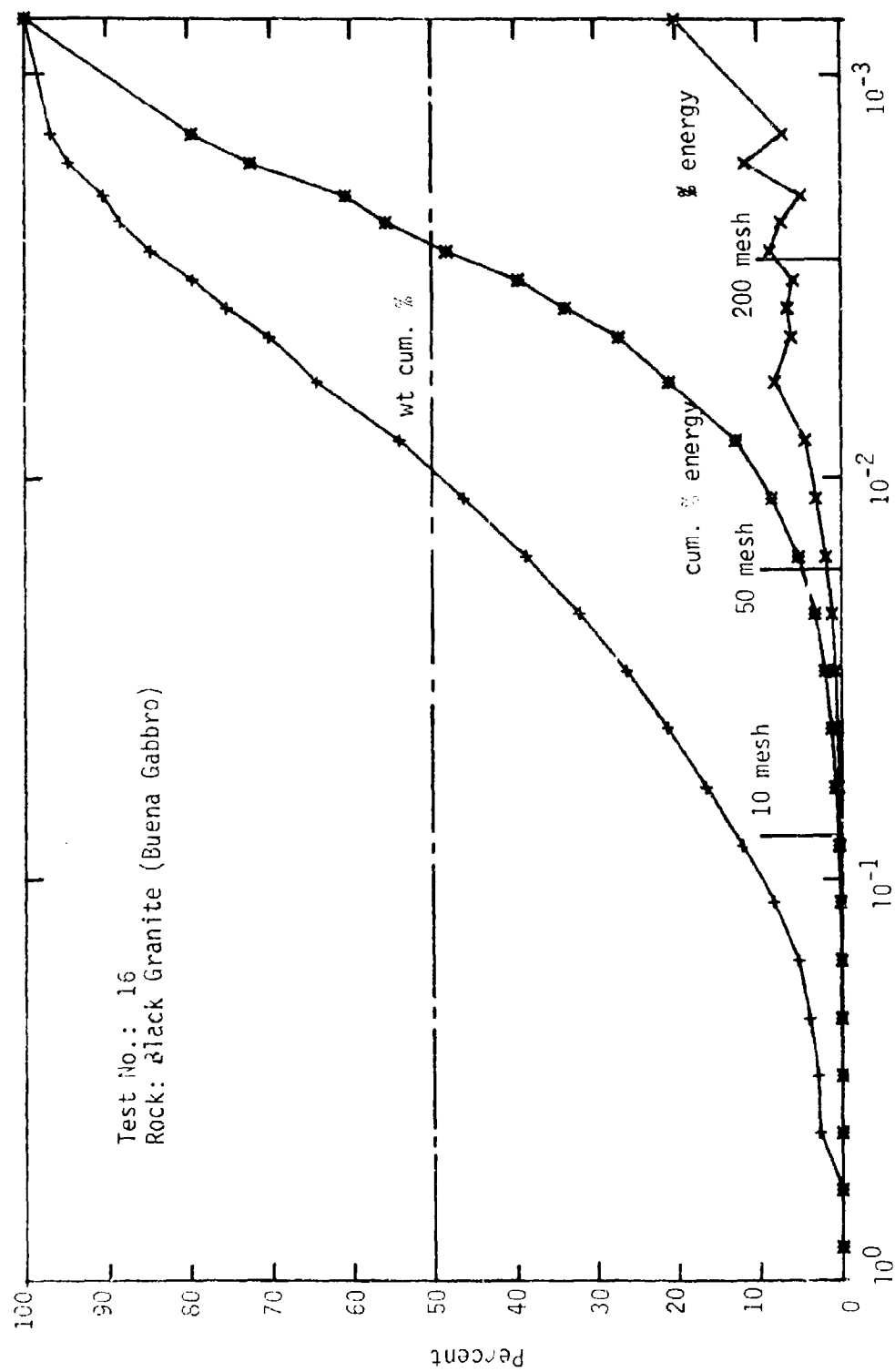
Fig. F-16. Particle Size Analysis - Fragmentation - Black Granite (Buena Gabbro)

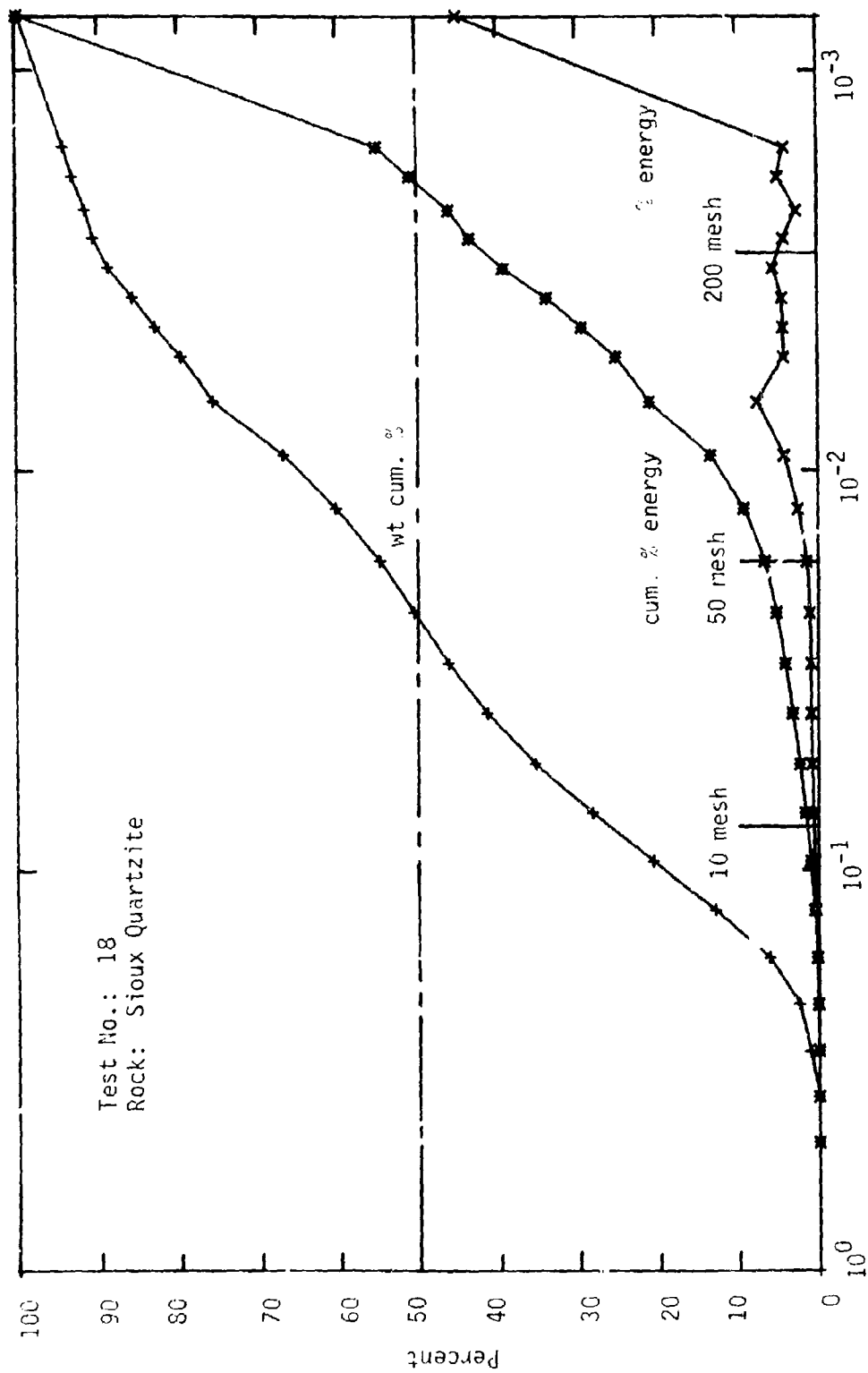Fig. F-17. Particle Size Analysis - Fragmentation - Sioux Quartzite

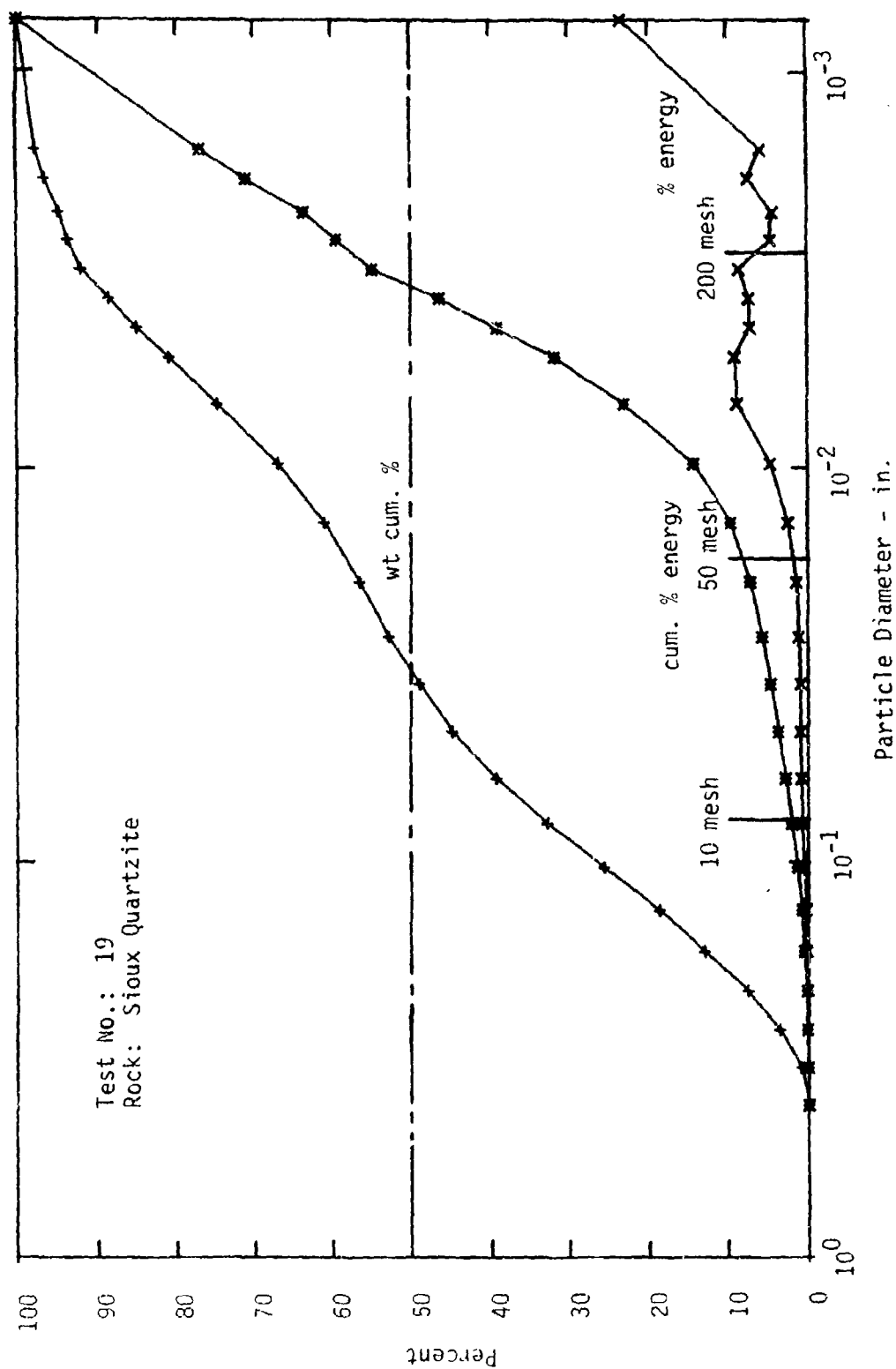Fig. F-18. Particle Size Analysis - Fragmentation - Sioux Quartzite

Test No.: 18
Rock: Sioux Quartzite

Fig. F-19. Particle Size Analysis - Fragmentation - Sioux Quartzite
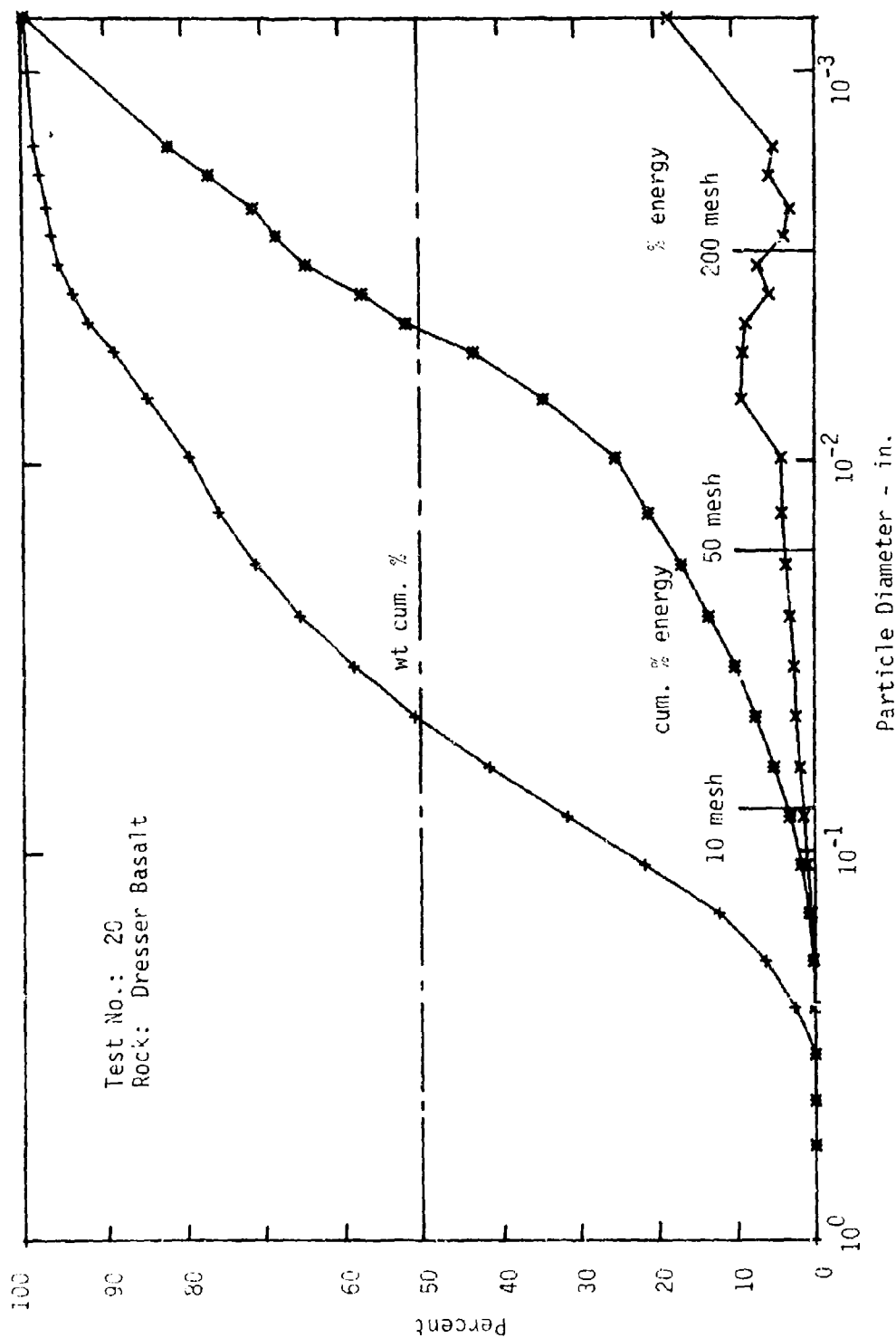
Test No.: 19
Rock: Sioux Quartzite

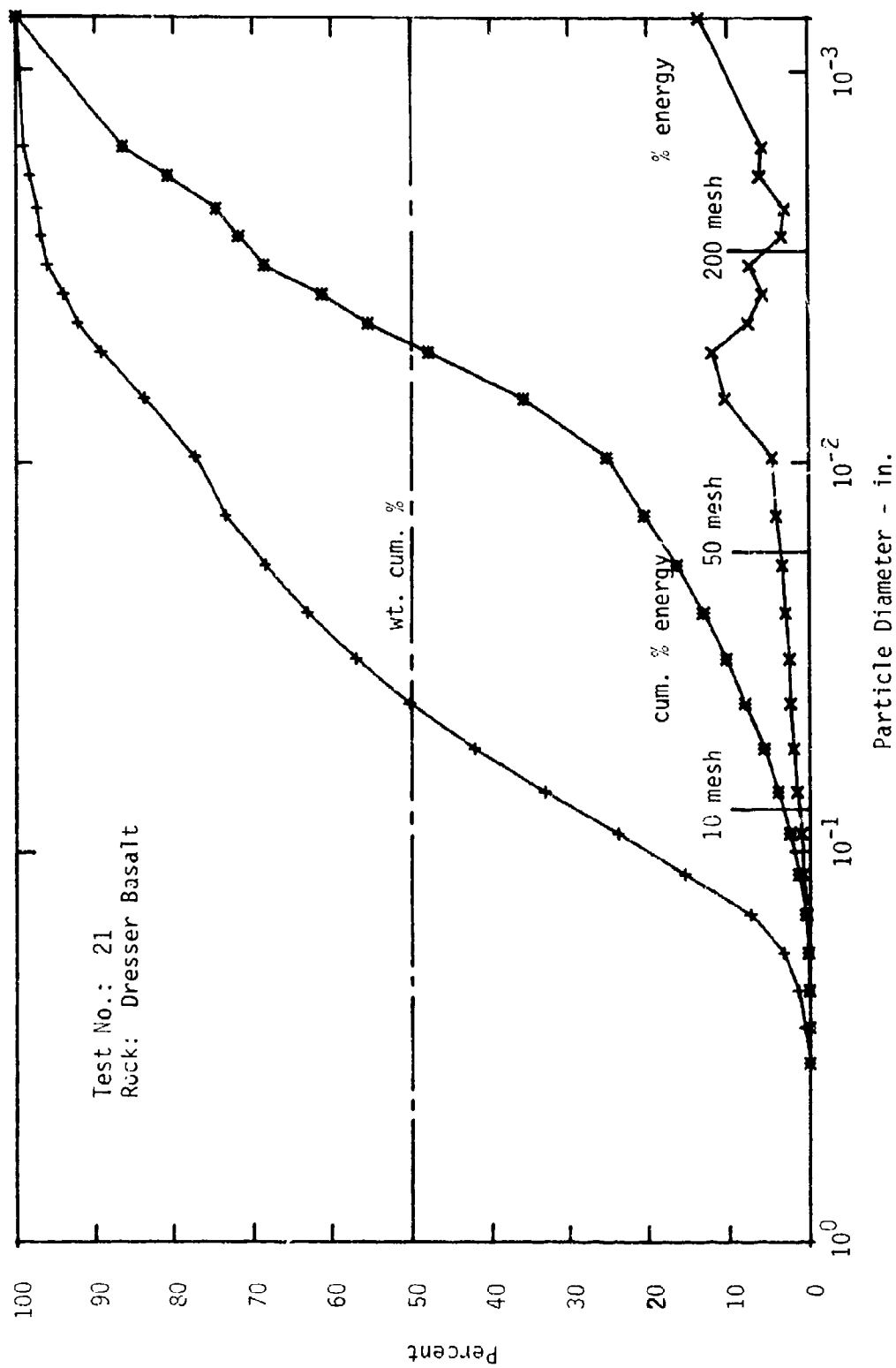Fig. F-20. Particle Size Analysis – Fragmentation – Dresser Basalt

Fig. F-21. Particle Size Analysis - Fragmentation - Dresser Basalt
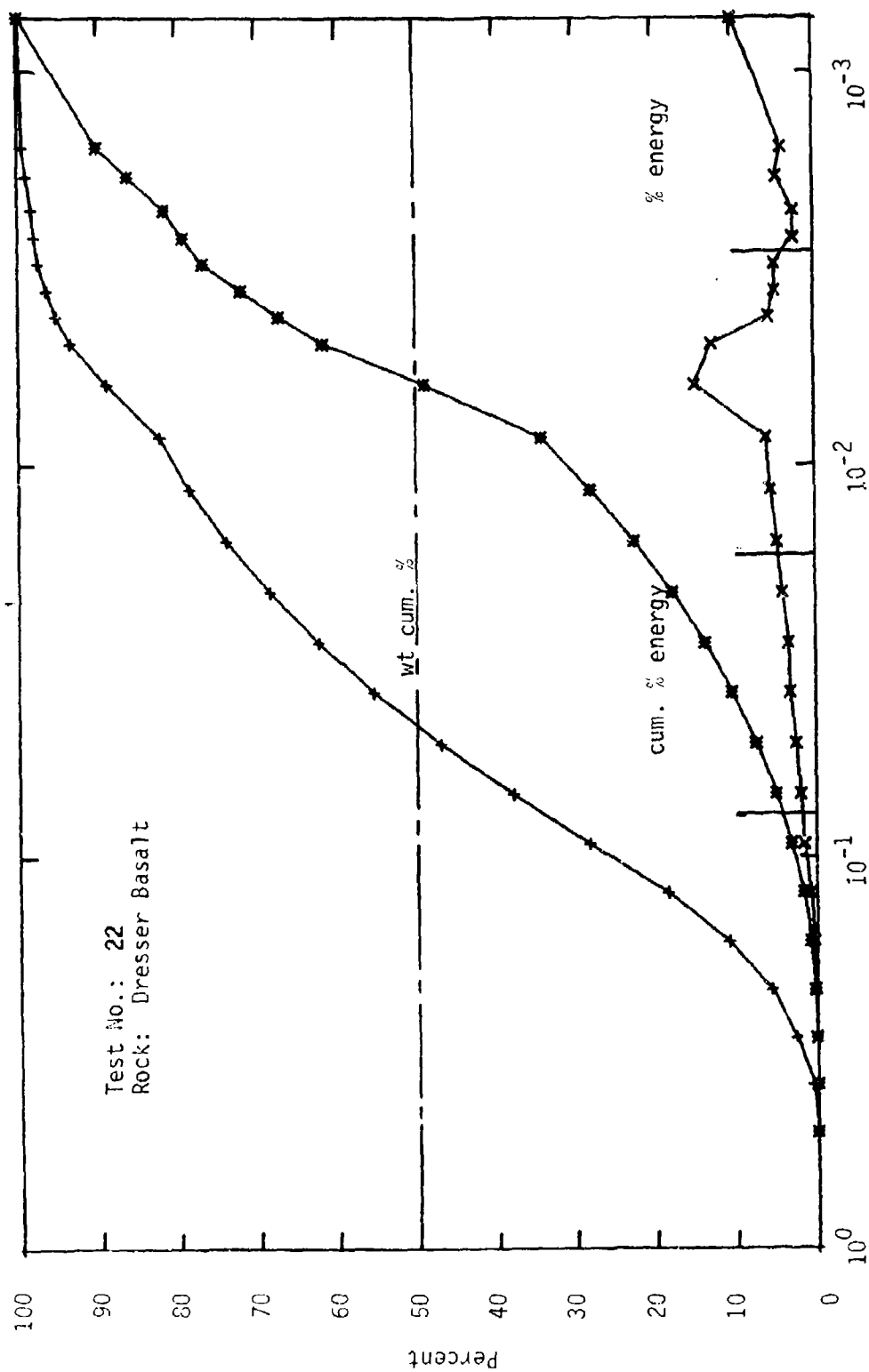
Fig. F-22 Particle Size Analysis – Fragmentation – Dresser Basalt
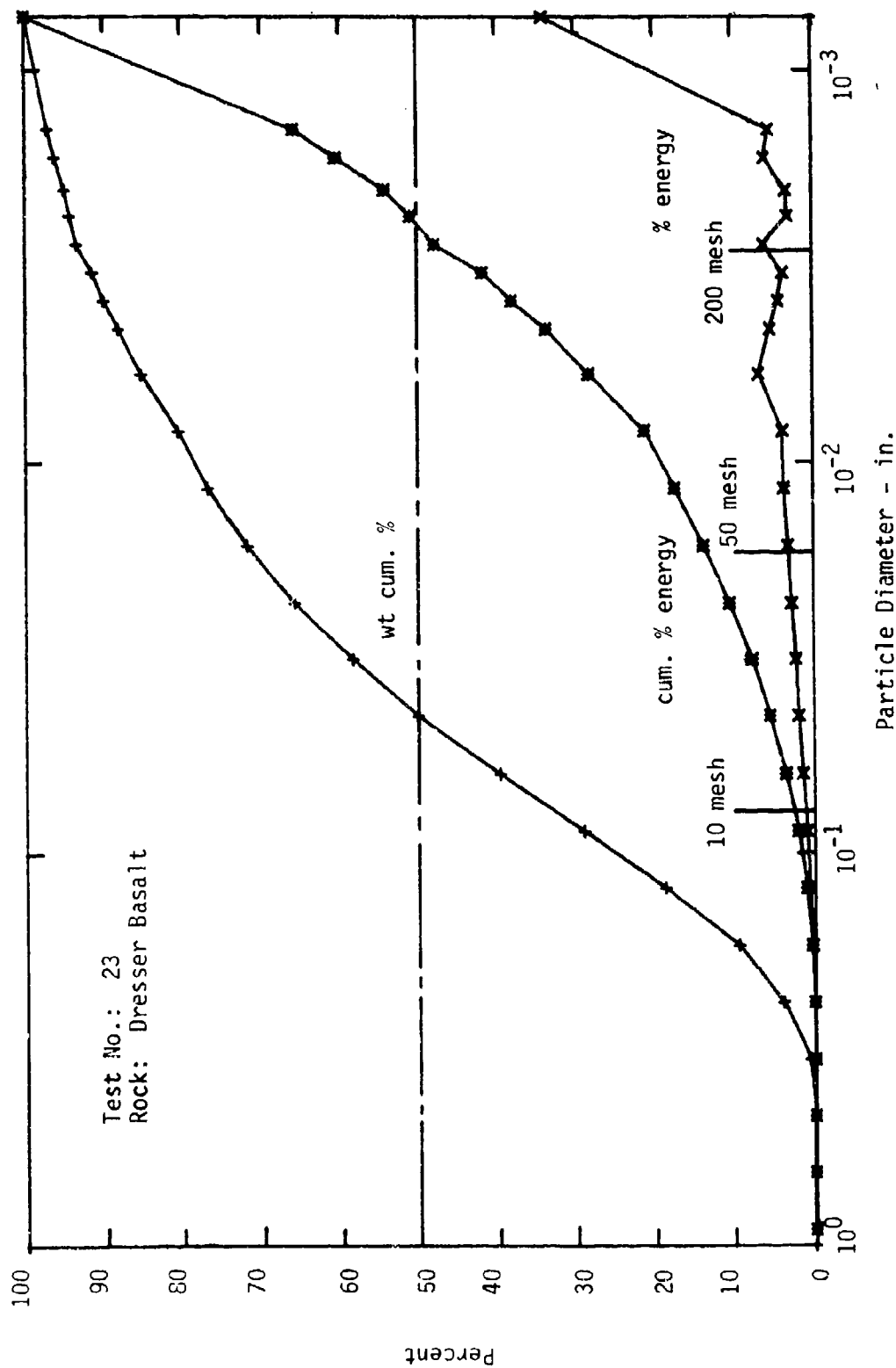
Fig. F-23. Particle Size Analysis - Fragmentation - Dresser Basalt

APPENDIX G

ENERGY TRANSFER IN THE PERCUSSIVE DRILLING OF ROCK

APPENDIX G

Energy Transfer in the Percussive Drilling of Rock

In percussive drilling, a piston is caused to accelerate along a cylinder by the application of compressed air to one side of the piston. The piston then impacts a drill steel, transferring all or part of its energy to the steel in the form of a strain wave. It is known that the amount of energy transferred to the steel is proportional to

$$\int_{t_i}^{t_f} \varepsilon^2(t)dt \qquad (G-1)$$

in the first incident wave, where $\varepsilon(t)$ is the strain at a particular point in the steel and (t_f-t_i) is the duration of the strain wave. The above assumes that the reflected wave does not interfere with the incident wave at the measuring point.

Rewriting (H-1) as an equation, we have

$$W_i = K\int_{t_i}^{t_f} \varepsilon^2(t)dt \qquad (G-2)$$

where K is the appropriate constant of proportionality and W_i is the amount of energy transferred. The constant K can be determined by impacting the drill steel with a projectile of known energy and dividing by the integral of the square of the resulting strain wave, under the assumption that 100 percent of the energy is transferred from the projectile to the steel.

The amount of energy transferred to the rock will be determined by monitoring the longitudinal strain waves in the drill steel. This was accomplished by Lindquist and Anderson (Ref. 76).

The output of the bridge circuit is a voltage proportional to the longitudinal strain at the bridge location.

That is,

$$v(t) = K_1 \varepsilon(t) \tag{G-3}$$

where $v(t)$ is the output voltage and K_1 is the constant relating strain
to voltage. Equation (H-2) can now be written as

$$W_i = K \int_{t_i}^{t_f} \varepsilon^2(t)dt = K K_1^2 \int_{t_i}^{t_f} v^2(t)dt \tag{G-4}$$

Assuming that the reflected wave does not interfere with the incident wave,
the energy in the first incident wave is

$$W_{i_1} = K K_1^2 \int_{T_{i_1}} v_{i_1}^2(t)dt \tag{G-5}$$

where T is the time interval during which the particular strain pulse is
being measured and where the subscript v_i denotes the fact that we have an
incident wave and the second subscript tells us we have the first wave of
a series. Similarly, for the energy in the first reflected wave we have

$$W_{r_1} = K K_1^2 \int_{T_{r_1}} v_{r_1}^2(t)dt \tag{G-6}$$

where the subscript r denotes a reflected wave. Note that the limits on
the integrals in (H-5) and (H-6) indicate that integration is performed
only over the duration of each strain wave. Further, since we have assumed
that the incident and reflected waves do not interfere, the integration
intervals are disjointed in time. This can be accomplished by proper selec-
tion of strain gage bridge location and length of drill steel for a parti-
cular hammer. Expressions for the energy in the second incident and re-
flected waves, respectively, are

$$W_{i_2} = K K_1^2 \int_{T_{i_2}} v_{i_2}^2(t)dt \tag{G-7}$$

$$W_{r2} = K\, K_i^2 \int_{T_{r2}} v_{r2}^2\, (t)dt \qquad (G\text{-}8)$$

The amount of energy transferred to the rock on the first incident wave is merely the difference between the energy in the first incident wave and the energy in the first reflected wave.* That is,

$$E_1 = W_{i_1} - W_{r_1} \qquad (G\text{-}9)$$

where E_1 is energy transferred on the first incident wave. Similarly, the energy transferred by the second wave, E_2; the third wave E_3, etc., is

$$E_2 = W_{i_2} - W_{r_2}$$

$$E_3 = W_{i_3} - W_{r_3} \qquad (G\text{-}10)$$

$$E_n = W_{i_n} - W_{r_n},$$

where n is the number of terms required to specify the amount of energy transferred for each piston blow. Experimental evidence shows this number to be less than ten. Since at most ten reflections are significant, the energy of each piston blow is transferred before the next piston blow occurs.

From the above discussion, it is seen that energy transferred for each piston blow is (E_T),

$$E_T = \sum_{j=1}^{n} E_i = \sum_{j=1}^{n} (W_{ij} - W_{rj}) = \sum_{j=1}^{n} W_{ij} - \sum_{j=1}^{n} W_{rj} \qquad (G\text{-}11)$$

For a conventional drill steel and bit, the incident wave is compressive and the reflected wave is tensile whether the bit is in intimate contact with the rock or whether it is not in contact, the latter occurring at low thrusts. The reason for this sign reversal is that the effective impedance

---

*It is assumed that there are no losses in the steel.

of the rock is less than that for the drill steel and that additional re-
flection occurs because of the poor coupling between the wedge bit and
the rock. Consequently, the output voltage of the bridge circuit will
be positive when the wave is compressive and negative when the wave is
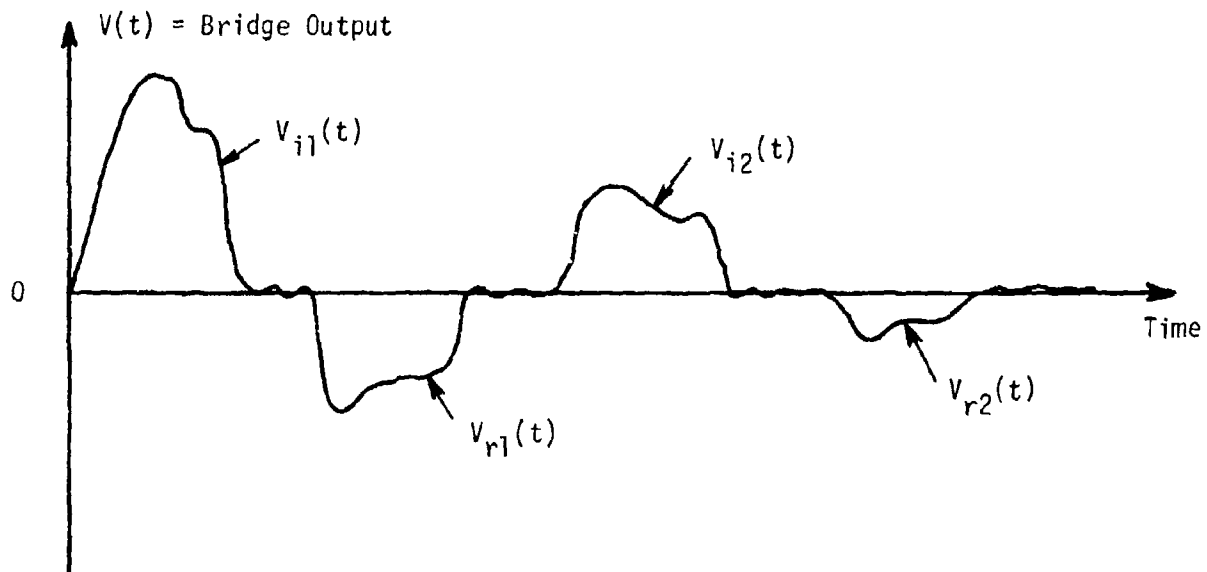tensile (Fig. G-1)

Fig. G-1. Typical Output of Bridge Circuit for Each Piston Blow

From Figure G-1 we see that the bridge output is a series of voltage
waveforms which are disjointed in time. Next, define $x(t)$ to be the
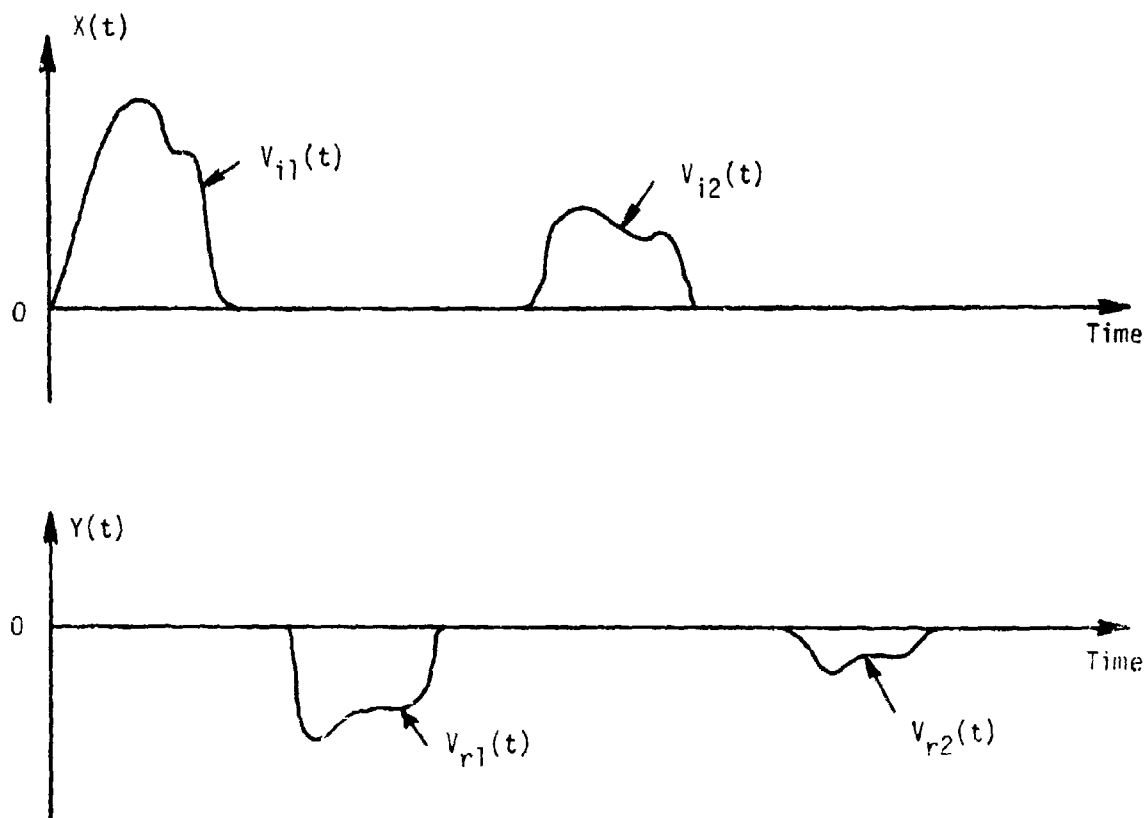positive voltages and $y(t)$ the negative voltages as shown in Figure G-2.

G-4

Fig. G-2. Bridge Output, v(t), Resolved into Positive Voltage
           Output, x(t) and Negative Voltage Output, y(t)

A device to separate v(t) into x(t) is easy to construct and will not be
discussed. For the purpose of reference we will choose to call this de-
vice a Quantizer.

Since x(t) and y(t) are disjointed in time, they are necessarily
orthogonal. From (H-11), we have

$$E_T = \sum_{j=1}^{n} W_{ij} - \sum_{j=1}^{n} W_{rj} = \sum_{j=1}^{n} KK_i^2 \int_{t_i}^{t_f} v_{ij}^2(t)dt - \sum_{j=1}^{n} KK_i^2$$

$$\int_{t_i}^{t_f} v_{rj}^2(t)dt \stackrel{\triangle}{=} KK_i^2 \int_{0}^{T} X^2(t)dt - KK_i^2 \int_{0}^{T} y^2(t)dt$$

(G-12)

The total amount of energy transferred to the rock for a large number of piston blows is difficult to obtain directly, but the average power (P_{ave}) transferred into the rock can be obtained easily by dividing the expression in (H-12) by the time interval, T: that is

$$P_{ave} = KK_1^2 \frac{1}{T}\int_0^T x^2(t)dt - KK_1^2 \frac{1}{T}\int_0^T y^2(t)dt \qquad (G-13)$$
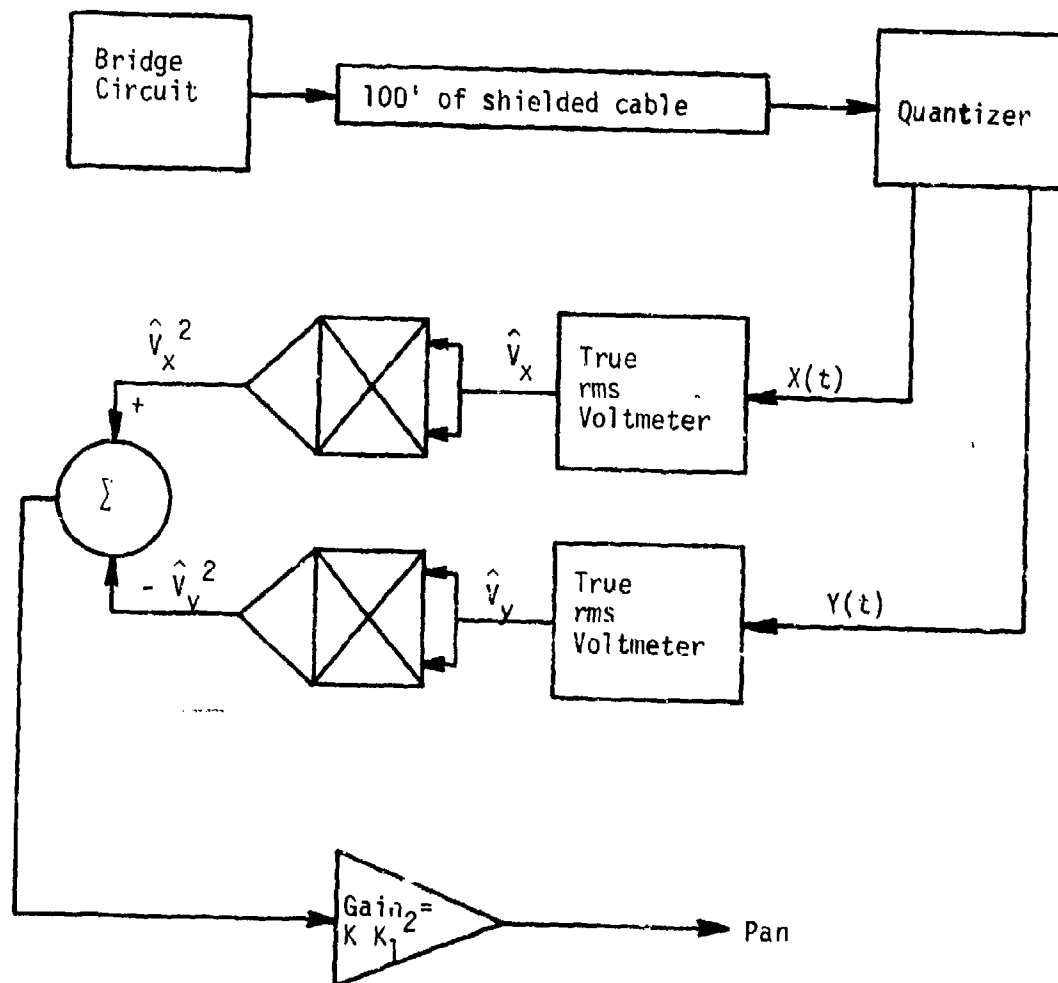
Since

$$\frac{1}{T}\int_0^T x^2(t)dt$$

equals the square of the rms value of $x(t)$ (similarly for $y(t)$), we have

$$P_{ave} = KK_1^2 \tilde{V}_x^2 - KK_1^2 \hat{V}_y^2 = KK_1^2(\hat{V}_x^2 - \hat{V}_y^2)$$

where $\hat{V}_x$ and $\hat{V}_y$ denote the rms values of $x(t)$ and $y(t)$ respectively.

G-6

Using the above logic, the following conditioning unit results:

Note that in actual practice it would be necessary to amplify $v(t)$ before connecting it to the Quantizer. This only changes the gain constant and the effect is easily determined.